UNIVERSITY OF NAPLES "FEDERICO II"

POLYTECHNIC AND BASIC SCIENCES SCHOOL

DEPARTMENT OF INDUSTRIAL ENGINEERING

THESIS MASTER'S DEGREE IN NAVAL ENGINEERING

HYDRODYNAMICS OF PLANING HULL BY CFD

SUPERVISOR

PROF. ERMINA BEGOVIC, PH.D.

CANDIDATE

MARCELLO IACONO

CORRELATOR

SIMONE MANCINI, PH.D. STUDENT

ACADEMIC YEAR 2014/2015

08 December 2015

Contents

He who becomes the slave of habit,
who follows the same routes every day,
who never changes pace,
who does not risk and change the colour of his clothes,
who does not speak and does not experience,
dies slowly.

He or she who shuns passion,
who prefers black on white,
dotting ones "it's" rather than a bundle of emotions, the kind that make your eyes glimmer,
that turn a yawn into a smile,
that make the heart pound in the face of mistakes and feelings,
dies slowly.

He or she who does not turn things topsy-turvy,
who is unhappy at work,
who does not risk certainty for uncertainty,
to thus follow a dream,
those who do not forego sound advice at least once in their lives,
die slowly.

He who does not travel, who does not read,
who does not listen to music,
who does not find grace in himself,
she who does not find grace in herself,
dies slowly.

He who slowly destroys his own self-esteem,
who does not allow himself to be helped,
who spends days on end complaining about his own bad luck,
about the rain that never stops,
dies slowly.

He or she who abandon a project before starting it,
who fail to ask questions on subjects he doesn't know,
he or she who don't reply when they are asked something they do know,
die slowly.

Let's try and avoid death in small doses,
reminding oneself that being alive requires an effort far greater than the simple fact of breathing.

Only a burning patience will lead
to the attainment of a splendid happiness.
Pablo Neruda

Abstract

The hydrodynamics performances of one monohedral hull and one warped hull are evaluated by utilizing the latest techniques in CFD. These two hulls are already experimentally studied by E. Begovic and C. Bertorello (2012) at Department of Naval Architecture, University of Naples Federico II, at steady speed in calm water. The code chosen was STAR CCM+, developed by CD-adapco, which can perform calculations of the discretized Reynolds Averaged Navier-Stokes (RANS) equations including viscous effects, turbulence modelling, and free surface constraints on unstructured adaptive grids. Hydrodynamics performances were also determined with empirical methods: resistance, trim and wetted surfaces through Savitsky method and longitudinal hydrodynamic pressure distribution through Morabito method. The results by experimental, empirical and numerical methods are compared.

Preface

An essential step in ship design is hydrodynamic performance evaluation. It allows the designer to determine whether a design will meet the given requirements. Several methods are commonly used, such as drawing on experience from similar vessels, using empirical data, or performing tests of a scaled-down prototype. For more advanced designs, the latter is preferred since these tests will generally give the best prediction of performance. Model tests, however, are costly, as they require the construction of a model prototypes to tight tolerances, as well as the use of a test facility and appropriate electronic instrumentation. An alternative to physical experiments is the use of numerical model tests where performance can be evaluated entirely by computer simulations. Although still being developed and improved, numerical simulations using computational fluid dynamics (CFD) techniques are now frequently used to augment, and occasionally replace, physical experiments. This is due to the potential of CFD for yielding both accurate and detailed predictions at a lower cost. Some of the strengths of numerical modelling have been summarized in the following excerpt:

"*Even though experimentation remains the tool most commonly used by designers to obtain accurate values of the hydrodynamic and aerodynamic forces acting on the boat, numerical simulations have some major advantages. In particular, they are relatively inexpensive and fast to use, so that it is possible to test and select different candidate geometries before setting up models for the towing tank or wind tunnel. Moreover, they allow the visualization of several quantities - such as the flow streamlines, the wave profiles or the pressure distribution - that are difficult to obtain from experiments. This is a very useful aid for the designer to understand the physics of the flow phenomena, at least from a qualitative point of view.*" (Caponnetto et al., 1998)

Research in the field of computational fluid dynamics (CFD) has progressed greatly over the last three decades as increases in computing power have made it possible to solve the equations governing fluid behaviour. These equations, which are generally unsolvable analytically (expect for a few special cases), can be approximated using numerical methods processed by a computer. The continuous domain of a problem is sub-divided into a series

of discrete points or elements. The governing equations are likewise discretized across these divisions. Complex differential equations are thereby transformed into a series of relatively simple coupled equations that can be solved by any number of numerical methods. This concept is not new, but the complexity of the equations and the enormity of the calculations have made its application impractical without the computational power of today's computers.

Acknowledgements

Although this thesis represents a very small drop in the ocean of research, I need to say that my work has been made possible by the constant support of my supervisor PROF. Ermina Begovic Ph.D and correlator Simone Mancini Ph.D student. They have represented to me not only a professional guide, but also a spiritual and mental guide always by my side to support and encourage me. You are a real example of devotion to the research and innovation.

The author gratefully acknowledge the availability of 32 processors at HPC Centre SCoPE of University of Naples "Federico II" and thanks to SCoPE academic staff for the given support.

List of Figures

List of Tables

Nomenclature

A_P projected area between chines, (m^2)

$A_P/V^{2/3}$ projected area to hull volume ratio, nondimensional

A_S total wetted spray area, (m^2)

A_{as} total area of whisker spray in both planes of bottom, (m^2)

a distance between D_f and CG (measured normal to D_f), (N)

B_C beam at chine, (m)

B_P B, b beam, (m)

B_{PA} mean beam over chines, $B_{PA} = A_P/L_P$

B_{PT} beam over chines at transom

B_{PX} maximum beam over chines

C_F frictional resistance coefficient according to ITTC57, $C_F = 0.075/(\log R_n - 2)^2$

C_f friction-drag coefficient, $C_f = D_f \cos\beta / \frac{\rho}{2} V_1^2 \lambda b^2$

C_{F-PA} frictional resistance coefficient of wetted surface $C_{F-PA} = C_F$

C_{F-WS} frictional whisker spray resistance coefficient

C_{L_0} lift coefficient at zero deadrise, $C_{L_0} = \Delta / \frac{\rho}{2} V^2 b^2$

C_{L_b} buoyant component of lift coefficient

C_{L_d} dynamic component of lift coefficient

$C_{L\beta}$ lift coefficient relative to dead rise angle β, $C_{L\beta} = \Delta / \frac{\rho}{2} V^2 b^2$

C_p distance of center of pressure (hydrodynamic force) measured along keel forward of transom, $C_p = l_p/\lambda b$

C_R residual resistance coefficient $C_R = C_{T-PA} - C_{F-PA}$

C_T total resistance coefficient

C_V Froude number based on beam $C_V = v/\sqrt{gB}$

C_Δ load coefficient $C_\Delta = \Delta/\rho g B^3$

CG center of gravity

c distance between N and CG(measured normal to N), (m)

D total horizontal hydrodynamic drag component, (N)

D_f frictional drag-force component along bottom surface, (N) $D_f = D cos\tau - \Delta sin\tau$

D_p resistance component due to pressure force, (N)

d vertical depth of trailing edge of boat (at keel) below level water surface, (m)

g acceleration of gravity, $9.80665\, m/s^2$

F_{rV} volumetric Froude number $F_{rV} = v/\sqrt{gV^{1/3}}$

F_s total viscous force in whisker spray area

f distance between T and CG (measured normal to T), (m)

h height of chine above BL, (m)

h_{SL} height of chine above BL at the intersection with stagnation line, (m)

h_{WS} height of chine above BL at the intersection with spray edge line, (m)

h^* height of chine at intersection with the mean wetted length of the whisker spray area, (m)

L_{OA} length over all, (m)

L_{A-B} length of clear part of models, (m)

L_b hydrostatic lift component, (N)

L_{CH}, L_C wetted chine length from transom, (m)

L_K wetted keel length from transom, (m)

L_M, L_m mean wetted length of the pressure area, (m) $L_M = L_{CH} + L_K/2$

L_{MWS} mean wetted length of the whisker spray area, (m) $L_{MWS} = 1/2\,(L_{SL} + L_{WS})$

L^*_{WS} characteristic whisker spray length, (m)

L_{SL} length of stagnation line, (m)

L_{WS} length of whisker spray edge, (m)

LCG longitudinal position of the centre of gravity from transom, (m)

L_1 difference between wetted keel and chine lengths, (m)

L_2 difference between keel and chine lengths wetted by level water surface, (m)

l_p distance from transom to point of intersection of hydrodynamic-force vector with keel (measured along the keel), (m)

N component of resistance force normal to bottom, (N)

R_T total resistance, (N)

R_{WS} resistance of whisker spray area, (N)

R_{BH} resistance of bare hull, (N) $R_{BH} = R_T - R_{WS}$

R_e Reynolds number, $R_e = V_1 \lambda b/\nu$

$R_{e_{WS}}$ Reynolds number of whisker spray, based on L^*_{WS}

T draught, (m)

T propeller thrust, (N)

T_{AP} draught at aft perpendicular, (m)

V horizontal speed of planing surface, (m/s)

V_1 mean velocity over bottom of planing surface, $f(\tau, \lambda)$, (m/s)

V displacement volume, (m^3)

VCG vertical position of the centre of gravity, from BL, (m)

WS wetted surface, (m^2)

$WS/V^{2/3}$ non dimensional wetted surface

WS_{PA} wetted surface of the pressure area, (m^2)

WS_{WS} wetted surface due to the whisker spray, area bounded by stagnation line, spray edge, and chine, (m^2)

Z_V sinkage at measured position, (m)

$Z_V/V^{1/3}$ non dimensional sinkage

α_{SL} angle between projected stagnation line and keel line, degrees

α_{WS} angle between projected spray edge and keel line, degrees

2α angle between spray edge and keel, assumed in Savitsky et al. (2006), degrees

β deadrise angle, degrees

β_e local deadrise of a warped hull, (deg)

β_T deadrise at transom, (deg)

β_X deadrise angle at B_{PX}, (deg)

Δ displacement, (N)

$\varepsilon_{SL} = \arcsin(h_{SL}/l_{SL})$ angle between stagnation line and BL plane, degrees

$\varepsilon_{WS} = \arcsin(h_{WS}/l_{WS})$ angle between spray edge of whisker spray area and BL plane, degrees

ϵ inclination of thrust line relative to keel line, degrees

τ running trim angle, degrees

τ_e trim angle of the ¼ buttock line relative to level water surface (hydrodynamic trim angle), (deg)

λ mean wetted length-beam ratio, $\lambda = (L_K - L_C)/2b$

$\Delta\lambda$ incremental increase in mean wetted length ratio due to whisker spray drag

λ_1 mean wetted length-beam ratio based on area below undisturbed water surface

ρ mass density of water, ω/g

ν kinematic viscosity of fluid, (S_t)

ω specific weight of water, (N/m^3)

γ angle between spray root line and keel line measured in plane parallel to keel, degrees

θ inclination of ¼ buttock line at λb relative to baseline projected on the plane of the keel, (deg)

$\vartheta = 2\alpha$ angle between the keel and spray edge measured in plane of bottom, degrees

DIN Department of Naval Architecture, University of Naples Federico II

HSC High Speed Craft

1 Introduction to planing hulls

1.1 Introduction

In each condition, static or dynamic, the weight of a craft is balanced by the pressure acting on the wetted surface. This pressure is composed by two components: hydrostatic, related to the buoyancy, and hydrodynamic, related to the speed of the craft. It is possible to classify the vessels according to the kind of pressure field acting during their steady motion:

- *displacement vessels*, if hydrostatic pressure is much higher than hydrodynamic ones
- *semi-displacement vessels*, if hydrostatic and hydrodynamic pressure have the same order of magnitude
- *planing vessels*, if hydrostatic pressure is much lower than hydrodynamic ones.

Per each family of craft, or per each kind of pressure field, there is a hull form that is the best one for achieving the lower value of resistance. Naval Architects commonly classify vessels in these three families (displacement, semi-displacement and planing) according to the vessel relative speed defined by Froude number F_r

$$F_r = \frac{V}{\sqrt{g L_{WL}}} \tag{1.1}$$

where V is the craft speed in m/s, L_{WL} is the waterline length in m and g is the acceleration of gravity m/s^2, we have:

- displacement vessels $F_r \leq 0.4$
- semi-displacement vessels $0.4 \leq F_r \leq 1.0$
- planing vessels $F_r > 1.0$

As the waterline length L_{WL} is not a constant and known quantity for semi-displacement and planing craft, another two definitions of F_r are used:

- the wetted beam B

$$F_{r_b} = \frac{V}{\sqrt{gB}} \qquad \text{beam Froude number} \qquad (1.2)$$

- the "volume" length $\nabla^{\frac{1}{3}}$

$$F_{r_V} = \frac{V}{\sqrt{g\nabla^{\frac{1}{3}}}} \qquad \text{volumetric Froude number} \qquad (1.3)$$

From an experimental point of view, a craft is in planing condition if $F_{r_b} > 3.0$ or $F_{r_V} > 5$.

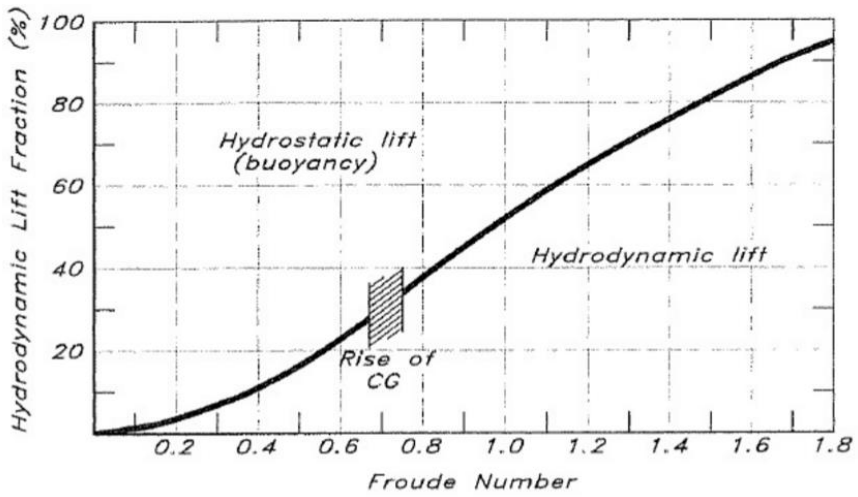

Fig. 1.1 Variation of forces acting on the hull according to Froude number

1.2 Characteristics of planing hulls

Planing occurs when the boat is travelling fast enough and the major part (more than 50%) of its weight to be supported by hydrodynamic forces, rather than hydrostatic force. The speed at which this occurs depends on the hull shape. The development of the phenomenon of planing is a gradual one: at very low speeds, the hydrodynamic effect is negative; the speed of the water over most of the hull surface is greater than that of the

forward speed of the boat, and this causes a drop in pressure. The suction forces the boat to squat, and also to assume a trim.

It is only when the speed increases sufficiently for the flow to separate from the bottom of the transom, that the form of the pressure distribution on the hull surface changes significantly and generates an upward force and a bow-up moment. For this reason, planing is commonly associated with the transom stern becomes dry.

Fig. 1.2 shows a typical high-speed planing hull. In order to avoid negative pressures relative to atmospheric pressure on the hull at high speed, it is essential to have flow separation at the transom and along the sides.

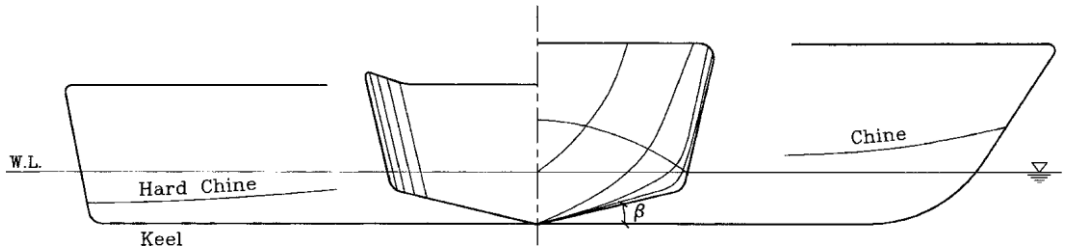

Fig. 1.2 Typical high-speed planing hull

Flow separation along the sides is usually accomplished by using a hard chine. A typical deadrise angle is 10° to 15° at the stern and up to a 35° (today even more) at the bow. The hard chines can be one or more.

A double-chine hull is shown in Fig. 1.3. The flow will separate from the lower chine at high speed, whereas the upper chine provides a large local beam at low speed. This is beneficial from a transverse hydrostatic stability point of view at zero speed. The position of the upper chine must be selected to avoid the separating flow from the lower chine at high speed from reattaching to the hull.

Some very fast planing boats are designed with the step. The flow will separate from the step at high speed, and the after body will be partially ventilated, reducing the wetted surface and hence the resistance without significantly affecting the hydrodynamic lift. The ventilated length is shortest along the keel. It increases with speed and is dependent on the height of the keel in the flow attachment area above the keel before the step.

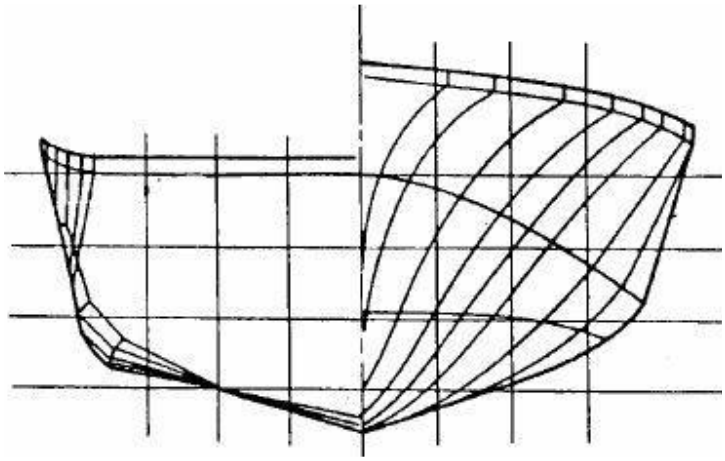

Fig. 1.3 Double-chine hull

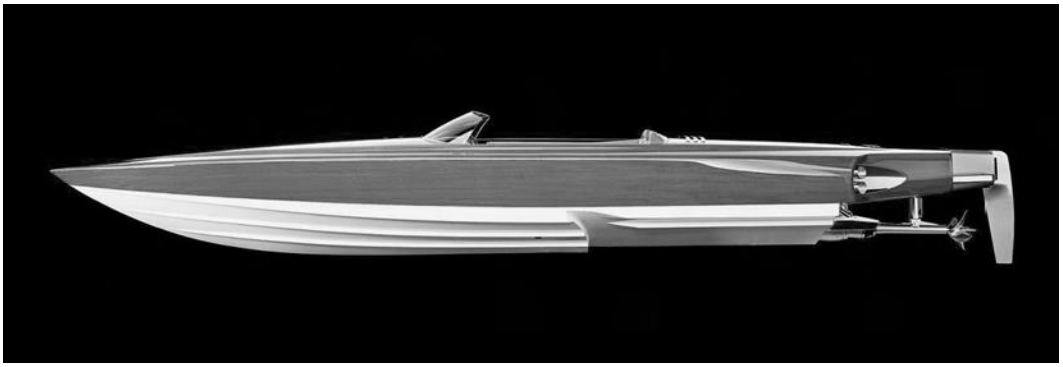

Fig. 1.4 The Alpha-Z stepped planing hull designed by Michael Peters

When the step is wet at lower speeds, vortex separation occurs at the step. This increases the resistance relative to no step. The viscous drag associated with a wet step is, roughly speaking, proportional to the step height.

Another feature of planing craft is the series of longitudinal spray rails (or spray strips). In addition to reducing the spray, rather like miniature chines, they help to define the actual wetted surface when under way. As the boat accumulates speed, it rises out of the water, and successive spray rails come into play. The only two spray rails that materially influence the water flow in this way are the last ones on each side that are still submerged. Spray rails are also fitted at the chine itself in order to increase its effects.

All these characteristics (hard chine, transom stern, step, spray rail) allow to reduce the wetted surface and trim angle in planing condition and so to reduce the resistance.

1.3 Hydrodynamics features evaluation

Generally, the total resistance can be divided in following components:

$$R_T = R_H + R_{AP} + R_A + R_{PAR} \tag{1.4}$$

where R_T is the total resistance, R_H is the bare hull drag (75-80% R_T), R_{AP} is the appendages drag (10-12% R_T), R_A is the air drag (7-8% R_T), R_{PAR} is the parasitic drag (1% R_T). Bare hull drag is a function of pressure drag and water frictional drag. The water frictional drag is often broken down into two categories, pressure area drag and spray area drag. To evaluate the appendages and air drag (e.g. skeg, rudder, shaft, strut barrel, bilge keel, etc.) we can utilize the equations present in the technical literature. The parasitic drag (e.g. all openings on the hull due ballast system) is often neglected not also because is the lower but because the technology implementation has much improved.

Bare hull drag can be evaluated by several methods:

- Experimental method (e.g.: Froude method)
- Empirical methods (e.g.: Savitsky' method [Savitsky 1964], Morabito [Ph.D Thesis 2010])
- Systematic series (e.g.: Series 62, Series 65, Series 62 Dutch, BK and MBK series, Kowalyshyn and Metcalf [2006], Taunton et al. [2011], Begovic and Bertorello [2012], De Luca and Pensa [2014])
- Statistical methods (e.g.: Radojcic's method [1985])
- CFD (Computational Fluid Dynamics)

In the following paragraphs will be given a brief introduction to experimental method, statistic method and systematic series. Empirical and numerical methods will be discussed in detail in the next chapters.

1.3.1 Froude method

The Froude method, considers the total model resistance as the sum of a frictional resistance component and a residuary resistance component. Under his hypothesis the two are separated and each scaled differently. The frictional component is scaled on Froude's experiments with flat plates towed under water. The residuary resistance is scaled by imposing the coefficient of residuary resistance to be the same for two geometrically similar ships traveling at corresponding speeds.

$$R = R_R + R_F = R_R + R_W = \frac{1}{2}\rho S V^2 C_F + \frac{1}{2}\rho S V^2 C_W$$

$$C_F = \frac{0.075}{(\log_{10} R_n - 2)^2}$$

$$C_W = C_R = C_T - (1 + k)C_F$$

Over the years towing tank facilities in different countries developed improvements to the basic Froude approach. In 1978 the International Towing Tank Congress (ITTC) adopted a updated standardized procedure for performing ship resistance experiments and calculations. The ITTC-78 method considers the total model resistance as the sum of a viscous component and a wave making component. The viscous component uses the 1957 ITTC friction line to estimate a frictional resistance coefficient. To include the effect of hull shape and viscous pressure drag a form factor is estimated and applied to the frictional resistance coefficient to make a viscous resistance coefficient. Froude's hypotheses is still applied to the wave making resistance, where the coefficient of wave making resistance is the same for two geometrically similar ships traveling at the same Froude number.

ITTC-78 method

For all model tests, we have to choose a scale λ. The size of the model will be restricted by the size of the tow tank facilities, available carriage speeds, and instrumentation. The geometric scale is

$$\lambda = \frac{L_S}{L_M} \qquad (1.5)$$

so all the lengths are scaled by λ, surface areas scaled by λ^2, and volumes and forces scaled by λ^3.

From the test results, we measure C_{TM} at each speed

$$C_{TM} = \frac{R_{TM}}{\frac{1}{2}\rho_M V_M^2 S_M} \tag{1.6}$$

where R_{TM} is the total model resistance measured, ρ_M is the fresh water density, V_M is the model speed and S_M is the model wetted surface.

The model frictional resistance coefficient C_{FM} using the ITTC-57 Model-Ship Correlation Line at each speed is given by

$$C_{FM} = \frac{0.075}{(\log_{10} R_{n_M} - 2)^2} \tag{1.7}$$

where

$$R_{n_M} = \frac{V_M L_M}{\nu_M} \tag{1.8}$$

and ν_M is the cinematic viscosity.

So, we can calculate the form factor k

$$\frac{C_{TM}}{C_{FM}} = (1 + k) + y\frac{F_r^4}{C_{FM}} \tag{1.9}$$

where k is the 3-D form factor and y is a coefficient (slope of the line). The residuary resistance coefficient $C_{RM} = C_{RS} = C_R$ at each speed is

$$C_R = C_{TM} - (1 + k)C_{FM} = C_W \tag{1.10}$$

Thus, we calculate the ship frictional resistance coefficient C_{FS} using the ITTC-57 Model-Ship Correlation Line at each speed

$$C_{FS} = \frac{0.075}{\left(\log_{10} R_{n_S} - 2\right)^2} \tag{1.11}$$

where

$$R_{n_S} = \frac{V_S L_S}{\nu_S} \tag{1.12}$$

and ν_S is the cinematic viscosity.

We evaluate the roughness allowance coefficient

$$C_A = \left(105\left(\frac{k_S}{L_{WL}}\right)^{1/3} - 0.64\right) * 10^{-3} \quad (1.13)$$

where k_S is the measure of surface roughness (default value is $150 * 10^{-6}$ meters) and L_{WL} is the length on the waterline.

We calculate the air resistance coefficient

$$C_{AA} = \frac{A_{VT}}{1000\,S} \quad (1.14)$$

where A_{VT} is the projected front area of the above water ship.

So, the total ship resistance coefficient is

$$C_{TS} = (1 + k)C_{FS} + C_W + C_A + C_{AA} + C_{Appendages} \quad (1.15)$$

and the total ship resistance for each speed is

$$R_{TS} = \frac{1}{2}\rho_S V_S^2 S_S C_{TS} \quad (1.16)$$

1.3.2 Statistical methods

The most used statistical method for planing hulls is that of Radojcic (1985). He presented two different regression models, based on the Series 62, Dutch Series 62 and Series 65B, for predicting the resistance and trim angle of bare stepless planing hulls in calm water. Volumetric Froude numbers covered are 1 to 3.5 for resistance and 1 to 4 for trim angle. The mathematical model based on the regression analysis of four hull forms and loading parameters (loading coefficient (area coefficient), ratio of length to beam, longitudinal center of gravity location, deadrise angle at 50% of L_P) and section shape. The presented method makes it possible to estimate the resistance of planing hulls in the early stage of design and is suitable for programming. The body plans of the three series are shown in Fig. 1.5, Fig. 1.6 and Fig. 1.7 and the parameters of the models are given in Tab. 1.2 and Tab. 1.3.

Parameters ranges	
$A_P/\nabla^{2/3}$	5,25 – 9,50
$\frac{LCG}{L_P} * 100$	30,0 – 44,8
L_P/B_{PA}	2,36 – 6,73
β, deg	13,0 – 37,4

Tab. 1.1 Particulars covered by mathematical regression, Radojcic (1985)

1.3.3 Systematic series

In a systematic series the hull models are generally developed by stretching or compressing a parent hull keeping some hull parameters constant while others are systematically varied. The most important planing hulls systematic series are:

- Series 62
- Series 65
- Series 62 Dutch
- BK series
- MBK series
- Kowalyshyn D. and Metcalf B. Series (2006)
- Taunton D. J. et al. Series (2011)
- Begovic E. and Bertorello C. Series (2012)
- De Luca F. and Pensa C. Series (2014)

Series 62 was developed in the early 60s. The body plan is given in Fig. 1.5. The series differs from modern designs in:

- Narrow transom
- Exceptionally blunt bow
- Maximum chine beam forward of midship

Five models, Models 4665, 4666, 4667-1, 4668 and 4669, were tested to explore the influence of length-beam ratio. The values of length-beam ratio tested in the series correspond to values of 2.00, 3.06, 4.09, 5.5 and 7.00. The speed range was from $F_{rv} = 0{,}2$ up to 6.00. The values of $\frac{A_p}{\nabla^{\frac{2}{3}}}$ tested were $5.5, 7.0, 8.5$. The LCG location were

$0, 4, 8, 12$ percent L_P aft of the centroid. Additional particulars of the models are given in Tab. 1.2.

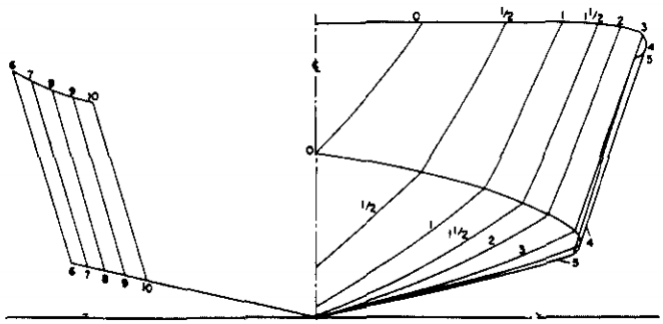

Fig. 1.5 Series 62 parent

Particulars	Models				
	4665	4666	4667-1	4668	4669
A_p (sq ft)	6,469	9,715	12,800	9,518	7,479
L_P (ft)	3,912	5,987	8,000	8,000	8,000
B_{PA} (ft)	1,654	1,623	1,600	1,190	0,935
B_{PX} (ft)	1,956	1,956	1,956	1,455	1,143
B_{PT} (ft)	1,565	1,386	1,250	0,934	0,734
L_P/B_{PA}	2,365	3,69	5,00	6,72	8,56
L_P/B_{PX}	2,00	3,06	4,09	5,50	7,00
B_{PX}/B_{PA}	1,18	1,21	1,22	1,22	1,22
B_{PT}/B_{PX}	0,80	0,71	0,64	0,64	0,64
x_p (ft)	0,475	0,482	0,488	0,488	0,488
β (deg)	13.0	13.0	13.0	13.0	13.0
β_T (deg)	12.5	12.5	12.5	12.5	12.5
LCG/L_P	0,41	0,42	0,43	0,43	0,43

Tab. 1.2 Particulars of the models of DTMB Series 62

Series 65 is divided in two series: Series 65A and Series 65B, each with its own unique parent hull, Fig. 1.6. Series 65A and 65B both have a fine and high deadrise fore body characteristic of pre-planing designs. Series 65A's exceptionally narrow stern (high beam taper) is unconventional and limits its applicability as a resistance prediction method. Series 65A is not normally used. In the Series 65 nine models were tested. The models experiments were conducted in the towing tank at Langley Field, Virginia. The speed range varies from $F_{rv} = 1{,}0$ up to $4{,}00$. The values of $\frac{A_p}{\frac{2}{V^3}}$ tested were $5.0, 5.5, 7.0, 8.5$. The series was also tested at low speeds only for $\frac{A_p}{\frac{2}{V^3}} = 4.00$. The series was tested by running the models at fixed weights and fixed trims. The speed range vary from $\tau = 0$ up to 8 degrees. The resistance is presented in the report in tabular and graphical forms at model scale as a function of dynamic or planing trim and weight for each model. Particulars of the models are given in Tab. 1.3.

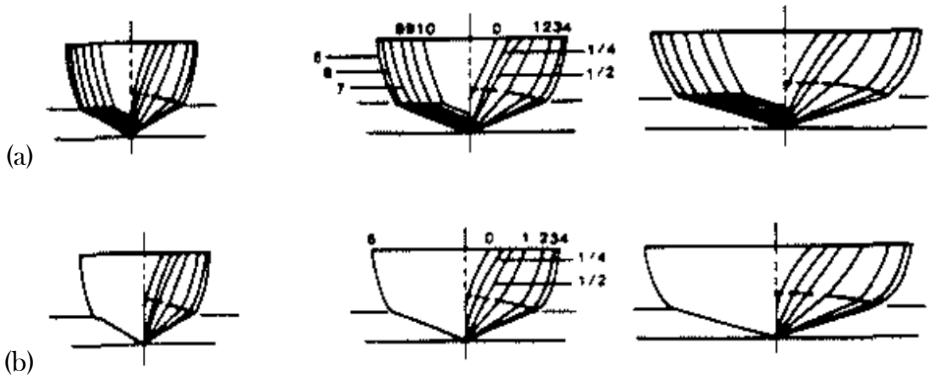

Fig. 1.6 Series 65-A (a) and series 65-B (b)

Particulars	Models								
	5237	5240	5239	5186	5184	5167	5236	5208	5238
L_P (ft)	6,142	6,142	8,687	6,142	6,142	8,687	6,142	8,687	8,687
A_p (sq ft)	11,85	8,38	11,85	8,38	5,92	8,38	5,92	8,38	5,92
B_{PA} (ft)	1,923	1,364	1,364	1,364	0,965	0,965	0,965	0,965	0,682
B_{PT} (ft)	2,600	1,838	1,838	1,838	1,300	1,300	1,300	1,300	0,919
B_{PX} (ft)	2,618	1,852	1,852	1,852	1,309	1,309	1,309	1,309	0,925
L_P/B_{PA}	3,18	4,50	6,36	4,50	6,36	9,00	6,36	9,00	12,73

L_P/B_{PX}	2,35	3,32	4,69	3,32	4,69	6,64	4,69	6,64	9,38
B_{PX}/B_{PA}	1,36	1,36	1,36	1,36	1,36	1,36	1,36	1,36	1,36
B_{PT}/B_{PX}	0,99	0,99	0,99	0,99	0,99	0,99	0,99	0,99	0,99
x_p (ft)	0,387	0,387	0,387	0,387	0,387	0,387	0,387	0,387	0,387
β (deg)	21.2	21.2	21.2	28.7	28.7	28.7	37.4	37.4	37.4
β_T (deg)	16.3	16.3	16.3	22.5	22.5	22.5	30.4	30.4	30.4
LCG/L_P	0,38	0,38	0,38	0,38	0,38	0,38	0,38	0,38	0,38

Tab. 1.3 Particulars of the models Series 65-B

The Dutch Series 62 was developed in the late 70s. It is a high-deadrise (25 deg) version of Series 62. The parent of the series is given in Fig. 1.7. The models number and characteristics are the same of the original Series 62, but with $\beta = 25.0°$. This series was tested at an even greater displacement range than the original Series 62. The data are presented in graphical and tabular formats at model size, and 10 000 and 100 000 lb scaled displacements as done in the original series. The series is particularly interesting at the extremes of the loading range.

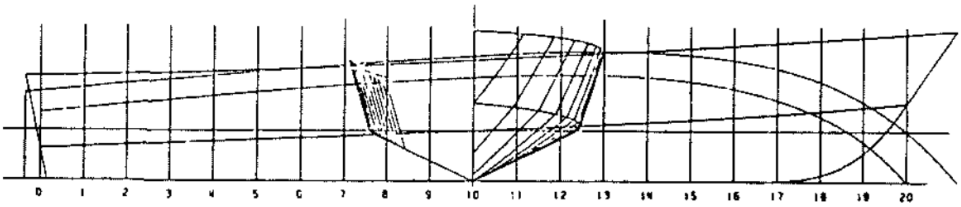

Fig. 1.7 Dutch series 62 parent

BK Series is an semi-planing series tested in the 60s by the Soviets. Series BK was composed by nine hull models with the same dimensions and different hull shape. The BK Series can be broken down into two separate groups. In the first group the principal nondimensional variables like Lp/Bp were kept constant and the hull shape was varied to determine its effect on resistance. The second group of the series kept the hull shape constant, shown in Fig. 1.8, and varied the nondimensional variables like Lp/Bp. In term of F_{rv}, the speed range was about 1.0 up to 4.5. The LCG locations, as percent of L_P

forward the transom stern, was about 0.35 up to 0.45; and in term of C_Δ the range was about 0.427 up to 0.854.

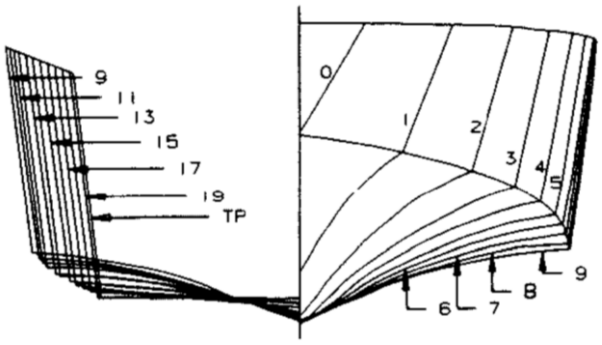

Fig. 1.8 BK series parent

MBK Series is very similar to the BK Series but differs in the parent, Fig. 1.9. The MBK Series was tested in the early 70s and is oriented towards smaller semi-planing hulls.

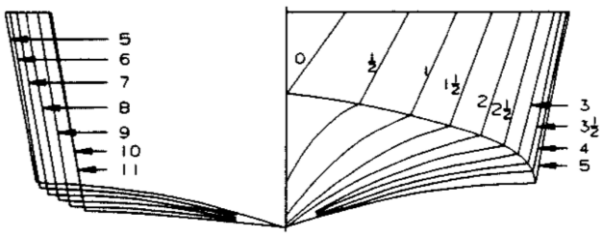

Fig. 1.9 MBK series parent

Ikeda et al.(1993) experimentally studied a series of hard-chine hulls with L/B variation from 3 to 6, Fig. 1.10. The deadrise angle of the series B vessels were kept constant while the dead rise angle of the series A ships become zero at transom stern. The result of these tests is that the Savitsky method can be used for non-monohedral hulls at Froude numbers higher than 0.9, choosing as "reference" deadrise angle the angle at the forward section midway the first keel wetted section and the first chine wetted section.

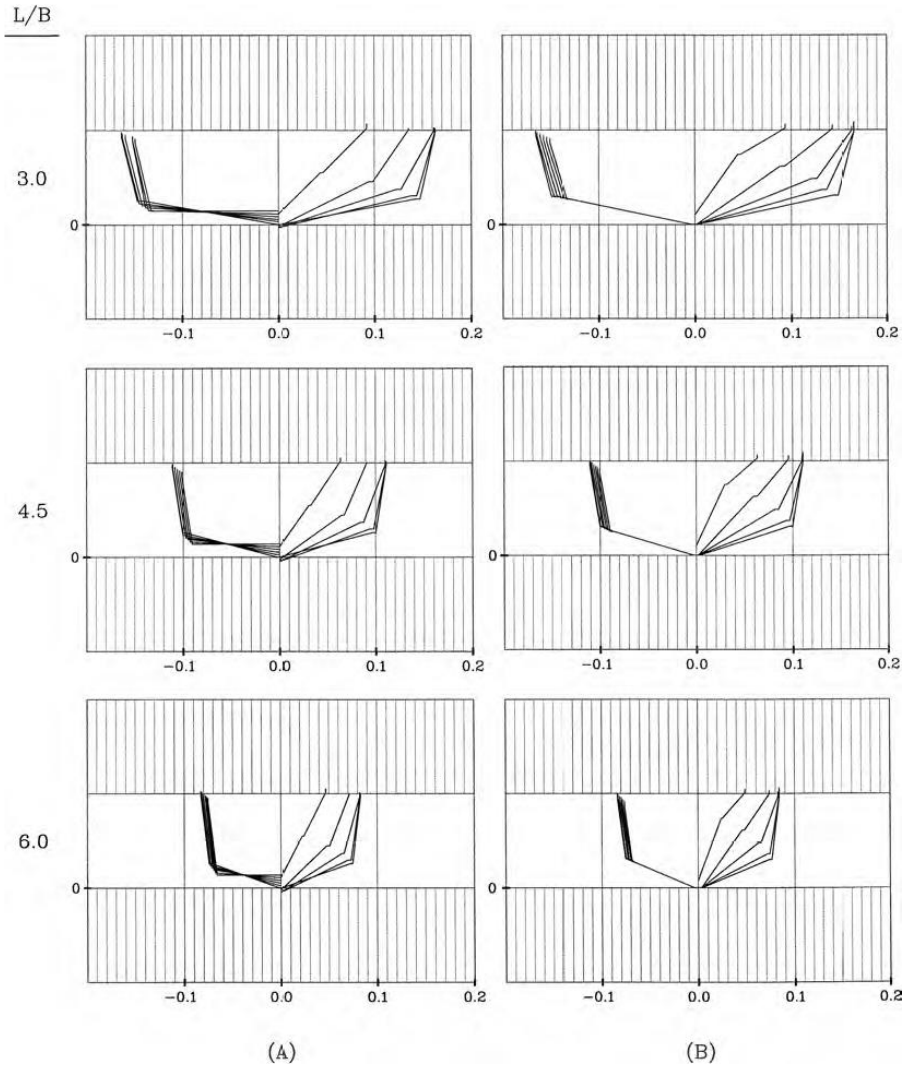

Fig.1.10 Body plans of planing vessels with hard chines studied by Ikeda et al. (1993)

Metcalf et al. (2005) and Kowalyshyn and Metcalf (2006) published the results of resistance experiments on a systematic series of models based on the United States Coast Guard 47-foot Motor Lifeboat (MLB) hull form, shown in Fig. 1.11. The series includes parent model 5628 which is substantially the MLB hull, other two models 5629 and 5630 with varied length-to-beam ratios and one model 5631 with transom deadrise angle variation. Each model has the same projected chine length L_p and projected planing area centroid A_p. Resistance tests were completed for a range of conditions, with displacements varying from 298 lbs to 680 lbs and longitudinal centre of gravity located at 38% and 42% of the length between perpendiculars in the C_v range from 1 to 6. Model particulars are given in Tab. 1.4.

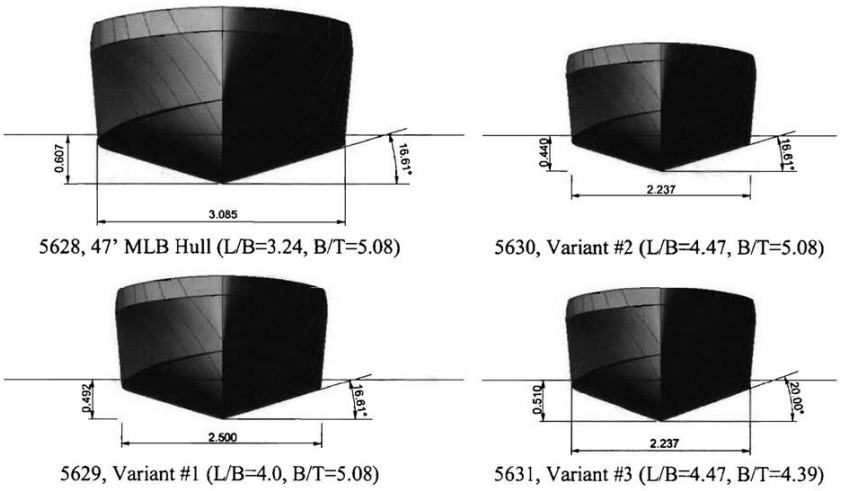

Fig. 1.11 Body plans of USCG systematic series models, Metcalf et al. (2005)

Model No.	Parent 5628	Variant 1 5629	Variant 2 5630	Variant 3 5631
LBP ft (m)	10 (3,05)	10 (3,05)	10 (3,05)	10 (3,05)
$Beam$ ft (m)	3,09 (0,94)	2,5 (0,76)	2,44 (0,68)	2,24 (0,68)
Draft ft (m)	0,61 (0,18)	0,49 (0,15)	0,44 (0,14)	0,51 (0,16)
L/B	3,24	4,0	4,47	4,47
B/T	5,08	5,08	5,08	4,39
β, deg	16,61	16,61	16,61	20,00
∇, ft^3 (m^3)	8,05 (0,23)	5,29 (0,15)	4,24 (0,12)	4,88 (0,14)

Tab. 1.4 Particulars of the models, Metcalf et al (2005)

Taunton et al.(2011) developed a series of four monohedral hulls given in Fig. 1.12 and Fig. 1.13, where L/B ranged from 6.25 to 3.77 corresponding to $\frac{L}{\nabla^{\frac{1}{3}}}$ from 8.70 to 6.25 and constant deadrise angle of 22.5 degrees. The speed range was from $F_{rv} = 2.71$ up to 8.02. For this systematic series there are also data of seakeeping performances in irregular sea. Model particulars are given in Tab. 1.5.

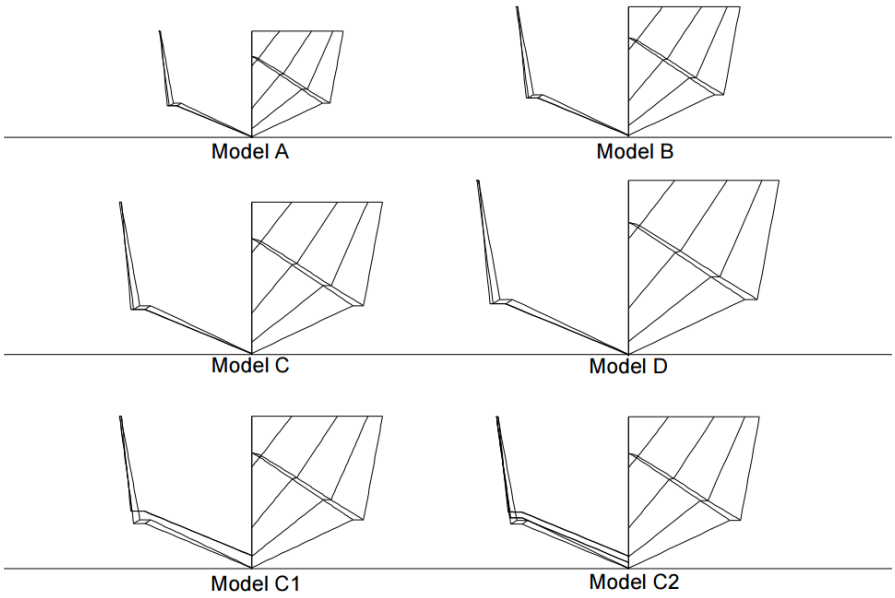

Fig. 1.12 Body plans of Southampton systematic series models, Taunton (2011)

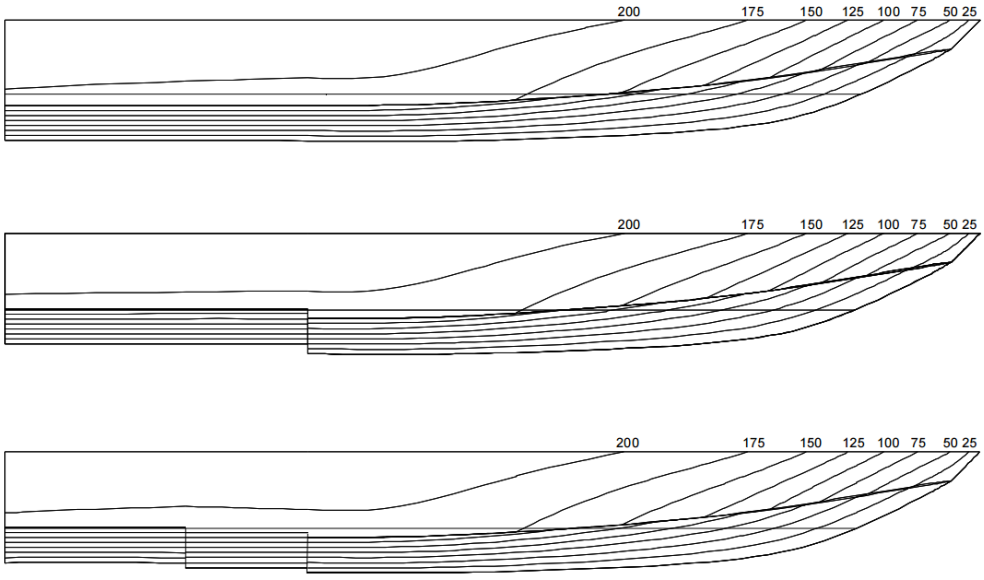

Fig. 1.13 Model profiles (Models A-D, Model C1, Model C2), Taunton (2011)

Model	A	B	C	D
L (m)	2,0	2,0	2,0	2,0
B (m)	0,32	0,39	0,46	0,53
T (m)	0,06	0,08	0,09	0,11
Δ (N)	119,25	175,83	243,40	321,95
$L/\nabla^{1/3}$	8,70	7,64	6,86	6,25
L/B	6,25	5,13	4,35	3,77
β, deg	22,5	22,5	22,5	22,5
LCG, $\%L$	0,33	0,33	0,33	0,33

Tab. 1.5 Particulars of the models, Taunton (2011)

E. Begovic and C. Bertorello (2012) developed a series of hard chine planing hull forms at Department of Naval Architecture, University of Naples. Three warped and one monohedral hulls were designed. The profiles of the models are reported in Fig. 1.14. The models have the same transversal section with 16.7 degrees deadrise angle at 0.25 L from the stern. Warped models had deadrise angle linearly varying along the hull length. Aim of the experimental program is the evaluation of the effect of deadrise angle variation along the hull length on hydrodynamic resistance and on seakeeping. The models have clear polycarbonate bottom to allow flow visualization and accurate wetted surface assessment. Resistance tests were performed for speed coefficient C_V ranging from 0.56 to 3.92 and for two load coefficient values: $C_\Delta = 0.428$ and 0.392. Reported results are wetted lengths of pressure area and whisker spray area, projected angles of stagnation line, wetted surface and whisker spray area, residual resistance coefficient, sinkage, presented in standard non-dimensional form, and running trim. Model particulars are given in Tab. 1.6.

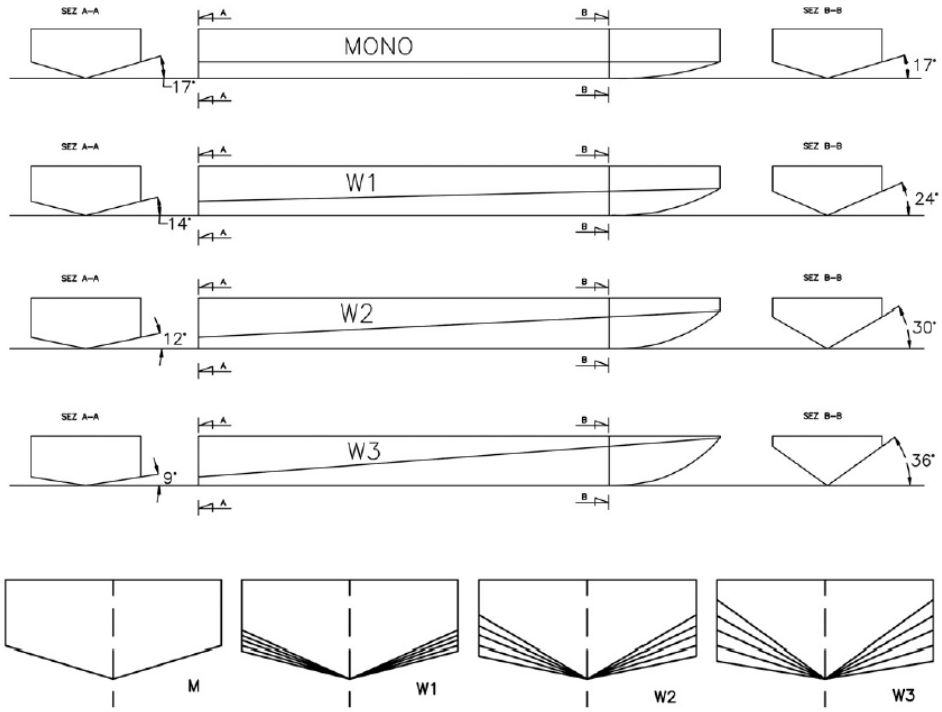

Fig. 1.14 The profile of DIN systematic series models

	MONO	WARP 1	WARP 2	WARP 3
L_{OA} (m)	1,900	1,900	1,900	1,900
L_{A-B} (m)	1,500	1,500	1,500	1,500
B (m)	0,424	0,424	0,424	0,424
T_{AP} (m)	0,096	0,106	0,110	0,108
Δ_1 (N)	319,697	320,383	319,697	318,520
$C_{\Delta 1}$	0,4277	0,4287	0,4277	0,4262
LCG (m)	0,697	0,660	0,609	0,586
VCG (m)	0,143	0,152	0,155	0,156
τ (deg)	1,660	1,660	1,660	1,660
Δ_2 (N)	286,354	287,531	287,433	289,885
$C_{\Delta 2}$	0,391	0,392	0,392	0,395
F_{r_V}	0,650 – 4,518	0,650 – 4,518	0,650 – 4,518	0,650 – 4,518
C_V	0,564 – 3,660	0,564 – 3,660	0,564 – 3,660	0,564 – 3,660
β	16,70	14,31 – 23,75	11,59 – 30,11	9,09 – 35,75

Tab. 1.6 Particulars of the models, Begovie and Bertorello (2012)

F. De Luca and C. Pensa (2014) experimentally studied a series of hard-chine hulls in planing and semiplaning speed range. Four warped models have been derived from a parent hull (Fig. 1.15). To simplify the construction of vessels with rigid panels (aluminium alloy, plywood or steel) the original hull form has been transformed to obtain developable hull surfaces. In the speed ranges $F_r = 0.5 - 1.6$ and $F_{r_V} = 1.1 - 4.2$, the series studies the influence of length-beam and length-displacement ratios that vary respectively in the ranges $3.45 - 6.25$ and $4.50 - 8.17$. Each model has been tested at two displacement and two longitudinal position of centre of gravity. At the same values of displacement and centre of gravity, the models have been tested with and without interceptors. Model particulars are given in Tab. 1.7.

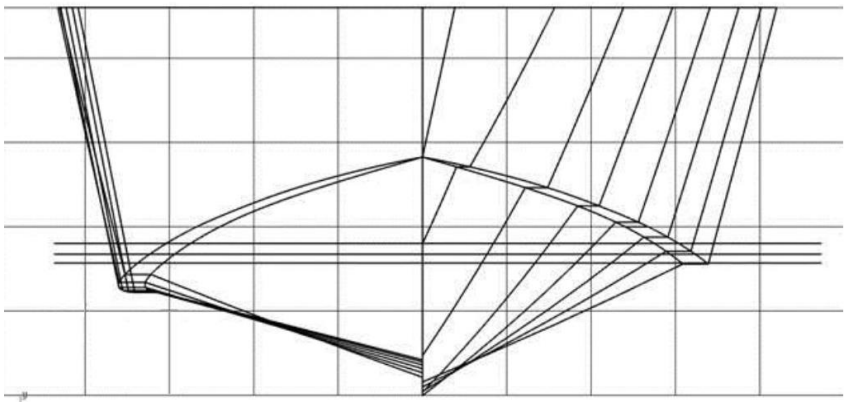

Fig. 1.15 C1 parent hull, F. De Luca and C. Pensa (2014)

Model	Scale factor	L/B	$L/\nabla^{\frac{1}{3}}$
C1	/	3,45	4,82 – 5,27
C2	0,888	3,89	5,00 – 5,73
C3	0,775	4,45	5,46 – 6,23
C4	0,664	5,19	5,80 – 6,97
C5	0,552	6,25	6,54 – 7,82

Tab. 1.7 Particulars of the models, De Luca and Pensa (2014)

2 Empirical methods

2.1 Savitsky method

To evaluate the hydrodynamic characteristics of a planing hull, two hypotheses have been introduced:

1. Monohedral hull, that is characterized with a constant deadrise angle β at least for aft half of the hull
2. Purely hydrodynamic condition, that is the condition in which the weight W of the hull is only balanced by the lift L

The first hypothesis allows to assimilate the bottom of a planing hull, in particular the aft half of the hull that is in contact with the water at planing speed, to a V plate of which we study the equilibrium.

2.1.1 Wave rise for flat planing surfaces

In the case of planing surfaces with no deadrise (flat bottom planing surfaces), water rises in front of the surface, thereby causing the running wetted length λ to be larger than the length defined by the undisturbed water level intersection with the bottom λ_1, Fig. 2.1. Wagner (1932) had made a mathematical study of the flow at the leading edge of a planing surface of infinite length and found that the rising water surface, mentioned in the foregoing, blends into a thin sheet of water flowing forward along the planing surface. This sheet is a source

of a spray in a planing surface and the region of its origin has been designed by Wagner as the ''spray-root'' region.

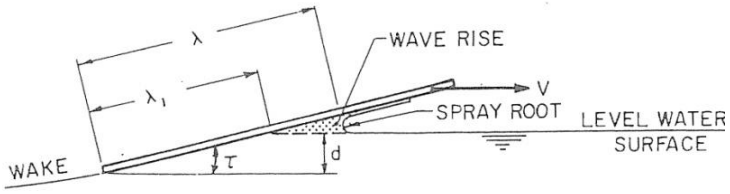

Fig. 2.1 Wave rise on a flat planing surface

Fig. 2.2 shows the spray root and the pressure distribution resulting from it. The term wetted area designates that portion of the wetted area over which water pressure is exerted and excludes the forward thrown spray sheet. The wetted area used in this sense is often designed in the literature as the ''pressure area'' and geometrically, includes all the wetted bottom area, aft of a line drawn normal to the planing bottom and tangent to the curve of the spray root. This line is clearly discernible from underwater photographs. As seen in Fig. 2.2, the stagnation pressure is developed at a short distance aft of the spray root. At very small values of trim angle the stagnation line and spray root line are nearly coincident. As the trim angle increases, the stagnation line moves farther aft of the spray root line.

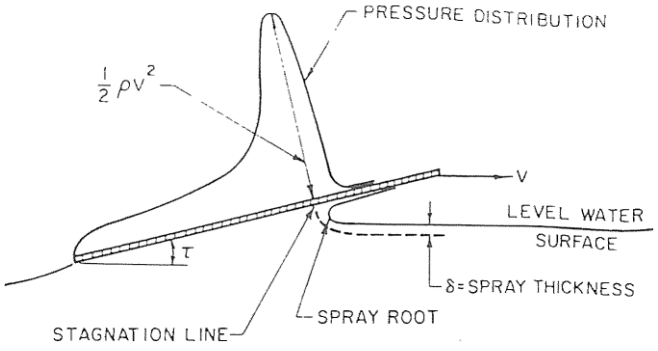

Fig. 2.2 Typical pressure distribution on flat planing surface

Flat plate wetted length data from all variable sources are shown plotted in the form of λ versus λ_1 in Fig. 2.3. Here λ represents the running mean wetted length to beam ratio and λ_1 represents the calm water length-beam ratio obtained from the relation $\lambda_1 = d/B\,sin\tau$, where d is the depth of the trailing edge of the planing surface below the level water surface during a planing run.

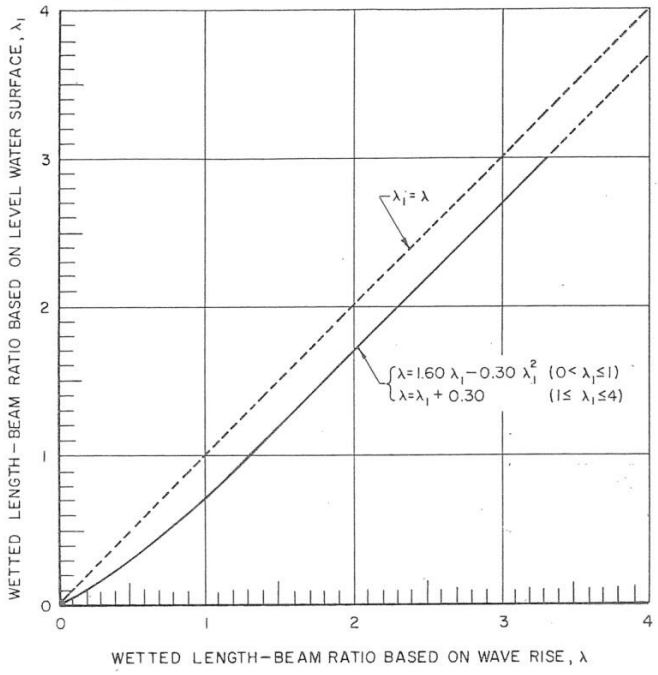

Fig. 2.3 Wave-rise variation for flat planing surfaces

The mean curve fitted through the test data is defined by the following empirical equations:

$$\lambda = 1.60\,\lambda_1 - 0.30\,\lambda_1{}^2 \qquad (0 \leq \lambda_1 \leq 1)$$

and (2.1)

$$\lambda = \lambda_1 + 0.30 \qquad (1 \leq \lambda_1 \leq 4)$$

The empirical wave-rise relation is given in the form of two equations since, for the average planing case, λ_1 is usually larger than unit and thus equations are reduced to very simple form of $\lambda = \lambda_1 + 0.30$. Equation (2.1) is applicable in the trim range from 2 to 24 deg; $\lambda \leq 4.0$; and $0.60 \leq Cv \leq 25.00$.

2.1.2 Wetted pressure area of deadrise planing surfaces

In the case of V-shaped planing surfaces, the intersection of the bottom surface with the undisturbed water surface is along two oblique lines (O-C) between the keel and chines, Fig. 2.4. Up to a trim angle of approximately 15 deg there appears to be no noticeable pile-up of water at the keel line. Aft of the initial point of contact, O, there is a rise of the water surface along the spray root line (O-B) located ahead of the line of calm water intersection. The location of the spray root line is easily seen from underwater photographs. It is generally found that the spray root line is slightly convex, but since the curvature is small, it is neglected. Thus the mean wetted length of a deadrise surface is defined as the average of the keel and chine lengths measured from the transom to the intersection with the spray root line.

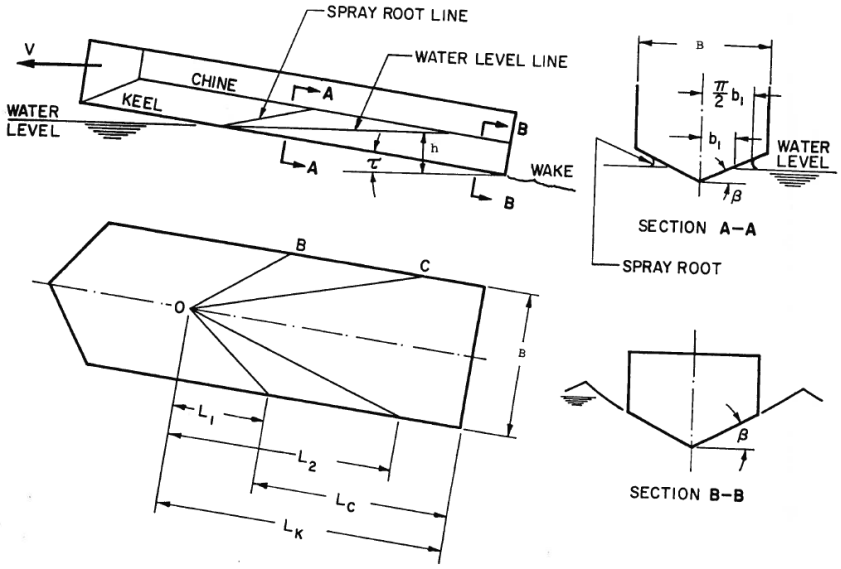

Fig. 2.4 Waterline intersection for constant deadrise surface

The difference between the wetted keel length and the chine length measured to the calm water intersection with the chine (L_k) is a fuction of trim and deadrise and is defined by

$$L_k = \frac{b\,tan\beta}{2\tan\tau} \tag{2.2}$$

and the difference between actual wetted keel length and chine length for a prismatic planing surface is given by

$$L_k - L_c = \frac{b\,tan\beta}{\pi \tan\tau} \tag{2.3}$$

A plot of this relationship is given in Fig. 2.5.

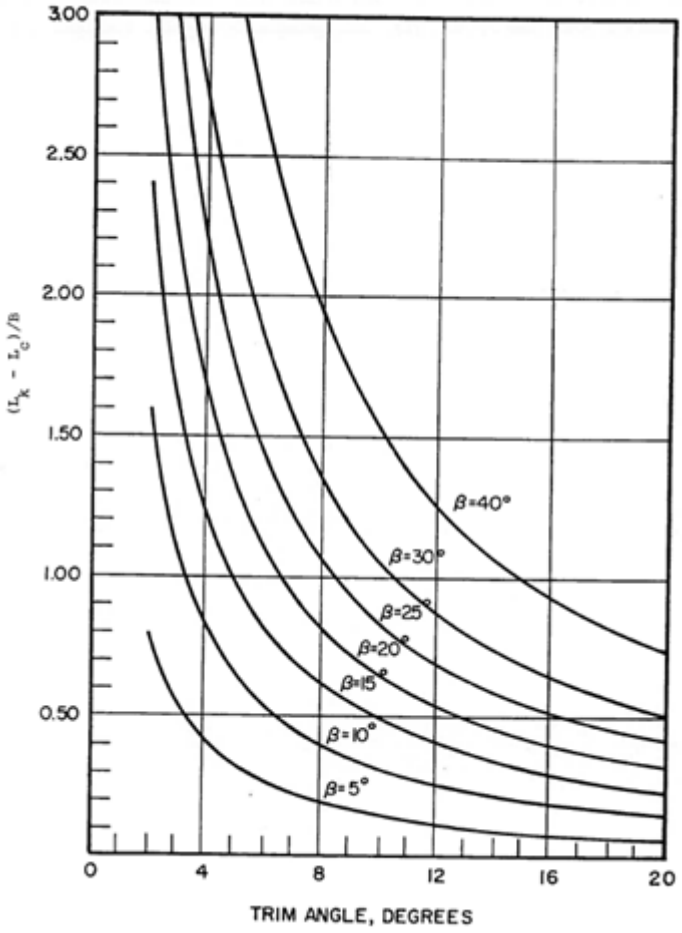

Fig. 2.5 $L_k - L_c$ versus trim and deadrise

Since the wetted keel length can be defined in terms of the draft of the aft end of the keel as

$$L_k = \frac{d}{sin\tau} \tag{2.4}$$

Then the mean wetted length-beam ratio, λ, which defines the pressure area is given as

$$\lambda = \frac{\left[\frac{d}{\sin\tau} - \frac{b\tan\beta}{2\pi\tan\tau}\right]}{b} = \frac{L_k + L_c}{2b} \tag{2.5}$$

2.1.3 Wetted spray area of deadrise planing surfaces

The total wetted bottom area of a planing surface is actually divided into two regions. One is aft of the spray root line, called pressure area and the other is forward of the spray root line, called spray root area. The pressure area, which has been defined in the preceding sections, is the load-carrying area of the planing bottom. The forward spray area contributes to the total drag but is not considered to support any portion of the load.

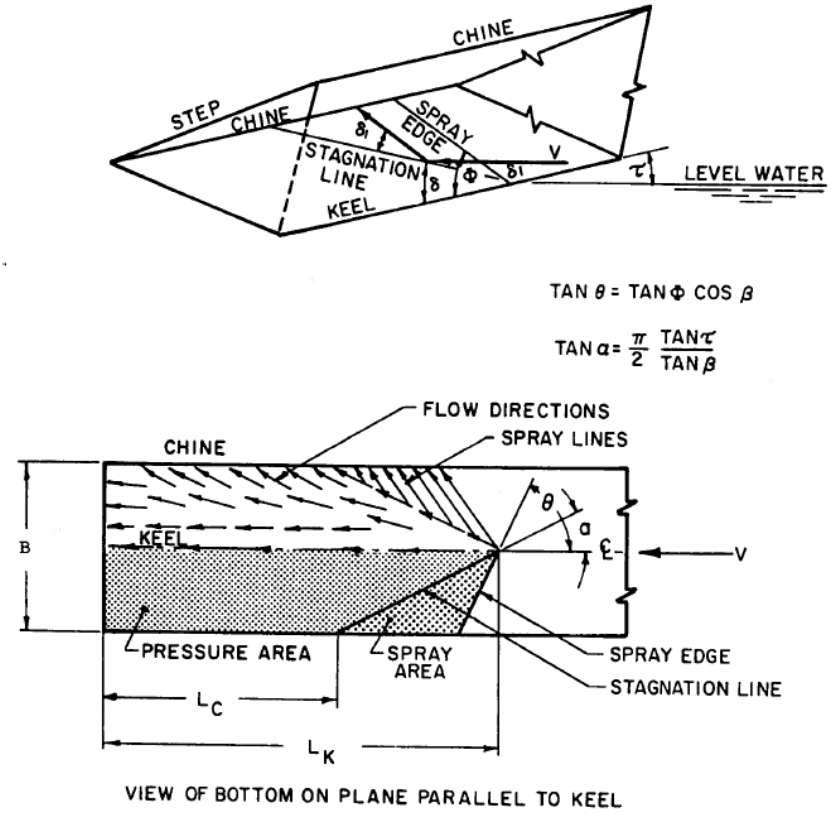

Fig. 2.6 Definition of wetted surface

Fig. 2.6 shows the flow directions. It is found that the flow in the pressure area is predominantly aft with some transverse flow along the chines. The flow along the spray

root line is primarily along the direction of the stagnation line. In the spray wetted area the directions of the fluid flow are such that the space angle between the oncoming fluid particles and the stagnation line is equal to the angle between the direction of the spray jets and the stagnation line; i.e. any line of motion in the spray area is nearly a reflection about the stagnation line of the incident velocity direction. Since the pressure in the spray area is nearly atmospheric, then, by Bernoulli, the spray velocity can be assumed to be equal to the planing speed.

The actual spray area extends from the spray root line forward to the spray edge. The angle ϑ between the keel and spray edge measured in the plane of the bottom is

$$\tan\vartheta = \frac{A + k_1}{1 - Ak_1} \tag{2.6}$$

where

$$A = \frac{\left\{sin^2\tau(1-2K) + K^2 tan^2\tau\left[\left(\frac{1}{sin^2\beta}\right) - sin^2\tau\right]\right\}^{\frac{1}{2}}}{cos\tau - K\, tan\tau \sin\tau}$$

$$k_1 = \frac{K\, tan\tau}{sin\beta}$$

and

$$K \approx \frac{\pi}{2}\left(1 - \frac{3\, tan^2\beta\, cos\beta}{1.7\pi^2} - \frac{tan\beta\, sin^2\beta}{3.3\pi}\right)$$

The total spray area, both sides, projected on a plane along the keel line is given by

$$A_S = \frac{b^2}{2}\left(\frac{tan\beta}{\pi tan\tau} - \frac{1}{4\, tan\vartheta\, cos\beta}\right) \tag{2.7}$$

2.1.4 Lift of flat planing surfaces

The lift on a planing surfaces (at fixed draft and trim) can be attributed to two separate effects; i.e., one is the dynamic reaction of the fluid against the moving surface, and the second is associated with the static pressure corresponding to a given draft and hull trim. In effect, the buoyant contribution represents the influence of gravity. At very low speed coefficients, the buoyant lift component predominates. As speed are increased, the

dynamic lift effects begin to developed. At first the dynamic effects tend to decrease the load which a given prismatic surface can support and then, as the speed is further increased, the pressure on a given surface will increase. At very high speed the dynamic contribution to lift predominates and the static pressure effects can be neglected.

From aerodynamic theory it is known that lifting surfaces of high aspect ratio (small λ) have a predominately longitudinal (chord wise) flow and that the lift is directly proportional to τ. For surfaces of very small span and infinite length, i.e., $\lambda = \infty$, the flow is in a transverse direction and lift is proportional to r^2. Hence for a normal low aspect-ratio planing surface, the lift can be expressed in the form

$$C_L = Ar + Br^2 \tag{2.8}$$

For the range of λ-values applicable to planing surfaces, the second term takes the form of a small correction to the first term and it is found that equation (2.8) can be approximated by using τ to the 1.1 power. Hence

$$\frac{C_L}{\tau^{1.1}} = f(\lambda, C_v) \tag{2.9}$$

$$C_V = v/\sqrt{gB}$$

Sottorf's analysis of high speed planing data, where the hydrostatic term is negligible, showed that, for a given trim angle, the dynamic component of the lift coefficient varied as $\lambda^{1/2}$. Hence we can consider this component

$$C_{L_d} = c\lambda^{1/2}\tau^{1.1} \tag{2.10}$$

where c is a constant to be determined.

The hydrostatic component of the lift for a flat plate of beam, B, mean length-beam ratio, λ, and angle of trim τ can be written as follows:

$$L_b = \frac{1}{2}\rho g b^3(\lambda - 0.30)^2 \tan\tau \tag{2.11}$$

Dividing both sides by $\frac{1}{2}\rho V^2 b^2$ and assuming that $(\lambda - 0.30)^2$ can be replaced by $K\lambda^n$ where D and n are constants to be determined, results in

$$C_{L_b} = \frac{D\lambda^n}{C_v^2}\, tan\tau^{1.1} \tag{2.12}$$

If the difference between $\tan\tau$ and $\tau^{1.1}$ is neglected C_{L_b} can be written

$$C_{L_b} = \frac{D\lambda^n}{C_v^2}\,\tau^{1.1} \tag{2.13}$$

Combining equations (2.10) and (2.13) gives a form of an empirical equation for the lift coefficient of a planing surface, i.e.

$$C_L = \tau^{1.1}\left(c\lambda^{\frac{1}{2}} + \frac{D\lambda^n}{C_v^2}\right) = f(\tau,\lambda) \tag{2.14}$$

As any empirical equation there are a several ways to formulate the equation for planing lift. The form of relation given in (2.14) has the advantage of readily illustrating the effect of the variables on planing lift and also is easily applied in design of planing hulls.

The constant c, D, and n are evaluated by applying the foregoing formula to the large number of planing data contained in the existing literature. As a result of this analysis the empirical planing lift equation for a zero deadrise surface is given as

$$C_L = \tau^{1.1}\left[0.0120\lambda^{1/2} + \frac{0.0055\lambda^{5/2}}{C_v^2}\right] \tag{2.15}$$

where τ is in degrees.

This empirical equation is applicable for $0.60 \le C_v \le 13.00$; $2° \le \tau \le 15°$; and $\lambda \le 4$. For convenience in use, equation (2.15) is plotted in Fig. 2.7 in the form $\frac{C_L}{\tau^{1.1}}$ versus λ for a wide range of C_v-values.

Examining this plot at a fixed value of λ it is clear that the buoyant contribution to lift is significant up to speed coefficients as high as approximately 10. At $C_v > 10$, the dynamic lift is predominant and the lift coefficient is then independent of speed. In fact, for $C_v > 10.0$ the flat plate lift coefficient can be simply expressed as $C_L = 0.0120\lambda^{1/2}\tau^{1.1}$.

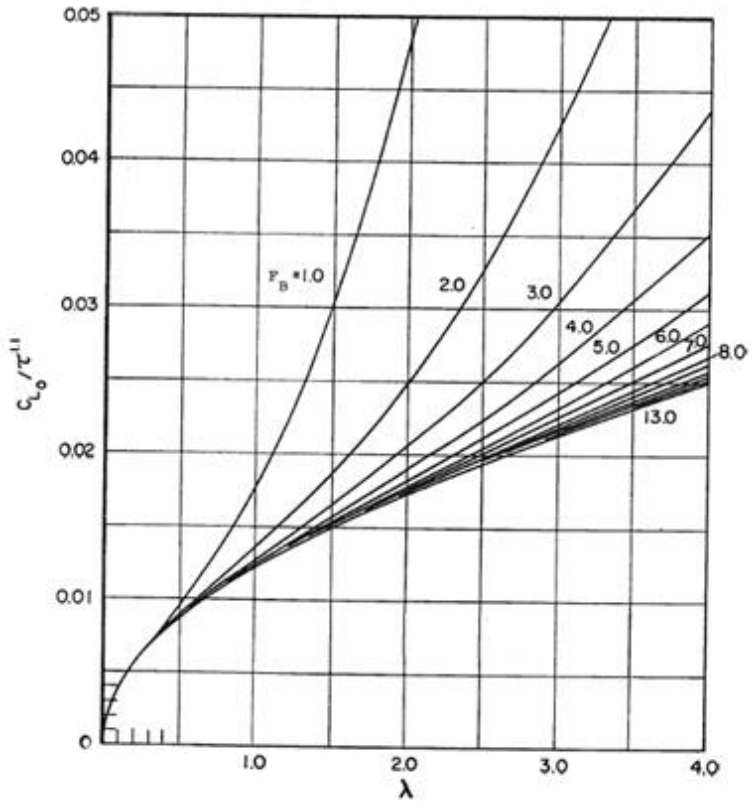

Fig. 2.7 Lift coefficient of a flat planing surface; $\beta = 0°$

2.1.5 Lift of deadrise planing surfaces

For a given trim and mean wetted length-beam ratio, the effect of increasing the deadrise angle is a reduction of planing lift. This lift reduction in the stagnation pressure at the leading edge of the wetted area. It will be recalled from the discussion of wetted areas that the angle between the stagnation line and keel is given by the equation $\gamma = tan^{-1}\,(\tan\frac{\tau}{2}\tan\beta)$. When $\beta = 0$ the stagnation line is normal to the keel and normal to the free stream velocity so that full stagnation pressure $\frac{1}{2}\rho V^2$ is developed. For increasing values of β, the angle γ decreases so that full stagnation pressures are no longer developed; hence the planing lift is reduced.

To formulate an empirical equation for the planing lift of a deadrise planing surface, the lift coefficient of a V-surface was compared with that of a flat plate at identical values of τ, λ, and C_v. The lift of a deadrise surface can be represented by the following equation:

$$C_{L_\beta} = C_{L_0} - 0.0065\beta C_{L_0}^{0.60} \qquad (2.16)$$

Where C_{L_β} is the lift coefficient for a deadrise surface, β is the deadrise angle (deg), C_{L_0} is the lift coefficient of a flat plate operating at the same τ, λ, and C_v as deadrise surface.

For convenience, the equation (2.16) is reported in Fig. 2.8.

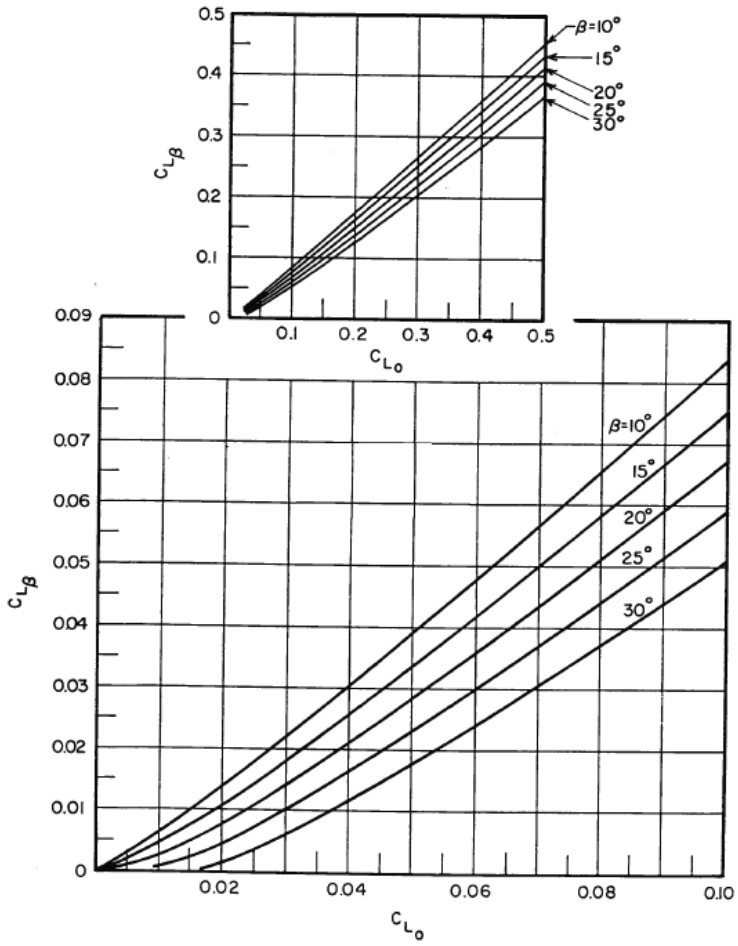

Fig. 2.8 Lift coefficient of a deadrise planing surface

2.1.6 Drag of planing surfaces

The total hydrodynamic drag of a planing surface is composed of pressure drag developed by pressures acting normal to the inclined bottom and viscous drag acting tangential to the bottom in both the pressure area and spray area. If there is side wetting then this additional component of viscous drag must be added to the hydrodynamic drag acting on the bottom

of the planing surface. For the present analysis it will be assumed that there is no side wetting of the hull.

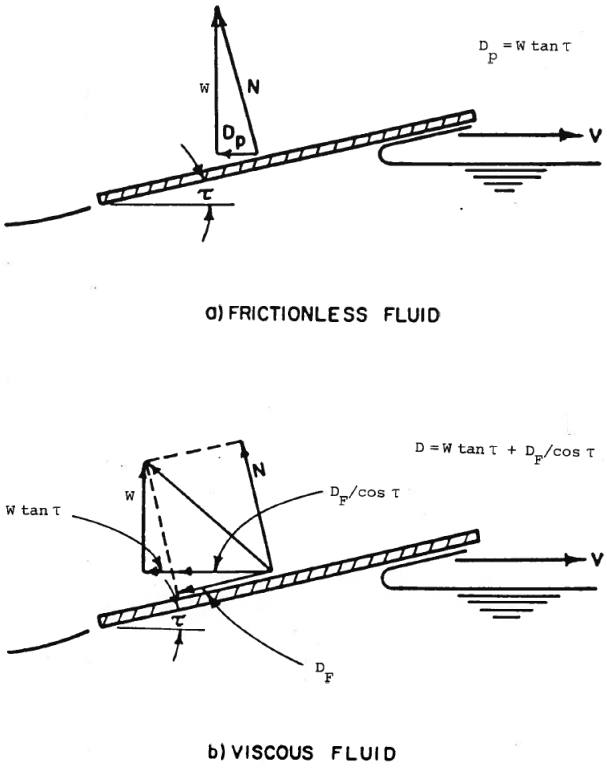

Fig. 2.9 Drag components on a planing surface

For a frictionless fluid, the tangential force is zero. Hence for a trim angle τ, a load Δ, and a force N normal to the bottom the resistance component D_p due to pressure forces is shown in Fig. 2.9 to be

$$D_p = \Delta \tan \tau \tag{2.17}$$

When the viscous drag D_f acting tangential to the bottom is added, the total drag, D, is shown in Fig. 2.9 to be

$$D = \Delta \tan \tau + \frac{D_f}{\cos \tau} \tag{2.18}$$

The friction component D_f is computed by the following equation:

$$D_f = \frac{C_f \rho V_1^2 (\lambda b^2)}{2 \cos \beta^4} \tag{2.19}$$

where

$C_f =$ Schoenherr turbulent friction coefficient

$V_1 =$ average bottom velocity $\qquad V_1 = V(1 - \frac{2p_d}{\rho V^2})^{1/2}$ (2.20)

$p_d =$ average dynamic pressure $\qquad p_d = \frac{\Delta}{\lambda b^2 \cos \tau} = \frac{0.0120 \tau^{1.1} V^2 \rho}{2 \lambda^{1/2} cos\, \tau}$ (2.21)

The average bottom velocity (V_1) is less than the forward planing velocity (V) owing to the fact that the planing bottom pressure is larger than the free stream pressure.

Substituting (2.21) into (2.20) gives

$$V_1 = V \left(1 - \frac{0.0120 \tau^{1.1}}{\lambda^{1/2} \cos \tau}\right)^{1/2} \qquad \text{for } \beta = 0° \tag{2.22}$$

The average bottom velocity for specific deadrise angles is computed in an analogous manner using the lift coefficient for deadrise surfaces given by (2.16). The ratios V_1/V have been computed for four deadrise angles and the results are plotted in Fig. 2.10 in a convenient form for use by the designer.

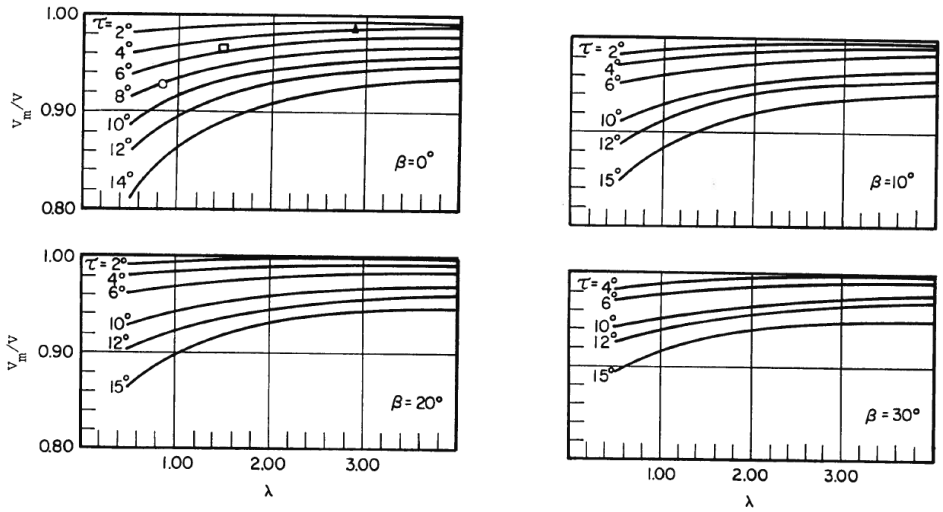

Fig. 2.10 Magnitude of average bottom velocity for a planing surface

It will be noted that these results were based mainly on data obtained at planing trim angles greater than 4 deg.

Finally, the hydrodynamic drag of a planing surface is given by the following equation:

$$D = \Delta \tan\tau + \frac{\rho V_1^2 C_f \lambda b^2}{2\cos\beta\cos\tau} \qquad (2.23)$$

2.1.7 Centre of pressure of planing surfaces

The resultant centre of pressure of planing surfaces can be fairly accurately evaluated by separate considerations of the buoyant and dynamic force components of the lift. The centre of pressure of the dynamic component is taken to be at 75% of the mean wetted length forward of the transom, while the centre of pressure of the buoyant force is assumed to be 33% forward of the transom. Adding the moments taken about the transom for each of the two components of the total load gives an expression for the distance of the centre of pressure forward of the transom.

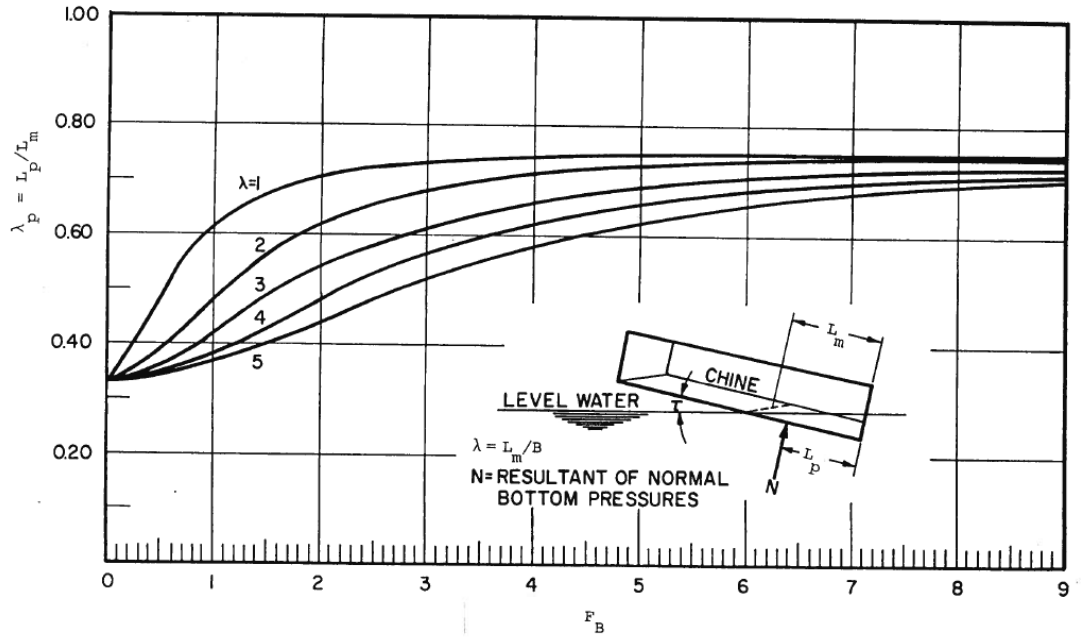

Fig. 2.11 Centre of pressure of planing surfaces

By using the values of the buoyant and dynamic force components given in (2.15), the centre of pressure, C_p, is found to be a distance forward of the transom equal to

$$C_p = \frac{L_p}{\lambda b} = 0.75 - \frac{1}{5.21\frac{C_v^2}{\lambda^2} + 2.39} \tag{2.24}$$

where C_p is the ratio of the longitudinal distance from the transom to the centre of pressure divided by the mean wetted length, Fig. 2.11. C_p is essentially independent of trim angle and/or deadrise angle. When the wetted length and speed coefficient are known, the value of C_p can be quickly determined from the chart.

2.1.8 Calculation of the equilibrium condition

In this section, we will apply the information presented in previous sections to the problem of determining the performance of a planing boat in which the following data is supplied: the beam B, the deadrise angle β, the weight W, propeller shaft-line inclination ε and its displacement from the centre of gravity f, the location of the centre of gravity ahead of the transom L_G, and above the keel H_G, and the speed of the boat V. We are interested in determining the running trim angle τ, the wetted length at the keel L_k and at the chine L_c, the total resistance D, the keel draft h, and the required propeller thrust T. These quantities are shown in Fig. 2.12 (a).

We can resolve the forces on the boat parallel to the keel to obtain

$$T\cos\varepsilon - W\sin\tau - D_f = 0 \tag{2.25}$$

And normal to the propeller-shaft line to get

$$N\cos\varepsilon - W\cos(\tau - \varepsilon) + D_F\sin\varepsilon = 0 \tag{2.26}$$

For equilibrium of the moments about the centre of gravity, we have

$$M = Tf - Nc - D_F a = 0 \tag{2.27}$$

In these equations, f is the moment arm for the thrust, N is the normal force on the hull, and c is the arm for its moment about the centre of gravity, which is given by

$$c = L_G - L_p \tag{2.28}$$

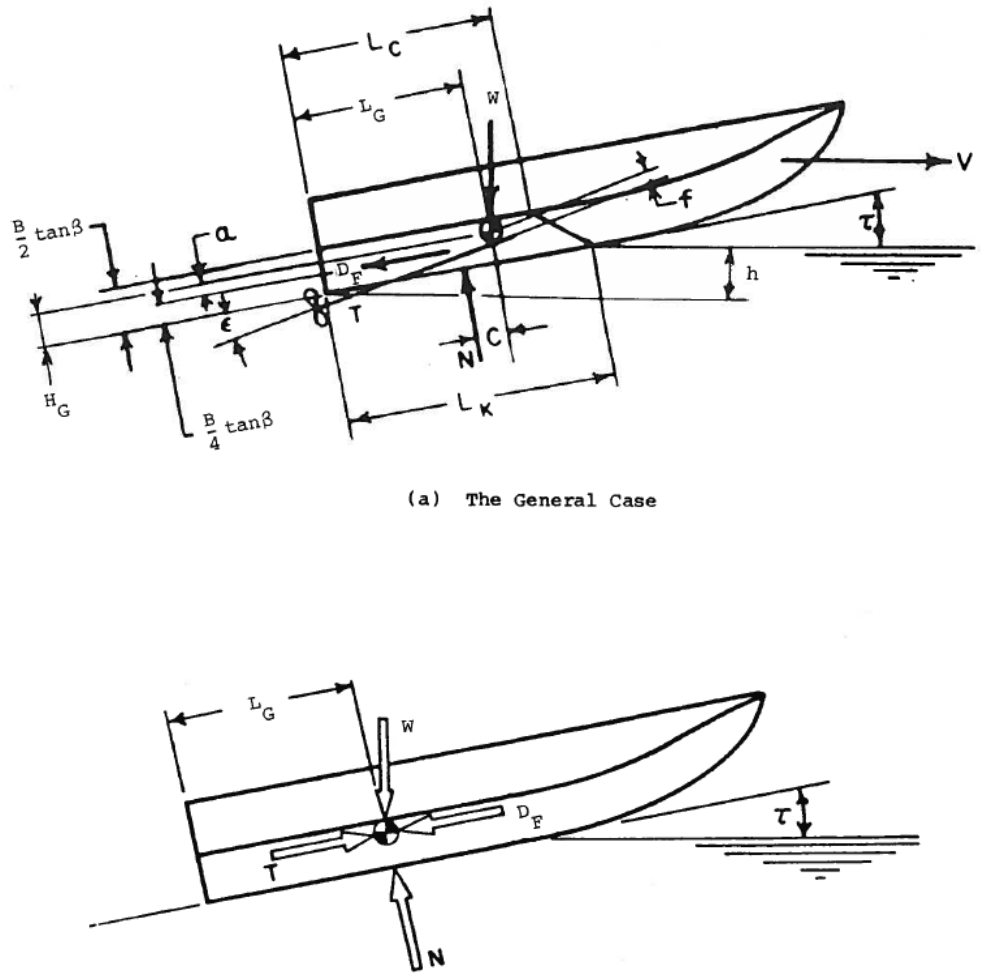

Fig. 2.12 Equilibrium of a planing boat

The arm for the moment of the frictional force is simply

$$a = H_G - \frac{1}{4} B \tan \beta \tag{2.29}$$

The effective power is given by the formula

$$P_e = DV \tag{2.30}$$

The draft of the keel at the transom is just

$$h = L_k \sin\tau \tag{2.31}$$

The difficulty in solving these equations lies in the fact that the trim angle is not known beforehand. It must be chosen to satisfy the equations of equilibrium. The *Savitsky long form* method starts with an assumed value of τ, from which the moment M in (2.27) can be computed directly. If M is not sufficiently close to zero, then the value of τ should be adjusted, and the calculation iterated. A modification which is more suitable for hand calculations is to use two trial values of τ, and to employ linear interpolation to find the value corresponding to zero moment. The value of C_{L_0} can be obtained graphically or using the Newton-Raphson method, or the method of repeated substitution. A good starting procedure is to take $C_{L_0} = C_{L_\beta}$. This iterative technique converges to four significant figures in about five iterations.

A simplification to this method is to assume that all the forces on the boat act through the centre of gravity (*Savitsky short form*). The situation is shown in Fig. 2.12 (b). In this case, no iteration is required, as the moment equation is automatically solved. However, (2.8) must be inverted. That is, we need to find λ in terms of F_B and $\frac{L_p}{B}$. The procedure has been simplified by the production of a monogram in Fig. 2.13. Again, the graphical procedure can be avoided in a numerical procedure.

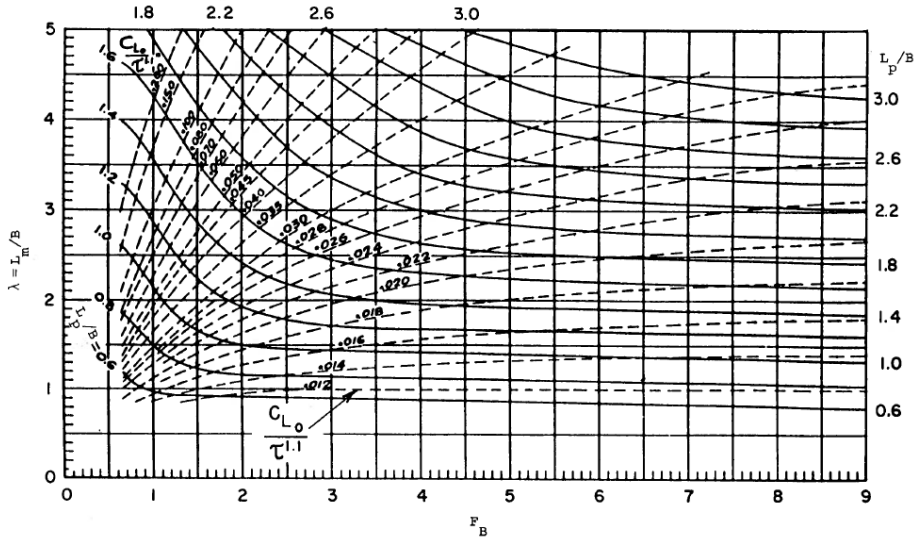

Fig. 2.13 Monogram for the case of concurrent forces

2.1.9 Inclusion of whisker spray drag

The planing hull performance prediction method explained in previous sections included only the viscous drag and pressure drag components in the bottom area aft of the stagnation line. As shown in Fig. 2.6, the whisker spray area is the wetted bottom region forward of the stagnation line and is referred to as the whisker spray area. This area can't be seen in underwater photographs of a non transparent hull but can be determined by other means. The direction of the fluid in this spray area is such that the space angle δ between the oncoming free-stream velocity and the stagnation line is equal to the space angle between the direction of the spray velocity and the stagnation line; that is, any line of motion in the spray area is nearly a reflection about the stagnation line of the incident free-stream velocity. Since the pressure in the spray area is nearly atmospheric, the spray velocity can be taken to be equal to the planing speed. The flow of the spray across the bottom develops a viscous force that has an aft component that adds to the resistance of the hull.

The total whisker spray area (two sides of the hull) projected on the plane through the keel and perpendicular to the hull centerplane is equal to

$$A_S = \frac{b^2 \pi \tan\tau}{16\, sin^2\alpha \tan\beta} \tag{2.32}$$

where α is defined as

$$\tan\alpha = \frac{\pi}{2}\frac{\tan\tau}{\tan\beta} \tag{2.33}$$

From (2.33) we can obtain

$$\tan\tau = \frac{2}{\pi}\tan\alpha \tan\beta \tag{2.34}$$

Substituting (2.34) in (2.32)

$$A_S = \frac{b^2}{4\ \sin 2\alpha} \tag{2.35}$$

The actual wetted area in the plane of the bottom surface of the hull is

$$A_{as} = \frac{A_S}{\cos\beta} \tag{2.36}$$

thus

$$A_{as} = \frac{b^2}{4\ \sin 2\alpha \cos\beta} \tag{2.37}$$

Since the velocity of the whisker spray is taken to be equal to the free stream velocity V, and the spray area is as defined above, the total viscous force in the spray area F_S is

$$F_S = \frac{1}{2}\rho V^2 A_{as} C_f \tag{2.38}$$

This force is in the plane of the bottom and makes an angle $\Theta = \left(\frac{\vartheta}{\cos\beta}\right)$ relative to the keel, Fig. 2.6.

The hydrodynamic resistance of a planing hull is defined as the horizontal component of force measured in a plane parallel to the level water surface and in the aft direction. The quantity F_S in the plane of the bottom, which has a trim angle and deadrise angle relative to the water surface. This is converted to a resistance component in the plane of the level water surface by the following equation

$$R_S = F_S \cos\Theta \cos\tau \tag{2.39}$$

Since the equilibrium trim angle of typical high speed planing craft is small (usually less than $6\ deg$) the value of $\cos\tau \cong 1.0$ so that this term will be neglected. Thus, R_S can be written as

$$R_S = \frac{1}{2}\rho V^2 A_{as} = \frac{b^2 \cos\Theta}{4\ \sin 2\alpha \cos\beta} C_f = \Delta\lambda b^2 \frac{1}{2}\rho V^2 C_f \tag{2.40}$$

where $\Delta\lambda b^2$ represents the increase in effective wetted bottom surface area that is attributed to the whisker spray contribution to total resistance.

Solving for the quantity $\Delta\lambda$

$$\Delta\lambda = \frac{b^2 \cos\Theta}{4\ \sin 2\alpha \cos\beta} \tag{2.41}$$

This expression is plotted in Fig. 2.14. $\Delta\lambda$ can be graphically obtained through this figure.

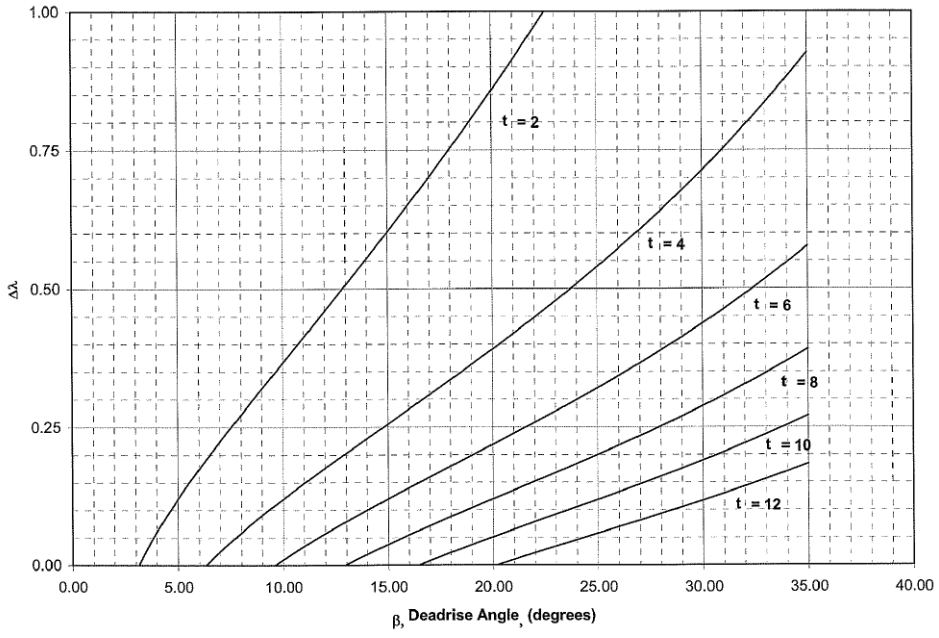

Fig. 2.14 Incremental increase in $\Delta\lambda$ due to spray contribution to drag

thus, the contribution of the spray viscous force to the total hull resistance can be then be written as

$$R_S = \frac{1}{2}\rho V^2 \Delta\lambda b^2 C_f \tag{2.42}$$

Fig. 2.15 is a graphical illustration of the effect of trim angle on whisker spray drag for a $15\ deg$ deadrise hull operating at a mean wetted length-beam ratio of 1.5. It is clear that a lowest trim angle of $2\ deg$, the whisker spray area F_S and its aft orientation are substantially larger than for the higher trim angles. As the trim angle is increased, these quantities are reduced, and finally at a trim angle of $9.5\ deg$ F_S is directed normal to the keel so that its resistance component is zero.

For combinations of small trim angles and high deadrise angles (which are typical for very high speed planing hulls) $\Delta\lambda$ is relatively large so that the spray drag for these hull will be significant. The whisker spray drag can be as large as 15% of the total drag. Fortunately, short longitudinal spray strips can be judiciously attached to the bottom to deflect the spray and thus avoid the large increase in drag.

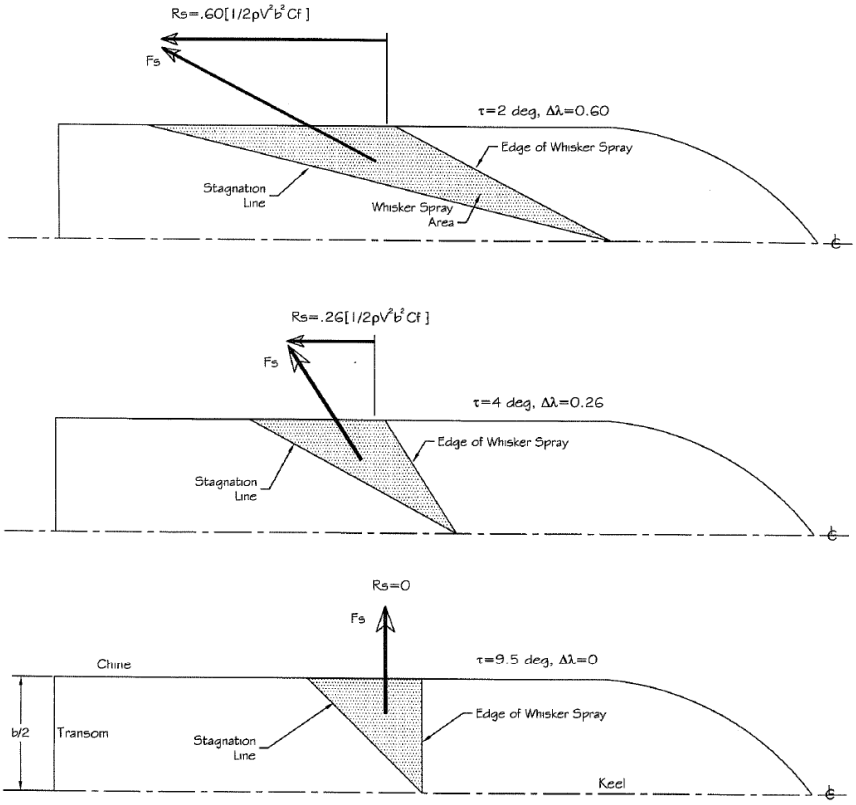

Fig. 2.15 Reduction of whisker spray resistance with increasing trim angle $\beta = 15°$, $\lambda = 1.5$

2.1.10 Modifications for a warped hull form

The present section relates to the hydrodynamics of hard chine hulls where the deadrise increases with increasing longitudinal distance forward of the transom. These are called "warped' hulls. Typically the warp increases gradually through the planing area and then increases rapidly in the bow area of the craft. Fig. 2.16 illustrates the various chine and keel geometric variations that will warp the hull bottom. These represent simplified profile views of hulls as included on hull lines drawings.

As a base line, sketch (a) is a prismatic hull. Note that the chine line, keel line, and longitudinal buttock lines are parallel. Thus the deadrise is constant along the planing area of the bottom and all longitudinal buttock lines (including the keel and chine) are at an identical trim angle relative to the level water surface.

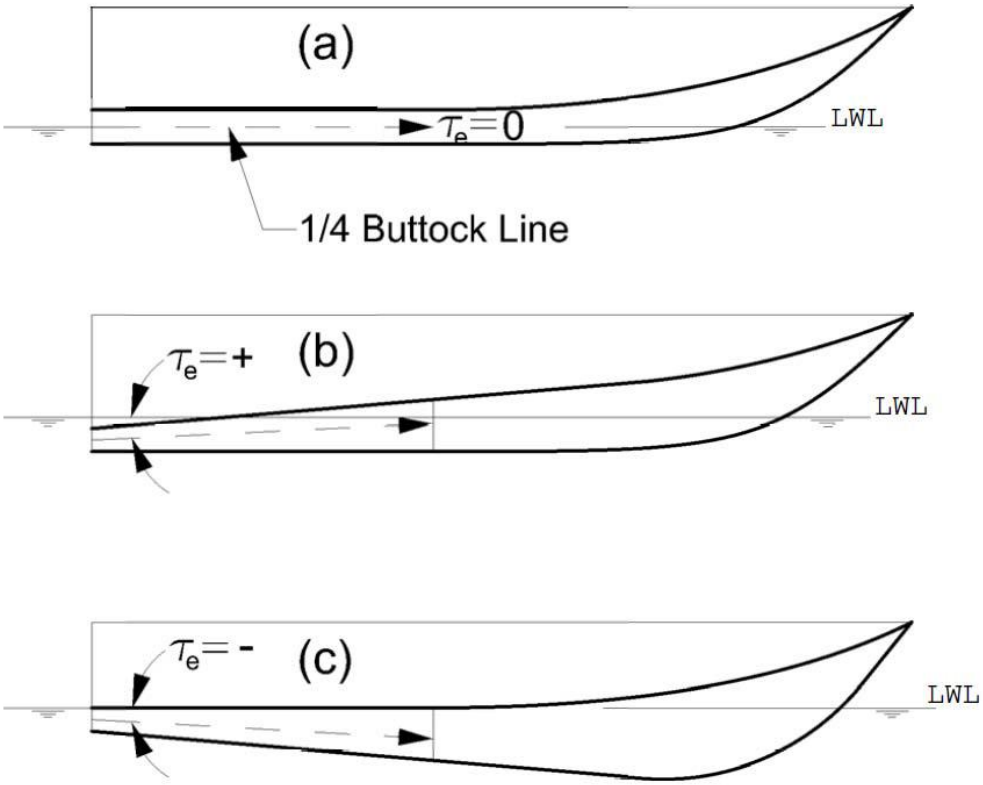

a) Prismatic Hull – Keel and Chine are Parallel

b) Warped Hull – Keel Horizontal; Chine Positive Trim

c) Warped Hull – Keel Negative Trim; Chine Horizontal

Fig. 2.16 Orientation of keel and chine lines to achieve warp (constant beam)

Sketch (b) represents a hull where the keel line is parallel to the level water surface but the chine line is at a positive trim angle relative to the keel. This combination forms a warped hull with the deadrise increasing forward of the transom. Of particular interest is that the trim angle of the chine line relative to the level water surface is greater than the keel trim angle. In fact, the trim angles of the longitudinal buttock lines increase with increasing transverse distance from the keel. It is reasonable to assume that the trim angle of the ¼ buttock line to be representative of the "hydrodynamic" trim angle of the planing bottom surface. The equilibrium trim angle calculated by the performance prediction method (Savitsky,1964) can be taken to be the trim angle of the ¼ buttock line for a warped hull.

This angle is of course larger that the trim angle of the keel and inherently provides a planing bottom with a positive angle of attack even at zero speed. This "built in" positive trim angle restrains the craft from attaining undesirable large running trim angles at high speed. Many designers recognize this effect and may use warp to modify the overall trim of the craft. Since the trim angle at the chine is greater than that at the keel it follows that, in any transverse plane, the dynamic bottom load at the chine is greater than that at the keel. Thus, it can be expected that, at planing speeds, the transverse stability of a warped planing hull will be greater than that of a prismatic hull.

Sketch (c) represents a hull where the chine line is horizontal and the keel line in the planing area has a negative trim relative to the level water line. This combination also results in a warped hull with the deadrise increasing forward of the transom. Unfortunately, the trim angle of the ¼ buttock line relative to the level water line will be negative in the static condition. To generate hydrodynamic lift in the planing condition the trim of the craft must first increase with increasing speed to overcome the "built-in" negative trim of the buttock lines and then must increase further to generate positive dynamic lift. Such designs will plane at relatively large running trim angles that may compromise the forward visibility from the craft. The designer can also incorporate transom flaps or transom interceptors in the design to provide variable trim control as required.

The parameter λ (the mean wetted length-beam ratio), is a primary input in the planing equations for prismatic hulls. For warped hulls, the local deadrise angle (β_e) increases with increasing λ. This relationship between β_e and λ can be established from the lines drawing of the hull if λ is known. Fortunately, the value of λ in any hull design can be uniquely defined by the LCG and the speed coefficient of the craft (both of which are known prior to a performance prediction analysis). The relation between representative deadrise (β_e) and λ is:

$$\beta_e = 10 + 3\lambda \tag{2.43}$$

The trim angle of the ¼ buttock line is equal to the trim angle of the keel relative to the level water surface + the angle of the ¼ buttock line relative to the keel:

$$\tau_e = \tau + \frac{1}{2}\vartheta \tag{2.44}$$

Where ϑ is shown in Fig. 2.17.

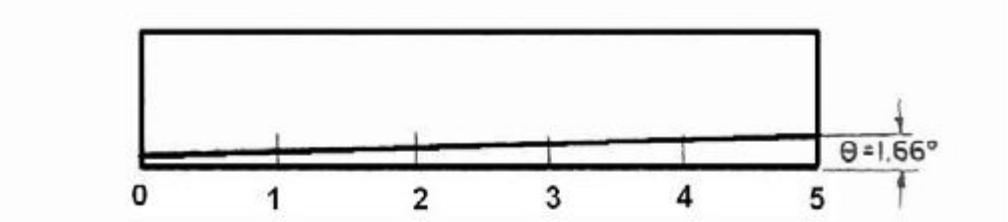

Fig. 2.17 Warped planing surface

The planing equations for lift of a warped surface are now taken to be the same as for a prismatic surface except the above values of β_e and τ_e are used. The equations for lift coefficient C_L of a warped surface can be written as:

$$C_{L_{\beta_e}} = C_{L_0} - 0.0065\beta_e C_{L_0}^{0.60} \tag{2.45}$$

where β_e is in degrees and

$$C_{L_0} = \tau_e^{1.1}\left(0.0120\lambda^{1/2} + 0.0055\frac{\lambda^{5/2}}{C_V^2}\right) \tag{2.46}$$

$$\lambda = \frac{1}{2}\frac{(L_k - L_c)}{B} = f(LCG, C_V) \tag{2.47}$$

$$C_V = \frac{V}{\sqrt{gb}} \tag{2.48}$$

The quantity $\frac{(L_k - L_c)}{B}$ for a warped hull is a little bit lower than the equivalent prismatic hull. This small difference ($\approx 4\%$), can be neglected.

As regard the center of pressure, we can utilize the same equations given for a monohedral hull, always utilizing β_e and τ_e.

2.1.11 Savitsky short form procedure

In the Savitsky short form, per each value of trim τ, all forces pass through Center of Gravity and the equilibrium equation (2.27) of the pitching moment is an identity always satisfied, as shown in Fig. 2.12 (b).

1. We calculate the beam Froude number

$$F_{r_b} = \frac{V}{\sqrt{gb}}$$

2. We get the lift coefficient of deadrise planing surface

$$C_{L_\beta} = \frac{W}{\frac{1}{2}\rho V^2 b^2}$$

3. From the equation

$$C_{L_\beta} = C_{L_0} - 0.0065\beta C_{L_0}^{0.60}$$

we get the lift coefficient of the equivalent flat plate.

4. Per each attempt value of trim angle τ, we calculate the ratio $\frac{C_{L_0}}{\tau^{1.1}}$.
5. From the equation

$$\frac{C_L}{\tau^{1.1}} = 0.0120\lambda^{1/2} + \frac{0.0055\lambda^{5/2}}{C_v^2}$$

we get the ratio $\lambda = \frac{L_W}{b}$, as well as the wetted length $L_W = \lambda b$

6. From the relation

$$C_p = \frac{L_{CP}}{\lambda b} = 0.75 - \frac{1}{5.21\frac{C_v^2}{\lambda^2} + 2.39}$$

we get the center pressure position C_P (L_{CP}).

7. By the knowledge of L_W, we get the Reynolds number

$$\mathrm{R_n} = \frac{\mathrm{VL_W}}{\nu}$$

8. By the knowledge of RN, we get the friction coefficient C_f

$$\mathrm{C_f} = \frac{0.075}{(\log_{10}\mathrm{R_n} - 2)^2}$$

9. By the knowledge of L_W, we get the wetted surface S_W

$$S_W = \frac{L_W b}{\cos\beta}$$

10. By the knowledge of C_f, we get the friction load D_f

$$D_f = \frac{1}{2}\rho V^2 S_W \left(C_f + \Delta C_f\right)$$

11. By the knowledge of τ and D_f, through Sottorf's formula, we get the bare hull resistance R_H

$$R_H = W \tan\tau + \frac{D_f}{\cos\tau}$$

12. By the knowledge of L_{CP} and R_H, per each value of τ, we let draw the diagram related to the speed V.
13. By the equilibrium condition $L_{CP} = L_{CG}$ we get the equilibrium trim angle τ and the bare hull resistance R_H related to.
14. Repeat this procedure per each value of speed.

2.2 Morabito method

Three-dimensional dynamic pressure distribution over a planing plane is depicted in Fig. 2.18. It is obvious that pressure at the stagnation line is far greater than pressure at other parts of the plane. The complexity of the problem makes it almost impossible to apply direct methods for calculation of the pressure distribution and therefore the pressure is calculated in length-wise and breadth-wise directions separately and it is then extended to a 3-dimensional distribution over the plane.

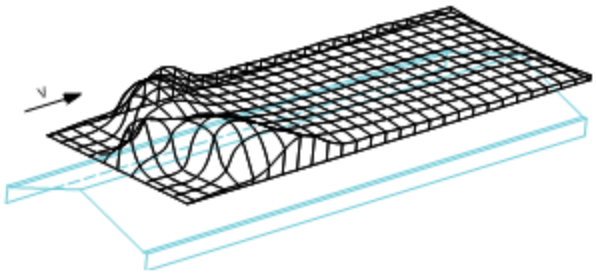

Fig. 2.18 Three dimensional distribution of the pressure over the bottom of a planing hull

The longitudinal distribution of the dynamic pressure over a planing plane exhibits a maximum at the stagnation point. After this peak, the pressure falls with a sharp steep and reaches the atmospheric pressure at each end of the plane.

2.2.1 Longitudinal pressure distribution over symmetry line

Equation (2.49) introduced by Morabito, is used to calculate the maximum pressure for the case of a planing hull as in

$$\frac{P_{max}}{q} = sin^2\alpha \tag{2.49}$$

Where P_{max} is the maximum pressure at stagnation line, at the intersection of the keel and waterline, while q is calculated as follows:

$$q = \frac{1}{2}\rho V^2 \tag{2.50}$$

The pressure behind the stagnation line falls from this value and vanishes at the transom. Smiley introduced the equation (2.51) for the pressure reduction behind the stagnation line and along the symmetry line.

$$\frac{P_L}{q} = 0.006\frac{\tau^{\frac{1}{3}}}{X^{\frac{2}{3}}} \tag{2.51}$$

Here, P_L is the pressure behind the stagnation line and X is the dimensionless distance from the stagnation line which is calculated using Equation (2.52). X is given by the equation

$$X = \frac{x}{b} \tag{2.52}$$

Where b is is the breadth. Morabito modified equation (2.51) in order to evaluate the dynamic pressure reduction over a planing hull and introduced

$$\frac{P}{q} = \frac{CX^{1/3}}{(X+K)} \tag{2.53}$$

In which, C and K are constants that can be evaluated using simple mathematical and differential equations as follows:

$$C = 0.006\tau^{\frac{1}{3}} \tag{2.54}$$

$$K = \frac{C^{1.5}}{2.588\left(\frac{Pmax}{q}\right)^{1.5}} \tag{2.55}$$

Pressure distribution over the longitudinal symmetry line can be measured using equation (2.53), but the result would not be accurate for the pressure values at the transom.

2.2.2 Effect of the transom stern

Morabito took into account the effect of the transom stern on the longitudinal distribution by introducing a coefficient such that with the multiplication of this coefficient and the longitudinal pressure distribution, the transom stern effect would be simulated. This will cause a major reduction of pressure starting from a half-breadth distance from the transom stern until the pressure vanishes at the transom. This coefficient is calculated using equation

$$P_T = \frac{(\lambda_y - X)^{1.4}}{(\lambda_y - X)^{1.4} + 0.05} \tag{2.56}$$

In which λ_y is the dimensionless distance between the transom stern and the stagnation line at each longitudinal section. This parameter is derived using the equation (2.57) as follows:

$$\lambda_y = \lambda - \frac{(Y - 0.25)}{\tan\alpha} \tag{2.57}$$

Where Y is the dimensionless transverse distance from the longitudinal symmetry line as in

$$Y = \frac{y}{b} \tag{2.58}$$

2.2.3 Longitudinal pressure distribution over other sections

The equations presented so far offer the longitudinal pressure distribution over the longitudinal symmetry line. As discussed earlier, the pressure decreases along the stagnation line and therefore at each longitudinal section, the maximum pressure is far less than that on the longitudinal symmetry line. Using Swept Wing Theory, Morabito calculated the pressure reduction. He considered the velocity vector to be a combination of

two components: one along the stagnation line and the other normal to it which is shown in Fig. 2.19.

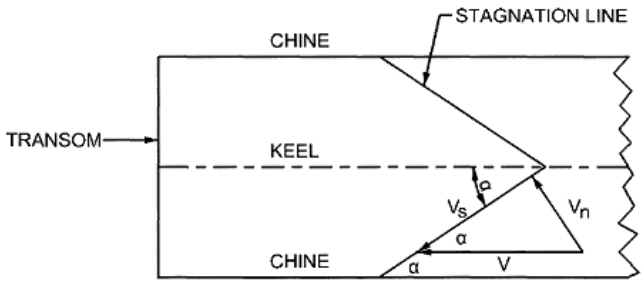

Fig. 2.19 Components of the planing plane velocity vector

The components of the velocity vector are presented as

$$V_n = V \sin \alpha \tag{2.59}$$

$$V_s = V \cos \alpha \tag{2.60}$$

V_n in equations (2.59) and (2.60) is the velocity component normal to the stagnation line and V_s is the component along the stagnation line. Using the normal component and the resulting pressure P_N, an empirical equation for the ratio of transverse pressure along the stagnation line $\left(P_{\gamma\, Stag}\right)$ and P_N is derived, which is given in (2.61). Multiplying this ratio by the maximum pressure gives the maximum pressure over the stagnation line at a desired longitudinal section. This is governed by (2.62).

$$\frac{P_{Y\, Stag}}{P_N} = [1.02 - 0.25Y^{1.4}]\frac{0.5-Y}{0.51-Y} \tag{2.61}$$

$$\frac{P_{max}}{q} = \frac{P_{Y\, Stag}}{P_N} sin^2\alpha \tag{2.62}$$

3 Numerical considerations

3.1 Introduction

Computational fluid dynamics is a comprehensive field covering a broad range of related topics. This section is intended to introduce the primary areas of CFD involved in the numerical simulations discussed in this thesis.

3.2 Grid Definition – Meshing

The numerical methods used to solve the governing equations of fluid flow require that the fluid domain be first discretized into geometrically simple cells or elements. Meshing is an important step in any computational method, since the accuracy of the solution can be directly related to the sizes and shapes of the mesh elements. This solution dependence on grid definition has led to a wide variety of techniques for their development and improvement. Meshes can take several forms, but are generally identified as being either structured or unstructured.

Structured meshes are currently the most common in CFD applications. This type of mesh requires a systematic scheme of node and element numbering related to the generation of the grid. One of the advantages of structured meshes is that the implicit nature of grid structure means that the mesh connectivity (a map of the grid structure) does not need to be stored, thereby reducing computer memory requirements. Structured grids also allow

the use of more efficient solution methods, which can reduce computer processing time. The primary disadvantage of structured meshes is that they can be difficult, and sometimes impossible, to create for complex geometries. The domain often needs to be segmented into topologically similar regions or blocks, which are then mapped with separate structured grids. This approach can decrease the time needed to build a mesh over fully structured grids, but the solver must have the ability to handle the resulting block interfaces, often resulting in a need for increased computer resources.

Unstructured meshes can be regarded as the extreme case of segmenting a domain into regions, brought to the point where the resulting 'blocks' become so small that the local structured meshes in each block are no longer required. Unlike structured mesh approaches, the elements are not ordered in any regular fashion, although they do conform exactly to the boundaries of the domain. For this type of mesh, the physical locations of the grid points or nodes must be stored along with the connectivity of the mesh: a listing of which nodes make up each element as well as the identities of their neighbouring elements. Unstructured grids are flexible, useful for complex geometries, and can be constructed with any type of element or with combinations of different element types (hybrid meshes). Using an unstructured hybrid mesh can greatly accelerate the meshing process of a CFD simulation. The drawbacks of this method are the increased computational resources required, and the fact that solvers have to be designed specifically to handle unstructured meshes. Examples are shown in Figure 3.1 of structured (in the 'C'), unstructured (in the 'F') and hybrid (in the 'D') meshes.

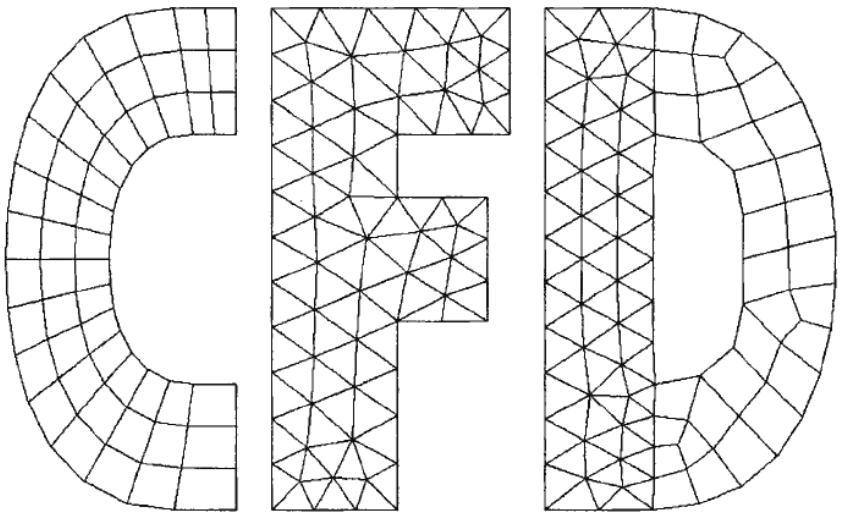

Fig. 3.1 Structured and unstructured meshes

An important advantage of unstructured meshes is the ease with which adaptive meshing techniques may be incorporated. These techniques allow the mesh to be altered, either refined or coarsened, based on any given criteria. Since there is no inherent structure to be preserved, adding or removing mesh elements only results in local updates to the connectivity. Adaptation can take several forms; two common types are hanging node and conformal.

When hanging node adaptation is used, elements in regions to be refined are subdivided into multiple smaller elements. There may be one or more nodes that split the interface between a refined and an unrefined element. These are hanging nodes and require special treatment by the solver. This method of refinement is straightforward and effective. However, after multiple levels of refinement are applied, the mesh connectivity and element shapes may degrade, resulting in highly skewed elements.

Conformal adaptation implies that there will be no hanging nodes after the refinement process. New nodes are inserted and the local connectivity of the mesh is recomputed in that region. Special techniques such as the Delaunay criteria are often required to minimize distortions in newly formed elements. This method is generally only used with triangular or tetrahedral meshes. Hanging node adaptation was used to refine the upper-left comer while conformal adaptation was used to refine the lower-right comer, Fig. 3.2.

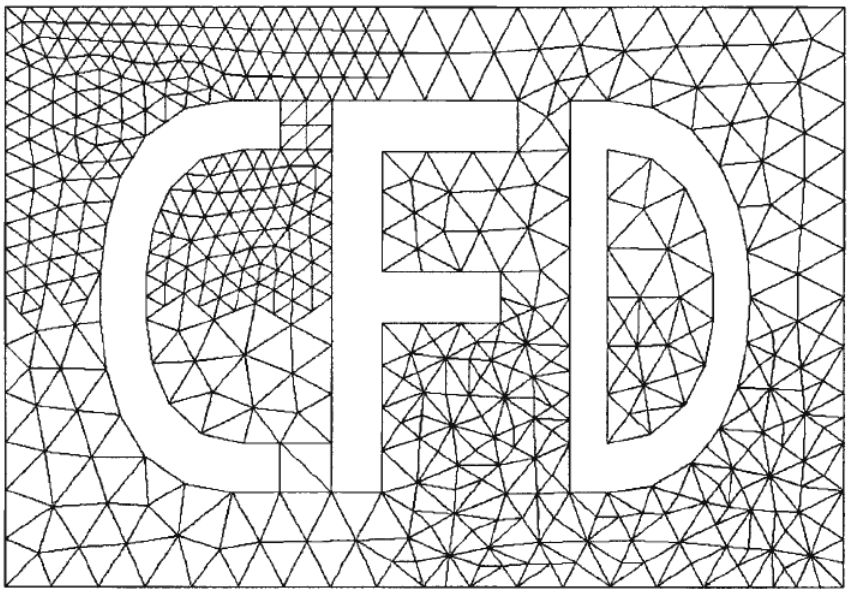

Fig. 3.2 Mesh refinement

Meshing is an essential part of performing CFD simulations. Choosing the appropriate meshing strategy is therefore an important aspect of any computational work. Structured grids are typically more difficult to implement, but have the advantage that more efficient methods can be used for the solution process. Unstructured grids are easier to apply and are more versatile in terms of geometrical adaptation, but require greater computational resources by the solver. However, as the speed and memory capacity of computers continues to increase, computational time becomes less of an issue, thereby making unstructured grids the favoured alternative.

3.3 Solution Techniques

The essential goal of any CFD program is to solve a set of equations with appropriate boundary and/or initial conditions. The Navier-Stokes equations governing the conservation of mass and momentum of fluid are a set of coupled, non-linear, mixed elliptic-parabolic partial differential equations. Although a few exact analytical solutions exist for some simplified cases, such as the laminar flow over an infinitely long plate, exact solutions cannot be determined for practical flows. It is therefore necessary to employ numerical methods to develop approximate solutions to these equations. Several techniques have been used to solve the Navier Stokes equations, including finite difference methods, finite element methods, finite volume methods, and spectral methods. The basic steps for each of these methods can be summarized as:

- Using simple functions to approximate unknown flow variables.
- Discretizing the governing flow equations with substitutions of the approximate functions followed by mathematical manipulations.
- Solving the resulting algebraic equations.

Finite difference methods employ approximations of derivatives by truncated Taylor series expansions given in terms of values at a given grid point and its immediate neighbours. Substitution of these discrete approximations in place of continuous derivatives in the governing equations results in algebraic equations for the unknown flow variables at each grid point. This was one of the first methods used to tackle flow problems, but was found to be sensitive to the grid structure.

Finite element methods employ simple piecewise functions to describe the variations of the flow variables on individual elements. When these functions are substituted into the

governing equations, an associated error, or residual, is produced. An attempt is then made to minimize the error, often with the use of weighting functions. The result of this operation is a set of algebraic equations defining the values of the coefficients of the original piecewise approximating functions defined for each element. Most commonly employed for structural problems, progress has been made towards improving this method for fluid equations.

Spectral methods use functions such as truncated Fourier series or Chebyshev polynomial series to approximate flow variables. However, unlike finite difference and finite element methods, these functions are applied to the entire flow domain instead of being restricted to local grid points or elements. The approximate functions are then substituted into the governing equations resulting in an error, or residual. A similar method as the finite element method can then be used to minimize this error, or the error can be made to vanish on specific grid points. The result is a set of algebraic equations defining the values of the coefficients of the approximating truncated series. Though theoretically sound, relatively few codes are based on this methodology.

The finite volume method (FVM) was originally developed to overcome certain restrictions in finite difference formulations and has since evolved to be a well established and thoroughly validated method for CFD problems. The procedure involves integrating the governing equations over all of the finite control volumes in the domain. Each control volume is associated with a discrete point at which the dependent variables such as velocity, pressure and temperature are to be calculated. Approximations of terms in the integrated governing equations representing such processes as convection, diffusion, and sources, are then made using finite difference type substitutions (various terms in the integration are approximated with grid point values of the dependent variables such as the velocity components). The result is a system of algebraic equations representing the conservation of flow variables for each control volume. Solving a system of algebraic equations, usually by an iterative method, is a step required by all the methods mentioned here.

The finite volume method can take full advantage of an arbitrary or unstructured mesh. Modifying the shape and location of the control volumes as well as varying the rules and accuracy for the evaluation of the flux through the control surfaces gives considerable flexibility to the method. In addition, as the conservation laws are discretized directly, the basic quantities of mass momentum and energy remain conserved at the discrete level. This is called *conservativeness* and is an important property for a numerical method. For a

general flow variable Φ, the conservation equation for a control volume is expressed in terms of the processes tending to increase or decrease its value as shown below.

$$\begin{bmatrix}\text{Rate of change}\\ \text{of } \Phi \text{ in the}\\ \text{control volume}\end{bmatrix} = \begin{bmatrix}\text{Net change of } \Phi\\ \text{due to convection}\\ \text{through surfaces}\\ \text{of control volume}\end{bmatrix} + \begin{bmatrix}\text{Net change of } \Phi\\ \text{due to diffusion}\\ \text{through surfaces}\\ \text{of control volume}\end{bmatrix} + \begin{bmatrix}\text{Net rate of creation}\\ \text{or destruction of } \Phi\\ \text{inside of control}\\ \text{volume}\end{bmatrix}$$

3.3.1 Segregated vs. Coupled Solvers

This solution option is related to how the equations are solved once discretized. It consists of "segregated" and "coupled" methods. Both schemes are based on a finite volume technique, but differ in the procedure used to determine the unknown flow variables. The segregated method solves the governing equations sequentially (i.e. segregated from one another). After each governing equation is solved, the code checks for convergence and then iterates stepwise through all the equations until convergence is achieved. In the coupled solver, the governing equations of momentum, continuity, and energy are solved simultaneously (coupled together). Any additional equations for scalars (such as turbulence kinetic energy and dissipation) are then solved sequentially using the procedure of the segregated solver. The choice of which solver to use depends on the type of problem being solved.

3.3.2 Implicit vs. Explicit Methods

Another aspect of the solution method is how the equations are formulated before they are solved by either the segregated or coupled schemes. The approach can be either "implicit" or "explicit". For an implicit scheme, the unknown value of a given variable in each cell is computed using a relation that includes both existing and unknown values from neighbouring cells. Therefore each unknown appears in more than one equation in the system, and these equations must be solved simultaneously to give the unknown quantities. For the explicit scheme however, the unknown value in each cell for a given variable is computed using a relation that includes only existing values. Therefore, each unknown appears in only one equation in the system, and the equations for the unknown value in each cell can be solved one at a time to give the unknown quantities.

3.3.3 Convection and Diffusion

An issue that can arise when using the finite volume method concerns the roles of convection and diffusion. It results from the fact that diffusive properties affect a given transported quantity in all directions, while convection spreads influence only in the direction of flow. The discretization scheme must be chosen such that the control volumes are influenced correctly by both of these factors. Several schemes have been developed for this purpose, such as the power law-scheme and the QUICK scheme. Both methods incorporate the effects of simultaneous convection and diffusion by means of weighted contributions in the discretized equations. The power-law scheme determines the weighting based on the Peclet Number[1] while the QUICK (Quadratic Upstream Interpolation for Convective Kinetics) scheme uses a higher order discretization based on an upstream weighted quadratic interpolation. Higher order schemes like QUICK are generally advantageous as they involve more neighbouring cells, thereby reducing error by bringing in a wider influence.

3.3.4 Pressure-Velocity Coupling

Another issue involved in the finite volume method comes from the treatment of pressure in the equations. Shown in equations (3.1) and (3.2) are the equations for conservation of momentum and mass, respectively.

$$\rho \frac{du_i}{dt} = \mu\left(\frac{\partial^2 u_i}{\partial x_j \partial x_j}\right) - \frac{\partial p}{\partial x_j} + S_i \qquad (3.1)$$

$$\frac{\partial u_i}{\partial x_i} = 0 \qquad (3.2)$$

The equations are intimately coupled in velocity but there is no clear transport equation for pressure, an important source term of momentum. This results in an indirect specification because the correct pressure field is needed while solving the momentum equations to ensure that the resulting velocity field will satisfy the continuity equation. Additional considerations and algorithms are therefore needed to perform the flow field calculation. One such method is the SIMPLE (Semi-Implicit Method for Pressure-Linked Equations) algorithm, which uses an iterative approach to overcome the problem. Initial guessed velocity and pressure fields are used to solve the momentum equations. A pressure

[1] Peclet Number is a measure of the relative strengths of convection and diffusion.

correction equation, deduced from the continuity equation, is then used to improve the guessed fields until convergence is achieved. Other pressure-velocity coupling techniques, such as SIMPLER (SIMPLE -Revised), SIMPLEC (SIMPLE-Consistent) and PISO (Pressure Implicit with Splitting of Operators), have also been developed.

3.3.5 Relaxation and Multi grid Methods

Once the equations have been discretized, it does not always follow that successive iterations will lead to a converged solution. At times, the values of an unknown flow variable, such as pressure, may oscillate or drift away from the true solution of the equations. A voiding such divergence of the iteration process has resulted in the development of various treatments of the discretization equations. One such approach is to slow down how quickly a given variable is corrected at each cycle. Should, for example, the pressure correction for a given iteration be large, it could result in unstable computations leading to divergence. This technique of reducing variable corrections is called under-relaxation (over-relaxation is when the variable values change more rapidly than without relaxation, and is sometimes used to accelerate convergence). Proper settings of the relaxation factors for a given problem can increase the efficiency of the solver.

Other numerical problems can also occur during the solution process. Traditional matrix solvers like the implicit Gauss-Seidel method are known to converge rapidly for the first few iterations, but slowly thereafter. These methods are most efficient for smoothing out errors of wavelengths comparable to the mesh size, but are ineffective in annihilating low-frequency components. As the grid is refined, these low frequency modes dominate the solution error and additional iterations become progressively less productive. One way of improving the convergence of these iterative matrix solvers is by using multi grid methods. These methods solve the equations using a sequence of successively coarser meshes so that all frequency components are reduced at comparable.

3.3.6 Boundary Conditions

The flow in a given problem is controlled by the boundary conditions imposed on the domain. Although many types of boundary conditions are available in a general purpose CFD code, only those related to the present research will be discussed here. These are: wall, velocity inlet, symmetry, and outlet flow boundary conditions.

Wall boundary conditions are used to define solid boundaries. No flow can pass through a wall boundary condition and in viscous flows the no slip condition is automatically imposed. Tangential wall velocities can, however, be set indirectly by specifying a "moving wall".

Velocity inlet boundary conditions are used to define the flow velocity, along with all relevant scalar properties of the flow (such as the volume fraction, i.e. inflow is water or air). For incompressible flows, this type of boundary condition produces a constant mass inflow rate.

Symmetry boundary conditions are used when the physical geometry of interest, and the expected pattern of the flow solution, both have mirror symmetry. Flow conditions of all variables at a symmetry boundary condition can be summarized as having zero normal velocity and zero normal gradient.

Outlet flow boundary conditions are used to model flow exits where the details of the flow velocity and pressure are not known prior to solving the flow problem. Conditions at outflow boundaries are not defined but extrapolated from the interior and hence have no impact on the upstream flow. The outflow velocity and pressure are updated in a manner that is consistent with a fully-developed flow assumption[2].

3.4 Turbulence Modelling

Despite advances in computing power and mathematics, full descriptions of practical turbulent flows are unreachable for now and for the foreseeable future. However, useful estimations of the mean turbulent flow characteristics can still be made if some approximations or models are employed in the solution of the Navier-stokes equations of fluid momentum. Reynolds (1895) proposed that for many applications, only the mean flow characteristics are desired. By decomposing the velocity and pressure terms into mean and fluctuating components (based on a long time average), the Navier-Stokes equations can be re-expressed in terms of these decomposed terms. These equations, called the Reynolds-averaged Navier-Stokes (RANS) equations for mean linear fluid momentum, form the basis for many of the methods of turbulence modelling. The Navier-Stokes equation for linear momentum is given below:

[2] Fully developed flows are flows in which the flow velocity profile (and/or profiles of other properties such as temperature) is unchanging in the flow direction

$$\frac{\partial u_i}{\partial t} + u_j \frac{\partial u_i}{\partial x_j} = -\frac{\partial p}{\partial x_i} + v\nabla^2 u_i \tag{3.3}$$

Velocity is decomposed into mean, $\overline{u_i}$, and fluctuating, $\overline{u_i'}$, parts as follows:

$$u_i = \overline{u_i} + \overline{u_i'} \tag{3.4}$$

Similarly for pressure,

$$p = \bar{p} + p' \tag{3.5}$$

Substituting the decomposed velocity and pressure into the momentum equation (3.3)

and taking an ensemble mean leads to the RANS equation:

$$\frac{\partial \overline{u_i}}{\partial t} + \overline{u_j} \frac{\partial \overline{u_i}}{\partial x_j} = -\frac{\partial \bar{p}}{\partial x_i} + v\nabla^2 \overline{u_i} - \frac{\partial \tau_{ij}}{\partial x_j} \tag{3.6}$$

Where,

$$\tau_{ij} = \overline{u_i' u_j'} \quad \text{is the Reynolds-stress tensor} \tag{3.7}$$

The Reynolds-stress tensor represents an additional set of unknowns to the momentum and continuity equations. These equations cannot be solved in the above form since the number of unknowns is greater than the number of available equations. This is called the Reynolds-stress closure problem.

There are several methods for obtaining closure to the RANS equations that range in both complexity and the need for computing power. It should be noted that the fundamental nature of these equations prevents them from being able to provide any detailed information about turbulent flow structures. They are instead intended to estimate mean values such as velocities, pressures, and turbulence intensity levels, which can then be used for design purposes. The ability of these equations to produce accurate information about these mean parameters directly depends on the quality of the models used to approximate the unknown terms.

Most common turbulence models are based on what is referred to as "eddy viscosity" and are classed as being; algebraic, one equation, two equation, or second order. These classifications relate to the level of mathematical sophistication used to derive the model, and also to the level of computational cost to the CFD solver. An algebraic model, for example, replaces the Reynold's stress terms with an algebraic expression containing the

velocity and/or pressure terms. Models like the two equation and second order type models rely on additional Reynold's averaged transport equations such as dissipation or kinetic energy to achieve closure. The unknown terms in these models are also replaced with algebraic expressions, but since they are of a higher order, the errors associated with them tend to be less significant to the lower order terms of interest. Higher order models, though potentially more accurate, do result in a considerable increase in processing and memory demands for the computations.

The turbulence models discussed below are available with STAR CCM+. The most commonly used model in ship flows are the one equation Spalart-Allmaras model and the standard $k-\varepsilon$ model although other models such as the Reynolds stress approach have also been attempted.

Spalart-Allmaras Model

The Spalart-Allmaras model is a relatively simple one equation model that solves a modelled transport equation for the kinematic eddy (turbulent) viscosity. It was designed specifically for aerospace applications involving wall-bounded flows and has been shown to give good results for boundary layers subjected to adverse pressure gradients.

Standard $k-\varepsilon$ Model

The standard $k-\varepsilon$ model requires the solution of two separate transport equations (kinetic energy and dissipation) to independently determine the turbulent velocity and length scales. This model is known for its robustness, economy, and has been shown to be reasonably accurate for a wide range of turbulent flows. It is a semi empirical model; its derivation relies on both phenomenological considerations and empiricism.

RNG $k-\varepsilon$ Model (ReNormalization Group)

The RNG $k-\varepsilon$ model was derived using a rigorous statistical technique (called renormalization group theory). It is similar in form to the standard $k-\varepsilon$ model, but includes certain refinements that make it applicable to a wider range of flows including rapidly strained and swirling flows.

Realizable $k-\varepsilon$ Model

The realizable $k-\varepsilon$ model is another improved version of the standard $k-\varepsilon$ model containing a new formulation for the turbulent viscosity and a new transport equation for

the dissipation rate. The term "realizable" means that the model satisfies certain mathematical constraints on the Reynolds stresses, consistent with the physics of turbulent flows (unlike the standard or RNG $k-\varepsilon$ models). It can generally provide superior performance for flows involving rotation, boundary layers under strong adverse pressure gradients, separation, and recirculation.

Reynolds Stress Model (RSM)

The Reynolds Stress Model achieves closure to the RANS equations by using transport equations for the Reynolds stresses, together with an equation for the dissipation rate (requiring the solution of seven transport equations in 3D flow). The rigorous nature of the RSM means that is it has greater potential to give accurate predictions for complex flows. However, the closure assumptions employed to model various terms in the transport equations can degrade its performance in some cases; results may not be better than the simpler models. However, use of the RSM is necessary when the flow features of interest are the result of anisotropy in the Reynolds stresses.

Large Eddy Simulation (LES)

LES provides an alternative approach in which the large eddies are computed in a time-dependent simulation that uses a set of "filtered" equations. Filtering is a manipulation of the exact Navier-Stokes equations to remove only the eddies that are smaller than the size of the filter, which is usually taken as the mesh size. Like Reynolds averaging, the filtering process creates additional unknown terms that must be modelled in order to achieve closure. Statistics of the mean flow quantities, which are generally of most engineering interest, are calculated during the time-dependent simulation. The attraction of LES is that, by modelling less of the turbulence (and solving more), the error induced by the turbulence model will be reduced. LES models are, however, quite recent and require substantially more computational time and memory than other models.

3.5 Free Surface Treatment

A free surface is the interface between water and air in a numerical simulation. It is determined by enforcing both kinematic and dynamic boundary conditions. The kinematic condition ensures that there is no flow across the wave surface. Dynamic conditions ensure that the normal stress at the free surface balances the ambient pressure and surface tension,

and that the tangential stress components vanish. Surface tension forces need not be modelled in ship flow simulations, as their effects are not generally significant. For the treatment of the free surface in numerical schemes, two main approaches can be distinguished:

- "free-surface fitting" methods in which one boundary of the computational domain coincides with the free surface and the grid is moved, stretched and compressed during the iteration process;
- "free-surface capturing" methods in which the numerical grid is fixed and the free surface is defined by some kind of scalar function. This function divides the domain into grid zones, which are either filled with fluid or not.

In surface fitting methods, the free surface is a sharp interface, the motion of which is followed. This is done by creating a grid in the fluid domain defining the free surface. During the solution process, the grid moves with or tracks the free surface by ensuring that the boundary conditions are always satisfied. Many finite-element methods use this approach. This method does, however, require that the mesh be adapted in the course of the solution process to ensure that it conforms to the changing free surface location. This grid adaptation may be either general or simplified (e.g. grid points sliding along predefined lines or spines). A background grid can also be defined that determines the paths along which grid points may slide.

Free surface fitting techniques are generally accurate and require little change to the RANS solver itself. But they are less suitable for large free surface distortions or topology changes such as breaking waves. Even large amplitude surface motions can be difficult to track without introducing re-gridding techniques such as the Arbitrary Lagrangian-Eulerian (ALE) method. Unstructured meshes could also be a solution in such cases. The majority of recent methods for steady flow around the hull in ship resistance codes use free surface fitting techniques.

The alternative approach, surface capturing, solves the RANS equations on a predetermined grid that is not fitted to the wave surface. The domain mesh extends into the air region, and therefore does not need to be adapted during the calculation process. The method does, however, require an addition algorithm to resolve the free surface within the meshed domain. Surface capturing methods have the potential to handle complicated ship forms (e.g. protruding bulbous bows, barge stems) and flow phenomena such as

breaking waves or spray. One such method, often used with FVM solvers such as STAR CCM+, is the volume-of-fluid (VOF) method.

The VOF method is based on the concept of a fluid volume fraction. Within each grid cell (control volume) it is customary to retain only one value for each flow quantity (e.g., pressure, velocity, temperature, etc.). The use of a single quantity (the fluid volume fraction in each grid cell) to define the free surface is consistent with the resolution of the other flow quantities. The fluid volume fractions in each cell are used to identify surfaces, as well as surface slopes and surface curvatures. Surfaces are located in cells partially filled with fluid or between cells full of fluid and cells that have no fluid. Slopes and curvatures are computed by using the fluid volume fractions in neighbouring cells. The use of a volume tracking as opposed to a surface tracking function means that the VOF method is robust enough to accommodate severe free surface movements such as sloshing or breaking waves.

4 Practical guidelines for ship CFD applications

We divide the CFD process into pre-processing, computation, and post-processing steps. The pre-processing step involves proper definition of the problem, grid generation and input setup to enable running of the computational code. The computation requires preparing the computer to run the problem, and running. The processing of the results of the computation to provide useful numbers and plots is called post-processing.

4.1 Pre-processing

4.1.1 Resistance

Define the Reynolds and Froude numbers. These are given by:

$$R_e = \frac{\rho U L_{PP}}{\mu}$$

$$F_r = \frac{U}{\sqrt{g L_{PP}}}$$

where ρ and μ are the density and viscosity of the fluid respectively, U is the ship speed, L_{PP} is the length between perpendiculars of the ship and g is the acceleration due to gravity. Note that the viscosity of water varies with temperature so that model scale tests

carried out in water at $10 - 15\,℃$ is different to the full scale viscosity of deep sea-water at $15\,℃$.

Estimate the expected free-surface wave-length and elevations. Estimate the distance to the wall where $y^+ \leq 1$ for near wall boundary conditions and $30 < y^+ < 100$ for logarithmic wall functions. This estimation of the distance to the wall should be based on an estimation of the skin friction as a function of the Reynolds number. This distance is described in terms of the non-dimensional parameter y^+. This can be defined in terms of the Reynolds number of the required flow as follows:

$$\frac{y}{L_{PP}} = \frac{y^+}{R_e\sqrt{\frac{C_f}{2}}}$$

$$\mathrm{C_f} = \frac{0.075}{(\log_{10}\mathrm{R_e} - 2)^2}$$

where y is the first required cell height and C_F is an estimate of the skin friction coefficient, based on the ITTC standard method. This gives an estimate of the skin friction coefficient at mid-ships.

Note that in the calculation above, C_F should be calculated using the full length of the ship which in the approach gives an approximation to mean value of the local C_F The ITTC model-ship correlation line should only be used in this estimate.

4.1.2 Wall function

To resolve the high velocity gradients in the inner part of a boundary layer, strong contraction of grid nodes is required towards solid surfaces. The cells that are thus occurring close to the wall have a high aspect ratio; typically for a ship at full scale they can be 1 meter long, 0.5 meter wide and only 10^{-3} millimetre high. This not only results in a high mesh count, but it also poses strong demands on the mathematics in the numerical solution procedure. This led to the introduction of so-called wall functions. For the laminar flow over an infinitely long flat plat at zero pressure gradient, the well-known Blasius solution exists, where the velocity profile is independent of the stream wise coordinate, when scaled appropriately. For turbulent flows such solutions only exist for the innermost part of the boundary layer. This gives the possibility to remove a significant part of the cells

close to the wall (which also have the highest aspect ratio), and impose the velocity at the first grid node adjacent to the wall (the wall function). However, wall functions are based on two-dimensional flow, typically at zero pressure gradient, and it is well known that the validity of these analytical expression becomes less, or even disappears, with increasing adverse pressure gradients. Thus it cannot be expected that the wall function approach leads to reliable and accurate solutions near a ship stern, where the flow is strongly three-dimensional and running up against an adverse pressure gradient. Thus it is a trade-off between accuracy and computational effort. Wall functions should be prevented if possible, and used with care when necessary.

4.1.3 Surface roughness

In ship viscous-flow computations and even in model testing the hull of a ship is considered to be hydrodynamically smooth. At full scale, however, during the operation of a ship the roughness increases due to use and fouling, thus increasing the frictional resistance. There are basically two methods to include roughness effects in RANS computations. Either through the adaption of wall functions (when used) or through the adaptation of the turbulence boundary conditions (for instance in the $k-\omega$ model). However, some major problems still remain. First the validity of the roughness model: to what extent does the equivalent sand-grain roughness that is typically used correctly adjust the velocity profile close to the wall? And second, how can the condition of the surface of a ship, sailing at any part of the world, be translated to an equivalent sand-grain roughness? Surface roughness is still an active field of research, and no general guidelines can yet be given.

4.1.4 Incident waves

Define the wavelength, amplitude, and encounter frequency. For irregular waves define spectrum and proper parameters. Define the cut-off frequency (highest frequency to be included in the simulation), and determine the corresponding wavelength.

4.1.5 Motions

Estimate the frequencies and amplitudes of each of the motions to be simulated (surge, sway, heave, roll, pitch, yaw) and the amplitude of displacement of the ship.

4.1.6 Flow features

Define location, size and characteristic frequency of the flow features to be resolved (vortices, separation, flutter, etc.).

4.1.7 Region of influence

Estimate the extent of the domain to be simulated to minimize interaction of the boundary conditions with the simulation results.

4.1.8 Geometry creation and modification

The geometry is generally provided as surface definitions in an IGES file format. Alternative file formats may be also used provided care is taken to ensure that sufficient accuracy is maintained during the file transfer process. The accuracy of the geometry should be checked to ensure that the surface definitions are reasonably smooth and connect within a given tolerance. The tolerances for the geometry should be based on the length between perpendiculars L_{PP}. The required geometry tolerance also depends on the Reynolds number required for the flow calculations. Generally, appropriate geometry tolerances are:

Scale	L_{PP}	R_e	Toll. (m)
Model	$1 < L_{PP} < 10$	$10^6 - 10^7$	10^{-5}
Intermediate	$10 < L_{PP} < 50$	$10^7 - 10^8$	$5x10^{-5}$
Full	$50 < L_{PP} < 250$	$10^8 - 10^9$	10^{-4}

Tab. 4.1 Appropriate geometry tolerance

Due care and attention is required to resolve geometry features such as trailing edges that may be less than an order of magnitude larger than the geometry tolerance. Geometry features that are smaller than the geometric tolerance do not need to be resolved.

Additional geometry is required for the grid generation process. It is recommended that this geometry is produced within the grid generation package to the same geometric tolerances as the surfaces. The required geometry components are:

- Bounding surfaces of the grid domain surrounding the geometry
- Intersection curves between the appendages and the hull
- Intersection curves between the hull and appendages and the vertical plane of symmetry
- Additional curves may also be required to assist in defining key details of geometry

Due consideration to the position and orientation of the origin of the geometry should be taken depending on the type of problem to be solved as forces and moments will be obtained about this origin and velocity and rotation directions depend on the orientation. It is recommended that a consistent coordinate system be used within an organization. Imported CAD definitions should then be modified to conform to this system.

4.1.9 Grid generation

Details on the grid generation process will largely depend on the solver and the type of grids it can handle (Cartesian, structured multiblock, unstructured, overset, etc.) Here are some general guidelines that apply to most solvers.

4.1.10 Definition of the domain boundaries

Ship viscous-flow computations typically have three fixed boundaries: the ship surface, the symmetry plane and the (still) water surface. Furthermore three additional boundaries have to be defined in order to have a closed domain around the ship. Independent of the grid type used these will include an inlet, an outlet and an exterior boundary, where approximate boundary conditions have to be defined. These boundaries have to be placed sufficiently far from the ship to minimize the effect of the location of these boundaries on the solution. For the inlet and exterior boundary either the uniform (undisturbed) flow is usually imposed, and in that case the these boundaries should be located 1-2 L_{PP} away from the hull. Alternatively potential flow can be imposed at these boundaries, which enables a reduction of the domain size. At the out-let in general zero gradients for all unknowns are imposed.

In case free-surface boundary conditions are imposed on the water surface, the domain size has to be increased further. Preferably the Kelvin wedge does not intersect with the exterior boundary, to prevent wave reflection.

Unsteady methods often require a damping zone downstream, to prevent wave reflection from the outlet boundary. There the outlet has to be placed 3-5 L_{PP} downstream.

4.1.11 Element type

Quadrilateral (2D, 4-sided) and hexahedral (3D, 6-sided) elements are the most popular element types supported by almost all CFD codes. Topological attributes of these elements – presence of opposing faces, and relative locations of cell centres and face centres – have been found to be beneficial to spatial accuracy of numerical solutions. In typical mappable, structured mesh-based solvers, the presence of stencils (e.g., *i, j, k* coordinates in the computational domain) readily accommodates high-order discretization schemes (e.g., 5^{th}-order convection scheme) that can enhance spatial accuracy. They are also efficient in terms of usage of elements, since they can be clustered and/or stretched as needed to economically re-solve the flow fields. The main downside of these structural mesh elements is that it is often very hard to generate high-quality structured meshes for complex geometry.

The "unstructured" mesh gives more flexibility in the choice of element types, facilitating mesh generation for complex geometry. The majority of unstructured mesh-based CFD solvers allow use of arbitrary polyhedral elements such as quadrilaterals (2D), triangles (2D), hexahedra, tetrahedra, wedges, pyramids, prisms, to name a few, and combination of all them (hybrid unstructured mesh). In a typical un-structured mesh frequently adopted in ship hydrodynamics, hull boundary layer is discretized using a prism mesh grown out of triangular mesh on hull surface, and tetrahedral mesh is used elsewhere away from hull. Compared to typical structured meshes, meshing time can be dramatically reduced with unstructured meshes. Spatial accuracy for unstructured mesh elements such as triangles, tetrahedra, and pyramids can be lower than that for quadrilateral and hexahedral elements. With unstructured meshes, one usually need a far greater number of computational elements than structured meshes in order to achieve a comparable accuracy. Furthermore, spatial accuracy of the majority of unstructured mesh-based finite-volume solvers is limited to 2^{nd}-order.

Which element types to use for a given problem really depends on many factors such as the solver (does your solver support unstructured mesh?), objective of the computation (do you need to resolve fine details of the flow?), and computer resource (do you have computers to run cases involving large meshes?). Here are general guidelines in choosing mesh and element types.

- For relatively simple configurations such as bare hulls, consider using a high-quality hexahedral mesh.
- For relatively simple configurations involving body-motion (free sinkage and trim), consider using overset grids if your CFD solver can take them and run on them.
- For complex configurations such as fully-appended ships for which a high-quality structured mesh is difficult to generate, consider using an unstructured mesh, preferably a hybrid unstructured mesh.
- Avoid using tetrahedral mesh in boundary layers, near free surface, and in the regions where high resolution of flow-fields is required. Use hexahedral grids or prismatic grids instead.

4.1.12 Grid points

Grid points distributions are determined with consideration of the following points:

- Based on the availability of computer time and power, determine the size (total number of grid points) of the grid as well as the grid size required for previous similar problems. This should determine if sufficient resources are available to obtain reliable results.
- Design the grid blocks in such a way that they will be properly decomposed for efficient computation, avoiding the use of too many small blocks.
- Use no less than 40 grid points per wave-length on the free surface. In irregular waves use at least 20 grid points for the shortest wave length to resolve. The number of grid points per wavelength also depends on the order of accuracy of the numerical scheme so if 40 points are required for a $3^{rd}/4^{th}$ order method then 80 points are required for a 2^{nd} order scheme to obtain the same accuracy (as provided by most commercial codes).

- comment on

  (1) the minimum number of points per wave-length: for too short wavelength (small Froude number) it is probably pointless to try to catch the small waves: the wave resistance component is likely negligible and

  (2) minimum grid density to capture flow details (e.g. wake at the propeller disk) or global forces (i.e. total resistance)

- Use no less than 20 grid points in the vertical direction where the free surface is expected

- Whenever possible use orthogonal grids to resolve a free surface

- For turbulence models integrating to the wall (Spalart-Allmaras, $k-\omega$, etc.) locate the first grid point at a distance from the ship's wall such that $y^+ = 1$. If wall functions are used this distance can increase such that $30 < y^+ < 300$, depending on the wall function implementation.

- Whenever possible use hyperbolic grid generators to guarantee as much as possible an orthogonal grid near the wall.

- Grids orthogonal to the domain boundaries, where the boundary conditions are imposed, are recommended. For some boundary conditions, such as symmetry conditions and wall conditions this orthogonality condition may be mandatory for some solvers.

- Provide refinement where flow features of interest are expected, in accordance with the size of the feature to be simulated. Where the flow features of interest are not known before-hand, it is necessary to use an iterative process to establish the existence of the key flow features of a given geometry. This requires an initial flow solution to be obtained and examined and subsequent grid refinement provided around the flow features. This should be carried out until some measure of grid refinement index is satisfied to ensure that flow features are sufficiently resolved.

- If overset grids are used, check that overlap is sufficient for the number of fringes that are needed in your code and order of accuracy.

- Ensure sufficient resolution of high curvature geometry is provided, especially around leading and trailing edges. An appropriate grid structure can enable more

efficient use of computing resources but at the expense of increased grid generation time and complexity.

- Check the grid quality to guarantee that all volumes are positive (positive Jacobian in structured grids), skewness and aspect ratio are acceptable, and that orthogonality is nearly satisfied in most places.

4.1.13 Grid topology

Grid topology is the mapping relation between the grid surface in physical (*x, y, z*) space and the computational (*i, j, k*) space in case of structured grid systems. In the single block grid around a ship hull, O-O or H-O topology is adopted in most cases, although C-O and H-H grids can be applied. In either topology, the grid lines in the girth-direction are O-type. The longitudinal grid lines in O-O grids wrap around a ship hull whereas those in H-O grids start from the inflow boundary and go through regions ahead of a ship, side of a hull and aft of a ship. Thus, when the total number of grid points and the number of grid points along the lines in the normal and in the girth directions are fixed, O-O grids can accommodate more grid points along a ship hull than H-O grids. Also, O-O grids can be adapted more easily to a blunt bow or a wide transom sterns which are typical in modern commercial ships. On the other hand, since the grid lines in the normal directions spread to the outer boundary in O-O grids, the grid resolution in the wake region and the region away from a hull tends to be lower than the H-O grids. Therefore choice of grid topologies should be based on the nature of ship hull geometry and on the consideration of which part or which feature of flow fields is more important than others.

4.1.14 Non conformal mesh

Non conformal grids may be required for highly complex geometries. This occurs when the level of detail of the geometry is increased and as more geometric entities such as propulsion shaft and bracket arrangements and bilge keel and roll stabilization systems are included in the geometry definition. These types of geometries are often required for wake flow analysis where it is important to capture small flow features. For these types of grids a non-conformal grid may be more appropriate where parts of the total grid do not fully connect. For these grids the flow solution algorithm must use special coding in order to interpolate between the non-connected grids. For some methods this interpolation scheme

may be defined by 'inter-faces' where the interpolation method is defined across grid boundary surfaces, for other methods the interpolation scheme is defined by 'overlaps' where the interpolation is defined across local grid volumes. For both of these types of interpolation schemes the formal order of accuracy is likely to be reduced, especially when there are large differences between the grid resolution and topology. However, this type of approach can be used to considerably simplify the grid generation process so that locally better quality grids can be produced around the various geometry components and assembled together to form a complete grid using the interpolation schemes.

Non conformal grids should be used with care, for example, for free-surface flows undesirable wave reflections can occur at the inter-faces or overlap if the interpolation scheme is unable to resolve the change in grid correctly. This can be alleviated by ensuring that the local change in the grid across the non conformal region is minimized with similar grid resolution and spacing used for both grid regions. Non con-formal grids can also use different types to assist the grid generation process, for example a grid for a detailed rudder with skeg and end plates can be produced using a local prism/tetrahedral grid which is embedded inside a multiblock grid for the hull.

4.1.15 Expansion ratio and number of grid points in boundary layer

The number of points within the boundary layer is determined by the level of accuracy required and the turbulence model chosen. A near wall turbulence model resolving the laminar sub-layer needs at least 3 points inside it, which for a $y^+ = 2$ results in an expansion ratio of 1.5, the largest acceptable. In most cases a $y^+ = 1$ will be used with expansion ratios around 1.2. Wall functions start farther out in regions of smaller velocity gradients and can use large expansion ratios, as large as 1.5 for coarse grids. In fine grids integrating all the way to the wall the total number of points within the boundary layer can be very large, on the order of 100, while for coarse grids with wall functions less than 10 will suffice.

4.1.16 Grid skewness

Typically the 3x3 determinant for structured grids should be greater than 0.3, as a measure of the Jacobian and associated skewness. However, it may be necessary to have a few small cells where the 3x3 determinant is no better than 0.15. For these cases it may be necessary

to use a smaller time step or increased under-relaxation in order to achieve converged results.

4.1.17 Boundary conditions

Choose boundary conditions that are compatible with the domain size chosen and problem approximations.

- Inlet conditions that are far from the field can impose pressure, velocity and free surface elevation as Dirichlet boundary conditions mimicking free flow. If the boundary is close to the ship Neumann boundary conditions (zero normal gradients) need to be imposed to relax the pressure and free surface.

- Far field boundary conditions can also be free flow if the boundary is far from the object (typically one ship length for Froude numbers larger than 0.2). If the boundary conditions are close or the Froude number is small then the ship will affect significantly the flow on the boundary, and Neumann conditions are preferred.

- Exit conditions usually are modelled with zero second derivative for velocities (zero traction) and zero gradient for pressure and free surface. This condition requires no inflow from this boundary, so it must be placed far down-stream enough to guarantee this throughout the computation. Otherwise zero normal gradient conditions can be attempted.

- The bottom can be treated as a far field if deep water is being simulated.

Sides and bottom may need to be treated as moving boundaries if shallow waters or a narrow towing tank are being simulated.

- In case of free surface flow simulations, the so-called radiation conditions must be imposed on exit or far field boundaries in order to pre-vent wave reflection on boundaries. Simple way to implement no reflection condition is to damp waves which go through boundaries with numerical dissipation by use of large grid space near the boundaries or by explicitly adding artificial damping terms to the governing equations. This is often called ‘numerical beach‘ approach

4.1.18 Choice of the time step

In explicit solvers the time step is chosen to satisfy the CFL condition or to resolve the flow features of interest, whatever results smaller. Usually the CFL condition is more demanding than the flow requirements. In implicit solvers the time step is decided by the flow features. As a rule of thumb:

- For waves, use at least 60 time steps per period for the shortest waves, or 100 time steps per period for regular waves.
- For other periodic phenomena (roll decay, vortex shedding, etc.) use at least 100 time steps per period.
- For complex unsteady phenomena, like wetted transom instabilities, use at least 20 time steps per period for the highest frequency to be resolved.
- For rotating propellers use at least 200 time steps per revolution.
- For standard pseudo-transient resistance computations, use $\Delta t = 0.005 \sim 0.01\ L/U$. The choice of time step will also depend on the complexity of the turbulence model. For Reynolds stress turbulence models it is more appropriate to use $\Delta t = 0.001 \sim 0.0025\ L/U$. This also requires a larger number of iterations to obtain reasonable convergence. In more unstable problems, as those with low Froude number, a smaller time step may be needed. Notice that naturally transient problems will not reach a steady-state solution.

4.1.19 Choice of convergence criteria

A number of convergence criteria should be defined and examined in order to ensure reliable convergence of solution.

At first hand the level of convergence should be assessed by the history of residual variations for the mass and momentum equations. Residuals indicate how far the present approximate solution is away from perfect conservation (balance) of mass and momentum. Thus the residual for a discretized equation is defined as the L_1-Norm of the imbalance between the left and the right hand side of that equation over all the computational cells. Usually in definition the residual is also scaled by a reference value. Sometimes L_2-Norm and L_∞-Norm are also used to define residual.

CFD users do not need to worry about the definition of residuals, as they are often pre-defined by code developers. Instead, attention should be paid to the selection of convergence criteria. The recommended criterion is "*the drop of scaled residuals by at least three orders of magnitude off their initial values*". However if this criterion cannot be achieved due to complexity of the problem or oscillatory convergence is found, then other criteria can be used to assess the convergence of the globally integrated parameters, for example:

- Forces and moments acting on the hull
- Thrust and torque produced by the propulsion system
- Velocity and turbulence parameters in key region of the flow field (e.g. at propeller plane for nominal wake calculations)

4.1.20 Choice of free surface model

There are two major categories in free surface models. First one is an interface fitting approach in which a numerical grid is aligned to deformed free surface shape and the other is an interface capturing approach in which a free surface shape is defined as an isosurface of a marker function and a grid does not to fit to a free surface. Choice of a free surface model is needed when a flow solver used offer both inter-face fitting and capturing models.

The interface fitting approach is more accurate and efficient than the capturing approach, since free surface boundary conditions can be applied in the exact free surface location. There-fore the interface fitting model may be selected whenever it is possible. However, it should be noted that re-gridding procedure is essential in the interface fitting method in order to keep the gridlines follow the deformation of free surface. This may cause severe distortion of gridlines even though the initial grid fitting to an undisturbed free surface has a good quality.

Difficulties in grid generation and/of re-gridding can be avoided in interface capturing approaches. Also, in the case that large deformation of free surface, such as overturning or breaking waves, is expected, interface capturing methods should be used. Since the capturing methods demand finer grid resolutions in the interface zones, grid generation requires more attentions. Choice of the level-set function method and volume-of-fluid method in the capturing approaches is little impact in the final solutions. Although details

of numerical procedures are different from each other, well-examined flow solvers provide similar results in both models.

4.1.21 Choice of turbulence model

Turbulence modelling has been an important research topic over the last decades. A large number of models have been proposed, tested and applied, but no 'universal' model has been developed. Thus one is forced to choose the best model available for each specific application. The majority of turbulence models is based on the so-called Boussinesq hypothesis, which de-fines a turbulence or eddy viscosity (as opposed to the molecular viscosity) to account for the effect the turbulence motion has on the mean flow.

Zero-equation, or algebraic models express the eddy viscosity in terms of the mean flow variables and mean flow gradients without solving any additional equations. They are hardly ever used in ship hydrodynamics.

One-equation models solve one additional equation (i.e. in addition to the momentum and mass conservation equations) for the eddy viscosity. Regularly encountered in ship hydrodynamics are models by Menter and by Spalart-Allmaras. These models are sometimes ex-tended with a correction for vortical flow, to improve wake field predictions.

Two-equation models solve two additional equations for the eddy viscosity, one for the turbulence kinetic energy (k), and one for its dissipation rate (typically ε or ω). These models have shown to be able to give accurate predictions in ship hydrodynamics, especially certain versions of the k-ω model and are by far the most applied ones (80% of the submissions for the Gothenburg 2010 Workshop).

An important class of turbulence models, not based on the Boussinesq hypothesis, are the Reynolds-stress models, and versions thereof. Rather than introducing an eddy-viscosity, they aim to solve the equations for the six Reynolds stress components directly. Apart from that, additional equations have to be solved, since terms in these equations require modelling as well. Consequently Reynolds-stress models are more computationally intensive, and often less easy to converge, compared to the one or two-equation models. However, they contain more physics and can be expected to be more accurate than eddy-viscosity models.

A more recent development is Large Eddy Simulation (LES). Other than the turbulence models discussed above it does not average the Navier-Stokes equations in time, but filters them in space. This results in transient computations on extremely dense grids as they aim to resolve all turbulence motion to a very small scale. Detached Eddy Simulation(DES) is a hybrid method that tries to reduce the required computational effort by solving the (unsteady) RANS equation in the boundary layer and applying LES in the rest of the domain. However, the very high Reynolds numbers encountered in ship hydrodynamics prevents the application of both methods in practical design projects.

4.1.22 Choice of numerical scheme

In the majority of industrial CFD codes, dif-fusion terms in the governing equations are discretized using a second-order (central differencing) scheme by default. Thus, spatial accuracy is largely determined by discretization scheme used for convection terms.

The first-order upwind (FOU) scheme, offered in many commercial CFD codes often as a default scheme, is famously stable. However, it introduces an unacceptably large amount of numerical (false) diffusion - that is why it is so stable. Therefore, it should be avoided at all costs. However, the very robustness of the FOU scheme can be exploited to start up the solution. For example, the first 100 iterations (or time steps) during which the solution is most susceptible to numerical instability and divergence) can be run using the FOU. As the flow-fields start settling down, one can switch to a high-order scheme.

The majority of high-order convection discretization schemes in popular use today formally have a second-order of accuracy with an upwind bias. All these second-order upwind (SOU) schemes differ from one another in terms of the flux limiter used to suppress unphysical oscillations in the solutions. Still higher-order schemes such as 5^{th}-order scheme exist. How-ever, not all CFD solvers offer such higher-order schemes. Even if they are available, the lack of robustness often makes them less useful than claimed. The SOU scheme that is both reasonably accurate and robust, and for that reason is an industrial workhorse for convection discretization. The SOU scheme is therefore recommended for all convection-diffusion type of transport equations.

Volume-fraction equation requires a special care, inasmuch as the transported quantity is essentially a step function in the vicinity of free surface, and the traditional convection schemes designed for convection-diffusion equations perform poorly in transporting the

step-function. It has been found that convection schemes with some degree of downwind bias resolve the sharp interface much better.

Second-order central differencing (CD) scheme is often used in large eddy simulation (LES) and direct numerical simulation (DNS) in favour of its low-dissipation that is critical to accurately resolve turbulent structures. How-ever, CD scheme is inherently unstable, giving troubles for cases involving fine meshes and small effective viscosity (large cell Reynolds number). One should consider using a stabilized form of central differencing.

4.2 Computation

At runtime, a few decisions need to be made:

a) In modern computers, choose the number of processors so that you use 50,000 to 200,000 grid points per processor.

b) To maximize performance, try to distribute the load evenly between nodes. For instance, if running in a Linux cluster with 2 dual-core processors (4 cores) per node, and your case needs 6 cores, you can distribute your load in two nodes using 4-2 or 3-3 configurations. The second balances the load per node better.

c) Modern workstations with shared memory are available with up to 48 processors, though much larger specialized systems are produced. High-performance clusters are typically cheaper per processor for large systems (thousands of cores) but use distributed memory. Shared-memory systems allow all processors access all memory, resulting in easier programming and better scalability of most applications. On the other hand, distributed memory systems provide massive number of processors for very large computations.

4.3 Post-processing

A number of post processing plots should be used as a minimum sub-set of information to ensure that the correct settings have been used for each computation. This should include the following:

- Contour plots of the pressure coefficient, skin friction coefficient and y^+ of the geometry surface
- Contour plots of the boundary layer profiles along the hull geometry
- Contour and vector plots of the nominal or powered wake upstream of the plane of the propulsor (Care should be taken to ensure that this plane does not lie within the propulsion disc/volume)

Reasonable checks should be carried out to ensure that these plots are smooth and continuous. In particular, regions of specially bad grid quality should be evaluated to check if the solver can handle properly less than optimal grids without causing unphysical artifacts.

4.4 Verification and validation

The definitions of errors and uncertainties directly follow those used in experimental uncertainty analysis. The simulation error δ_S is defined as the difference between a simulation result S and the truth T and is composed of additive modelling δ_{SM} and numerical δ_{SN} errors (i.e., $\delta_S = S - T = \delta_{SM} - \delta_{SN}$). For certain conditions, both the sign and magnitude of the numerical error can be estimated as $\delta_{SN} = \delta_{SN}^* + \varepsilon_{SN}$ where δ_{SN}^* is an estimate of the sign and magnitude of δ_{SN} and ε_{SN} is the error in that estimate. The simulation value is corrected to provide a numerical benchmark S_C, which is defined

$$S_c = S - \delta_{SN}^* \tag{4.1}$$

Verification is defined as a process for assessing simulation numerical uncertainty U_{SN} and, when conditions permit, estimating the sign and magnitude δ_{SN}^* of the simulation numerical error itself and the uncertainty in that error estimate U_{S_CN}. For the uncorrected simulation approach, numerical error is decomposed into contributions from iteration number δ_I, grid size δ_G, time step δ_T, and other parameters δ_P, which gives the following expression for simulation numerical uncertainty

$$U_{SN}^2 = U_I^2 + U_G^2 + U_T^2 + U_P^2 \tag{4.2}$$

For the corrected simulation approach, the solution is corrected to produce a numerical benchmark S_C and the estimated simulation numerical error δ_{SN}^* and corrected uncertainty U_{S_CN} are given by

$$\delta_{SN}^2 = \delta_I^2 + \delta_G^2 + \delta_T^2 + \delta_P^2 \tag{4.3}$$

$$U_{S_C N}^2 = U_{I_C}^2 + U_{G_C}^2 + U_{T_C}^2 + U_{P_C}^2 \tag{4.4}$$

Validation is defined as a process for assessing simulation modelling uncertainty U_{SM} by using benchmark experimental data and, when conditions permit, estimating the sign and magnitude of the modelling error δ_{SM} itself. The comparison error E is given by the difference in the data D and simulation S values

$$E = D - S = \delta_D - (\delta_{SM} + \delta_{SN}) \tag{4.5}$$

Modelling errors δ_{SM} can be decomposed into modelling assumptions and use of previous data. To determine if validation has been achieved, E is compared to the validation uncertainty U_V given by

$$U_V^2 = U_D^2 + U_{SN}^2 \tag{4.6}$$

If $|E| < U_V$, the combination of all the errors in D and S is smaller than U_V and validation is achieved at the U_V level. If $U_V \ll |E|$, the sign and magnitude of $E \approx \delta_{SM}$ can be used to make modelling improvements. For the corrected simulation, equations equivalent to equations (4.5) and (4.6) are

$$E_C = D - S_C = \delta_D - (\delta_{SM} + \delta_{SN}) \tag{4.7}$$

$$U_{V_C}^2 = U_{E_C}^2 - U_{SM}^2 = U_D^2 + U_{S_C N}^2 \tag{4.8}$$

4.5 Verification procedures

4.5.1 Convergence studies

Iterative and parameter convergence studies are conducted using multiple solutions (at least 3) with systematic parameter refinement by varying the kth input parameter Δ_{x_k} while holding all other parameters constant. The present work assumes input parameters can be expressed such that the finest resolution corresponds to the limit of infinitely small parameter values. Many common input parameters are of this form, e.g., grid spacing, time step, and artificial dissipation. Additionally, a uniform parameter refinement ratio:

$$r_k = \frac{\Delta x_{k_2}}{\Delta x_{k_1}} = \frac{\Delta x_{k_3}}{\Delta x_{k_2}} = \cdots = \frac{\Delta x_{k_m}}{\Delta x_{k_{m-1}}}$$

between solutions is assumed for presentation purposes, but not required. Iterative errors must be accurately estimated or negligible in comparison to errors due to input parameters before accurate convergence studies can be conducted.

Careful consideration should be given to selection of uniform parameter refinement ratio. The most appropriate values for industrial CFD are not yet fully established. Small values (i.e., very close to one) are undesirable since solution changes will be small and sensitivity to input parameter may be difficult to identify compared to iterative errors. Large values alleviate this problem; however, they also may be undesirable since the finest step size may be prohibitively small (i.e., require many steps) if the coarsest step size is designed for sufficient resolution such that similar physics are resolved for all m solutions. Also, similarly as for small values, solution changes for the finest step size may be difficult to identify compared to iterative errors since iterative convergence is more difficult for small step size. Another issue is that for parameter refinement ratio other than $r_k = 2$, interpolation to a common location is required to compute solution changes, which introduces interpolation errors. Roache (1998) discusses methods for evaluating interpolation errors. However, for industrial CFD, $r_k = 2$ may often be too large. A good alternative may be $r_k = \sqrt{2}$, as it provides fairly large parameter refinement ratio and at least enables prolongation of the coarse-parameter solution as an initial guess for the fine-parameter solution.

Convergence studies require a minimum of $m = 3$ solutions to evaluate convergence with respect to input parameter. Note that $m = 2$ is inadequate, as it only indicates sensitivity and not convergence, and that $m > 3$ may be required. Changes between medium-fine $\varepsilon_{k_{21}} = \hat{S}_{k_2} - \hat{S}_{k_1}$ and coarse-medium $\varepsilon_{k_{32}} = \hat{S}_{k_3} - \hat{S}_{k_2}$ solutions are used to define the convergence ratio

$$R_k = \frac{\varepsilon_{k_{21}}}{\varepsilon_{k_{32}}} \tag{4.9}$$

and to determine convergence condition where $\hat{S}_{k_1}$, $\hat{S}_{k_2}$, $\hat{S}_{k_3}$ correspond to solutions with fine, medium, and coarse input parameter, respectively, corrected for iterative errors. Three convergence conditions are possible:

(*i*) Monotonic convergence: $0 < R_k < 1$

(*ii*) Oscillatory convergence: $R_k < 0$ (4.10)

(*iii*) Divergence: $R_k > 1$

For condition (*i*), generalized Richardson extrapolation (RE) is used to estimate U_k or δ_k^* and U_k. For condition (*ii*), uncertainties are estimated simply by attempting to bound the error based on oscillation maximums S_U and minimums S_L, i.e., $U_k = \frac{1}{2}(S_U - S_L)$. For oscillatory convergence (*ii*), the solutions exhibit oscillations, which may be erroneously identified as condition (*i*) or (*iii*). This is apparent if one considers evaluating convergence condition from three points on a sinusoidal curve (Coleman et al., 2001). Depending on where the three points fall on the curve, the condition could be incorrectly diagnosed as either monotonic convergence or divergence. Bounding the error based on oscillation maximum and minimum for condition (*ii*) requires more than $m = 3$ solutions. For condition (*iii*), errors and uncertainties cannot be estimated.

4.5.2 Generalized Richardson Extrapolation

For convergence condition (*i*), generalized RE is used to estimate the error δ_k^* due to selection of the kth input parameter and order of accuracy p_k. The error is expanded in a power series expansion with integer powers of Δx_k as a finite sum. The accuracy of the estimates depends on how many terms are retained in the expansion, the magnitude (importance) of the higher-order terms, and the validity of the assumptions made in RE theory.

With three solutions, only the leading term can be estimated, which provides one-term estimates for error and order of accuracy

$$\delta_{RE_{k_1}}^{*(1)} = \frac{\varepsilon_{k_{21}}}{r_k^{p_k}} \tag{4.11}$$

$$p_k = \frac{\ln\left(\varepsilon_{k_{32}} - \varepsilon_{k_{21}}\right)}{\ln r_k} \tag{4.12}$$

With five solutions, two terms can be estimated, which provides two-term estimates for error and orders of accuracy

$$\delta_{RE_{k_1}}^{*(2)} = \frac{r_k^{q_k}\varepsilon_{21_k} - \varepsilon_{32_k}}{\left(r_k^{q_k} - r_k^{p_k}\right)\left(r_k^{p_k} - 1\right)} - \frac{r_k^{p_k}\varepsilon_{21_k} - \varepsilon_{32_k}}{\left(r_k^{q_k} - r_k^{p_k}\right)\left(r_k^{q_k} - 1\right)} \tag{4.13}$$

$$p_k = \frac{\ln\left\{\frac{\left(a_k + \sqrt{b_k}\right)}{\left[2\left(\varepsilon_{21_k}\varepsilon_{43_k} - \varepsilon_{32_k}^2\right)\right]}\right\}}{\ln r_k} \tag{4.14}$$

$$q_k = \frac{\ln\left\{\frac{\left(a_k - \sqrt{b_k}\right)}{\left[2\left(\varepsilon_{21_k}\varepsilon_{43_k} - \varepsilon_{32_k}^2\right)\right]}\right\}}{\ln r_k}$$

where

$a_k = \varepsilon_{21_k}\varepsilon_{54_k} - \varepsilon_{32_k}\varepsilon_{43_k}$

$b_k = -3\varepsilon_{32_k}^2\varepsilon_{43_k}^2 + 4\left(\varepsilon_{21_k}\varepsilon_{43_k}^3 + \varepsilon_{32_k}^3\varepsilon_{54_k}\right) - 6\varepsilon_{21_k}\varepsilon_{32_k}\varepsilon_{43_k}\varepsilon_{54_k} + \varepsilon_{21_k}^2\varepsilon_{54_k}^2$

Solutions for analytical benchmarks show that the range of applicability for equations (4.13) and (4.14) is more restrictive than that for equations (4.11) and (4.12) since all five solutions must be both monotonically convergent and sufficiently close to the asymptotic range to evaluate p_k and q_k in Eq. (4.14). In general, $m = 2n + 1$ solutions are required to estimate the first n terms of the error expansion.

4.5.3 Estimating errors and uncertainties with correction factor

The concept of correction factors is based on verification studies for $1D$ wave equation, $2D$ Laplace equation, and Blasius boundary layer analytical benchmarks for which it is shown that a multiplicative correction factor is useful as a quantitative metric to determine proximity of the solutions to the asymptotic range, to account for the effects of higher-order terms, and for estimating errors and uncertainties. The error is defined as

$$\delta_{k_1}^* = C_k\delta_{RE_{k_1}}^* = C_k\left(\frac{\varepsilon_{k_{21}}}{r_k^{p_k} - 1}\right) \tag{4.15}$$

where two expressions for the correction factor C_k were developed. The first is based on solution of (4.15) for C_k with $\delta_{RE_{k_1}}^*$ based on (4.11) but replacing p_k with the improved estimate $p_{k_{est}}$

$$C_k = \frac{r_k^{p_k} - 1}{r_k^{p_{k_{est}}} - 1} \tag{4.16}$$

$p_{k_{est}}$ is an estimate for the limiting order of accuracy of the first term as spacing size goes to zero and the asymptotic range is reached so that $C_k \to 1$. Similarly, the second is based on a two-term estimate of the power series which is used to estimate $\delta^*_{RE_{k_1}}$ where p_k and q_k are replaced with $p_{k_{est}}$ and $q_{k_{est}}$

$$C_k = \frac{\left(\frac{\varepsilon_{k_{23}}}{\varepsilon_{k_{12}}} - r_k^{q_{k_{est}}}\right)\left(r_k^{p_k} - 1\right)}{\left(r_k^{p_{k_{est}}} - r_k^{q_{k_{est}}}\right)\left(r_k^{p_{k_{est}}} - 1\right)} + \frac{\left(\frac{\varepsilon_{k_{23}}}{\varepsilon_{k_{12}}} - r_k^{p_{k_{est}}}\right)\left(r_k^{p_k} - 1\right)}{\left(r_k^{p_{k_{est}}} - r_k^{q_{k_{est}}}\right)\left(r_k^{q_{k_{est}}} - 1\right)} \tag{4.17}$$

Eq. (4.16) roughly accounts for the effects of higher-order terms by replacing p_k with $p_{k_{est}}$ thereby improving the single-term estimate, while Eq. (4.17) more rigorously accounts for higher-order terms since it is derived from a two-term estimate. Both expressions for C_k only require three solutions to estimate errors using Eq. (4.15). Solutions for analytical benchmarks show that correction of error estimates with both expressions for C_k yields improved error estimates.

Expressions for uncertainties are developed from error estimates in Eq. (4.15). When solutions are far from the asymptotic range, C_k is sufficiently less than or greater than 1 and only the magnitude of the error is estimated through the uncertainty U_k . Eq. (4.15) is used to estimate U_k by bounding the error $\delta^*_{k_1}$ by the sum of the absolute value of the corrected estimate from RE and the absolute value of the amount of the correction

$$U_k = [|C_k| + |1 - C_k|]\left|\delta^*_{RE_{k_1}}\right| \tag{4.18}$$

It is shown by Wilson and Stern (2002) that Eq. (4.18) is not conservative enough for $C_k < 1$, which motivates development of an improved estimate

$$U_k = [2|1 - C_k| + 1]\left|\delta^*_{RE_{k_1}}\right| \tag{4.19}$$

When solutions are close to the asymptotic range, C_k is close to 1 so that δ^*_k is estimated using Eq. (4.15) and U_{k_C} is estimated by

$$U_{k_c} = |(1 - C_k)|\left|\delta^*_{RE_{k_1}}\right| \tag{4.20}$$

Eq. (4.20) has the correct form for both $C_k < 1$ and $C_k > 1$. However, Eq. (4.20) has shortcoming that for $C_k = 1$, 0 U_{k_C}, which is unrealistic; therefore for $C_k = 1$, alternatively the factor of safety approach is recommended as discussed in previous sections and Eq.

(4.22) should be used. It should be recognized that using the corrected simulation approach requires in addition to C_k close to 1 that one have confidence in Eq. (4.15). There are many reasons for lack of confidence, especially for complex three-dimensional flows.

4.5.4 Estimating uncertainties with factor of safety

Alternatively, a factor of safety approach (Roache, 1998) can be used to define the uncertainty U_k where an error estimate from RE is multiplied by a factor of safety F_S to bound simulation error

$$U_k = F_S \left| \delta^*_{RE_{k_1}} \right| \tag{4.21}$$

where $\delta^*_{RE_{k_1}}$ can be based on a single- or two term estimate as given by Eq. (4.11) or (4.13), respectively with either assumed or estimated order of accuracy. If order of accuracy is assumed (e.g., based on theoretical values), only two or three solutions are required for evaluation of Eq. (4.11) or (4.13), respectively.

Although not proposed by Roache (1998), the factor of safety approach can be used for situations where the solution is corrected with an error estimate from RE as

$$U_k = (F_S - 1) \left| \delta^*_{RE_{k_1}} \right| \tag{4.22}$$

The exact value for factor of safety is somewhat ambiguous and $F_S = 1.25$ is recommended for careful grid studies and 3 for cases in which only two grids are used and order of accuracy is assumed from the theoretical value p_{th}.

4.5.5 Discussion of Fundamental and Practical Issues

It should be recognized that implementation of verification procedures is not easy and require both experience and interpretation of results, especially for practical applications. However, their importance cannot be overemphasized to ensure fidelity and quality of CFD solutions.

Fundamental issues include from the outset selection of multiple vs. single grid approaches for estimating errors and uncertainties. However, the former approach can be used to establish convergence and is relatively inexpensive to implement and therefore recommended at this time. For multiple-grid approaches, important fundamental issues include appropriateness of power series representation [Eq. (4.25) of Stern et al. (2001)] and its convergence characteristics along with assumptions that $p_k^{(i)}$ and $g_k^{(i)}$ are independent of Δx_k. Also, issues concerning definitions and nature of solutions in asymptotic vs. non-asymptotic ranges.

These fundamental issues are exacerbated for practical applications along with additional issues, including selection of parameter refinement ratio, procedures for generation of multiple systematic grids and solutions, number of grids required and variability between grid studies, selection of appropriate verification procedures, and interpretation of results.

Selection of parameter refinement ratio was discussed previously wherein use of uniform value $r_k = \sqrt{2}$ was recommended; however, non-uniform and larger/smaller values may also be appropriate under certain circumstances. Wilson and Stern (2002) discuss procedures for generation of multiple systematic grids and solutions. Multiple systematic grids are generated using $r_k = \sqrt{2}$ and a post-processing tool in which the coarse grid is obtained by removing every other point from the fine grid and the medium grid is obtained by interpolation. Multiple solutions are obtained by first obtaining a solution for the coarse grid with a uniform flow initial condition, which is then used as an initial condition for obtaining a solution on the medium grid, which is then used as an initial condition for obtaining a solution on the fine grid. This procedure can be used to obtain solutions on all three grids in about $1/3$ the time required to obtain only the fine grid solution without this procedure.

For complex flows with relatively coarse grids, solutions may be far from asymptotic range such that some variables are convergent while others are oscillatory or even divergent. Order of accuracy and therefore correction factors and factors of safety may display large variability indicating the need for finer grids. Clearly, more than 3 grids are required to estimate errors and uncertainties for such cases. Eca and Hoekstra (1999, 2000) propose a least squares approach to estimate the error by computing the three unknown parameters from RE when more than three grids are used and there is variability between grid studies.

Both correction factor and factor of safety verification approaches have been presented with selection a user option. Wilson and Stern (2002) have shown that the factor of safety

approach is over conservative when solutions are close to the asymptotic range and under conservative when solutions are far from the asymptotic range. Nonetheless some users may prefer factors of safety over correction factors. An alternative is to select the more conservative uncertainty from the correction factor and factor of safety approaches. For the uncorrected simulation approach the more conservative uncertainty from Eqs. (4.19) and (4.21) is given by

$$U_k = max[(2|1 - C_k| + 1), F_S] \left|\delta^*_{RE_{k_1}}\right| \tag{4.23}$$

For the corrected simulation approach, the more conservative uncertainty from Eq. (4.20)and (4.22) is given by

$$U_{k_c} = max[|(1 - C_k)|, (F_S - 1)] \left|\delta^*_{RE_{k_1}}\right| \tag{4.24}$$

For $F_S = 1.25$, uncorrected uncertainty estimates from Eq. (4.23) are based on the factor of safety approach when C_k is close to one (i.e., $0.875 < C_k < 1.125$) and on the correction factor approach outside this range (i.e., $|1 - C_k| > 0.125$). For the corrected approach, uncertainties from Eq. (4.24) are based on the correction factor approach when $|1 - C_k| > 0.125$. When using correction factors an important issue is selection of the best estimate for the limiting order of accuracy. Theoretical values can be used or values based on solutions for simplified geometry and conditions. In either case, preferably including the effects of stretched grids.

Lastly, analysis and interpretation of results is important in assessing variability for order of accuracy, levels of verification, and strategies for reducing numerical and modeling errors and uncertainties; since, as already mentioned, there is limited experience and no known solutions for practical applications in the asymptotic range for guidance.

4.6 Validation procedures

4.6.1 Interpretation of the results of a validation effort

First, consider the approach in which the simulation numerical error is taken to be stochastic and thus the uncertainty U_{SN} is estimated. From a general perspective, if we consider the three variables U_V, E, and U_{reqd} there are six combinations (assuming none of the three variables are equal):

1) $|E| < U_V < U_{reqd}$
2) $|E| < U_{reqd} < U_V$
3) $U_{reqd} < |E| < U_V$
4) $U_V < |E| < U_{reqd}$ (4.25)
5) $U_V < U_{reqd} < |E|$
6) $U_{reqd} < U_V < |E|$

In cases 1, 2 and 3, $|E| < U_V$; validation is achieved at the U_V level; and the comparison error is below the noise level, so attempting to estimate δ_{SMA} is not feasible from an uncertainty standpoint. In case 1, validation has been achieved at a level below U_{reqd}, so validation is successful from a programmatic standpoint.

In cases 4, 5 and 6, $U_V < |E|$, so the comparison error is above the noise level and using the sign and magnitude of E to estimate δ_{SMA} is feasible from an uncertainty standpoint If $U_V \ll |E|$, then E corresponds to δ_{SMA} and the error from the modelling assumptions can be determined unambiguously. In case 4, validation is successful at the $|E|$ level from a programmatic standpoint.

Now consider the approach in which the simulation numerical error is taken to be deterministic and thus δ_{SN}^* and the uncertainty U_{V_C} are estimated. A similar set of comparisons as those in equation (25) can be constructed using $|E_C|$, U_{V_C} , and U_{reqd}. Since E_C can be larger or smaller than E, but U_{V_C} should always be less than U_V, the results for a given corrected case are not necessarily analogous to those for the corresponding uncorrected case. That is, a variable can be validated in the corrected but not in the uncorrected case, or vice versa. For cases 4, 5, and 6 in which $U_{V_C} < |E|$, one can argue that E_C is a better indicator of δ_{SMA} than is E, assuming that one's confidence in using the estimate δ_{SN}^* is not misplaced.

4.6.2 Use of corrected vs. Uncorrected simulation results

The requirements for correcting the solution are that the correction factor be close to one and that confidence in solutions exist. Since the variability of the order of accuracy cannot be determined from solutions on three grids, confidence is difficult to establish in this case. As a result, caution should be exercised when correcting solutions using information from only three grids.

If a validation using the corrected approach is successful at a set condition, then if one chooses to associate that validation uncertainty level with the simulation's prediction at a neighbouring condition that prediction must also be corrected. That means enough runs are required at the new condition to allow estimation of the numerical errors and uncertainties. If this is not done, then the comparison error E and validation uncertainty U_V corresponding to the use of the uncorrected S and its associated (larger) U_{SN} should be the ones considered in the validation with which one wants to associate the prediction at a new condition.

(Whether to and how to associate an uncertainty level at a validated condition with a prediction at a neighbouring condition is very much unresolved and is justifiably the subject of much debate at this time.)

5 Numerical simulations

5.1 Experimental reference work

In Fig. 5.1 the profiles of the monohedral hull and of the warped 2 models are presented. The transversal Section 2 is the same for both models and is positioned at $0.25L_{OA}$ from stern.

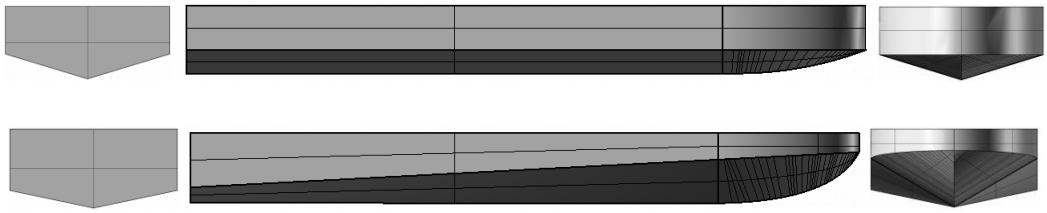

Fig. 5.1 The profile of DIN systematic series models, Begovic and Bertorello (2012)

L/B ratio is the same for both models $\frac{L}{B} = 4$. The models were built with clear bottom and deck in order to allow the visual inspection of the fluid flow and the assessment of the wetted surface.

For each models the principal characteristics were determined and are reported in the Tab. 5.1.

	MONO	WARP 2
L_{OA} (m)	1.900	1.900
L_{A-B} (m)	1.500	1.500
B (m)	0.424	0.424
T_{AP} (m)	0.096	0.110
Δ (N)	319.697	319.697
C_{Δ}	0.4277	0.4277
LCG (m)	0.697	0.609
VCG (m)	0.143	0.155
τ $(\mathbf{deg})$	1.660	1.660
F_{r_V}	0.650 – 4.518	0.650 – 4.518
C_V	0.564 – 3.660	0.564 – 3.660
β	16.70	11.59 – 30.11

Tab. 5.1 DIN models principal characteristics, Begovic and Bertorello (2012)

5.2 Pre processing

The following settings are to be considered identical for both hulls, Monohedral hull and Warped 2 hull, independently by type of figure to which they refer, except where specifically mentioned.

1. Fig. 5.2 shows the refinement system. I fixed the refinement system in Rhino of hulls in:

$$X = LCG \qquad Y = 0 \qquad Z = T$$

2. I saved in *.stp format. I imported the Surfafe Mesh in STAR CCM+ (File -> Import -> Import Surface Mesh -> Monohedral hull.stp) and I setted up the properties, shown in Fig. 5.3.
3. I setted a rotation of -1.66 deg around the Y-axis (Geometry -> Parts -> Right clic on MONO -> Transform -> Rotate), Fig. 5.4.

4. I created the computational domain (Geometry -> Right clic on Parts -> New Shape Part -> Block) that it was chosen with values shown in Tab. 5.2 and Tab. 5.3.
5. I dragged the new Block in the Parts into the scene (Part Displayer -> Add to Geometry 1). I selected both the Block and the hull and I have done a Boolean Subtraction (Parts -> Right clic on it -> Boolean -> Subtract Parts), Fig. 5.5.
6. I have splitted the domain (Geometry -> Parts -> Subtract -> Right clic on Block Surface -> Split by Patch) and I renamed the boundaries in Inlet, Outlet, Symmetry, Up, Down and Side. I assigned parts to Region (Geopetry -> Parts -> Right clic on Subtract -> Assign Parts to Regions...) with commands shown in Fig. 5.6.
7. I changed the boundary condition type in ''Velocity inlet'' for Inlet, Side, Up and Down; similarly, ''Outlet pressure'' for Outlet and ''Symmetry plane'' for Symmetry (Regions -> Region -> Boundaries -> Subtract.Inlet, and in the Properties window below I changed the Type of boundary to Velocity Inlet. The same applies to Subtract.Side, Subtract.Down, Subtract.Up. Similarly, I selected Pressure Outlet and Symmetry for the other two external boundaries), Fig. 5.7, Fig. 5.8, Fig. 5.9.
8. I selected the Meshing Models (Right clic on Continua -> New -> Mesh Continuum, and than Right clic on Mesh 1 -> Select Meshing Models) and I setted reference values, shown in Fig. 5.10 and Tab. 5.4.
9. I created 6 volume shapes refinements around water level (Tools -> Volume Shapes -> Block). Here, I just reported dimensions for Block 1 and Block 5 Monohedral hull, Fig. 5.11, Tab. 5.5 and Tab 5.6.
10. I assigned each Block to Volumetric Controls (Continua -> Mesh 1 -> Right clic on Volumetric Controls -> New, and than in the Properties window below, clic on [] alongside Shapes and I selected Block 1. The same applies to Block 2, Block 3, Block 4 and Block 5). I selected Trimmer and I unabled the customization anisotropic size.
11. To well capture the wake generated by models, I performed another more specific refirement by creating a triangular geometry, shown in Fig. 5.12, (Geometry -> Right clic on Parts -> New Shape Part -> Block, and I renamed it in Wake Refinement) with dimensions shown in Tab. 5.7. In order to rotate this new block it was necessary creating a new coordinate system Z-rotated about 5° respect to the absolute reference system. Similarly to previously created volumetric control, I enabled the customization of isotropic size in Trimmer propreties.

12. To better capture the separation of the fluid from the edge, I created a new Block called Chine, shown in Fig. 5.13, (Geometry -> Right clic on Parts -> New Shape Part -> Block) with dimensions shown in Tab 5.8. Similarly to previously created volumetric control, I enabled the customization of isotropic size in Trimmer propreties.
13. To better definition of the refinement of the wake ant for avoiding to see the edge of the block that it represents the body of refining, I created a Cylinder, shown in Fig. 5.14, (Geometry -> Right clic on Parts -> New Shape Part -> Cylinder) with dimensions shown in Tab. 5.9. Similarly to previously created volumetric control, I enabled the customization of isotropic size in Trimmer propreties.
14. In order to avoid the incident of the ventilation, I created a new Block, shown in Fig. 5.15, (Geometry -> Right clic on Parts -> New Shape Part -> Block) with dimensions shown in Tab. 5.10. Similarly to previously created volumetric control, I enabled the customization of isotropic size in Trimmer propreties.
15. I created 4 box refinements near the models, Fig. 5.16, (Tools -> Volume Shapes -> Block) and, after associated these 4 box to Volumetric Controls, I unabled only customize isotropic size in the Trimmer node.
16. I generated the Volume mesh, Fig. 5.17, Fig. 5.18 and Fig. 5.19.
17. In Derived Parts I created the Isosurface (Right clic on Derived Parts -> New Part -> Isosurface...), with properties shown in Tab 5.11.
18. In Derived Parts, I created a vertical section plane and an horizontal section plane (Right clic on Derived Parts -> New Part -> Section -> Plane) with properties shown in Tab. 5.12 and Tab. 5.13.
19. I setted up Phisics models (Right clic on Continua -> New -> Phisics Continuum, and then Right clic on Phisics 1 -> Select models...), Fig. 5.20.
20. I definited the multiphase (Water and Air) mixture (Continua -> Phisics 1 -> Eulerian Multiphase -> Eulerian Phases, Right clic to create a new phase [repeat twice], Rename the two phases Water and Air, Right clic on the Water node and select the models Liquid and Costant Density, Right clic on the Air node and select the models Gas and Costant Density), Fig. 5.21.
21. I definited the X-component of VOF Waves model for each simulation (Continua -> Phisics 1 -> Models -> VOF Waves -> Right clic on Wave -> New -> Flat, and in the Properties of FlatVofWave 1, set the X-component of the Current and Wind velocities for all range of velocity, and set CFL_I to 500.0 and CFL_u to 1000.0), Fig. 5.22.

22. I setted up the initial conditions (Continua -> Phisics 1 -> Initial conditions, clic on Pressure and set the Method to Field Function, and do the for the Velocity node, clic on Volume Fraction and set the Method to Composite, then for its subnodes Water and Air set the Method on Field Function, clic on Pressure -> Field Function and select as Scalar Function ''Hydrostatic Pressure of FlatVow Wave 1'', clic on Velocity -> Field Function and select as Scalar Function ''Velocity of FlatVofWave 1'', for the Water and Air Field Functions, select ''Volume Fraction of Heavy Fluid of FlatVofWave 1'' and ''Volume Fraction of Light Fluid of FlatVofWave 1'' respectively), Fig. 5.23.
23. I setted up Boudary Conditions for Inlet, Outlet, Up, Down and Side (Regions -> Region -> Boundaries -> Subtract.inlet -> Physics Conditions, and set the Velocity Specification to Components, then extend the Physics Values, Similary to the setting of Initial Conditions, set the Velocity Method to Field Function and select ''Velocity of FlatVofWave 1'', for the Volume Fraction, select Composite then the two field functions already used for the Initial Conditions. The same it was done for Subtract.Up, Subtract.Down and Subtract.Side. Extend the node Subtract.Outlet -> Physics Values, set the Pressure Method to Field Function and select ''Hydrostatic Pressure of FlatVofWave 1'', for the Volume Fraction, select Composite then the two field functions already used for the Initial Conditions).
24. I setted Damping in proximity of the Outlet (Regions -> Region -> Physics Conditions -> VofWave Damping Option: enable the Damping, Physics Values -> VofWave Damping Length) with lengths shown in Tab. 5.14. Thus, I switched the Method on ''Yes'' (Regions -> Region -> Boundaries -> Subtract.Outlet -> Physics Conditions -> VofWaveBampingBoundaryOption).
25. I setted up Solvers and Stopping Criteriea, making attention that Courant-Frederich-Lewis (CFL) number in the main flow direction, i.e. $U\frac{\Delta t}{\Delta x}$ should be less than unity for better results, Tab. 5.15.
26. I prepared:
    - Volume fraction of water on the symmetry plane, Fig. 5.24
    - Position (Z) Scenes, Fig. 5.25
    - Hydro Pressure Scenes, Fig. 5.26
    - Velocity: Magnitude Scene, Fig. 5.27
    - Drag and Lift Plots, Fig. 5.28
    - Trim, Sinkage and Wetted Surface Plots, Fig. 5.29, Fig. 5.30 and Fig. 5.31
    - Pressure Line Plots, Fig. 5.32

27. I setted free Z-traslation and Y-rotarion motions (Tools -> Right clic on Motions -> New -> DFBI Rotation and Traslation, and then Regions -> Region -> Physics Values -> Motion Specification, and set the Motion property to DFBI Rotation and Traslation).
28. I setted up the Body Mass (1/2 Body Mass), Moments of Inertia, Release Time and Ramp Time (DFBI -> Right clic on 6-DOF Bodies -> New, and in the Body 1 Properties I selected the parts associated to the hull, and the I switched ON ''Free motion'' on Z-Motion and Y-Rotation), Tab. 5.16.

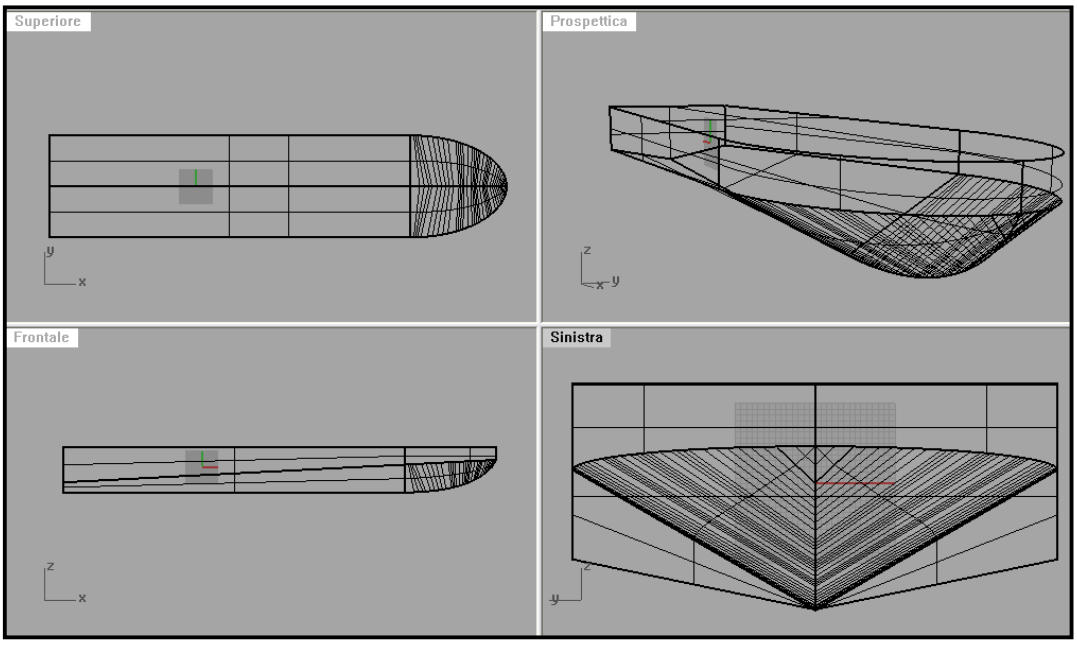

Fig. 5.2 Reference system of Warped 2 hull

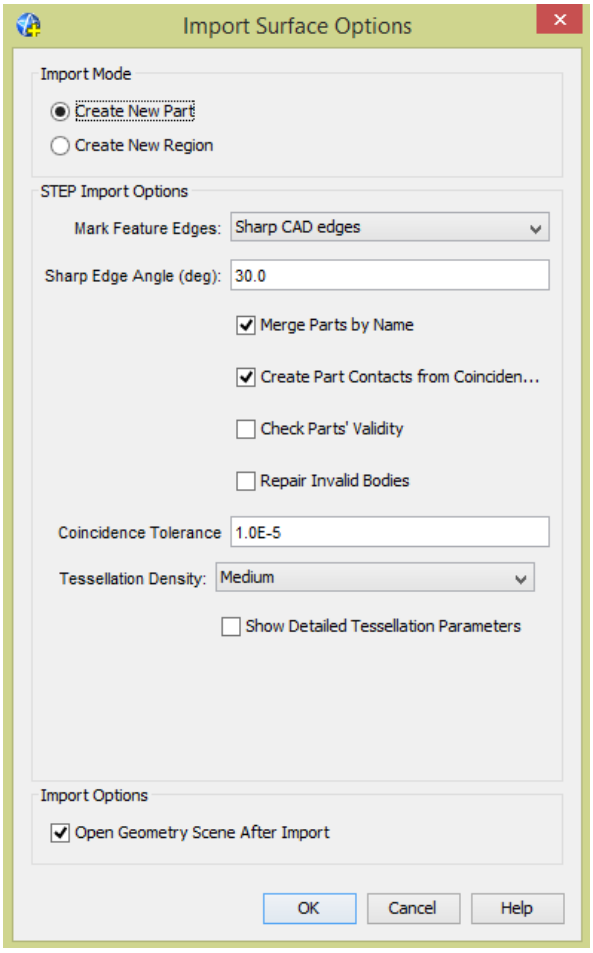

Fig. 5.3 Import Surface Options

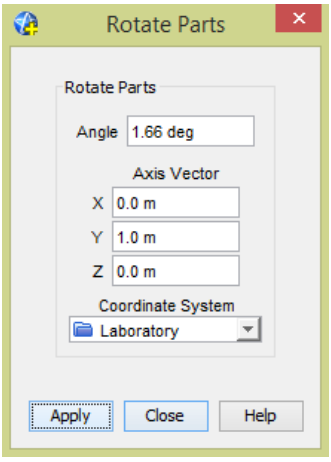

Fig. 5.4 Rotate Parts

Corner 1	Corner 2
X = -16.0 m	X = 5.0 m
Y = 0.0 m	Y = 6.0 m
Z = -5.0 m	Z = 3.0 m

Tab. 5.2 Monohedral hull – Computational domain

Corner 1	Corner 2
X = -12.0 m	X = 5.0 m

Y = 0.0 m	Y = 5.0 m
Z = -5.0 m	Z = 3.0 m

Tab. 5.3 Warped 2 hull – Computational domain

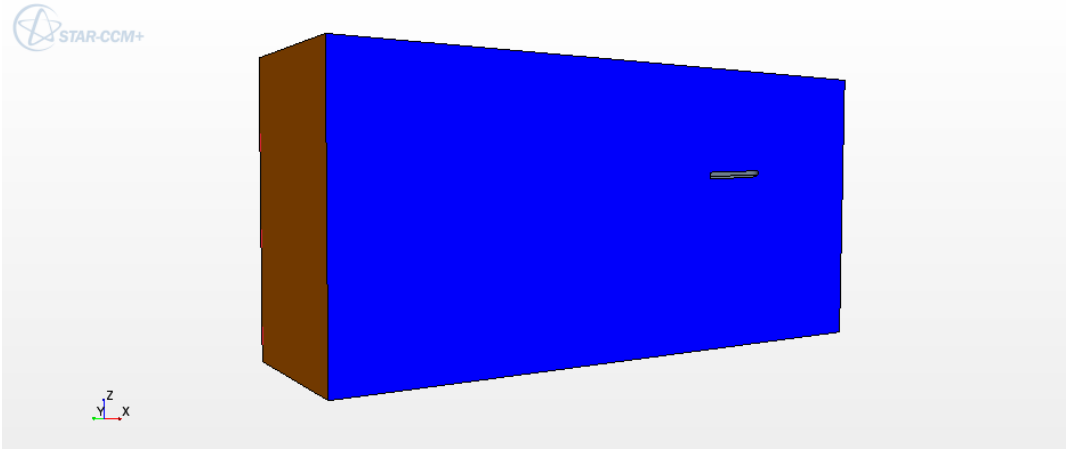

Fig. 5.5 Geometry of Boolean Subtraction of Warped 2 hull

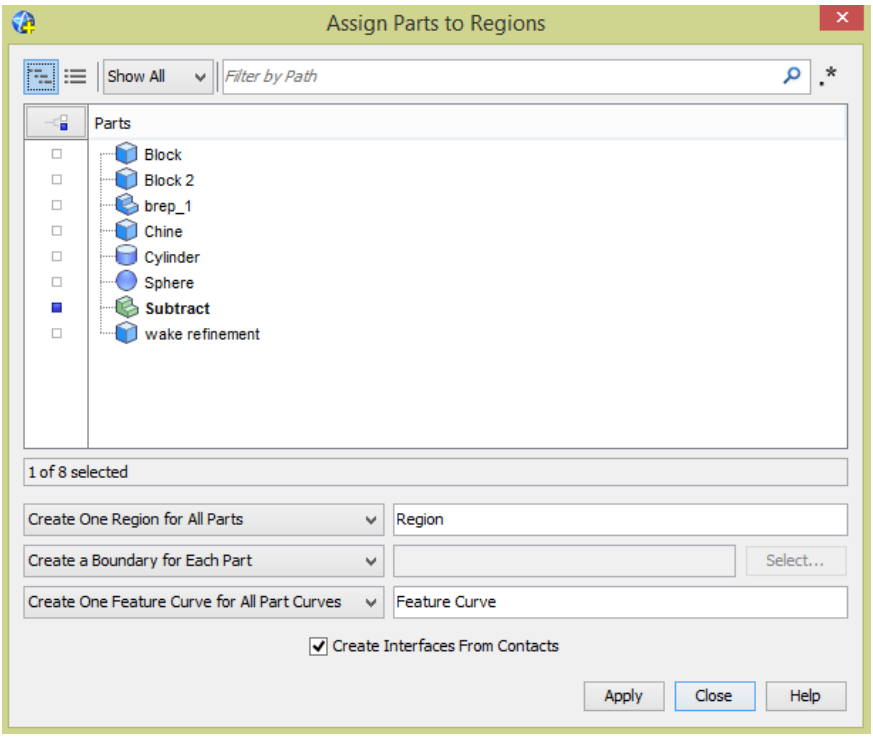

Fig. 5.6 Parts to Regions

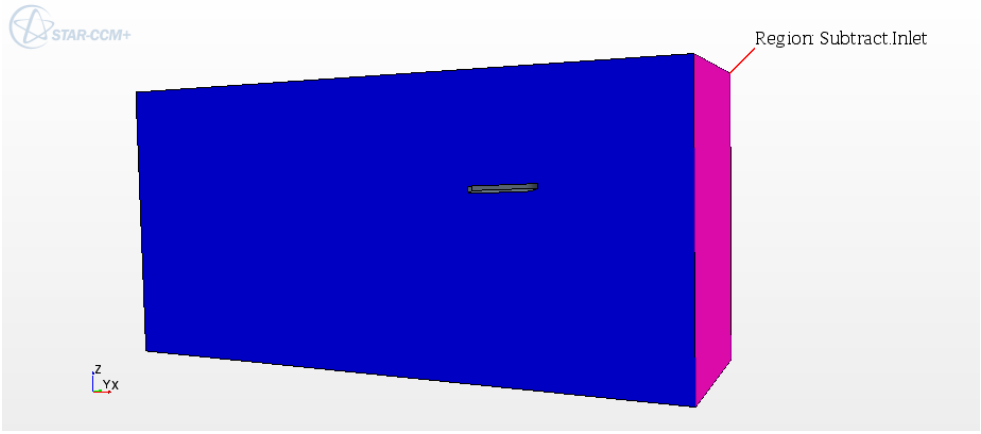

Fig. 5.7 Subtract Inlet of Warped 2 hull

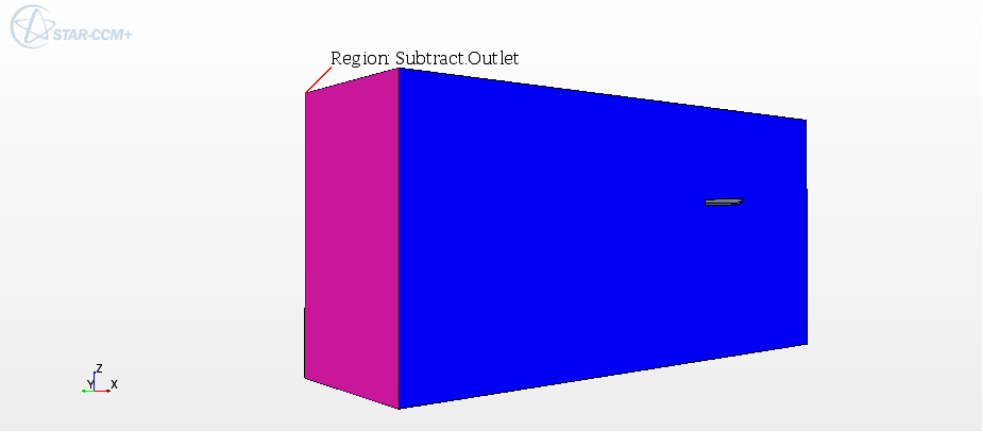

Fig. 5.8 Subtract Outlet of Warped 2 hull

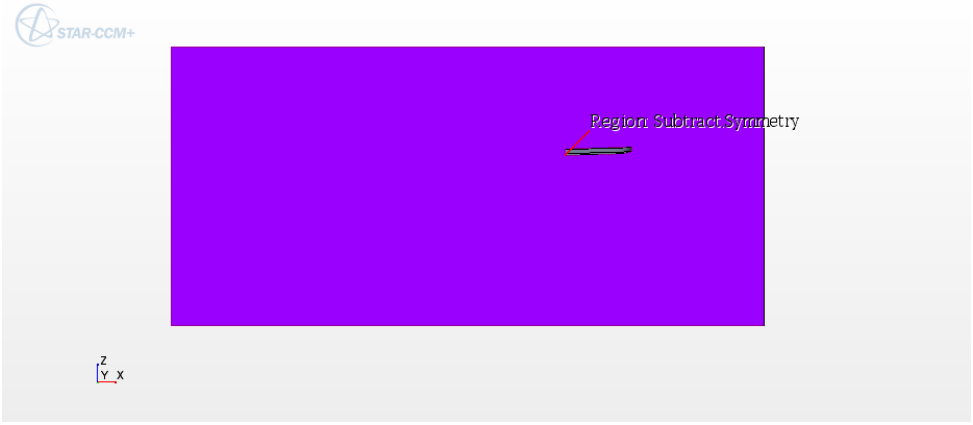

Fig. 5.9 Subtract Symmetry of Warped 2 hull

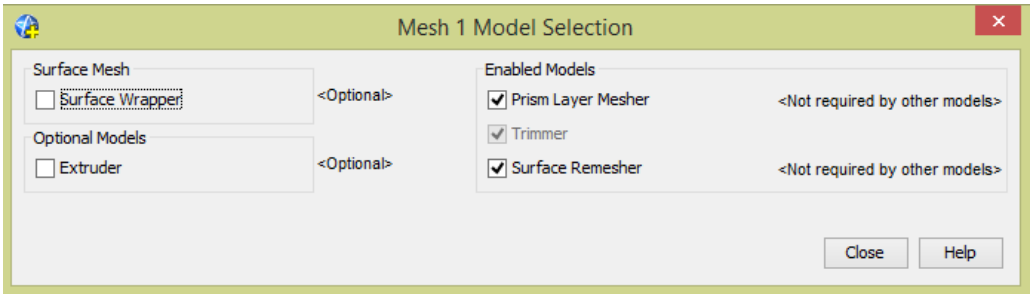

Fig. 5.10 Meshing models

Base size	6 m
Maximum cell size > Relative size	500 %
Number of prism layers	12
Prism Layer Stretching	1.3
Prism layer thickness > Relative size	0.04 %
Surface Growth Rate	1.3
Surface Siza > Relative Minimum Size	10 %
Surface Siza > Relative Target Size	200 %
Template Growth Rate	Fast, Fast

Tab. 5.4 Reference values

Corner 1	Corner 2
X = -16.0 m	X = 5.0 m
Y = 0.0 m	Y = 6.0 m
Z = -0.15 m	Z = 0.15 m

Tab. 5.5 Corners refinement Block 1

Corner 1	Corner 2
X = -16.0 m	X = 5.0 m
Y = 0.0 m	Y = 6.0 m
Z = -4 m	Z = 0.45 m

Tab. 5.6 Corners refinement Block 6

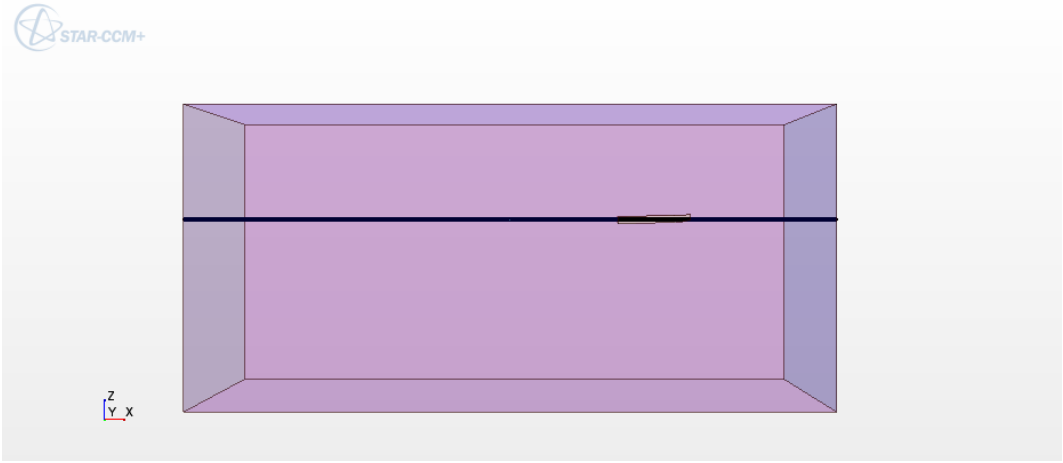

Fig. 5.11 Refinement around water level (Block 1)

Corner 1	Corner 2
X = -16.0 m	X = 2.4 m
Y = -2.5 m	Y = 1.0 m
Z = -0.5 m	Z = 0.5 m

Tab. 5.7 Corners wake refinement

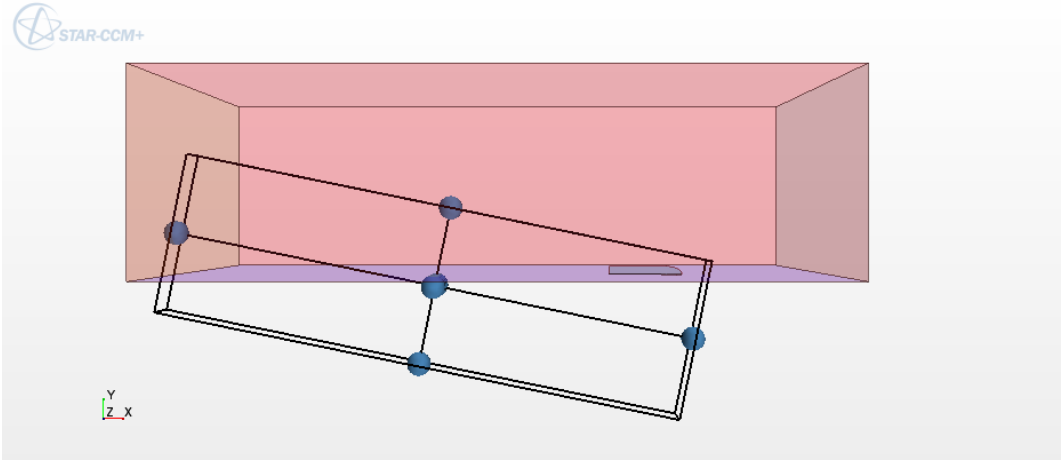

Fig. 5.12 Specific refinement by creating a triangular geometry

Corner 1	Corner 2
X = -0.64 m	X = 0.06 m
Y = 0.18 m	Y = 0.25 m
Z = -0.04 m	Z = 0.06 m

Tab. 5.8 Corners chine refinement

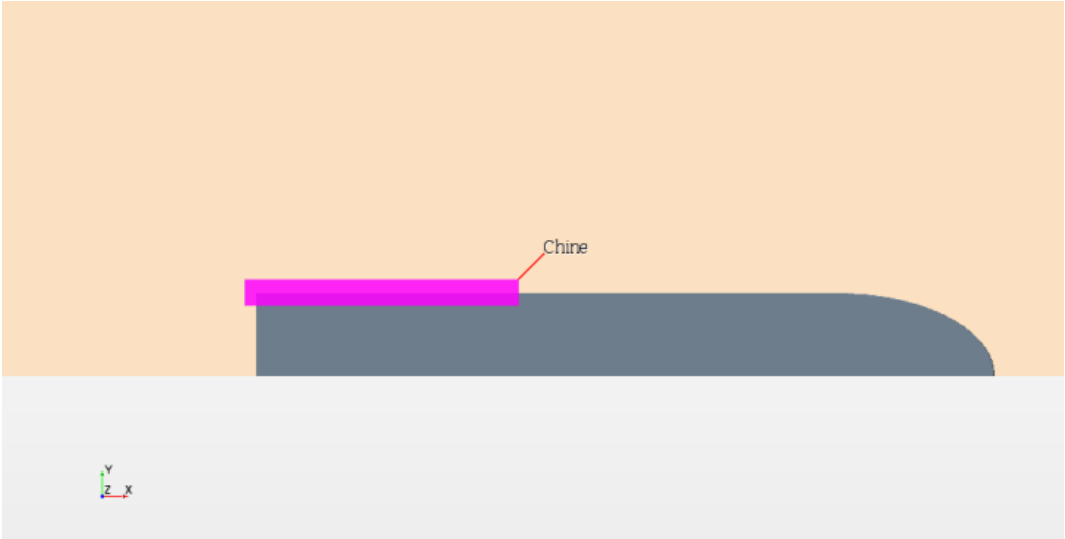

Fig. 5.13 Chine Block

Start Coordinate	End Coordinate
2.5 m	2.5 m
0.0 m	0.0 m
0.5 m	- 0.5 m

Tab. 5.9 Coordinate cylinder refinement

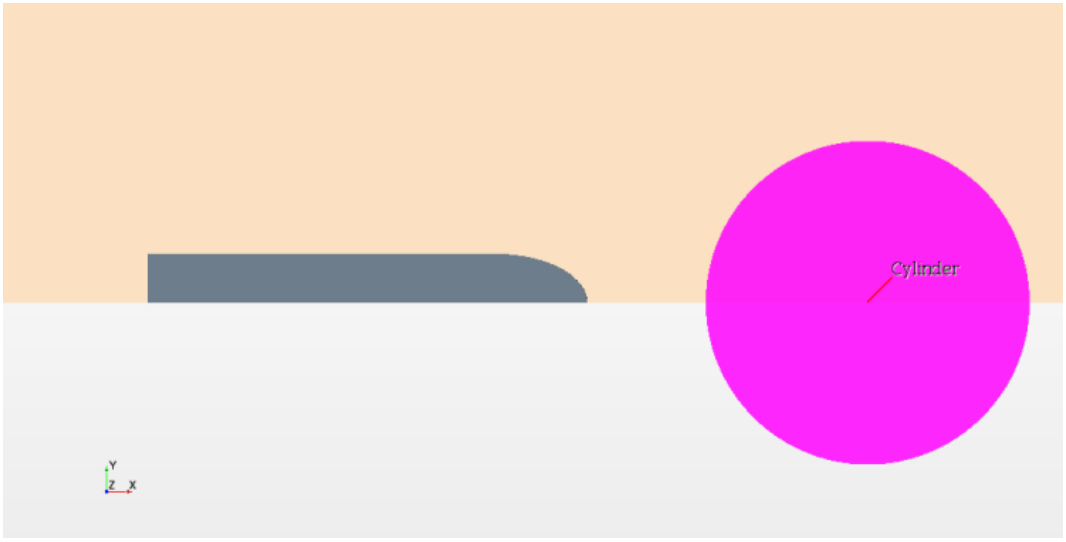

Fig. 5.14 Cylinder Block

Corner 1	Corner 2
X = -0.63 m	X = 1.23 m
Y = -0.01 m	Y = 0.08 m
Z = -0.14 m	Z = 0.01 m

Tab. 5.10 Corners keel refinement

Fig. 5.15 Keel Block

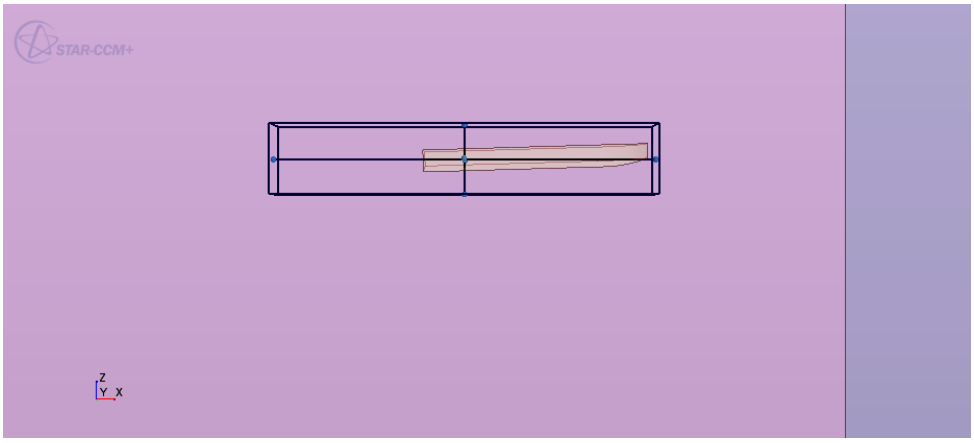

Fig. 5.16 Box refinements near the models

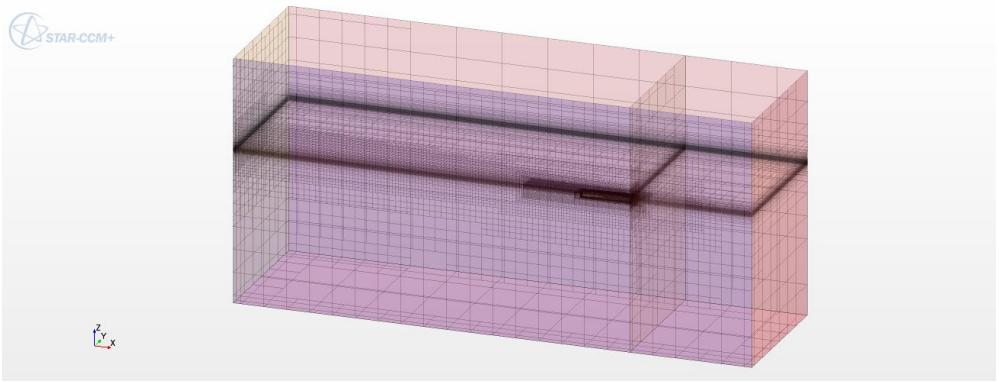

Fig. 5.17 Volume mesh

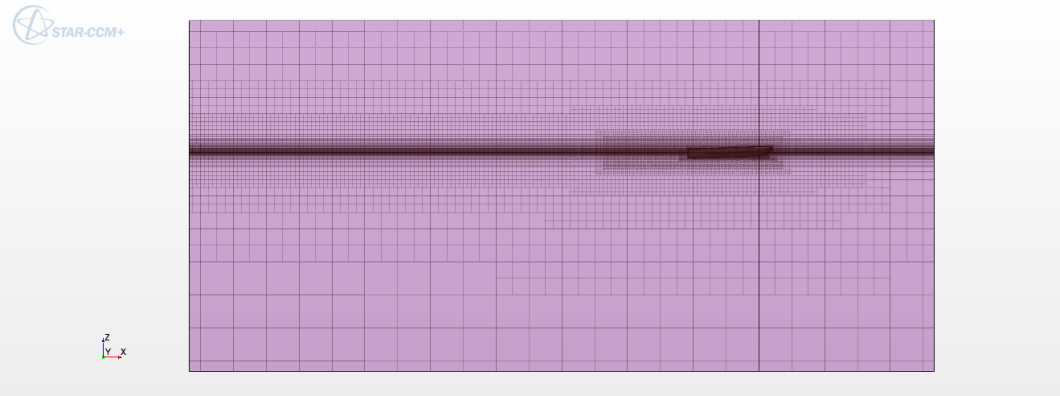

Fig. 5.18 Volume mesh in XZ-plane

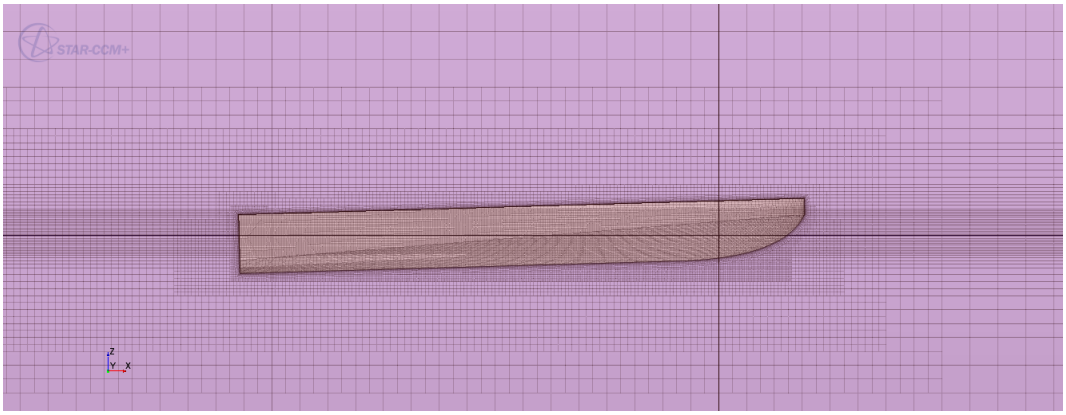

Fig. 5.19 Volume mesh near Warped 2 hull

Input Parts	Region
Scalar	Volume fraction > Volume fraction of Air
Isovalue	0.5
Display	New Scalar Displayer

Tab. 5.11 Isosurface properties

Input Parts	Region
Origin	(1.0, 0.0, 0.0)
Normal	(1.0, 0.0, 0.0)
Display	Existing Displayer > Mesh 1

Tab. 5.12 Vertical section plane properties

Input Parts	Region
Origin	(0.0, 0.0, 0.0)
Normal	(0.0, 0.0, 1.0)
Display	Existing Displayer > Mesh 1

Tab. 5.13 Horizontal section plane properties

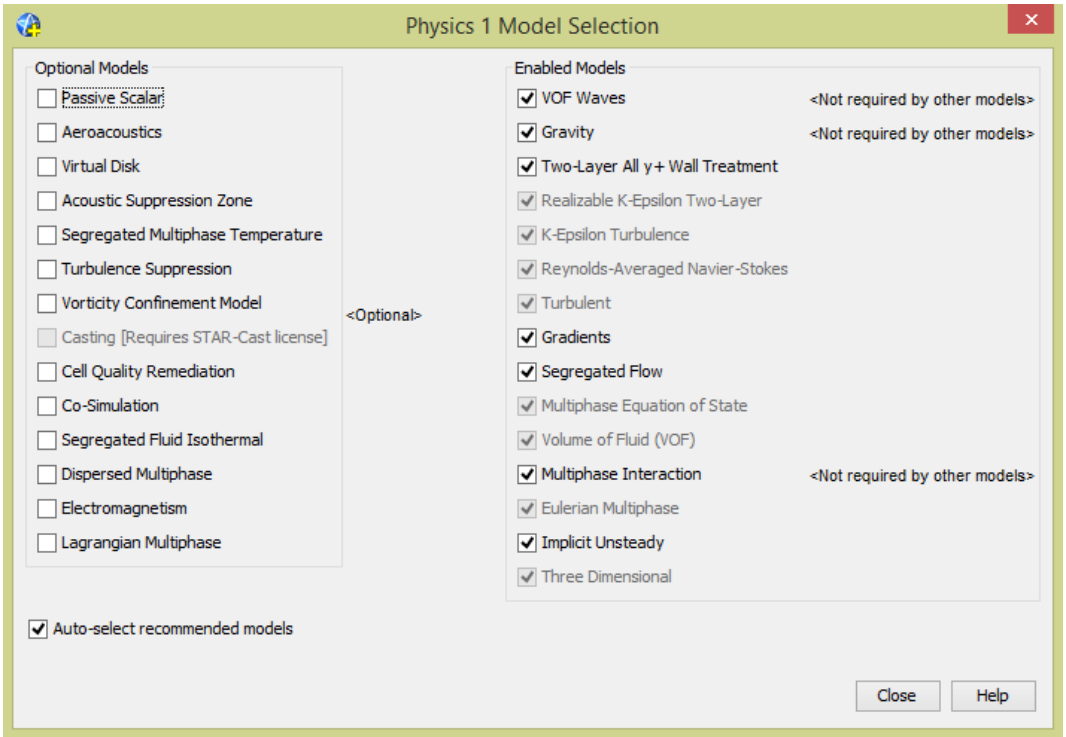

Fig. 5.20 Physics models

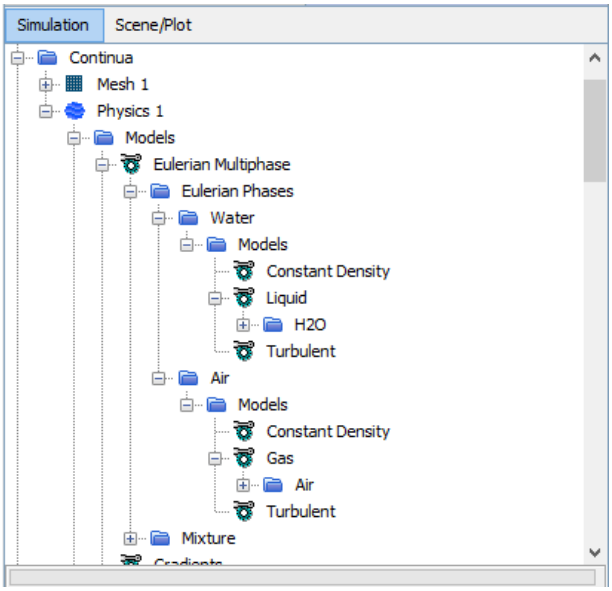

Fig. 5.21 Eulerian multiphase

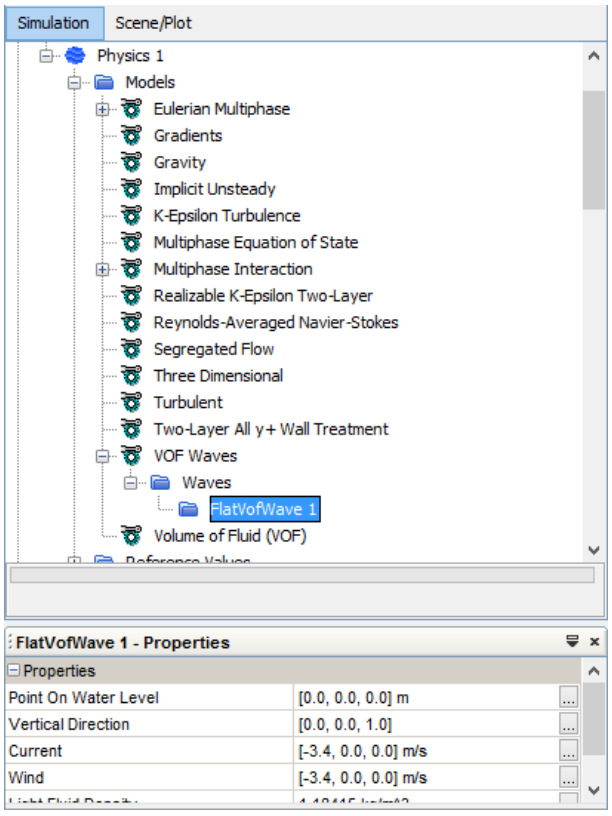

Fig. 5.22 X-Component of VOF waves

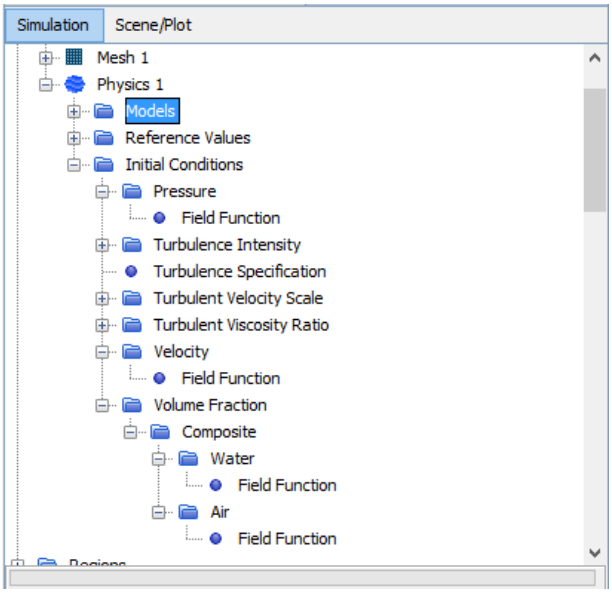

Fig. 5.23 Initial conditions

Monohedral hull	8.0 m
Warped 2 hull	4.0 m

Tab. 5.14 Damping length

Implicit Unsteady	0.005 – 0.002 s
Maximum Inner Iterations	3
Maximum Phisical Time	20.0 – 25.0 s
Maximum Steps	Enabled
Stop File	Enabled

Tab. 5.15 Solvers properties

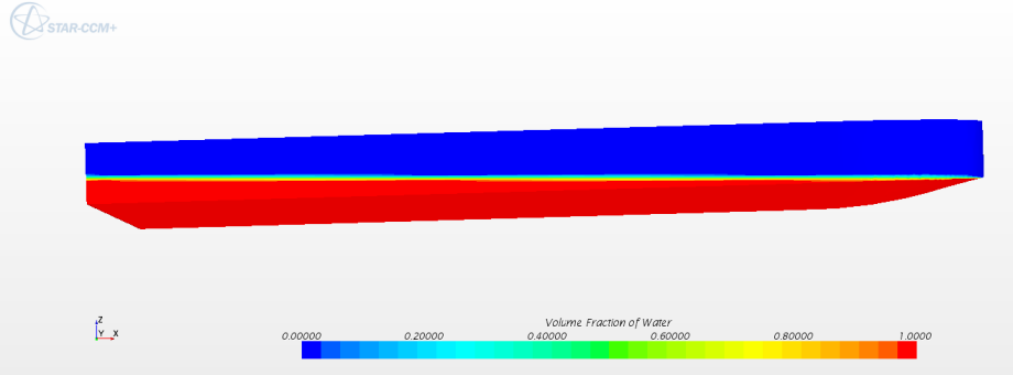

Fig. 5.24 Volume fraction of water (Monohedral hull)

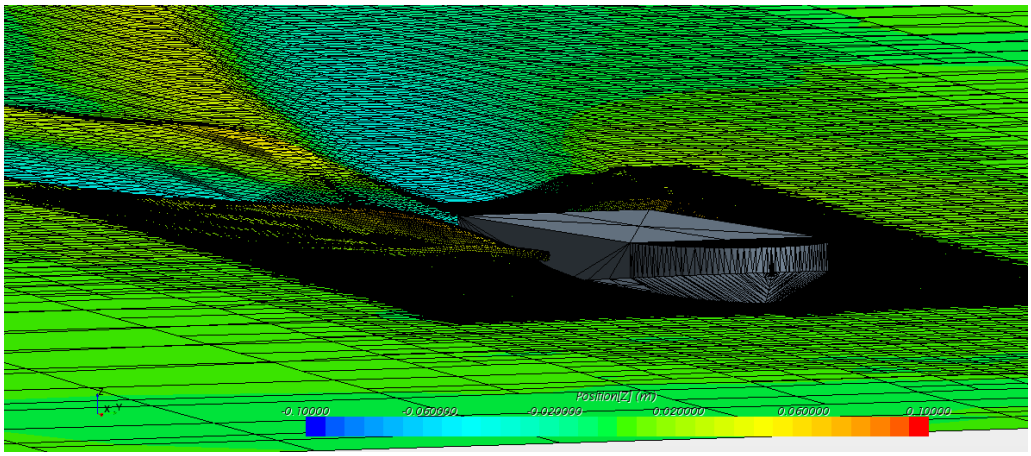

Fig. 5.25 Position (Z) (Warped 2 hull)

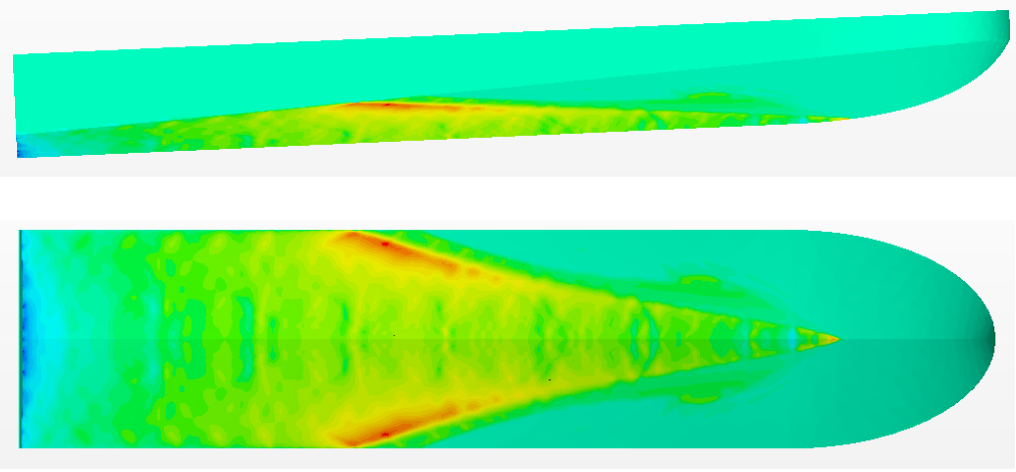

Fig. 5.26 Hydro Pressure (Warped 2 hull)

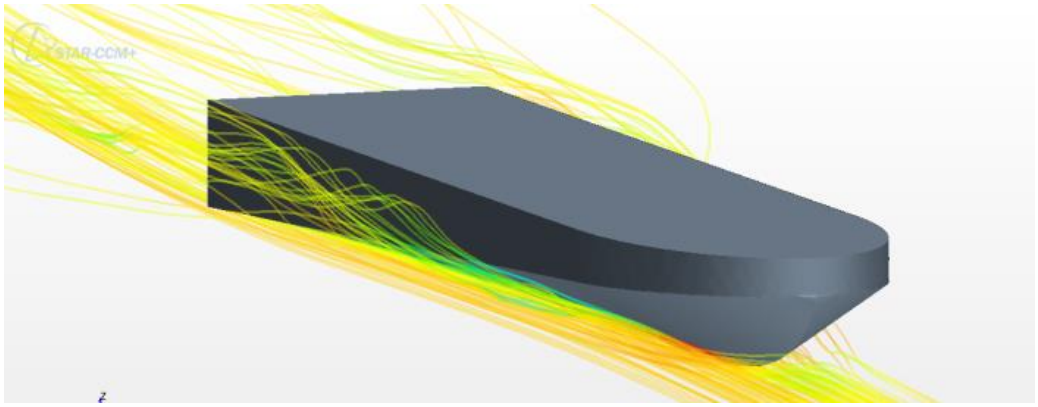

Fig. 5.27 Velocity: Magnitude (Warped 2 hull)

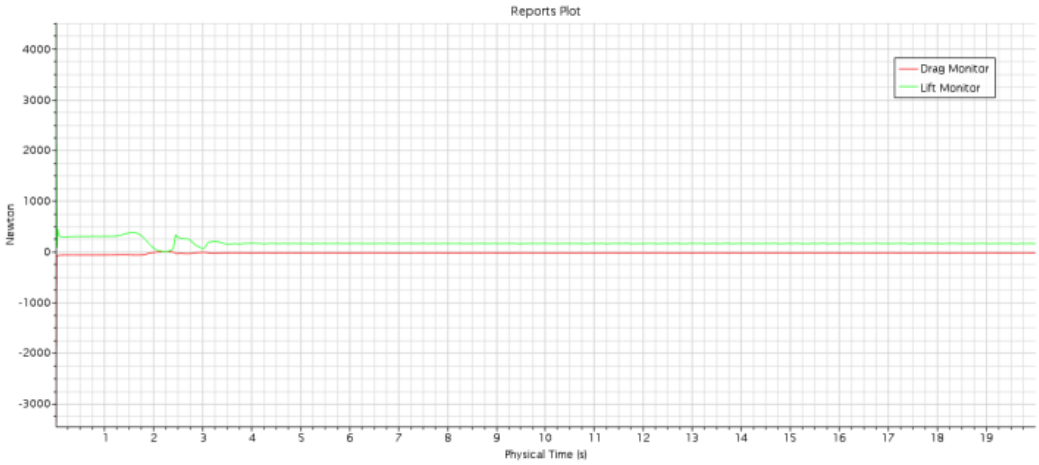

Fig. 5.28 Drag and Lift (Warped 2 hull)

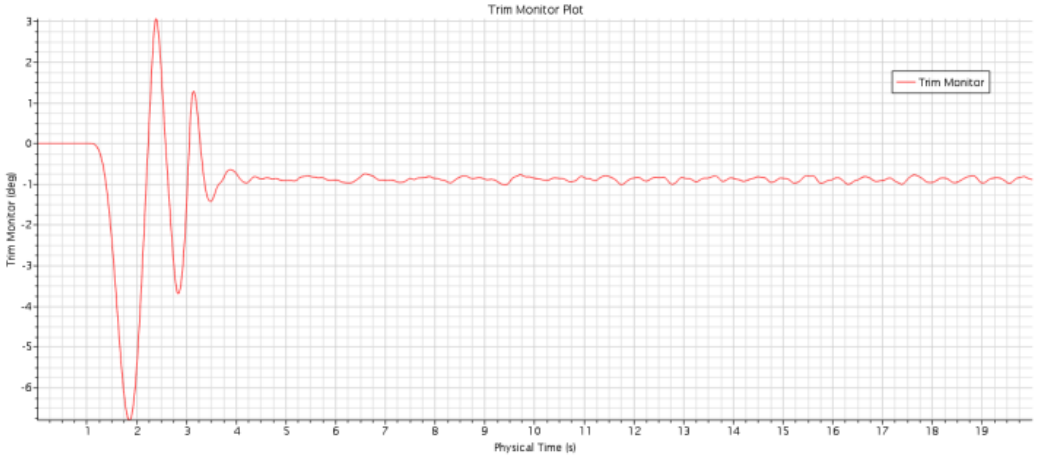

Fig. 5.29 Trim (Warped 2 hull)

Fig. 5.30 Sinkage (Warped 2 hull)

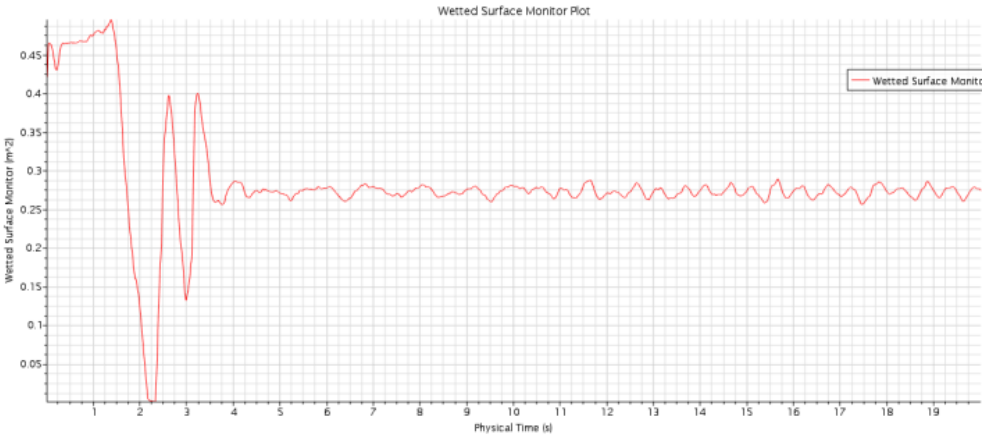

Fig. 5.31 Wetted Surface (Warped 2 hull)

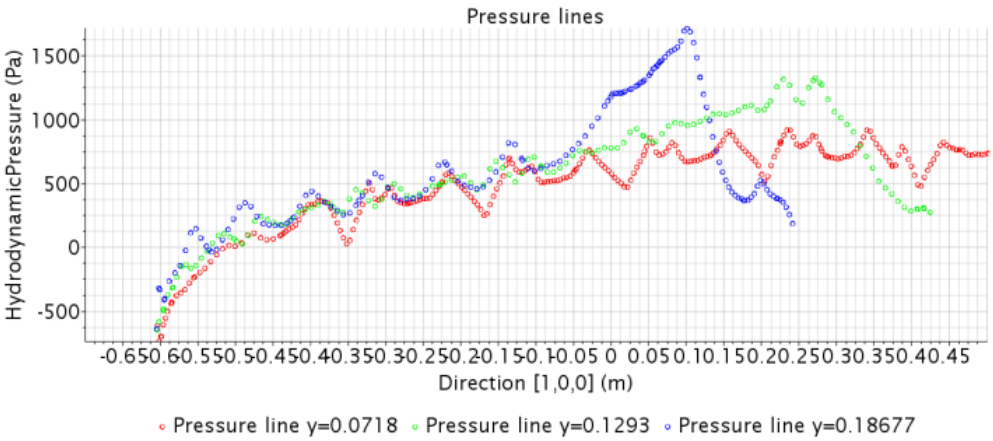

Fig. 5.32 Pressure Lines (Warped 2 hull)

Body Mass Monohedral Hull	16.315 Kg (half hull)
Body Mass Warped 2	16.315 Kg (half hull)
Moments of Inertia Monohedral Hul	[0.0543; 1.1083; 1.1083] Kgm^2
Moment of Inertia Warped 2	[0.0545; 1.0433; 1.0433] Kgm^2
Release Time	1.0 s
Ramp Time	5.0 s

Tab. 5.16 Hull properties

5.3 Results and comparison

The simulations were performed with three different numbers of cells:

	Monohedral	Warped
Coarse grid	1 004 229 cells	984 437 cells
Medium grid	1 432 240 cells	1 422 707 cells
Fine grid	2 147 253 cells	2 090 231 cells

Tab. 5.17 Numbers of cells for each grid

At four different velocities: 3.4 m/s, 4.6 m/s, 5.75 m/s and 6.32 m/s.

All calculations have been performed at High Performance Computing Centre of University of Naples "Federico II" (SCoPE), using 32 processors.

Monohedral hull

Resistance

		Experiment	CFD									SAVITSKY Short Form		
			Coarse Grid			Medium Grid			Fine Grid					
			1 004 229 cells			1 432 240 cells			2 147 252 cells					
C_V	v	R_T	R_T	Difference	Difference	R_T	Difference	Difference	R_T	Difference	Difference	R_T	Difference	Difference
	m/s	*N*	*N*	*N*	%	*N*	*N*	%	*N*	*N*	%	*N*	*N*	%
1,667	3,4	38,756	37,2280	1,5280	3,94	38,0394	0,7166	1,85	38,3202	0,4358	1,12	38,016	0,7400	1,91
2,256	4,6	46,474	44,9858	1,4882	3,20	45,6824	0,7916	1,70	46,0268	0,4472	0,96	47,184	-0,7100	-1,53
2,819	5,75	52,044	49,7872	2,2568	4,34	50,8372	1,2068	2,32	51,1690	0,8750	1,68	53,044	-1,0000	-1,92
3,098	6,32	56,172	53,1582	3,0138	5,37	54,7007	1,4713	2,62	55,2365	0,9355	1,67	56,162	0,0100	0,02

Trim

		Experiment	CFD									SAVITSKY Short Form		
			Coarse Grid			Medium Grid			Fine Grid					
			1 004 229 cells			1 432 240 cells			2 147 252 cells					
C_V	v	τ	τ	Difference	Difference	τ	Difference	Difference	τ	Difference	Difference	τ	Difference	Difference
	m/s	*deg*	*deg*	*deg*	%	*deg*	*deg*	%	*deg*	*deg*	%	*deg*	*deg*	%
1,667	3,4	3,972	3,6217	0,3503	8,82	3,7878	0,1842	4,64	3,8226	0,1494	3,76	4,322	-0,3500	-8,81
2,256	4,6	4,174	4,0153	0,1587	3,80	4,0952	0,0788	1,89	4,1348	0,0392	0,94	4,794	-0,6200	-14,85
2,819	5,75	4,024	3,8548	0,1692	4,20	3,9314	0,0926	2,30	3,9725	0,0515	1,28	4,374	-0,3500	-8,70
3,098	6,32	3,720	3,2571	0,4629	12,44	3,4816	0,2384	6,41	3,5522	0,1678	4,51	4,040	-0,3200	-8,60

Sinkage

		Experiment	CFD								
			Coarse Grid			Medium Grid			Fine Grid		
			1 004 229 cells			1 432 240 cells			2 147 252 cells		
C_V	v	Z_V	Z_V	Difference	Difference	Z_V	Difference	Difference	Z_V	Difference	Difference
	m/s	*mm*	*mm*	*mm*	%	*mm*	*mm*	%	*mm*	*mm*	%
1,667	3,4	-3,648	0,2896	-3,9376	107,9	-0,5162	-3,1318	85,8	-0,9056	-2,7424	75,2
2,256	4,6	9,705	10,7423	-1,0373	-10,7	12,3216	-2,6166	-27,0	11,7865	-2,0815	-21,4
2,819	5,75	17,425	22,4561	-5,0311	-28,9	21,9876	-4,5626	-26,2	21,9473	-4,5223	-26,0
3,098	6,32	24,096	31,6085	-7,5125	-31,2	32,6562	-8,5602	-35,5	31,2589	-7,1629	-29,7

Wetted Surface

		Experiment			CFD									SAVITSKY Short Form		
					Coarse Grid			Medium Grid			Fine Grid					
					1 004 229 cells			1 432 240 cells			2 147 252 cells					
C_V	v	WS_{PA}	WS_{WS}	WS_{ALL}	WS_{ALL}	Difference	Difference	WS_{ALL}	Difference	Difference	WS_{ALL}	Difference	Difference	WS_{PA}	Difference	Difference
	m/s	m^2	m^2	m^2	m^2	m^2	%	m^2	m^2	%	m^2	m^2	%	m^2	m^2	%
1,667	3,4	0,668	0,036	0,704	0,7980	-0,0937	11,74	0,7574	-0,0531	7,01	0,7356	-0,0313	4,26	0,727	-0,0227	-3,23
2,256	4,6	0,582	0,041	0,623	0,6672	-0,0439	6,58	0,6538	-0,0305	4,66	0,6356	-0,0123	1,93	0,634	-0,0106	-1,70
2,819	5,75	0,516	0,047	0,563	0,5842	-0,0212	3,64	0,5772	-0,0142	2,47	0,5698	-0,0068	1,20	0,567	-0,0036	-0,65
3,098	6,32	0,497	0,041	0,538	0,5786	-0,0410	7,08	0,5589	-0,0213	3,81	0,5489	-0,0113	2,05	0,545	-0,0070	-1,31

Warped 2 hull

		Resistance												
		Experiment	CFD									SAVITSKY Short Form		
			Coarse Grid			Medium Grid			Fine Grid					
			984 437 cells			1 422 707 cells			2 090 231 cells					
C_V	v	R_T	R_T	Difference	Difference	R_T	Difference	Difference	R_T	Difference	Difference	R_T	Difference	Difference
	m/s	*N*	*N*	*N*	%	*N*	*N*	%	*N*	*N*	%	*N*	*N*	%
1,667	3,4	45,101	42,4916	2,6094	5,79	43,3232	1,7778	3,94	43,8668	1,2342	2,74	44,361	0,7400	1,64
2,256	4,6	50,740	48,3912	2,3488	4,63	49,2921	1,4479	2,85	49,8968	0,8432	1,66	51,450	-0,7100	-1,40
2,819	5,75	55,535	51,5748	3,9602	7,13	52,6106	2,9244	5,27	53,3442	2,1908	3,94	56,535	-1,0000	-1,80
3,098	6,32	59,722	54,8532	4,8688	8,15	56,2046	3,5174	5,89	56,8370	2,8850	4,83	59,712	0,0100	0,02

		Trim												
		Experiment	CFD									SAVITSKY Short Form		
			Coarse Grid			Medium Grid			Fine Grid					
			984 437 cells			1 422 707 cells			2 090 231 cells					
C_V	v	τ	τ	Difference	Difference	τ	Difference	Difference	τ	Difference	Difference	τ	Difference	Difference
	m/s	*deg*	*deg*	*deg*	%	*deg*	*deg*	%	*deg*	*deg*	%	*deg*	*deg*	%
1,667	3,4	4,179	3,8780	0,3010	7,20	4,0121	0,1669	3,99	4,0561	0,1229	2,94	4,529	-0,3500	-8,38
2,256	4,6	4,145	3,8995	0,2455	5,92	4,0198	0,1252	3,02	4,0768	0,0682	1,65	4,765	-0,6200	-14,96
2,819	5,75	3,221	2,7417	0,4793	14,88	2,9798	0,2412	7,49	3,0936	0,1274	3,96	3,571	-0,3500	-10,87
3,098	6,32	2,771	2,2551	0,5159	18,62	2,4849	0,2861	10,32	2,6260	0,1450	5,23	3,091	-0,3200	-11,55

		Sinkage										
		Experimen	CFD									
			Coarse Grid			Medium Grid			Fine Grid			
			984 437 cells			1 422 707 cells			2 090 231 cells			
C_V	v	Z_V	Z_V	Difference	Difference	Z_V	Difference	Difference	Z_V	Difference	Difference	
	m/s	*mm*	*mm*	*mm*	%	*mm*	*mm*	%	*mm*	*mm*	%	
1,667	3,4	4,965	4,8656	0,0994	2,00	4,4877	0,4773	9,61	5,0333	-0,0683	-1,38	
2,256	4,6	22,501	27,2388	-4,7378	-21,06	26,5729	-4,0719	-18,10	26,6373	-4,1363	-18,38	
2,819	5,75	29,601	40,0453	-10,4443	-35,28	39,1827	-9,5817	-32,37	39,3463	-9,7453	-32,92	
3,098	6,32	35,559	42,9588	-7,3998	-20,81	42,6545	-7,0955	-19,95	42,4512	-6,8922	-19,38	

		Wetted Surface														
		Experiment			CFD									SAVITSKY Short Form		
					Coarse Grid			Medium Grid			Fine Grid					
					984 437 cells			1 422 707 cells			2 090 231 cells					
C_V	v	WS_{PA}	WS_{WS}	WS_{ALL}	WS_{ALL}	Difference	Difference	WS_{ALL}	Difference	Difference	WS_{ALL}	Difference	Difference	WS_{ALL}	Difference	Difference
	m/s	m^2	m^2	m^2	m^2	m^2	%	m^2	m^2	%	m^2	m^2	%	m^2	m^2	%
1,667	3,4	0,617	0,035	0,652	0,7612	-0,1094	14,37	0,7092	-0,0574	8,09	0,6942	-0,0424	6,11	0,663	-0,0109	-1,67
2,256	4,6	0,538	0,023	0,561	0,5964	-0,0355	5,95	0,5782	-0,0173	2,99	0,5695	-0,0086	1,51	0,568	-0,0070	-1,25
2,819	5,75	0,498	0,033	0,531	0,5502	-0,0195	3,55	0,5445	-0,0138	2,54	0,5405	-0,0098	1,82	0,532	-0,0015	-0,27
3,098	6,32	0,498	0,033	0,531	0,5751	-0,0445	7,74	0,5531	-0,0225	4,07	0,5426	-0,0120	2,21	0,534	-0,0037	-0,70

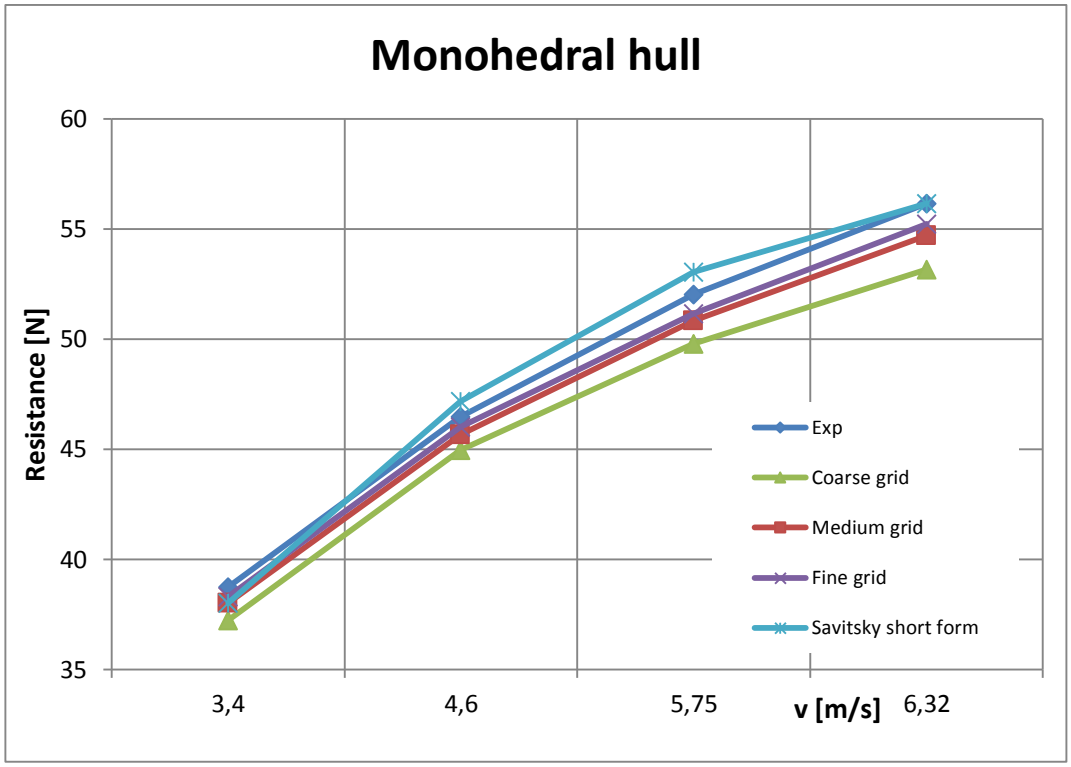

Fig. 5.33 Monohedral hull - Resistance comparison

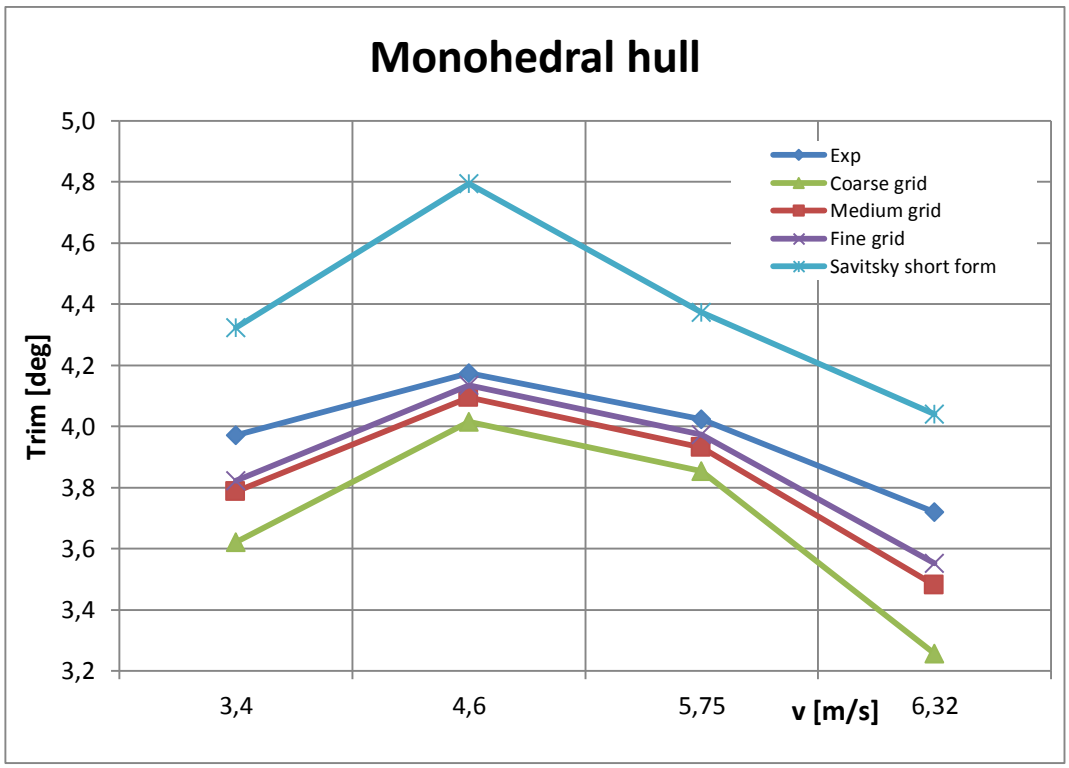

Fig. 5.34 Monohedral hull - Trim comparison

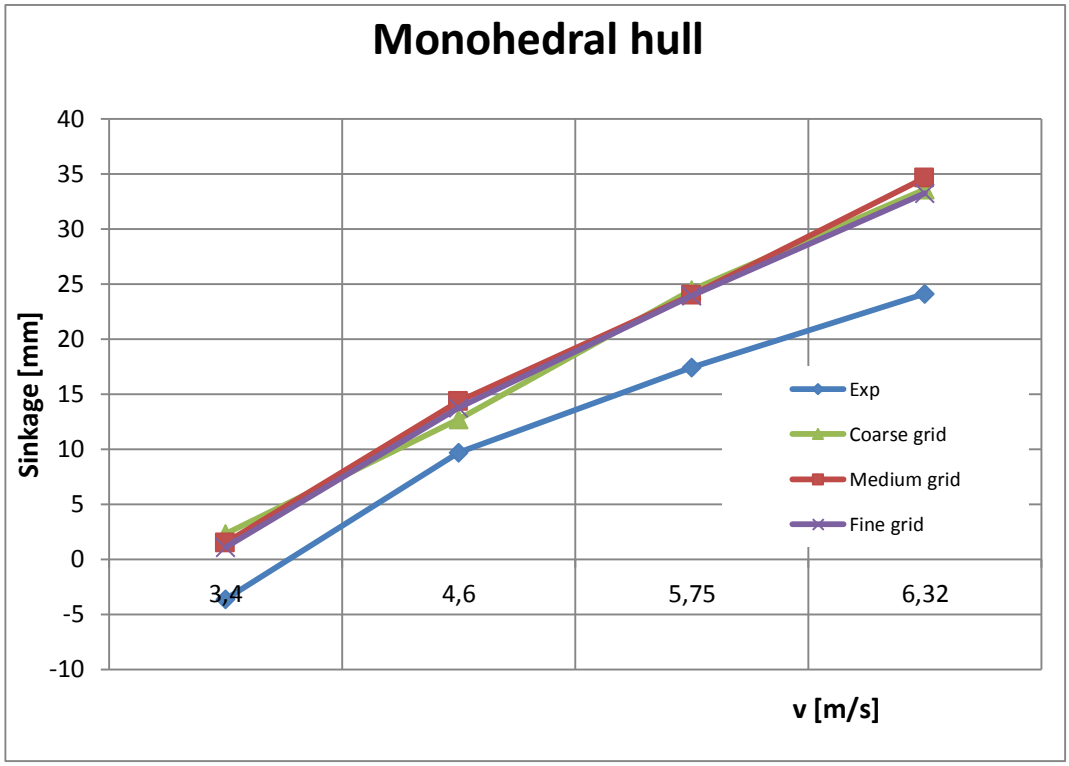

Fig. 5.35 Monohedral hull - Sinkage comparison

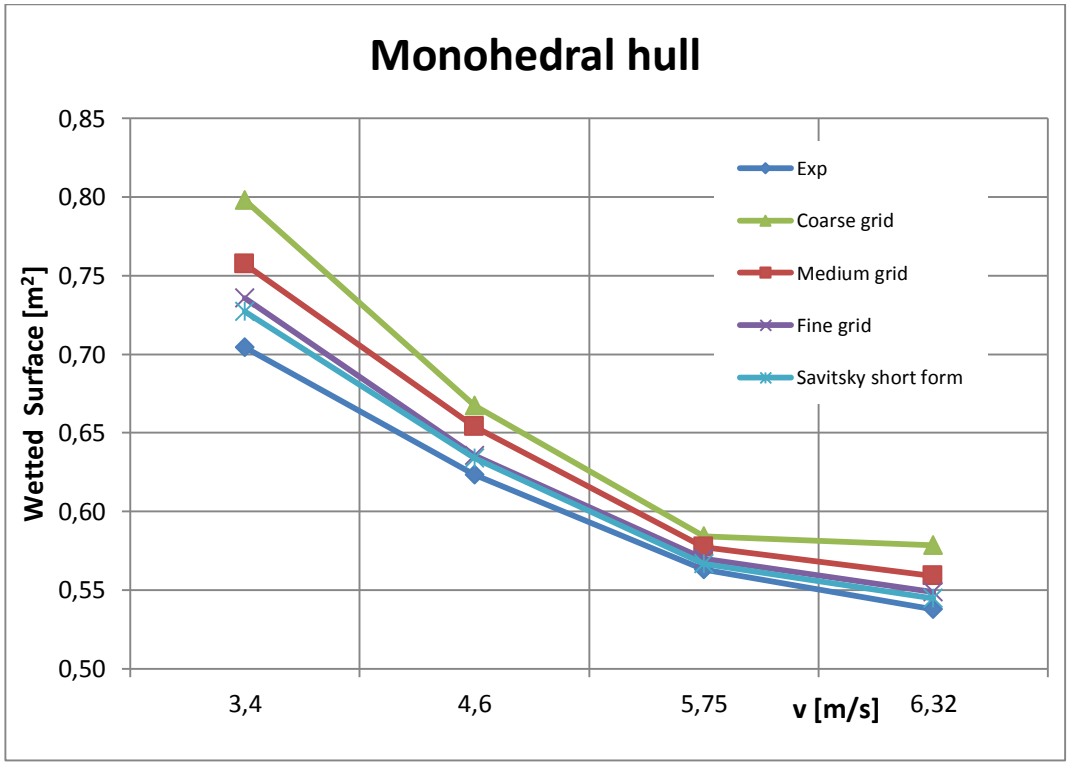

Fig. 5.36 Monohedral hull – Wetted surface comparison

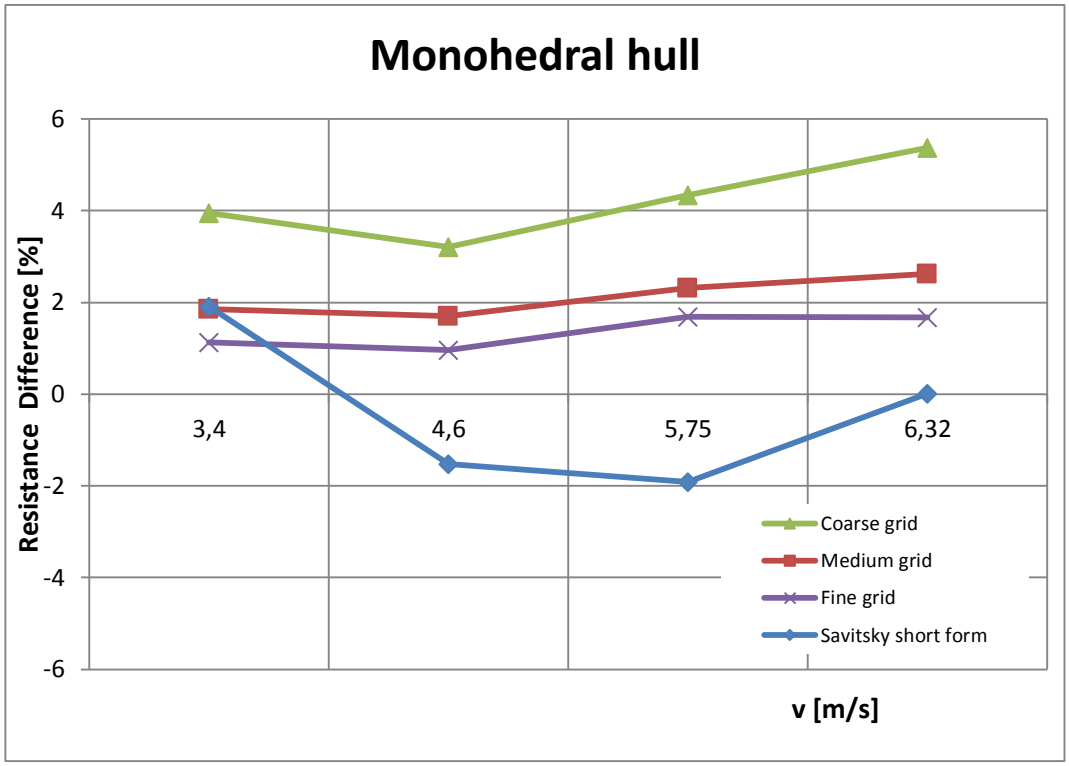

Fig. 5.37 Monohedral hull – Resistance comparison (percentage)

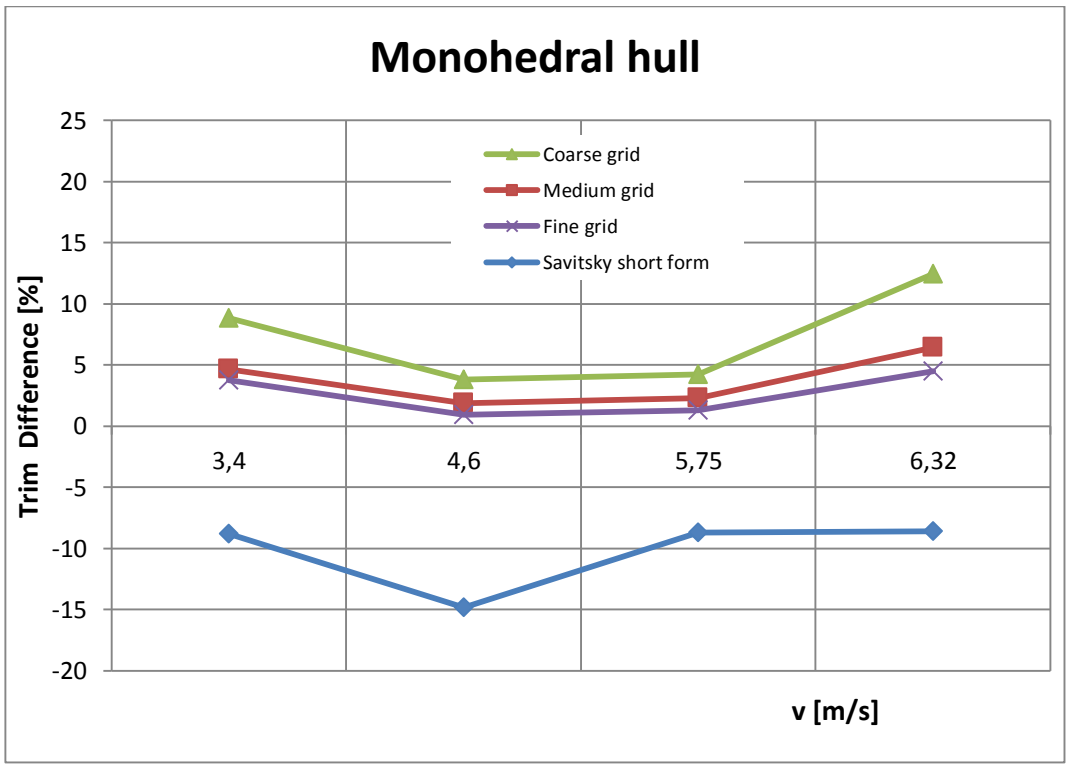

Fig. 5.38 Monohedral hull – Trim comparison (percentage)

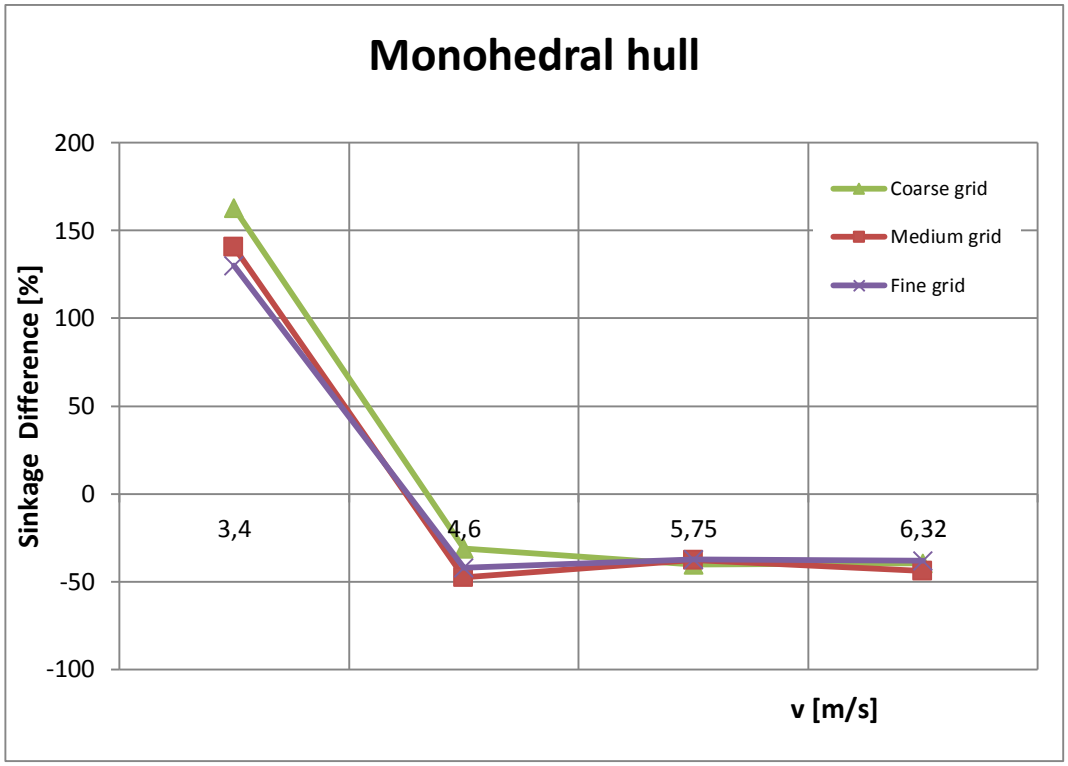

Fig. 5.39 Monohedral hull – Sinkage comparison (percentage)

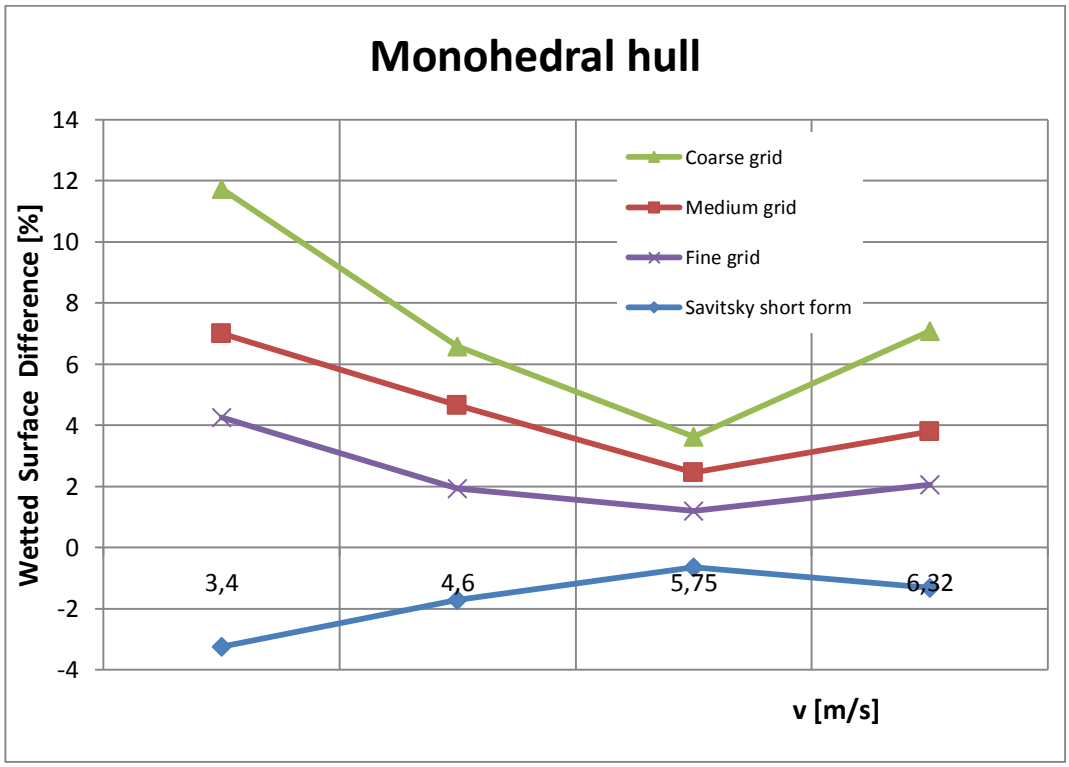

Fig. 5.40 Monohedral hull – Wetted surface comparison (percentage)

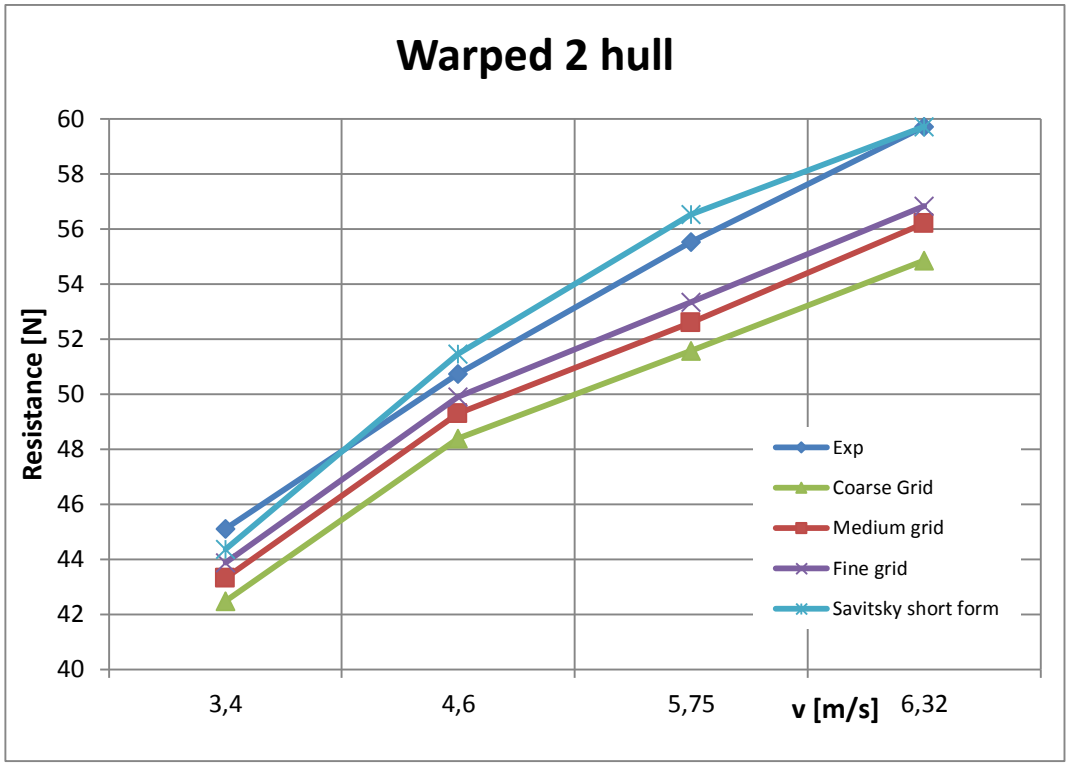

Fig. 5.41 Warped 2 hull – Resistance comparison

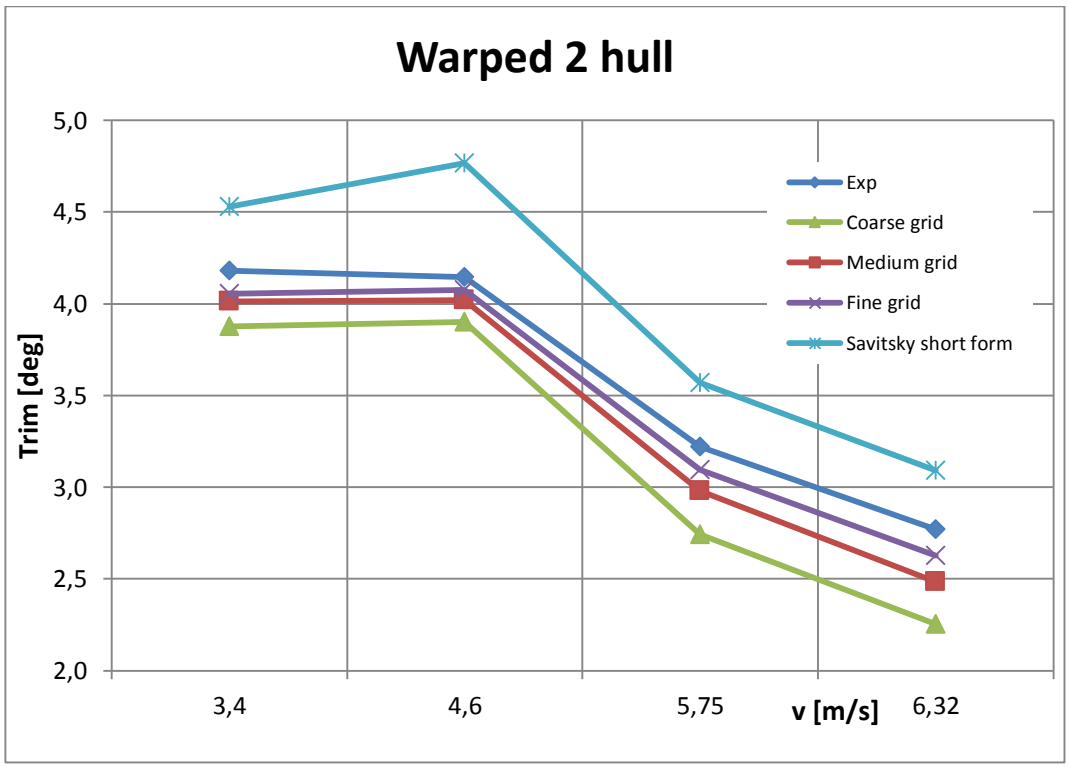

Fig. 5.42 Warped 2 hull – Trim comparison

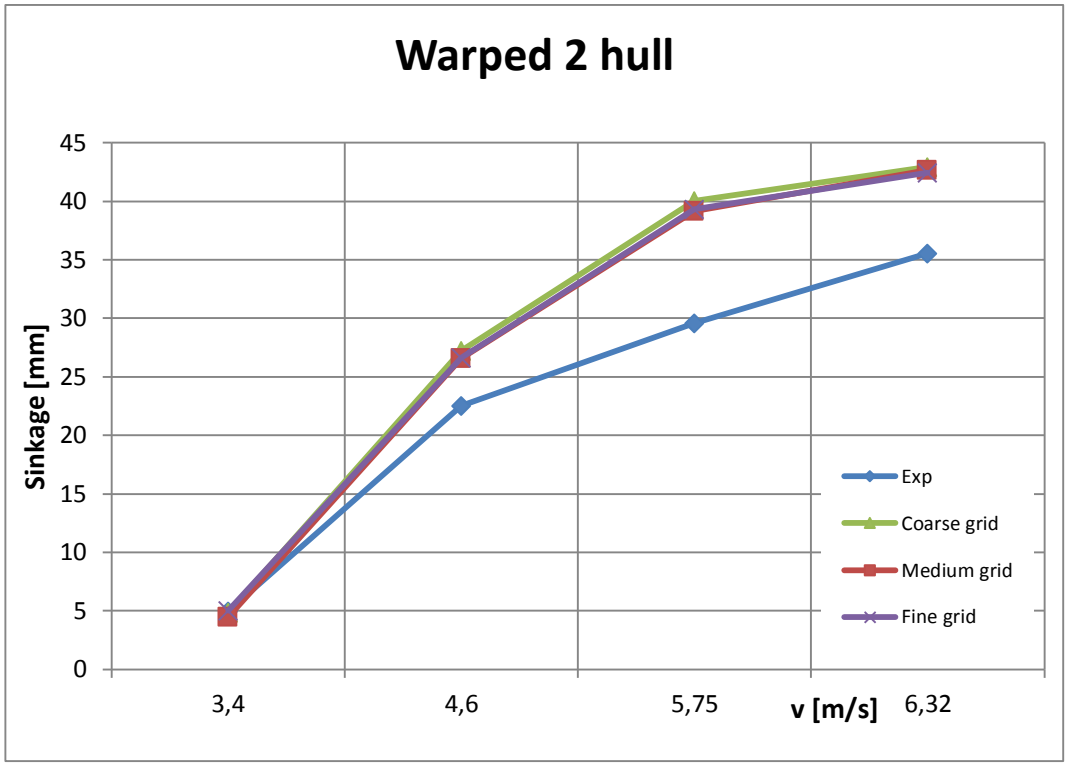

Fig. 5.43 Warped 2 hull – Sinkage comparison

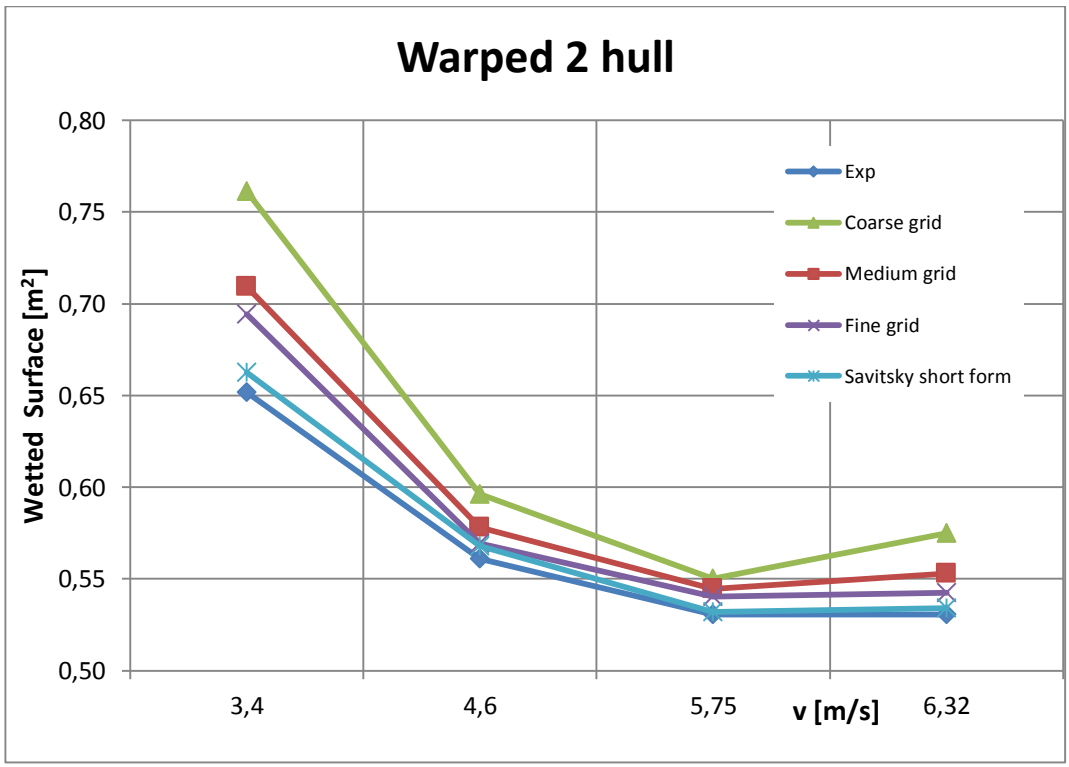

Fig. 5.44 Warped 2 hull – Wetted surface comparison

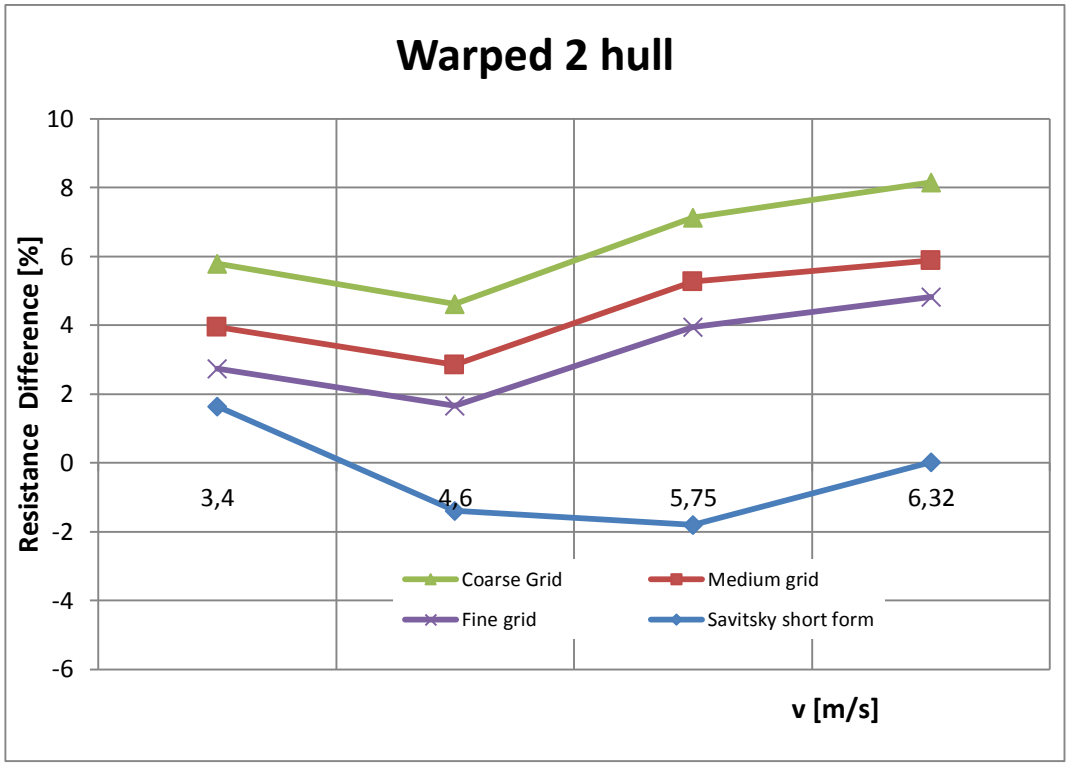

Fig. 5.45 Warped 2 hull – Resistance comparison (percentage)

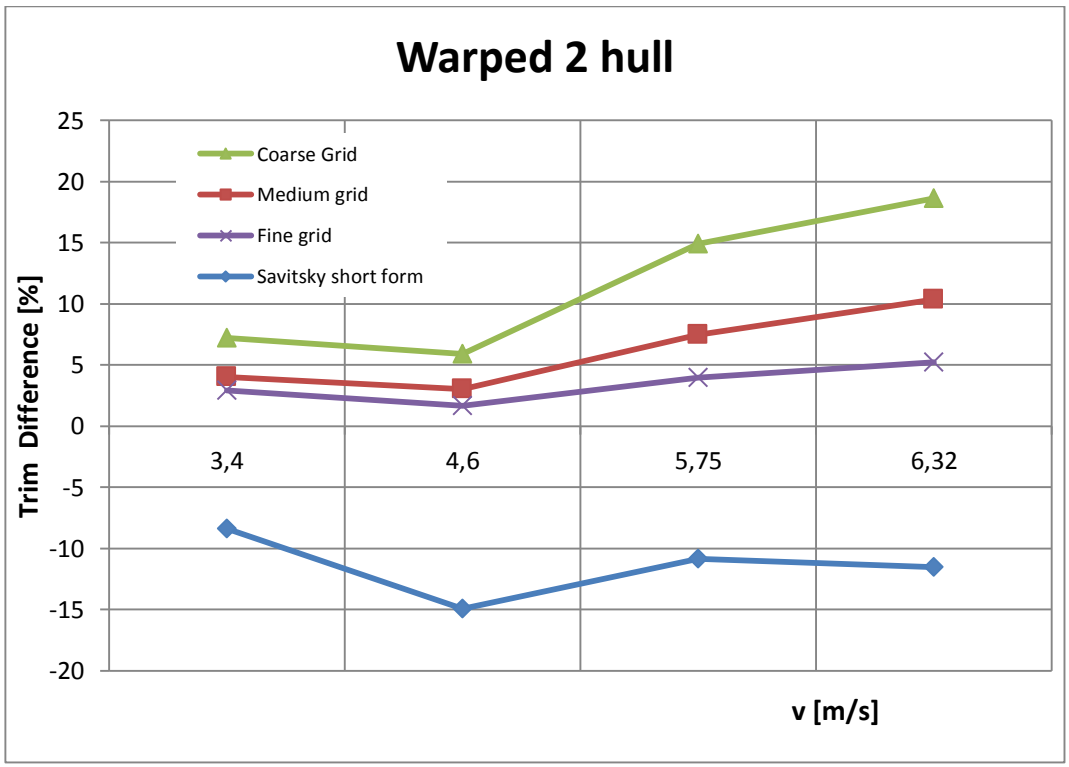

Fig. 5.46 Warped 2 hull – Trim comparison (percentage)

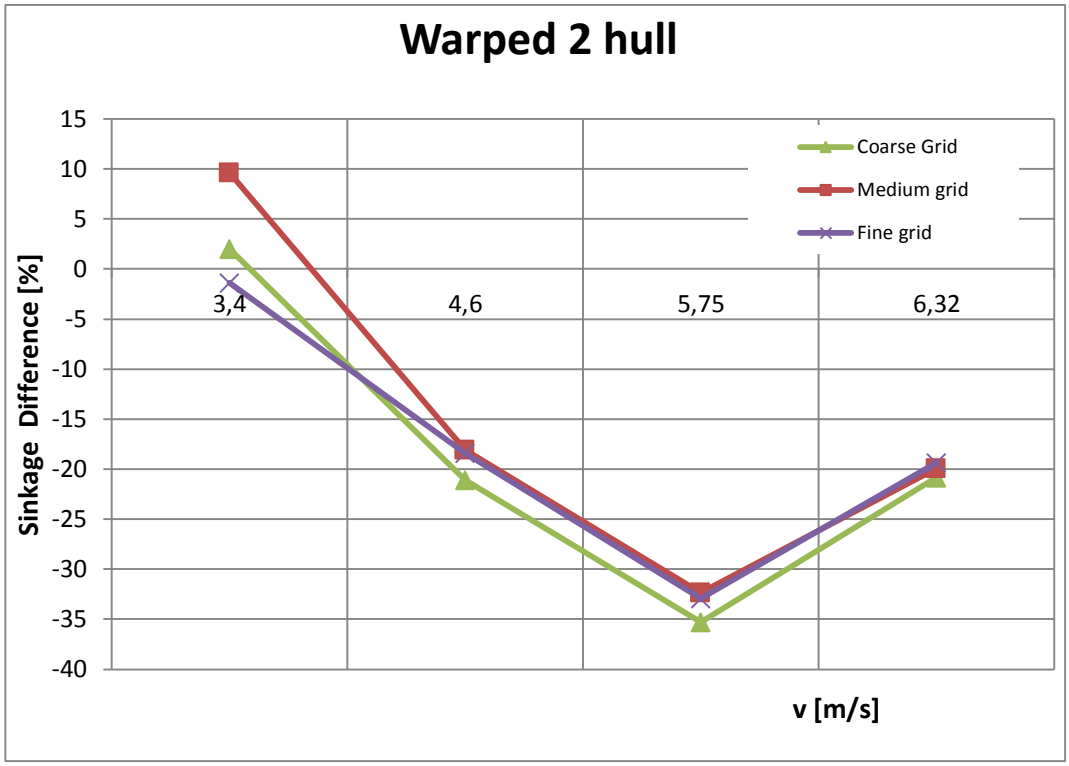

Fig. 5.47 Warped 2 hull – Sinkage comparison (percentage)

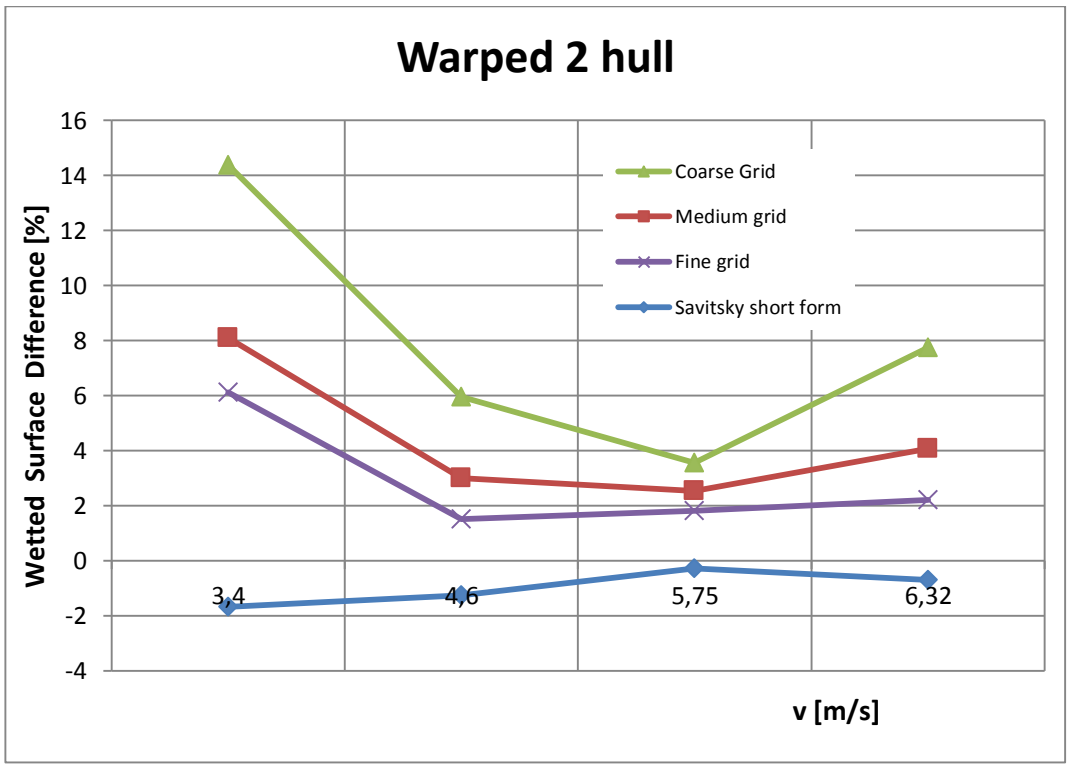

Fig. 5.48 Warped 2 hull – Wetted surface comparison (percentage)

WETTED SURFACES RESULTS FOR DIFFERENT MESH QUALITIES

MONOHEDRAL HULL at v=3.4 m/s

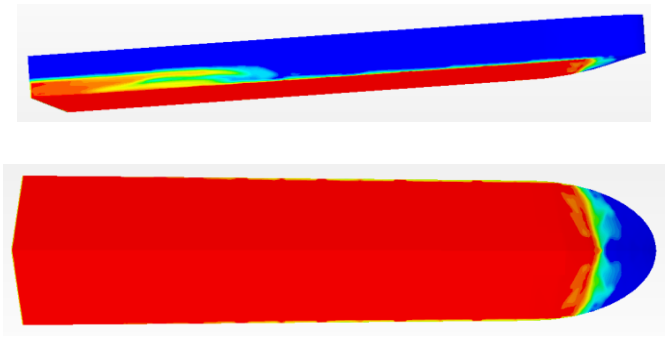

Coarse grid at v=3.4 m/s

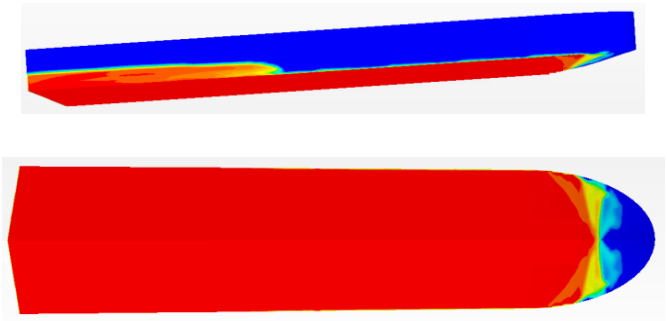

Medium grid at v=3.4 m/s

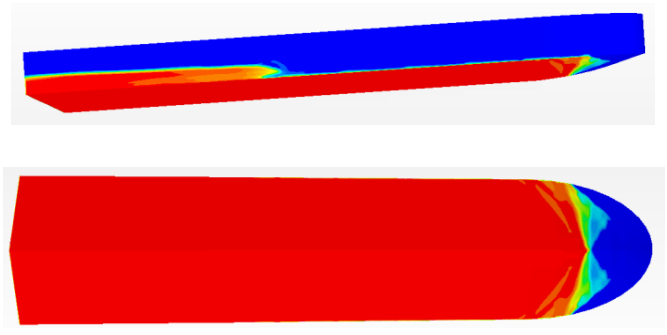

Fine grid at v=3.4 m/s

Fig. 5.49 Monohedral hull – Wetted surfaces comparison from different grids, v=3.4 m/s

WETTED SURFACES RESULTS FOR DIFFERENT MESH QUALITIES

MONOHEDRAL HULL at v=4.6 m/s

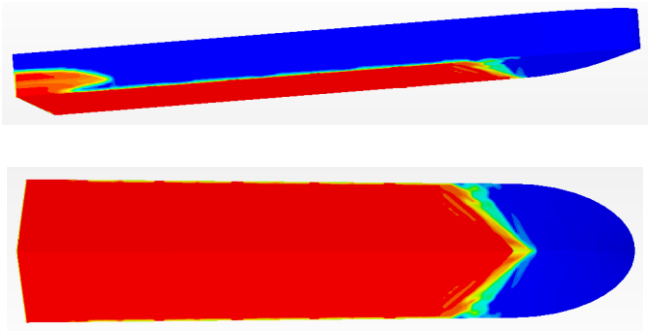

Coarse grid at v=4.6 m/s

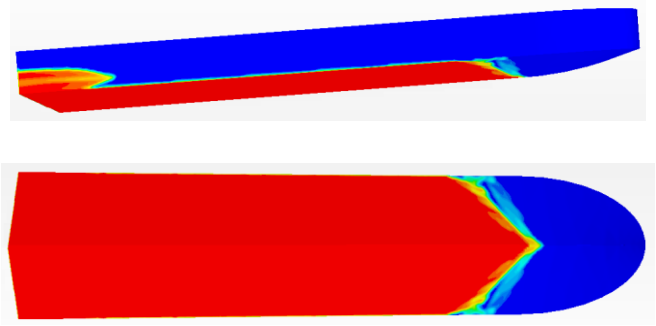

Medium grid at v=4.6 m/s

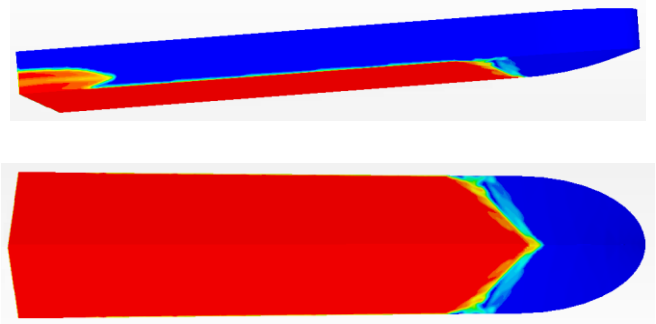

Fine grid at v=4.6 m/s

Fig. 5.50 Monohedral hull – Wetted surfaces comparison from different grids, v=4.6 m/s

WETTED SURFACES RESULTS FOR DIFFERENT MESH QUALITIES

MONOHEDRAL HULL at v=5.75 m/s

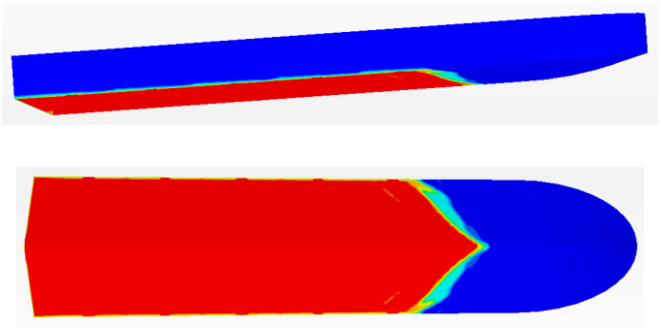

Coarse grid at v=5.75 m/s

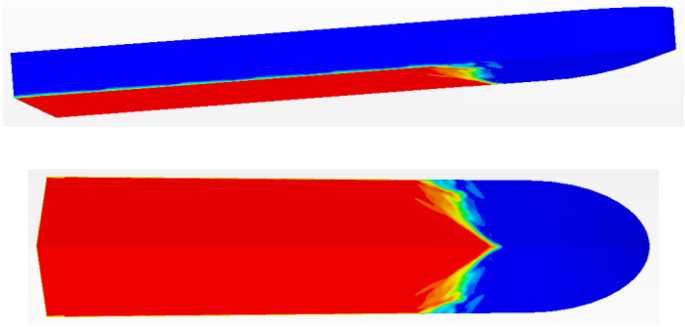

Medium grid at v=5.75 m/s

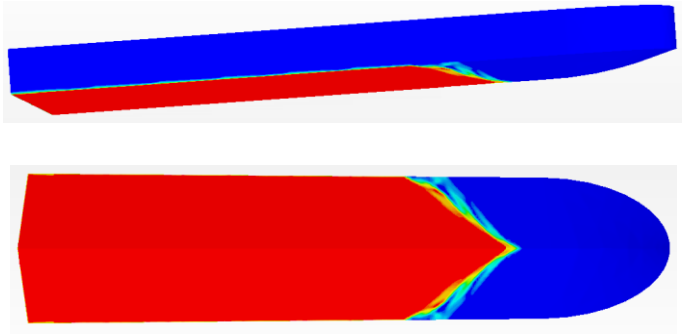

Fine grid at v=5.75 m/s

Fig. 5.51 Monohedral hull – Wetted surfaces comparison from different grids, v=5.75 m/s

WETTED SURFACES RESULTS FOR DIFFERENT MESH QUALITIES

MONOHEDRAL HULL at v=6.32 m/s

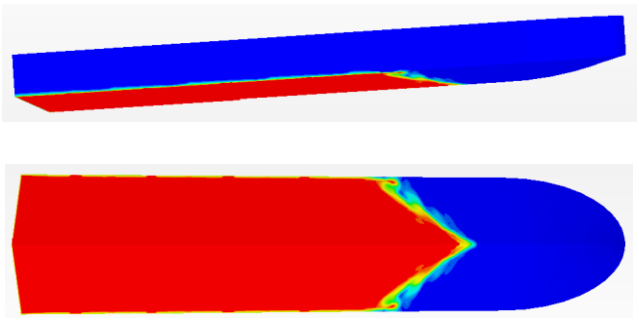

Coarse grid at v=6.32 m/s

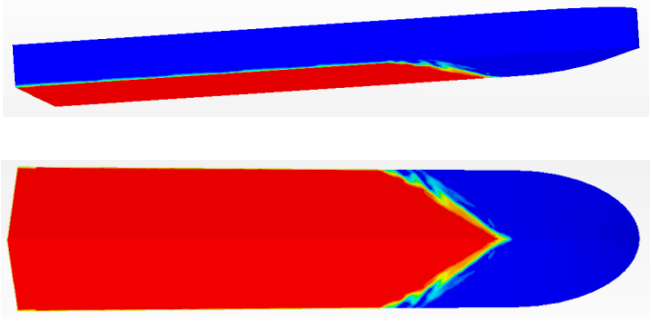

Medium grid at v=6.32 m/s

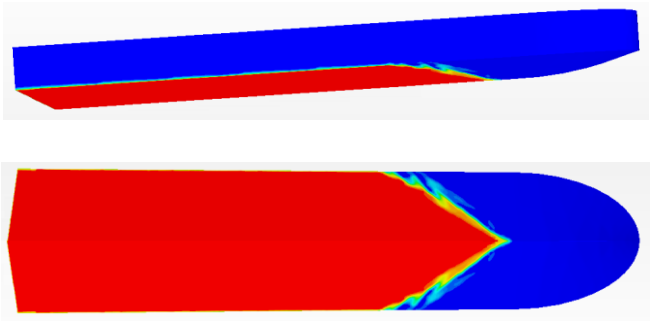

Fine grid at v=6.32 m/s

Fig. 5.52 Monohedral hull – Wetted surfaces comparison from different grids, v=6.32 m/s

WETTED SURFACES RESULTS FOR DIFFERENT MESH QUALITIES

WARPED 2 HULL at v=3.4 m/s

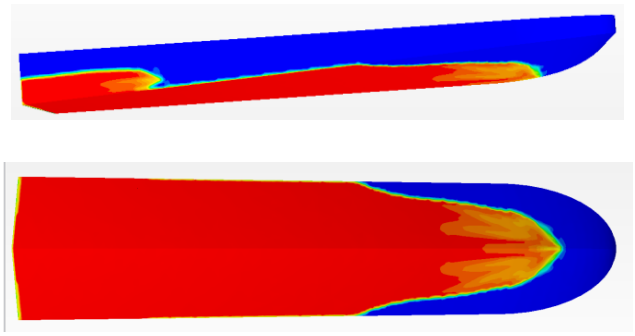

Coarse grid at v=3.4 m/s

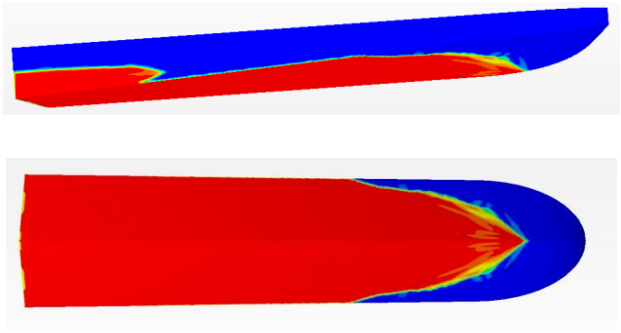

Medium grid at v=3.4 m/s

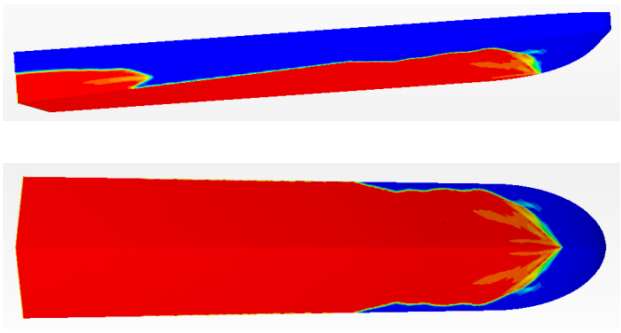

Fine grid at v=3.4 m/s

Fig. 5.53 Warped 2 hull – Wetted surfaces comparison from different grids, v=3.4 m/s

WETTED SURFACES RESULTS FOR DIFFERENT MESH QUALITIES

WARPED 2 HULL at v=4.6 m/s

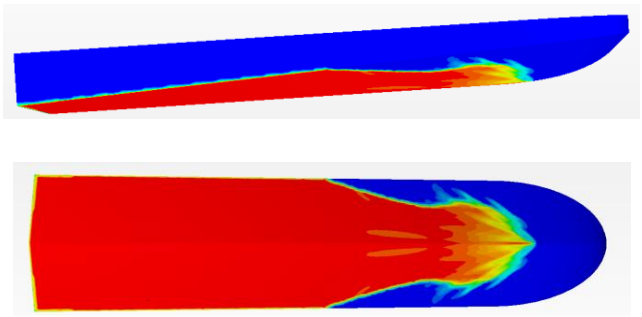

Coarse grid at v=4.6 m/s

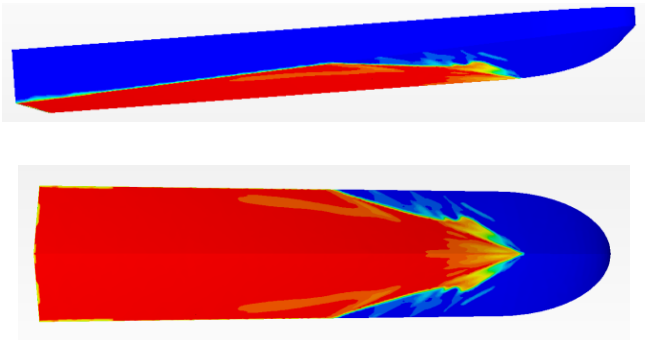

Medium grid at v=4.6 m/s

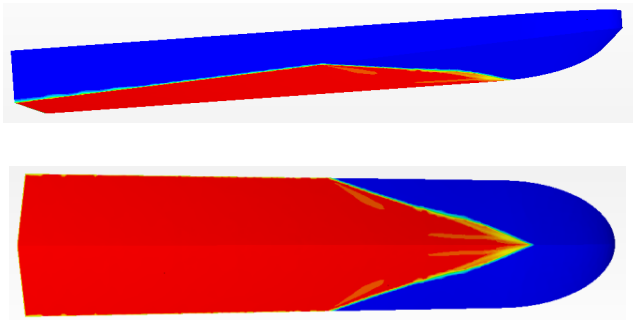

Fine grid at v=4.6 m/s

Fig. 5.54 Warped 2 hull – Wetted surfaces comparison from different grids, v=4.6 m/s

WETTED SURFACES RESULTS FOR DIFFERENT MESH QUALITIES

WARPED 2 HULL at v=5.75 m/s

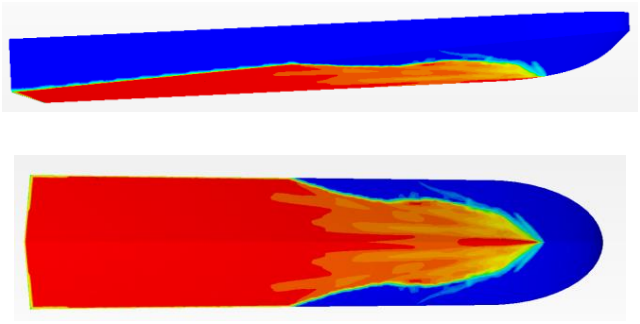

Coarse grid at v=5.75 m/s

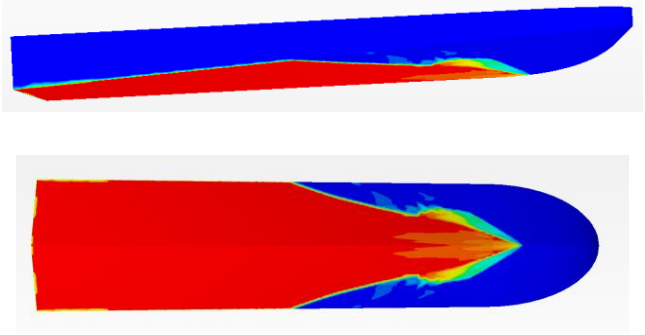

Medium grid at v=5.75 m/s

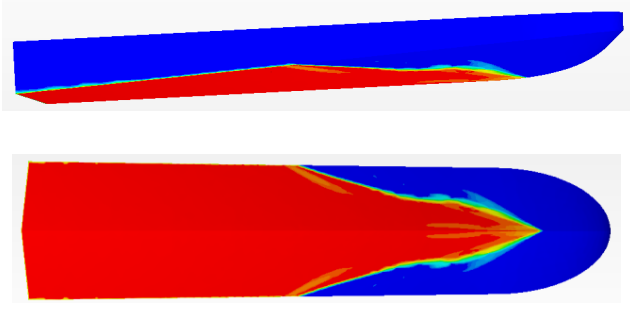

Fine grid at v=5.75 m/s

Fig. 5.55 Warped 2 hull – Wetted surfaces comparison from different grids, v=5.75 m/s

WETTED SURFACES RESULTS FOR DIFFERENT MESH QUALITIES

WARPED 2 HULL at v=6.32 m/s

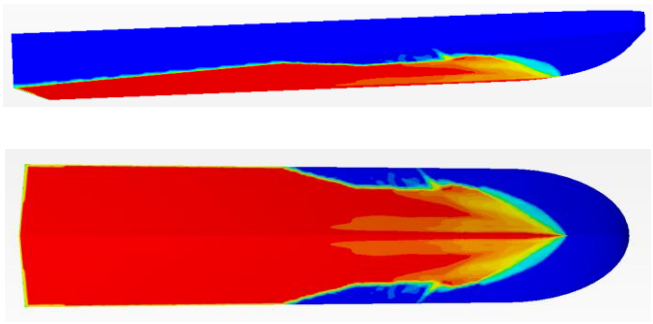

Coarse grid at v=6.32 m/s

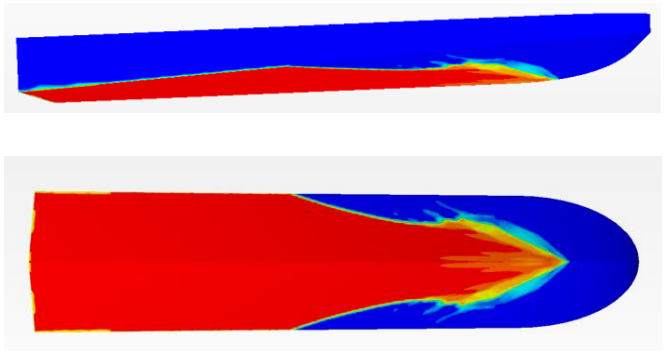

Medium grid at v=6.32 m/s

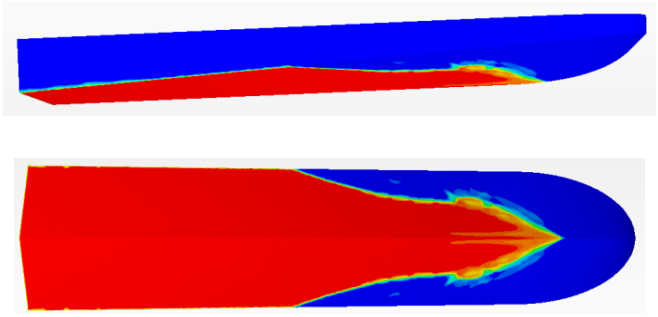

Fine grid at v=6.32 m/s

Fig. 5.56 Warped 2 hull – Wetted surfaces comparison from different grids, v=6.32 m/s

COMPARISON WETTED SURFACES

MONOHEDRAL HULL at v=3.4 m/s

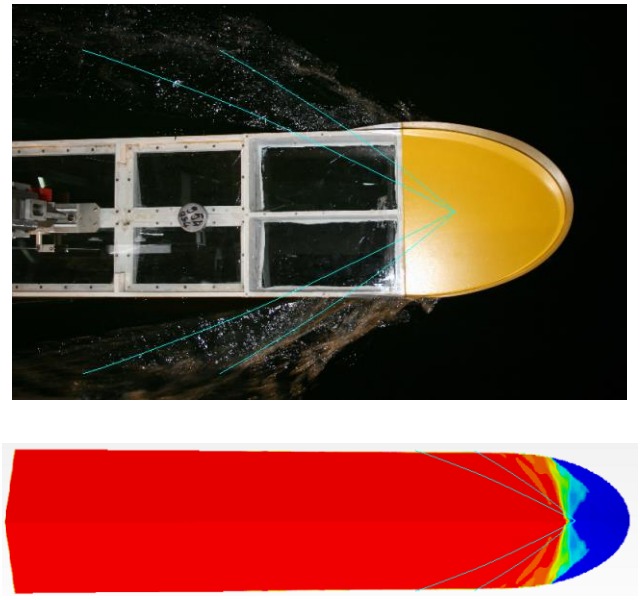

Fig. 5.57 Monohedral hull – Experimental and numerical wetted surfaces, v=3.4 m/s

MONOHEDRAL HULL at v=4.6 m/s

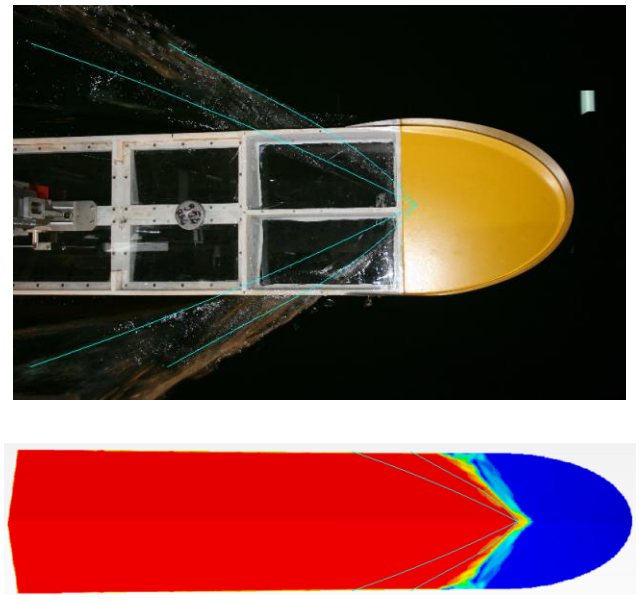

Fig. 5.58 Monohedral hull – Experimental and numerical wetted surfaces, v=4.6 m/s

COMPARISON WETTED SURFACES

MONOHEDRAL HULL at v=5.75 m/s

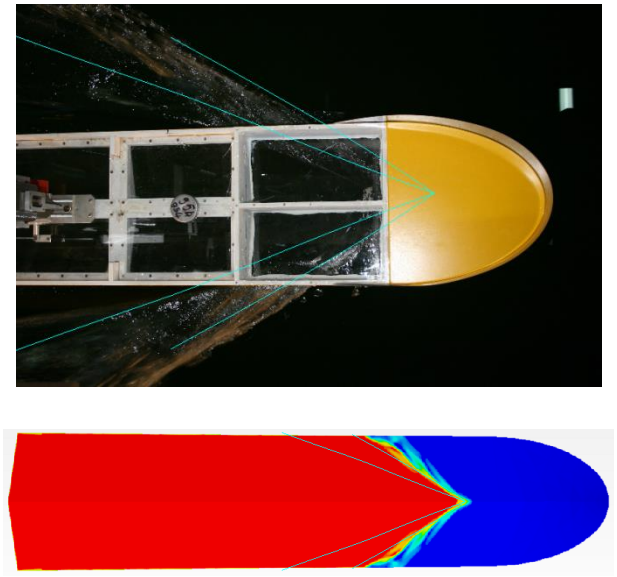

Fig. 5.59 Monohedral hull – Experimental and numerical wetted surfaces, v=5.75 m/s

MONOHEDRAL HULL at v=6.32 m/s

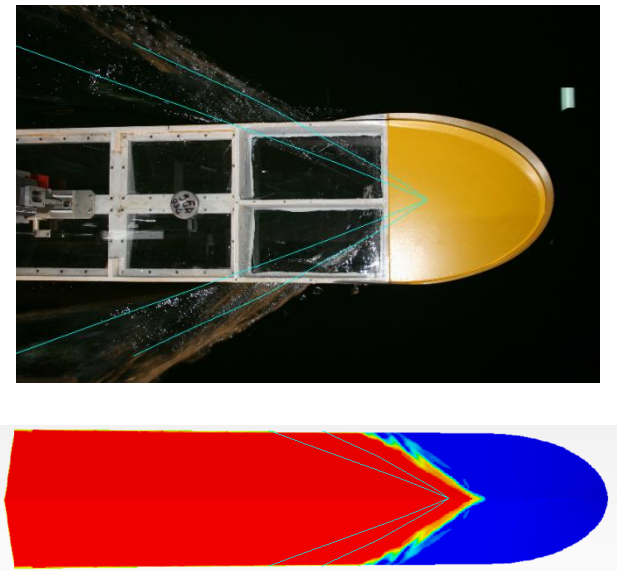

Fig. 5.60 Monohedral hull – Experimental and numerical wetted surfaces, v=6.32 m/s

COMPARISON WETTED SURFACES

WARPED 2 HULL at v=3.4 m/s

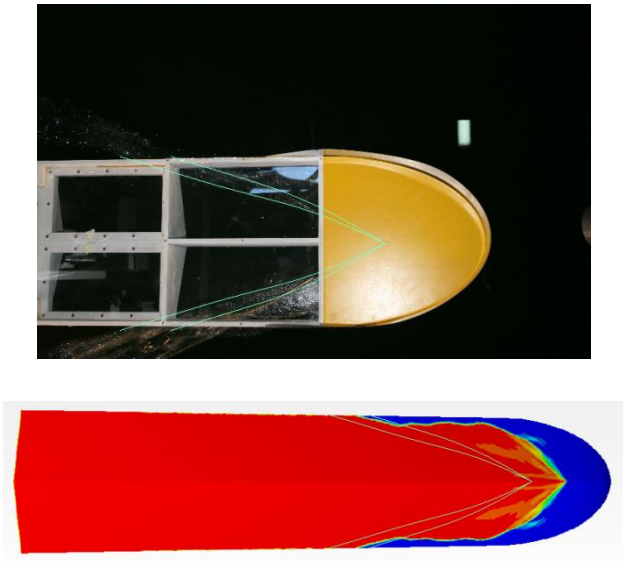

Fig. 5.61 Warped 2 hull – Experimental and numerical wetted surfaces, v=3.4 m/s

WARPED 2 HULL at v=4.6 m/s

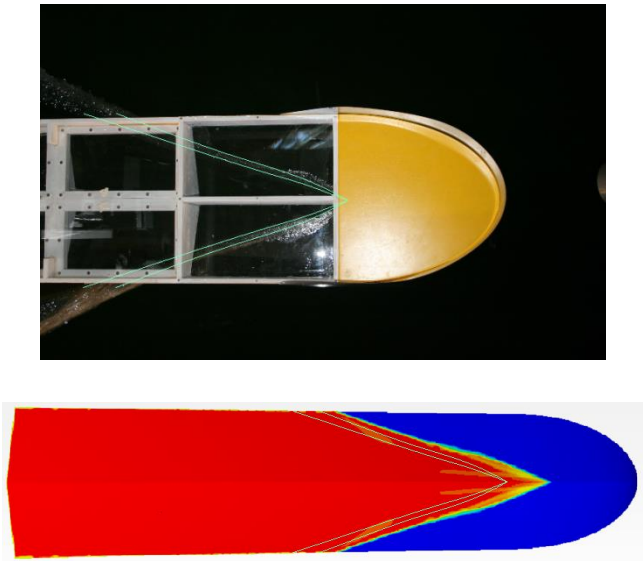

Fig. 5.62 Warped 2 hull – Experimental and numerical wetted surfaces, v=4.6 m/s

COMPARISON WETTED SURFACES

WARPED 2 HULL at v=5.75 m/s

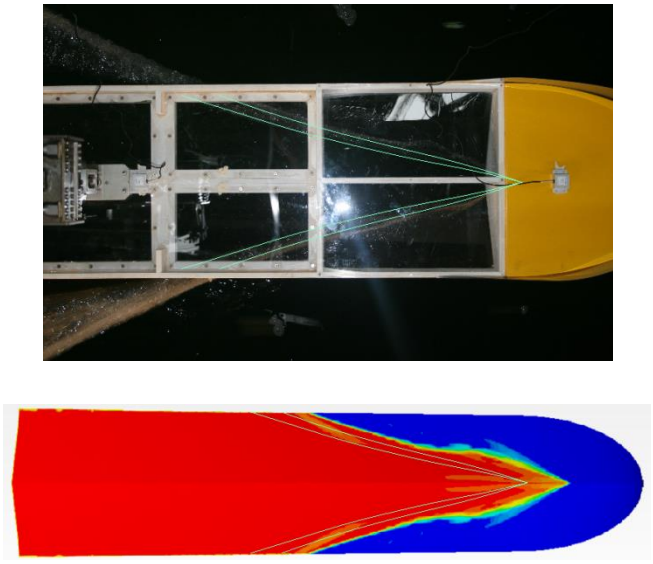

Fig. 5.63 Warped 2 hull – Experimental and numerical wetted surfaces, v=5.75 m/s

WARPED 2 HULL at v=6.32 m/s

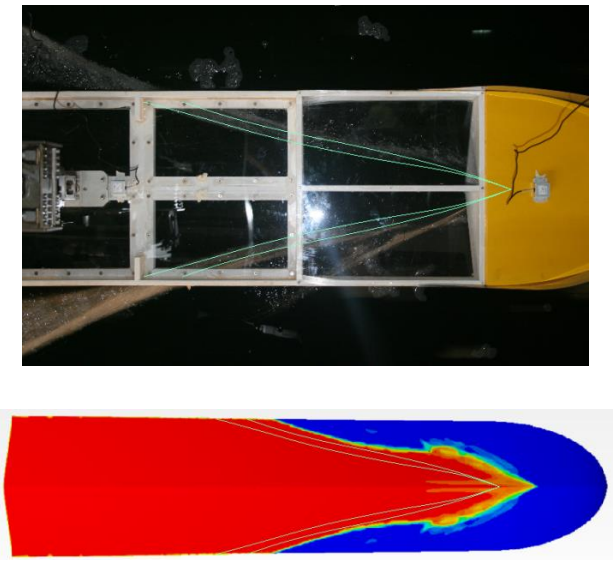

Fig. 5.64 Warped 2 hull – Experimental and numerical wetted surfaces, v=6.32 m/s

LONGITUDINAL PRESSURE DISTRIBUTION

MONOHEDRAL HULL at v=3.4 m/s

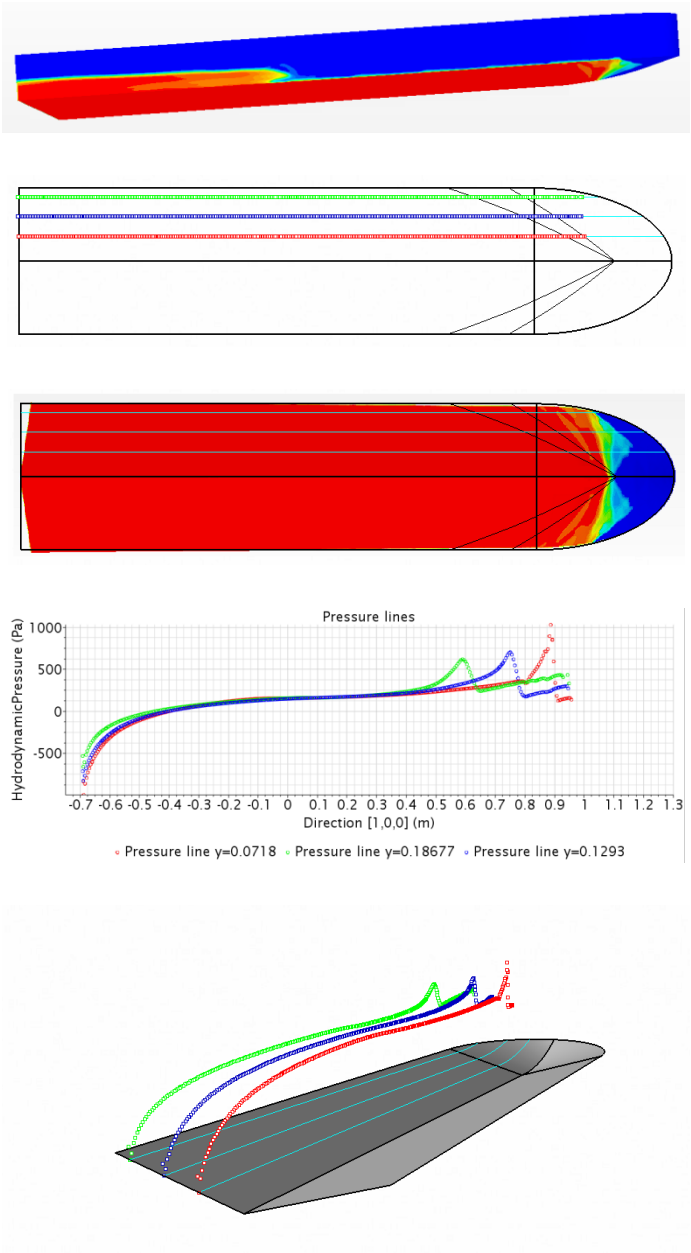

Fig. 5.65 Monohedral hull - Longitudinal pressure distribution at v=3.4 m/s

LONGITUDINAL PRESSURE DISTRIBUTION

MONOHEDRAL HULL at v=4.6 m/s

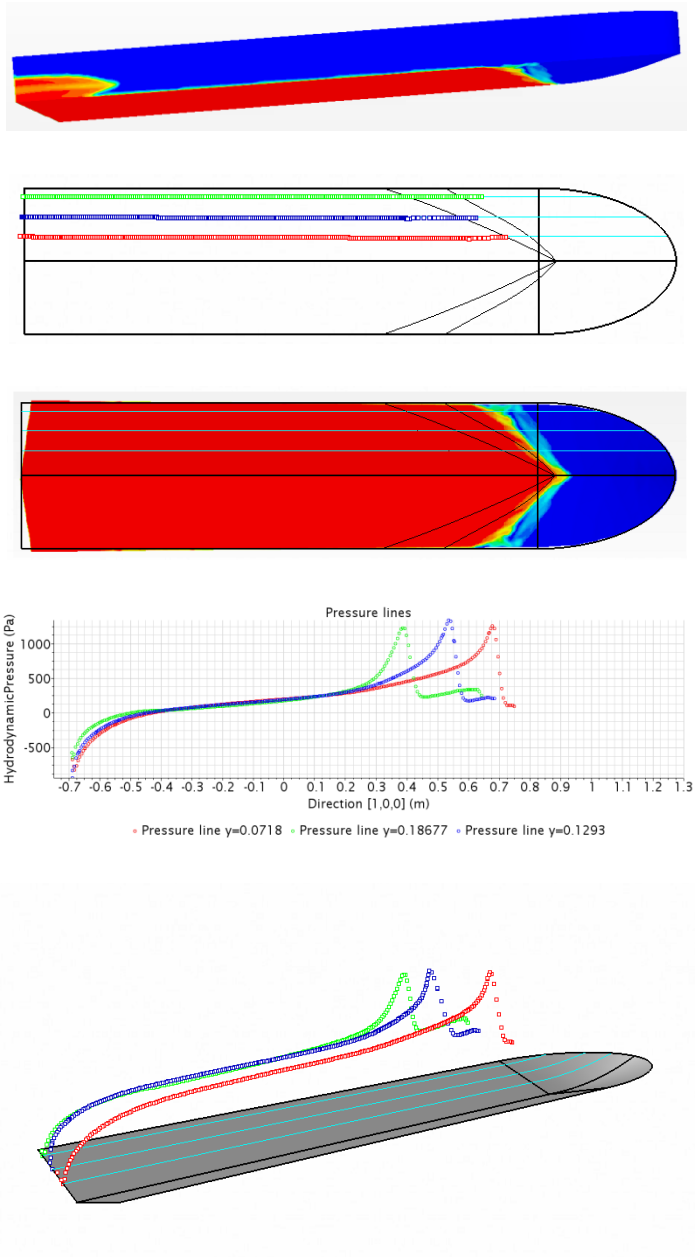

Fig. 5.66 Monohedral hull - Longitudinal pressure distribution at v=4.6 m/s

LONGITUDINAL PRESSURE DISTRIBUTION

MONOHEDRAL HULL at v=5.75 m/s

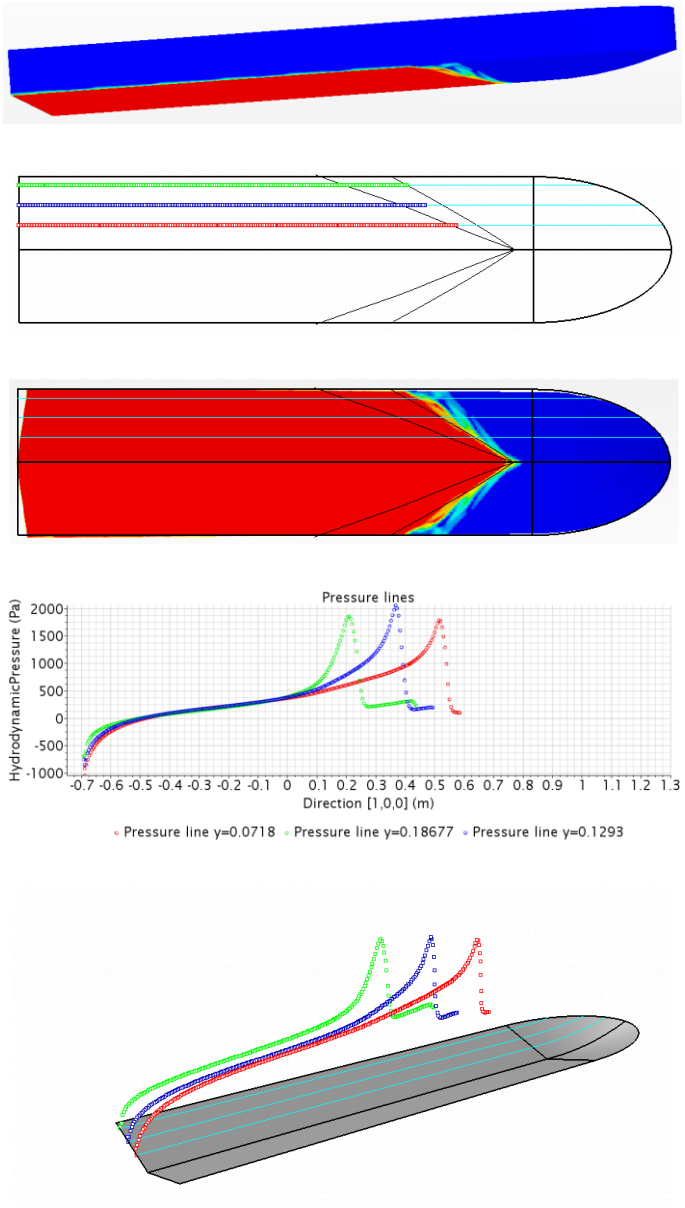

Fig. 5.67 Monohedral hull - Longitudinal pressure distribution at v=5.75 m/s

LONGITUDINAL PRESSURE DISTRIBUTION

MONOHEDRAL HULL at v=6.32 m/s

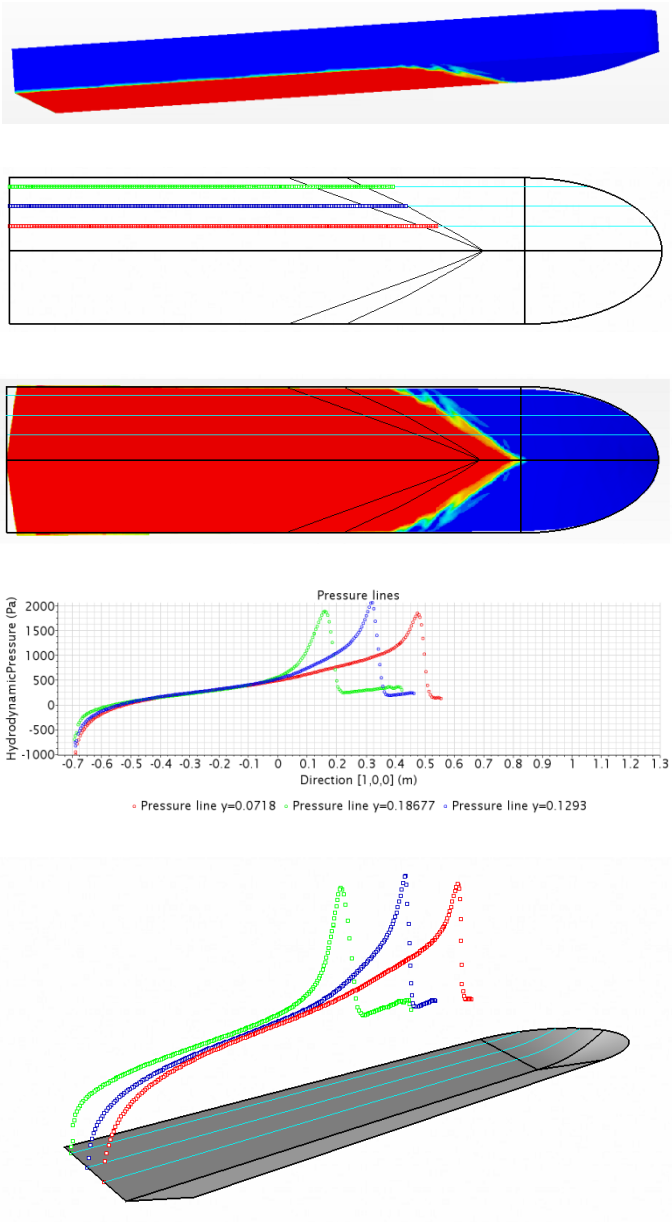

Fig. 5.68 Monohedral hull - Longitudinal pressure distribution at v=6.32 m/s

LONGITUDINAL PRESSURE DISTRIBUTION

WARPED 2 HULL at v=3.4 m/s

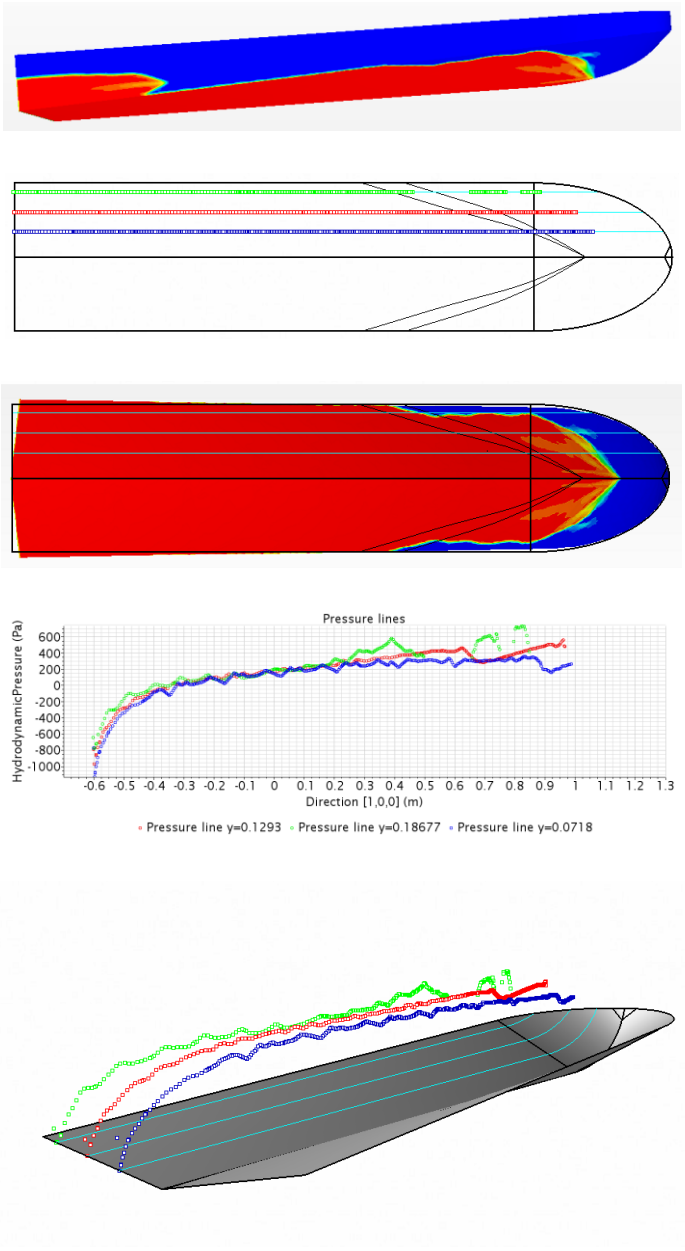

Fig. 5.69 Warped 2 hull - Longitudinal pressure distribution at v=3.4 m/s

LONGITUDINAL PRESSURE DISTRIBUTION

WARPED 2 HULL at v=4.6 m/s

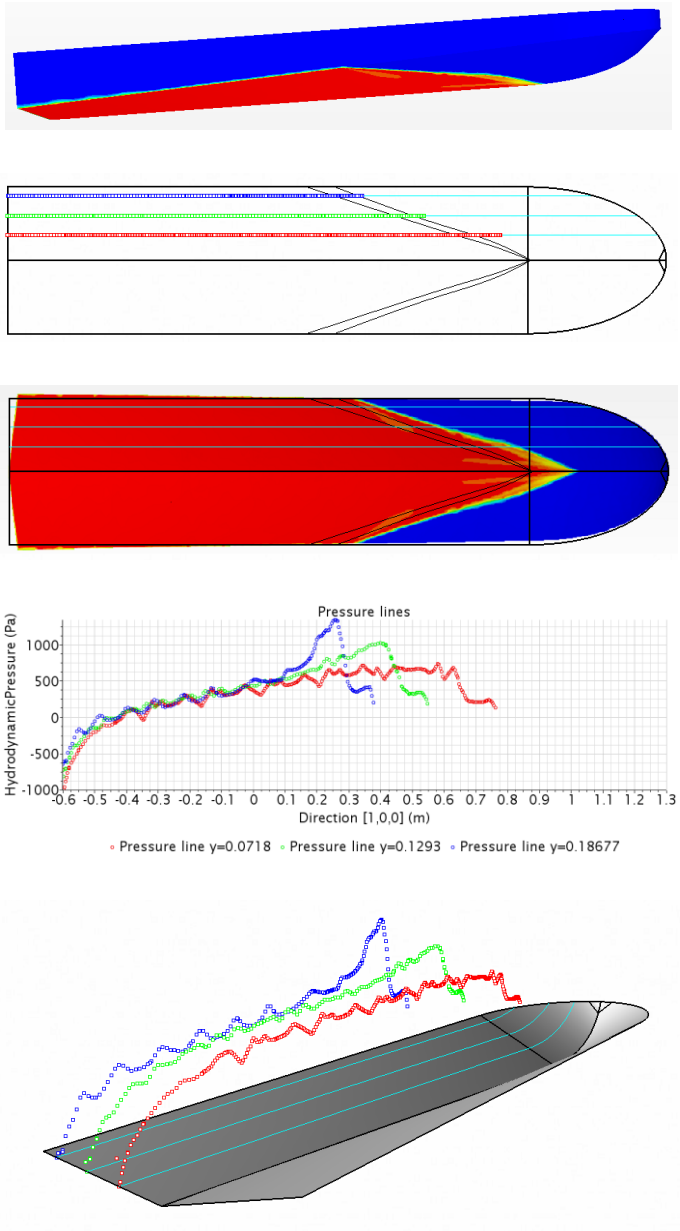

Fig. 5.70 Warped 2 hull - Longitudinal pressure distribution at v=4.6 m/s

LONGITUDINAL PRESSURE DISTRIBUTION

WARPED 2 HULL at v=5.75 m/s

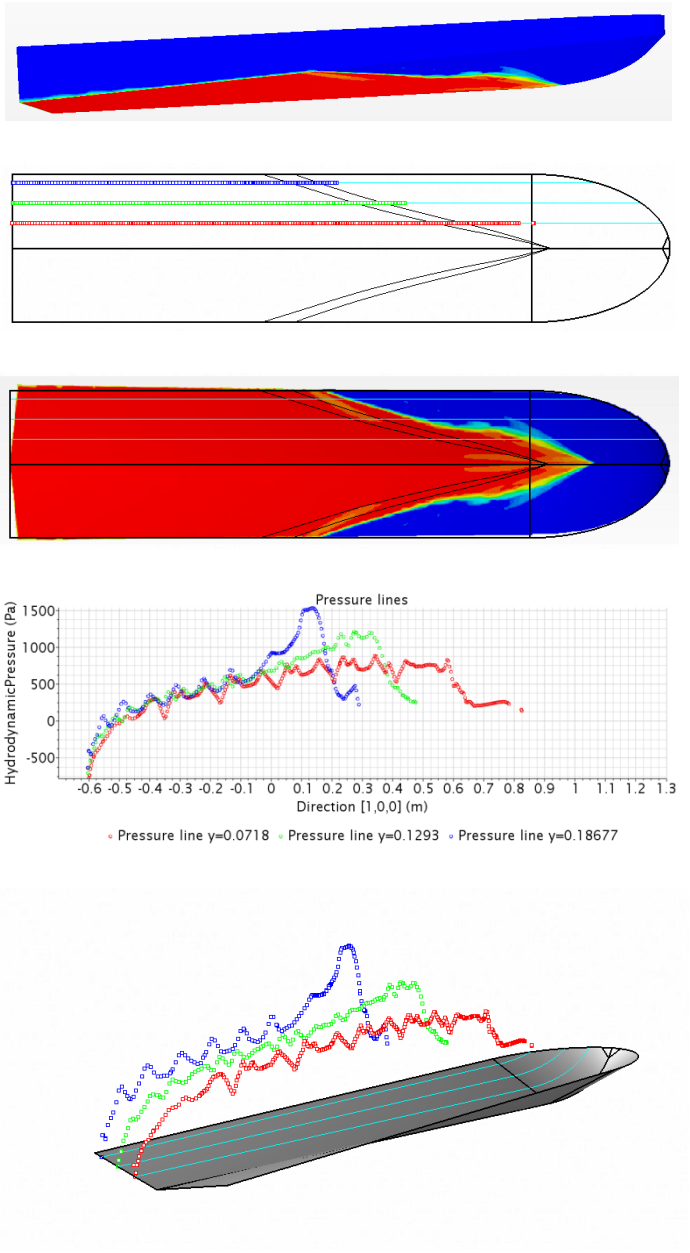

Fig. 5.71 Warped 2 hull - Longitudinal pressure distribution at v=5.75 m/s

LONGITUDINAL PRESSURE DISTRIBUTION

WARPED 2 HULL at v=6.32 m/s

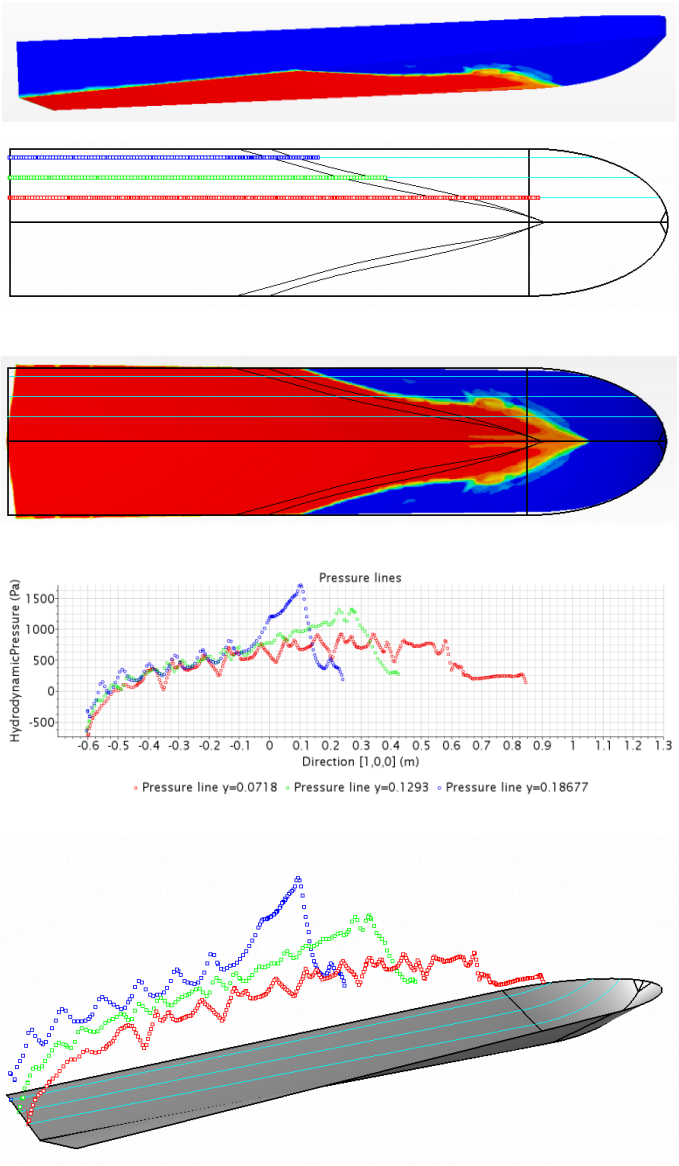

Fig. 5.72 Warped 2 hull - Longitudinal pressure distribution at v=6.32 m/s

TRANSVERSAL PRESSURE DISTRIBUTION

MONOHEDRAL HULL at v=3.4 m/s

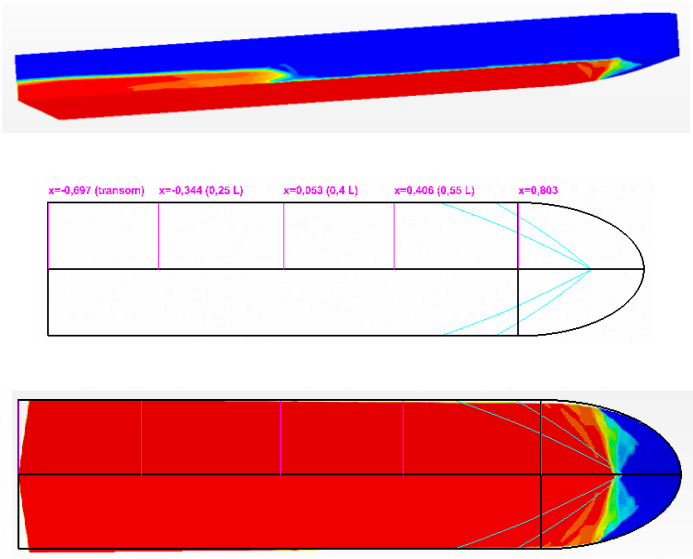

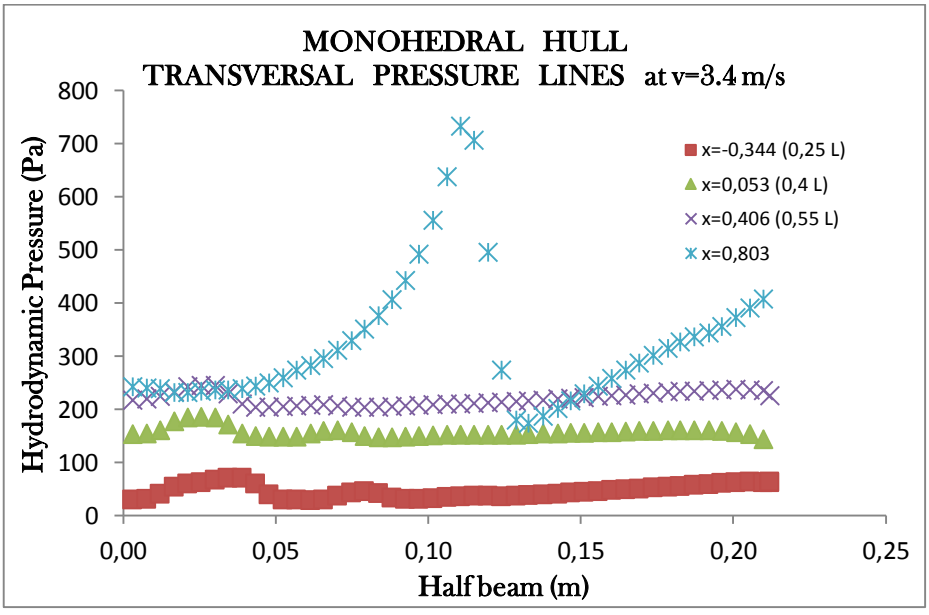

Fig. 5.73 Monohedral hull - Transversal pressure distribution at v=3.4 m/s

TRANSVERSAL PRESSURE DISTRIBUTION

MONOHEDRAL HULL at v=4.6 m/s

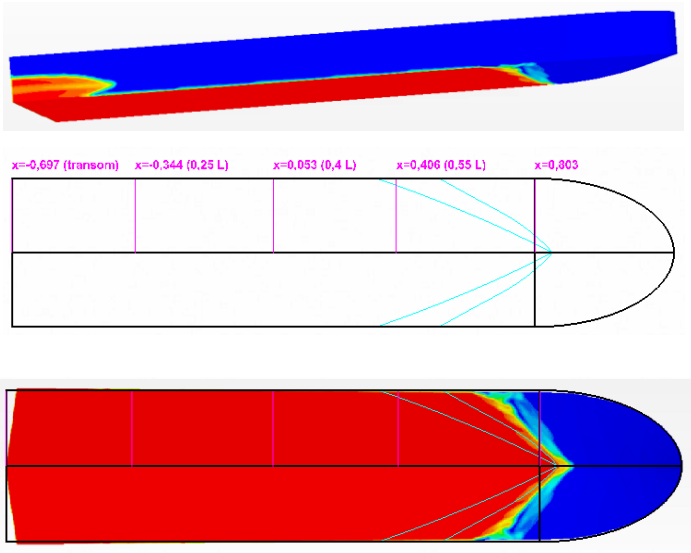

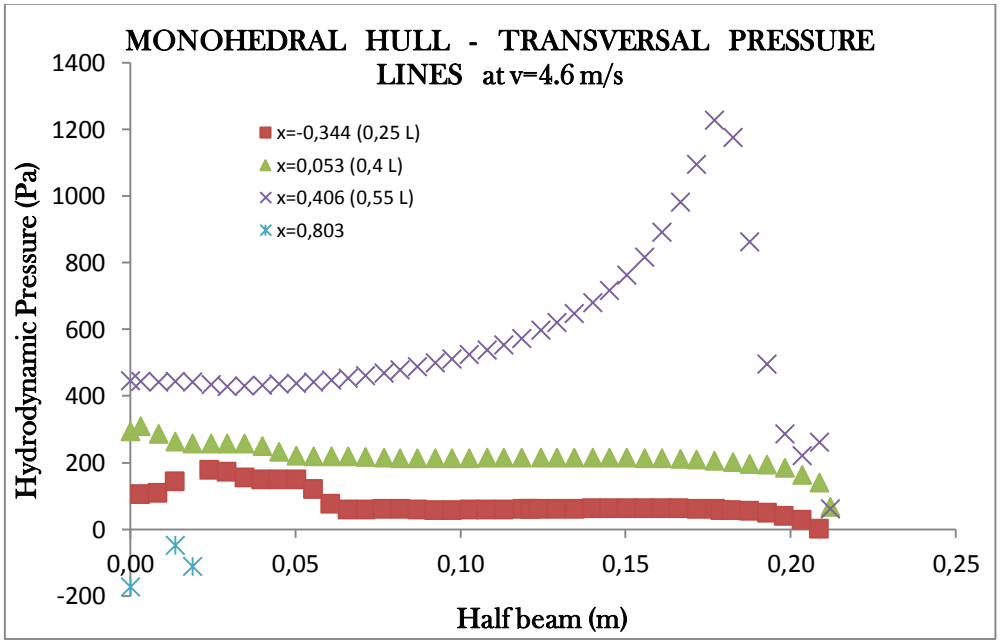

Fig. 5.74 Monohedral hull - Transversal pressure distribution at v=4.6 m/s

TRANSVERSAL PRESSURE DISTRIBUTION

MONOHEDRAL HULL at v=5.75 m/s

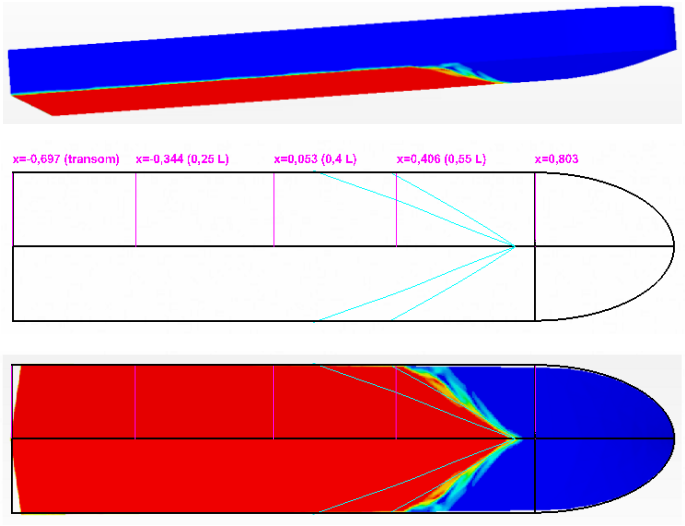

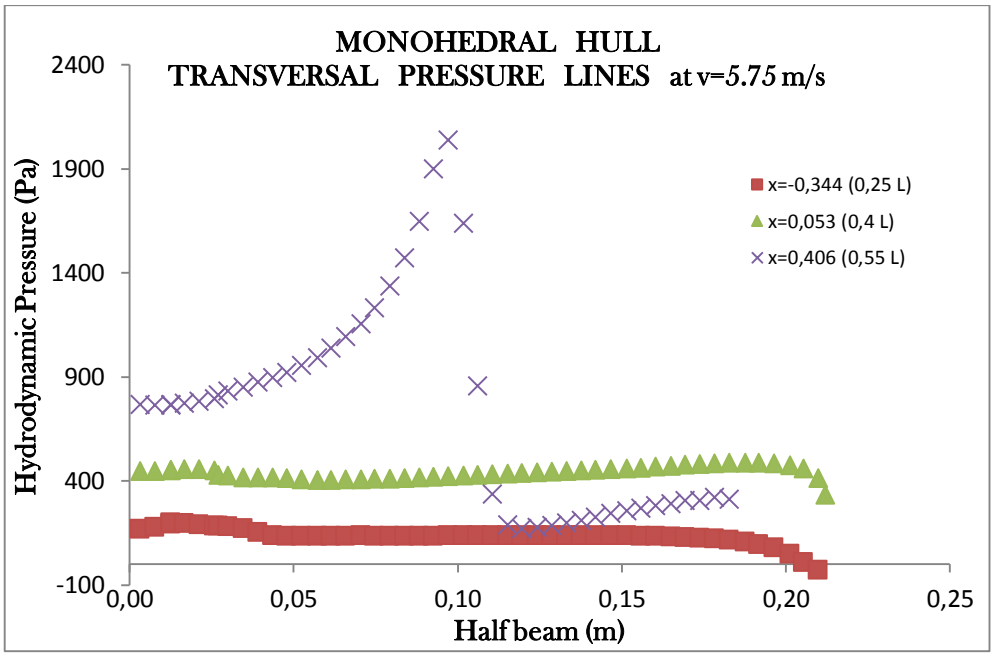

Fig. 5.75 Monohedral hull - Transversal pressure distribution at v=5.75 m/s

TRANSVERSAL PRESSURE DISTRIBUTION

MONOHEDRAL HULL at v=6.32 m/s

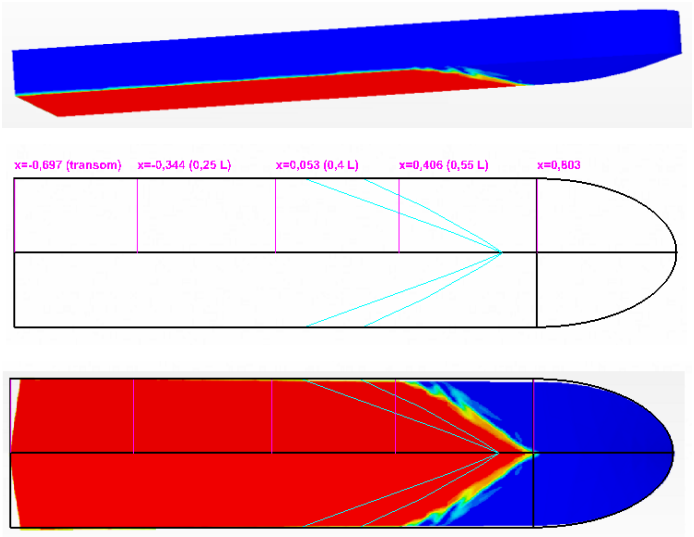

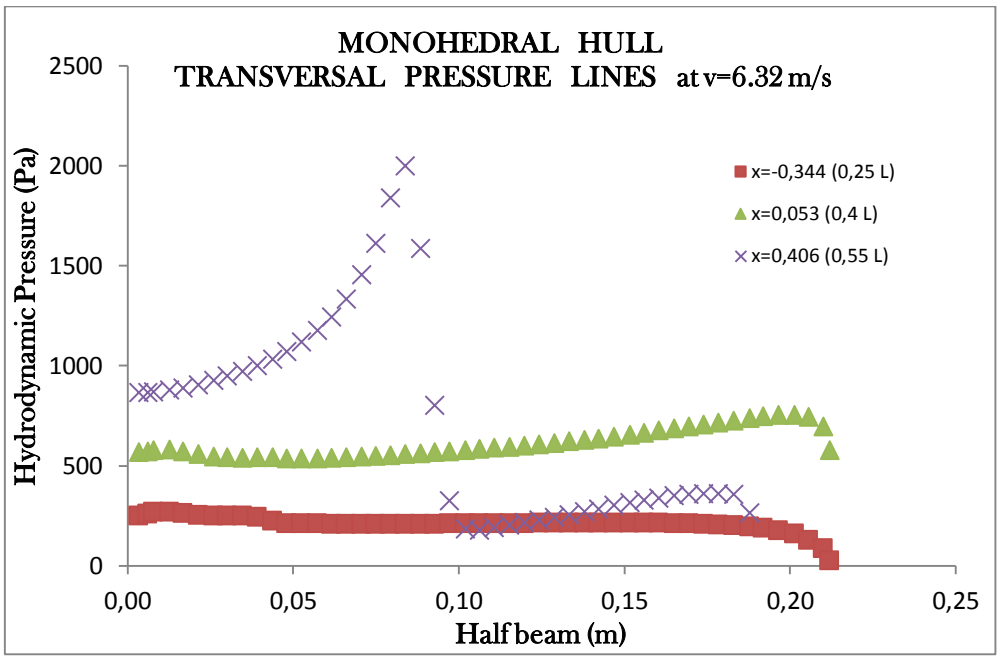

Fig. 5.76 Monohedral hull - Transversal pressure distribution at v=6.32 m/s

TRANSVERSAL PRESSURE DISTRIBUTION

WARPED 2 HULL at v=3.4 m/s

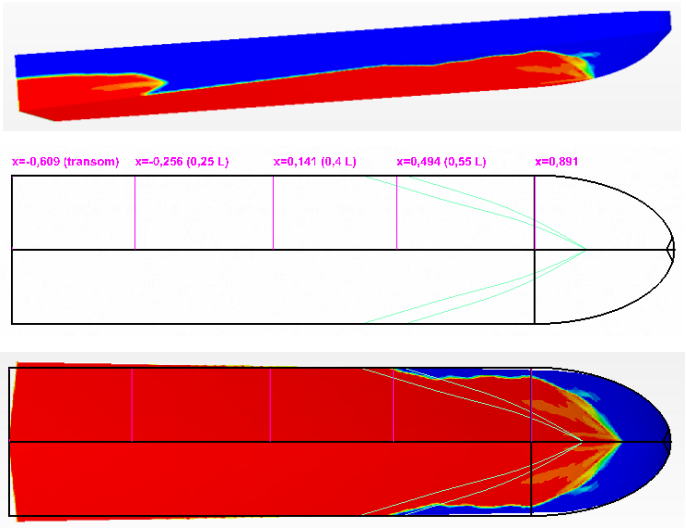

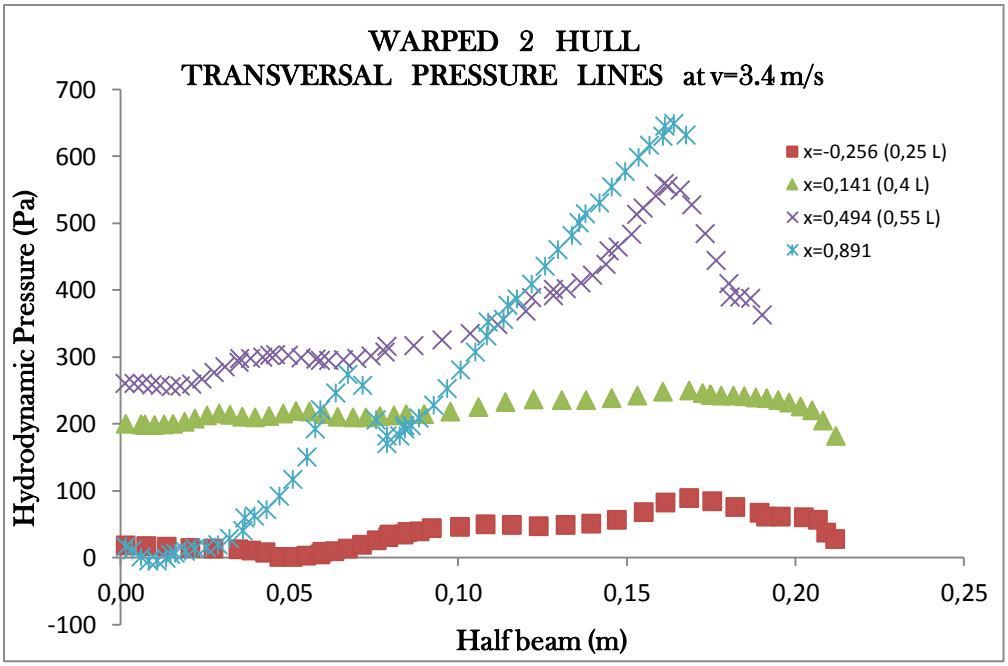

Fig. 5.77 Warped 2 hull - Transversal pressure distribution at v=3.4 m/s

TRANSVERSAL PRESSURE DISTRIBUTION

WARPED 2 HULL at v=4.6 m/s

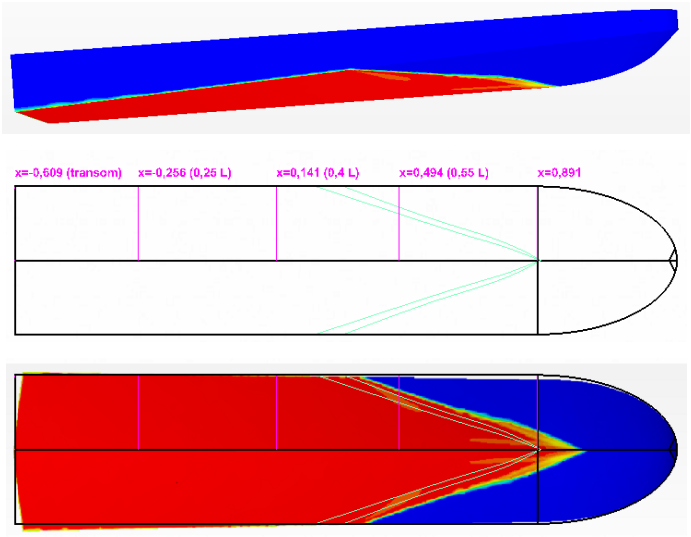

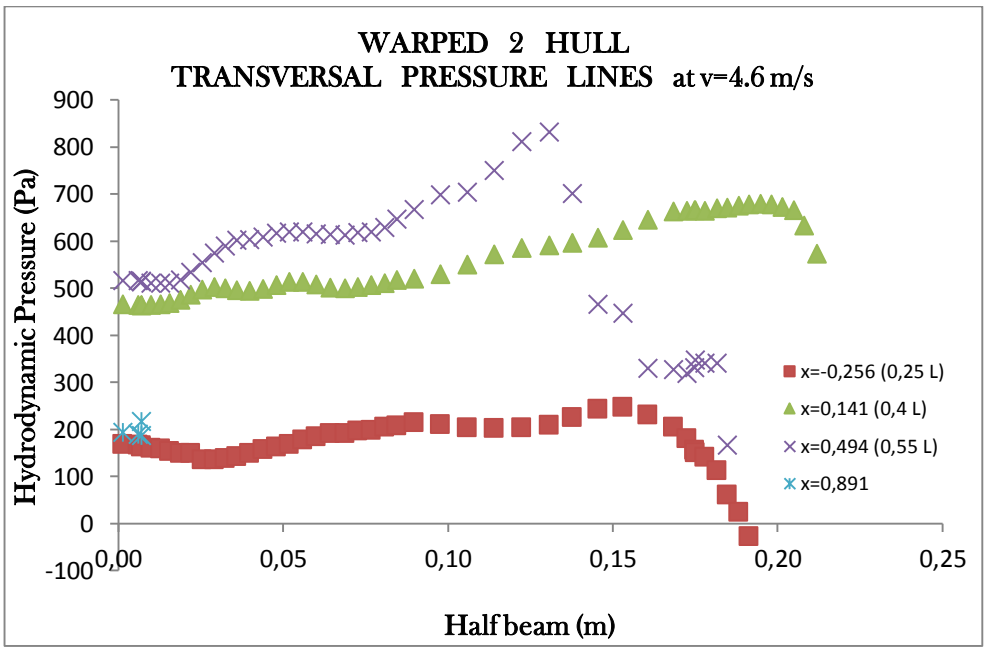

Fig. 5.78 Warped 2 hull - Transversal pressure distribution at v=4.6 m/s

TRANSVERSAL PRESSURE DISTRIBUTION

WARPED 2 HULL at v=5.75 m/s

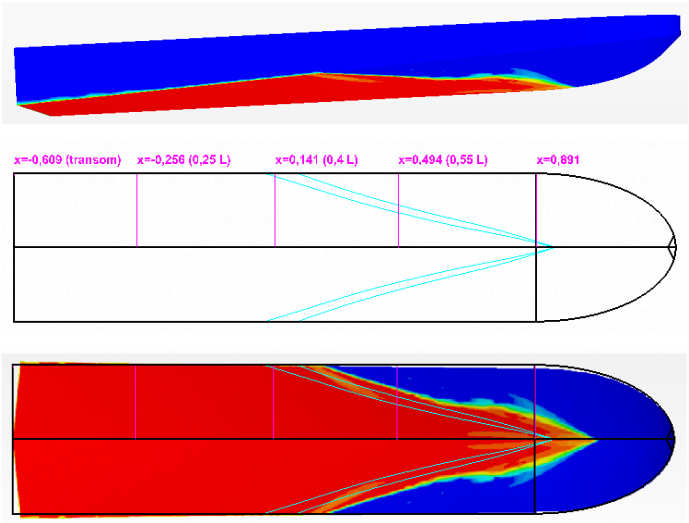

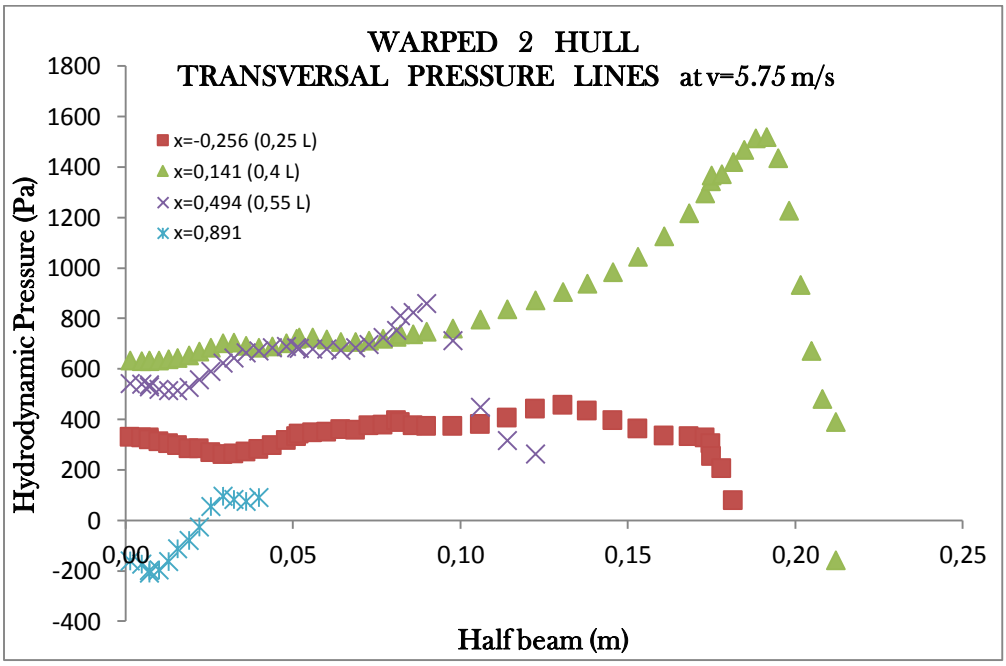

Fig. 5.79 Warped 2 hull - Transversal pressure distribution at v=5.75 m/s

TRANSVERSAL PRESSURE DISTRIBUTION

WARPED 2 HULL at v=6.32 m/s

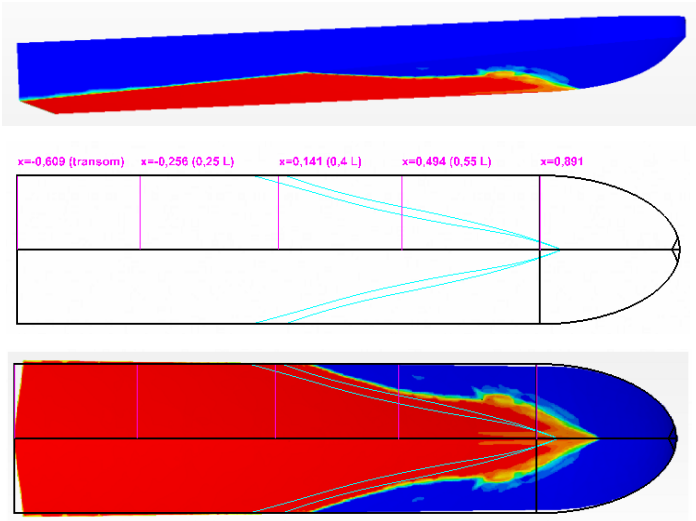

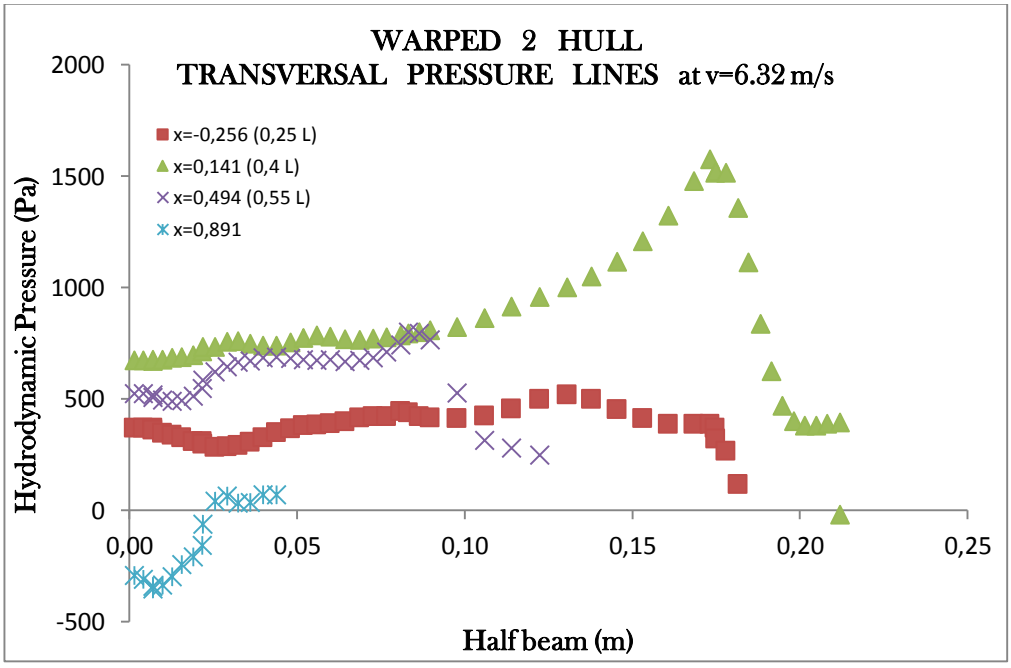

Fig. 5.80 Warped 2 hull - Transversal pressure distribution at v=6.32 m/s

COMPARISON TRANSVERSAL PRESSURE DISTRIBUTION at 0.25 L

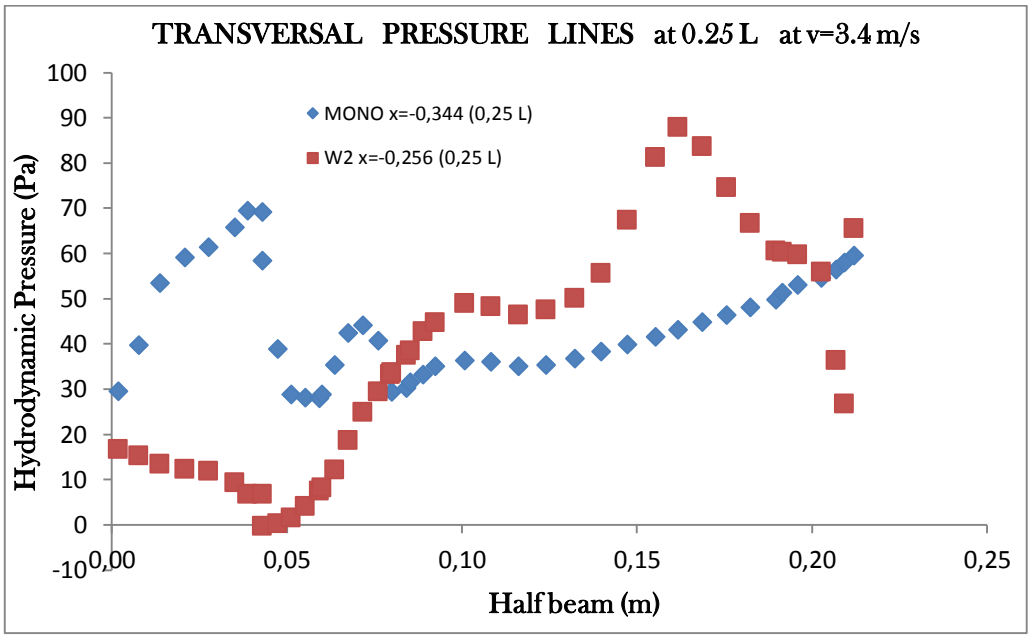

Fig. 5.81 Transversal pressure distribution at 0.25 L at v=3.4 m/s

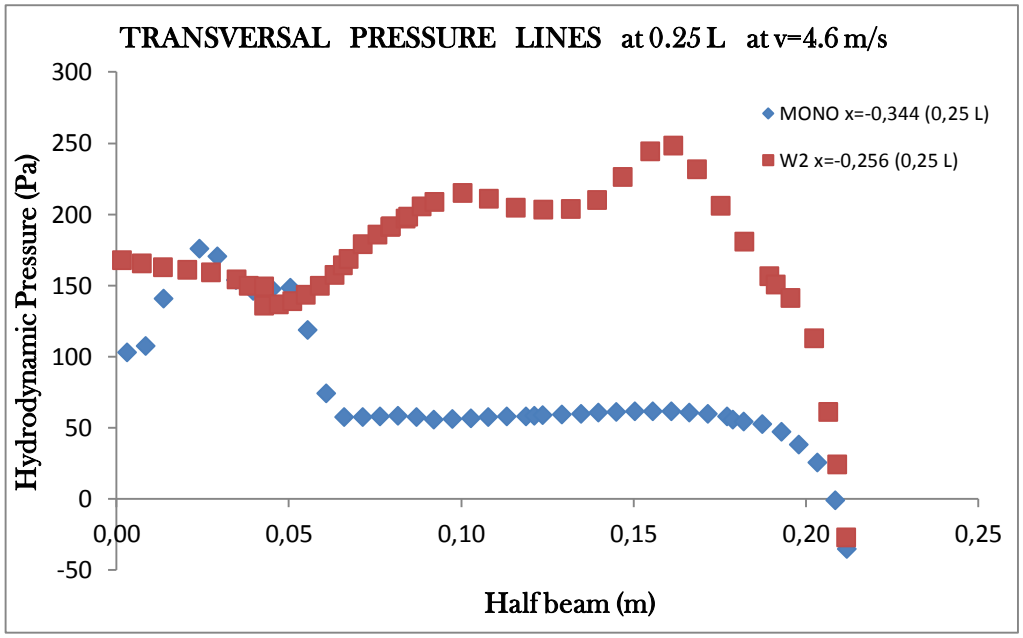

Fig. 5.82 Transversal pressure distribution at 0.25 L at v=4.6 m/s

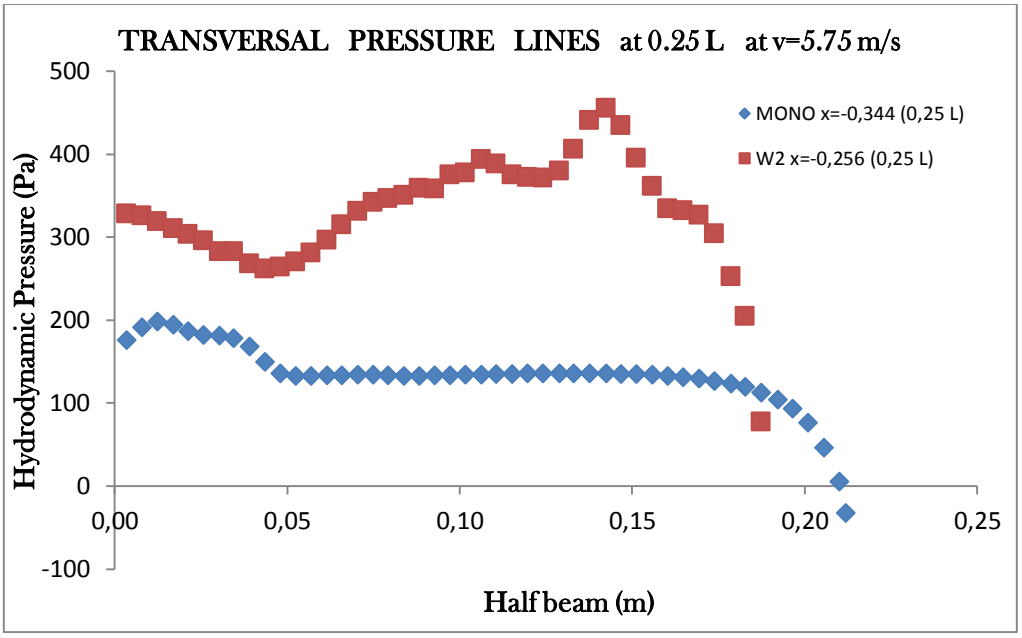

Fig. 5.83 Transversal pressure distribution at 0.25 L at v=5.75 m/s

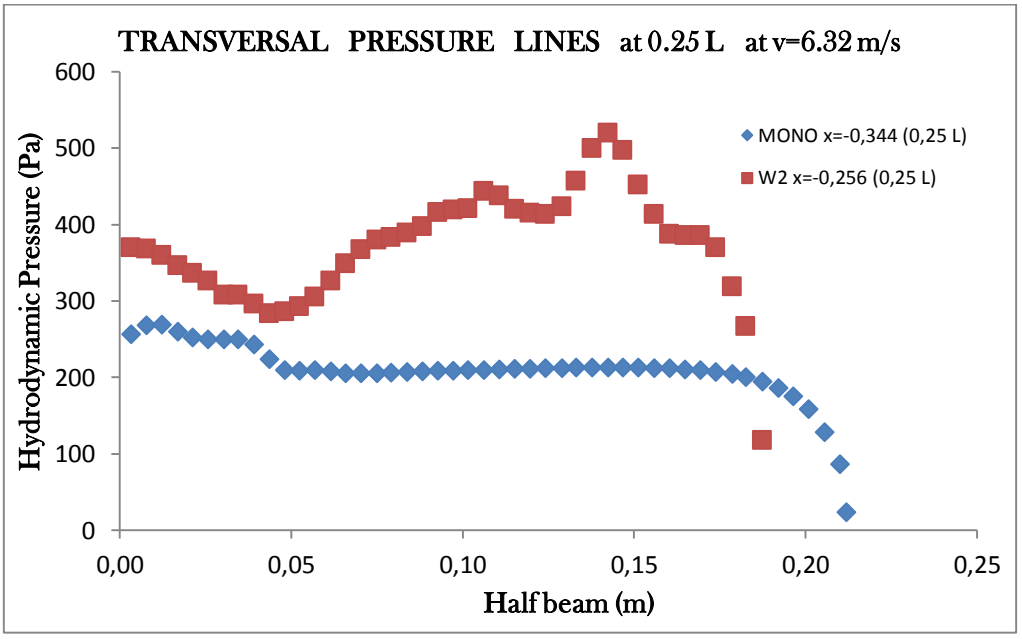

Fig. 5.84 Transversal pressure distribution at 0.25 L at v=6.32 m/s

COMPARISON TRANSVERSAL PRESSURE DISTRIBUTION at 0.4 L

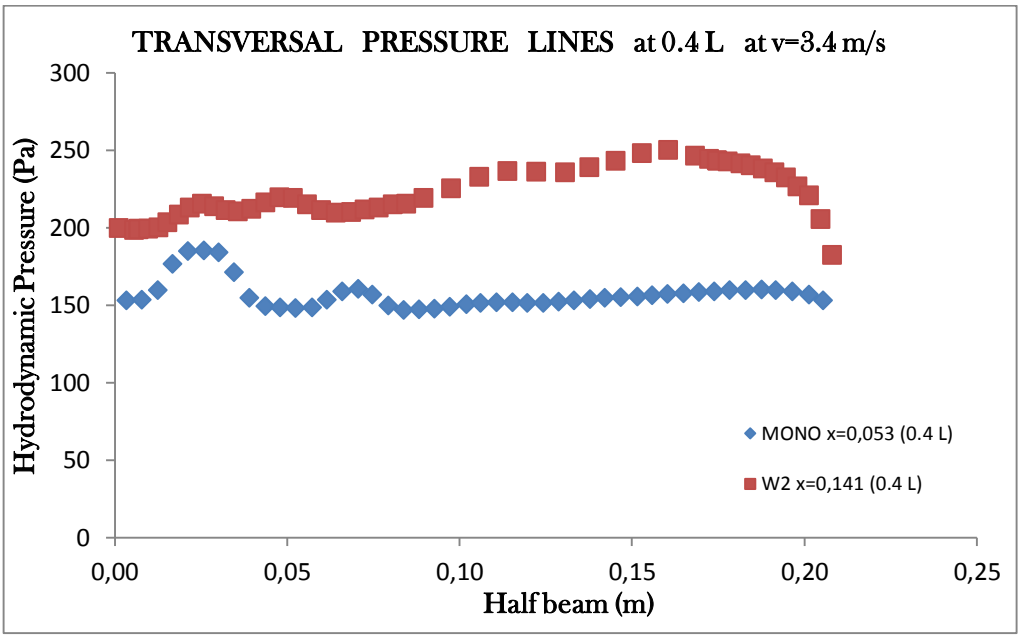

Fig. 5.85 Transversal pressure distribution at 0.4 L at v=3.4 m/s

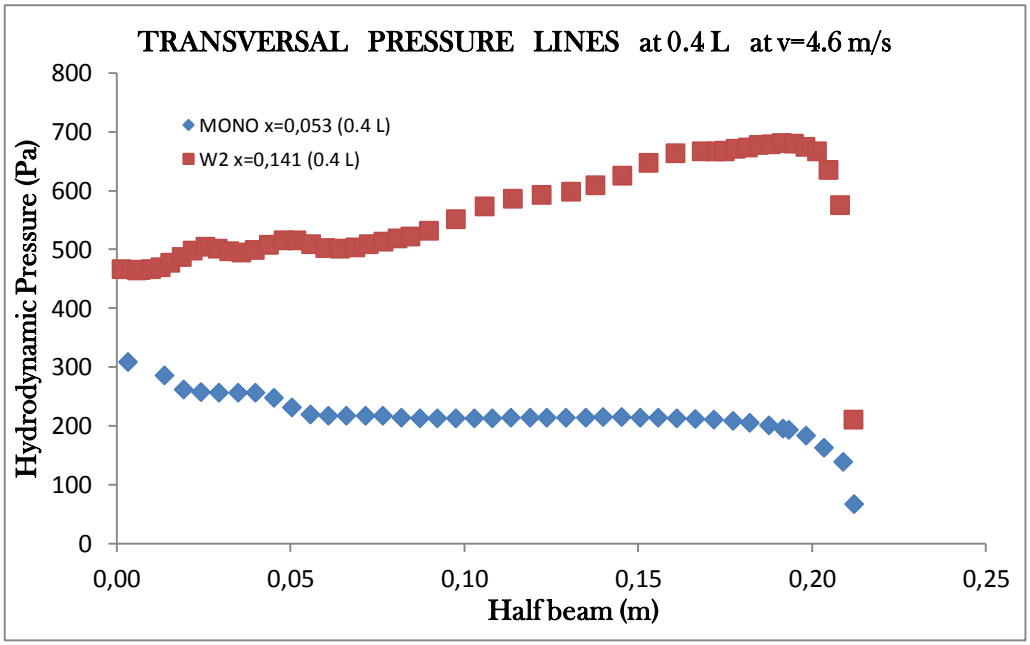

Fig. 5.86 Transversal pressure distribution at 0.4 L at v=4.6 m/s

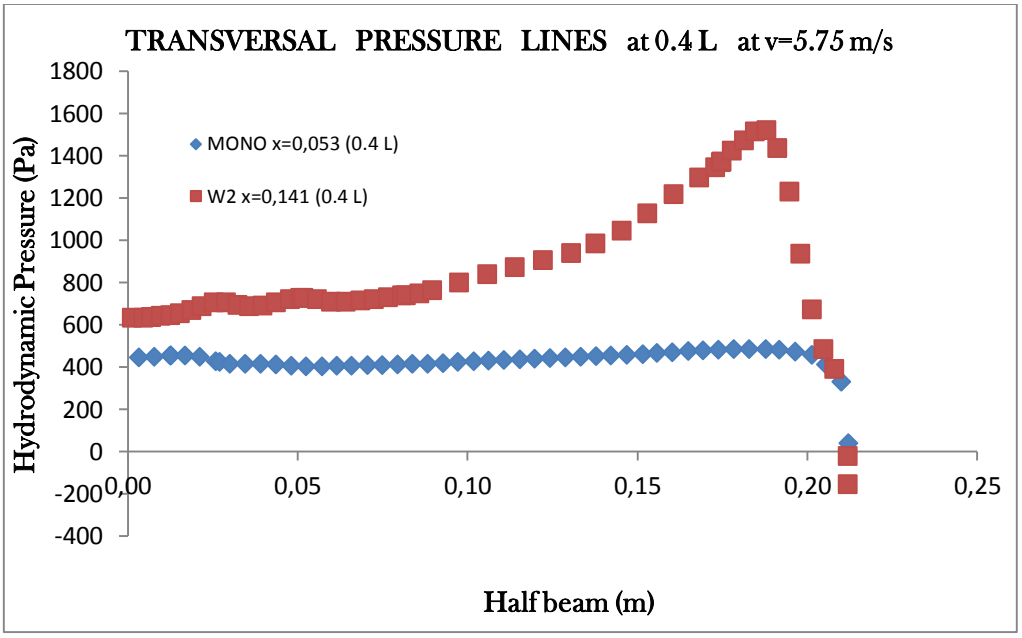

Fig. 5.87 Transversal pressure distribution at 0.4 L at v=5.75 m/s

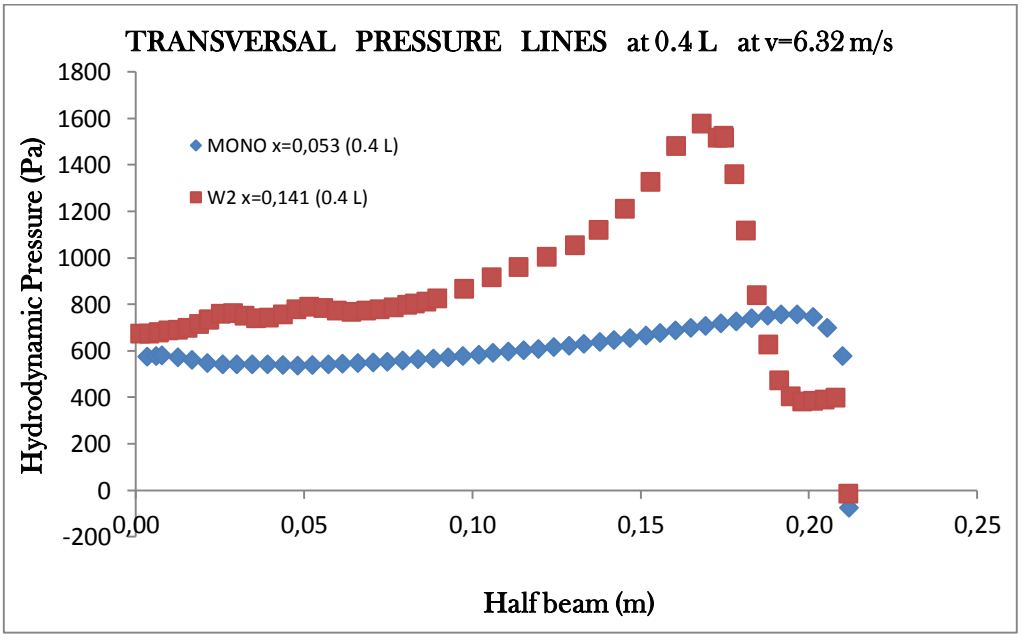

Fig. 5.88 Transversal pressure distribution at 0.4 L at v=6.32 m/s

COMPARISON TRANSVERSAL PRESSURE DISTRIBUTION at 0.55 L

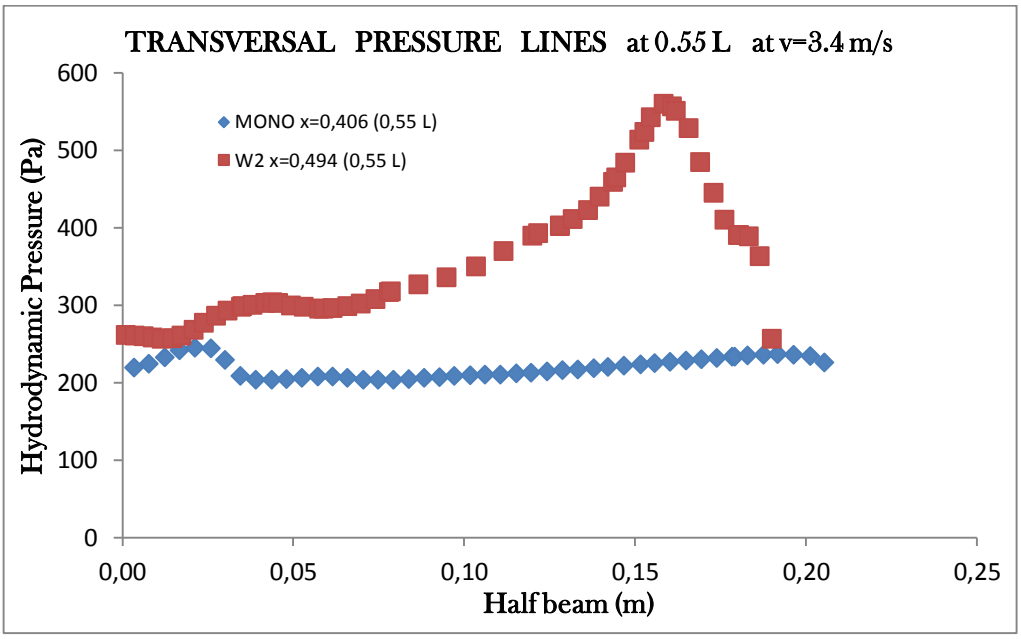

Fig. 5.89 Transversal pressure distribution at 0.55 L at v=3.4 m/s

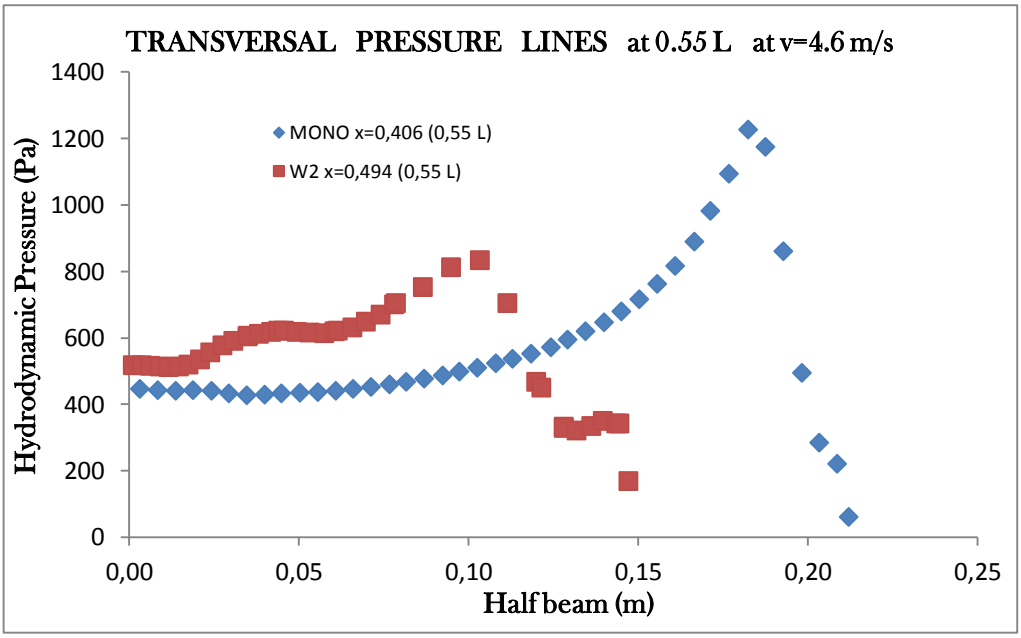

Fig. 5.90 Transversal pressure distribution at 0.55 L at v=4.6 m/s

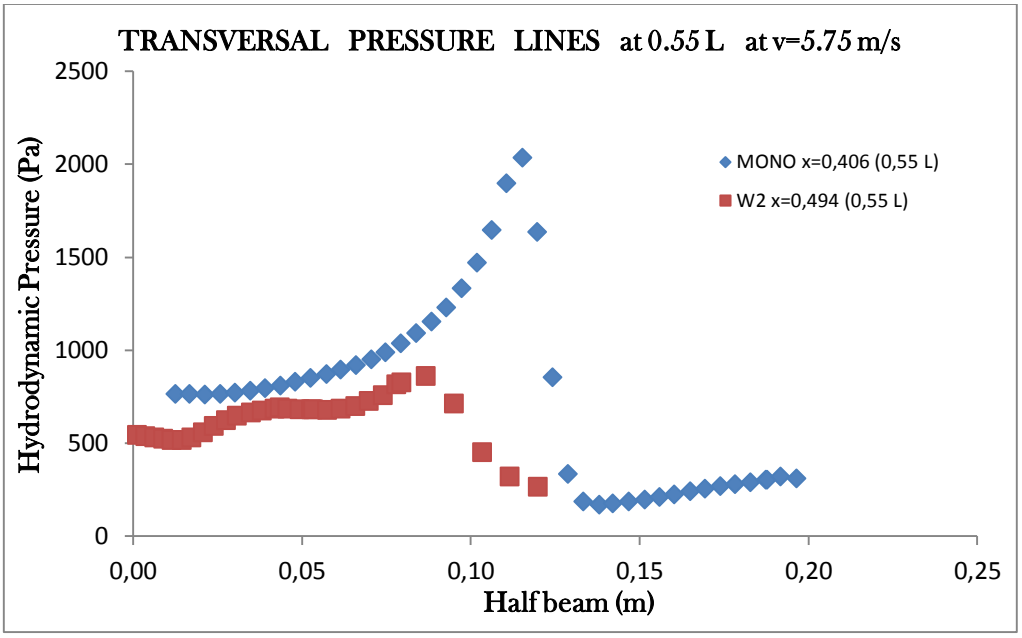

Fig. 5.91 Transversal pressure distribution at 0.55 L at v=5.75 m/s

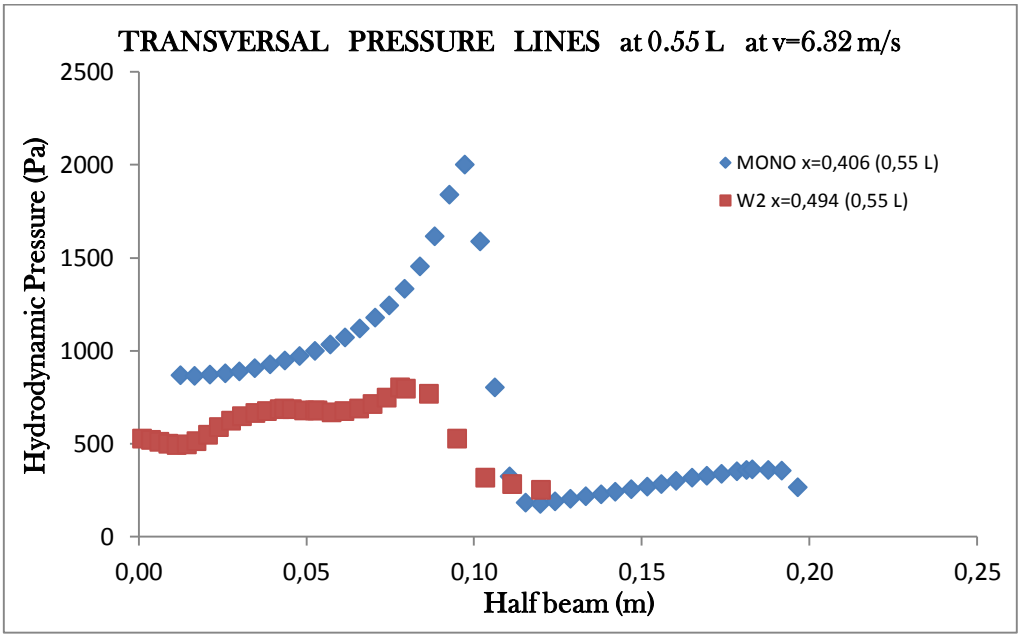

Fig. 5.92 Transversal pressure distribution at 0.55 L at v=6.32 m/s

LONGITUDINAL PRESSURE DISTRIBUTION

MONOHEDRAL HULL at v=3.4 m/s

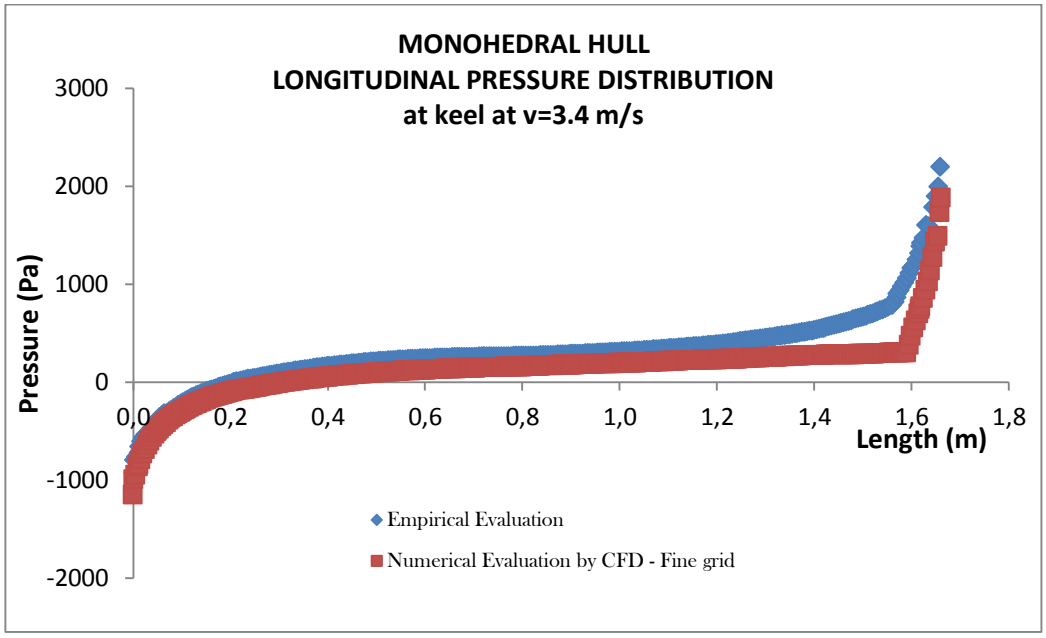

Fig. 5.93 Monohedral hull – Longitudinal pressure distribution at keel at v=3.4 m/s

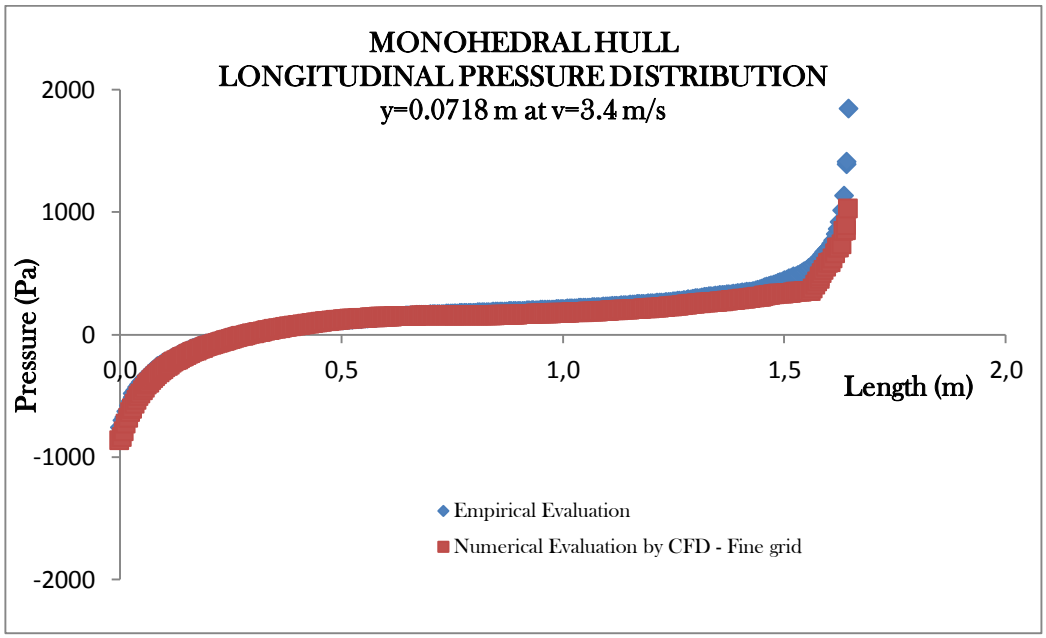

Fig. 5.94 Monohedral hull – Longitudinal pressure distribution at y=0.0718 at v=3.4 m/s

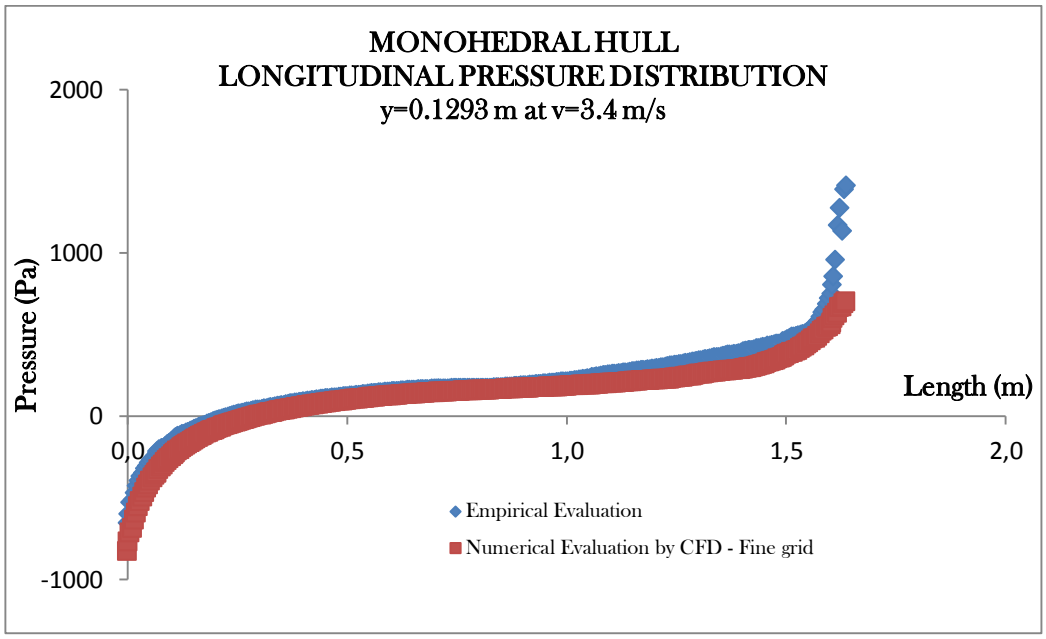

Fig. 5.95 Monohedral hull – Longitudinal pressure distribution at y=0.1293 at v=3.4 m/s

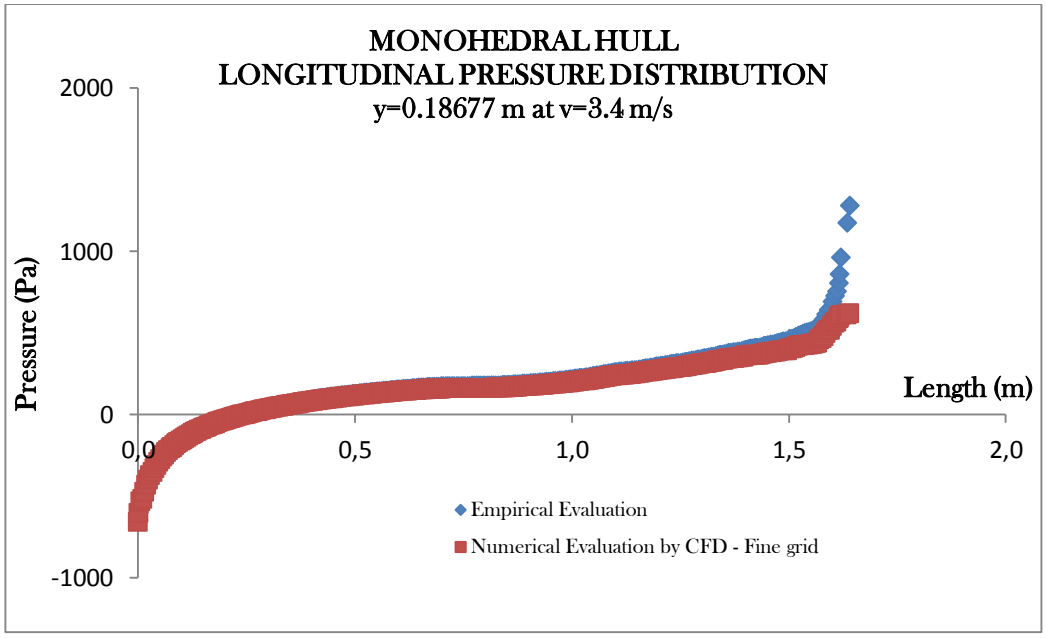

Fig. 5.96 Monohedral hull – Longitudinal pressure distribution at y=0.18677 at v=3.4 m/s

LONGITUDINAL PRESSURE DISTRIBUTION

MONOHEDRAL HULL at v=4.6 m/s

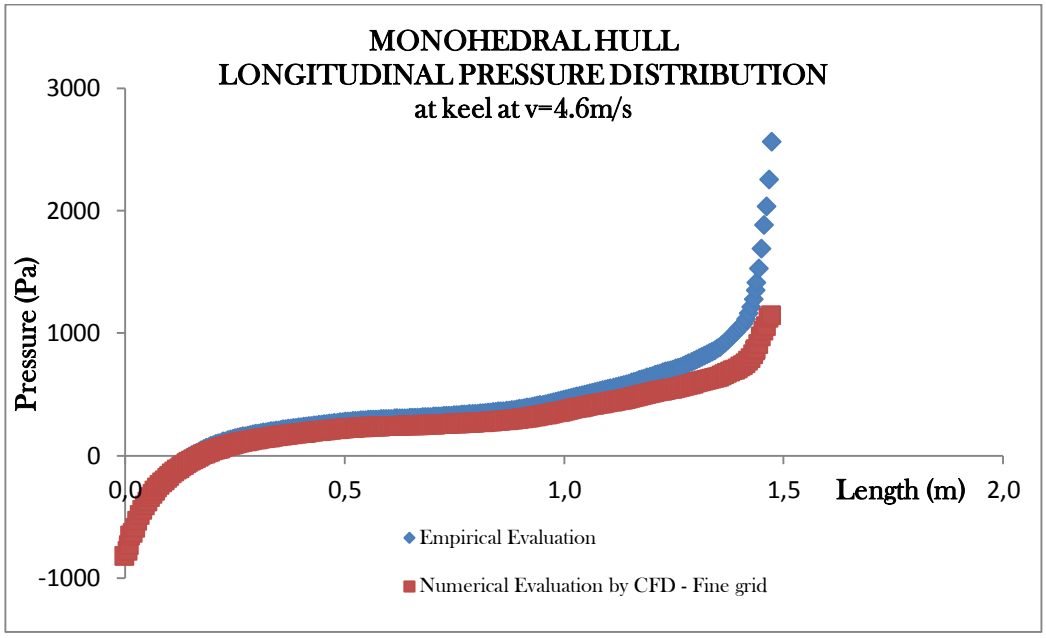

Fig. 5.97 Monohedral hull – Longitudinal pressure distribution at keel at v=4.6 m/s

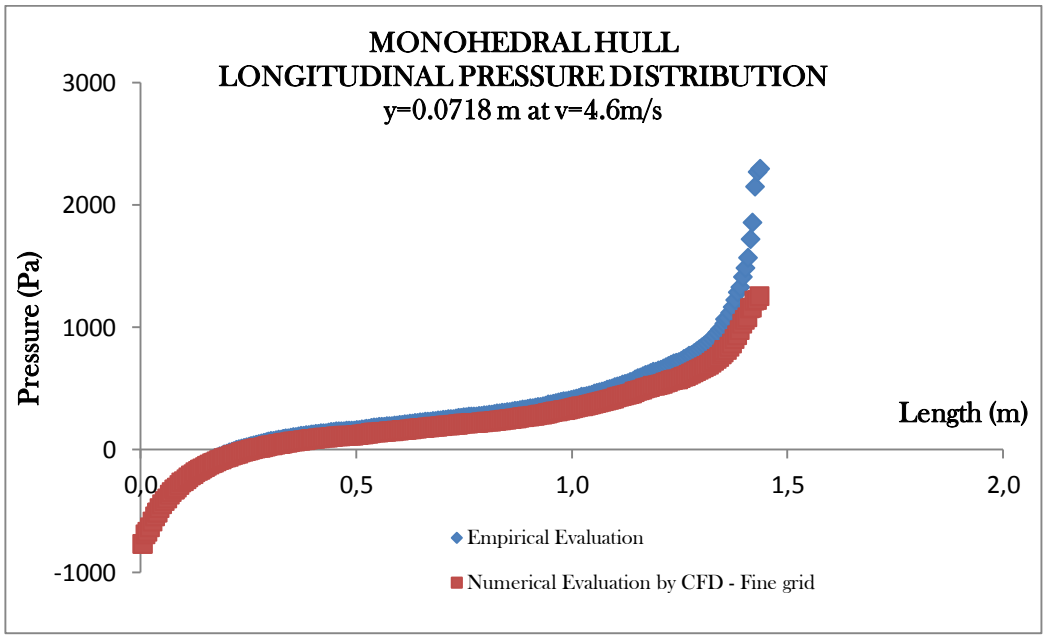

Fig. 5.98 Monohedral hull – Longitudinal pressure distribution at y=0.0718 at v=4.6 m/s

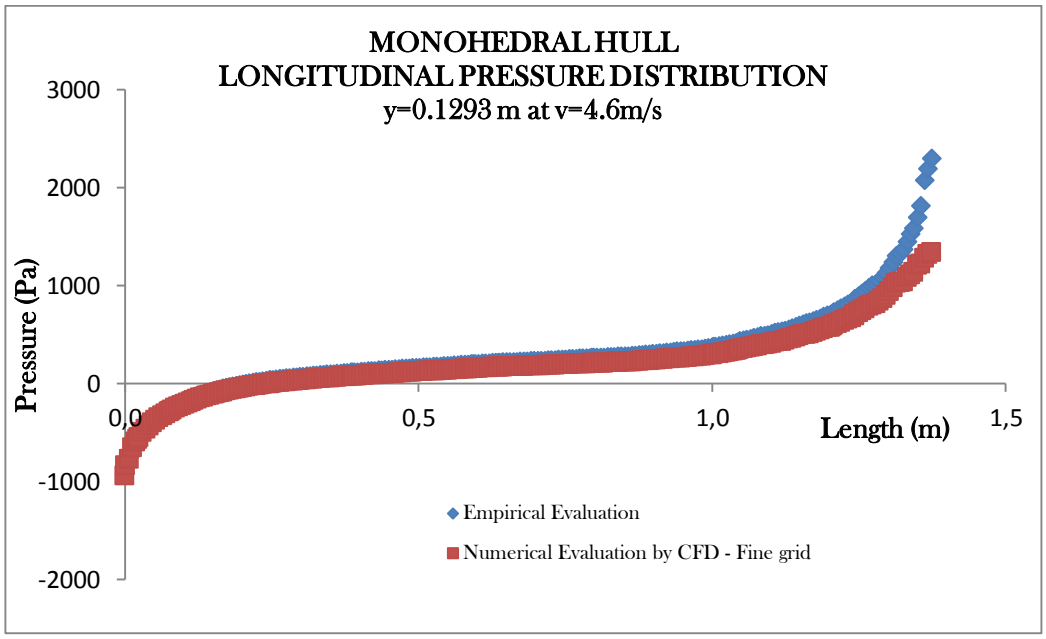

Fig. 5.99 Monohedral hull – Longitudinal pressure distribution at y=0.1293 at v=4.6 m/s

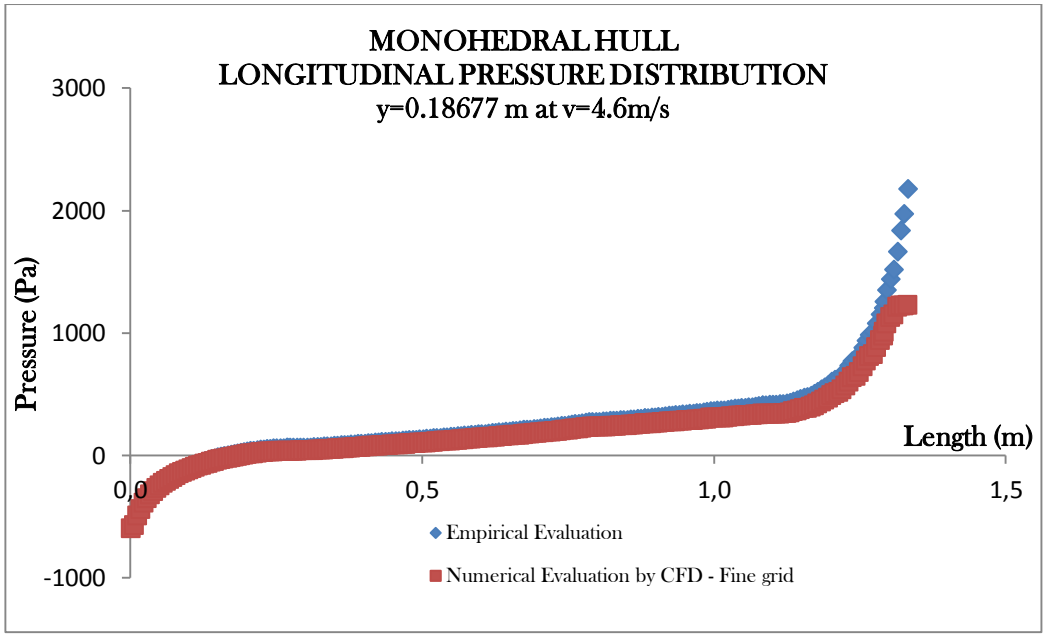

Fig. 5.100 Monohedral hull – Longitudinal pressure distribution at y=0.18677 at v=4.6 m/s

LONGITUDINAL PRESSURE DISTRIBUTION

MONOHEDRAL HULL at v=5.75 m/s

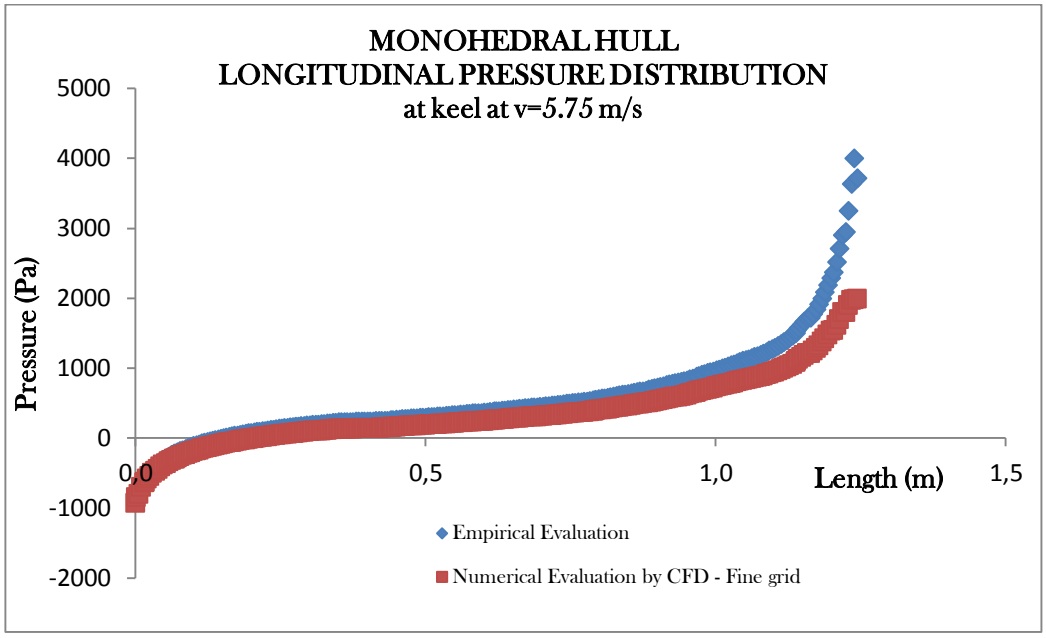

Fig. 5.101 Monohedral hull – Longitudinal pressure distribution at keel at v=5.75 m/s

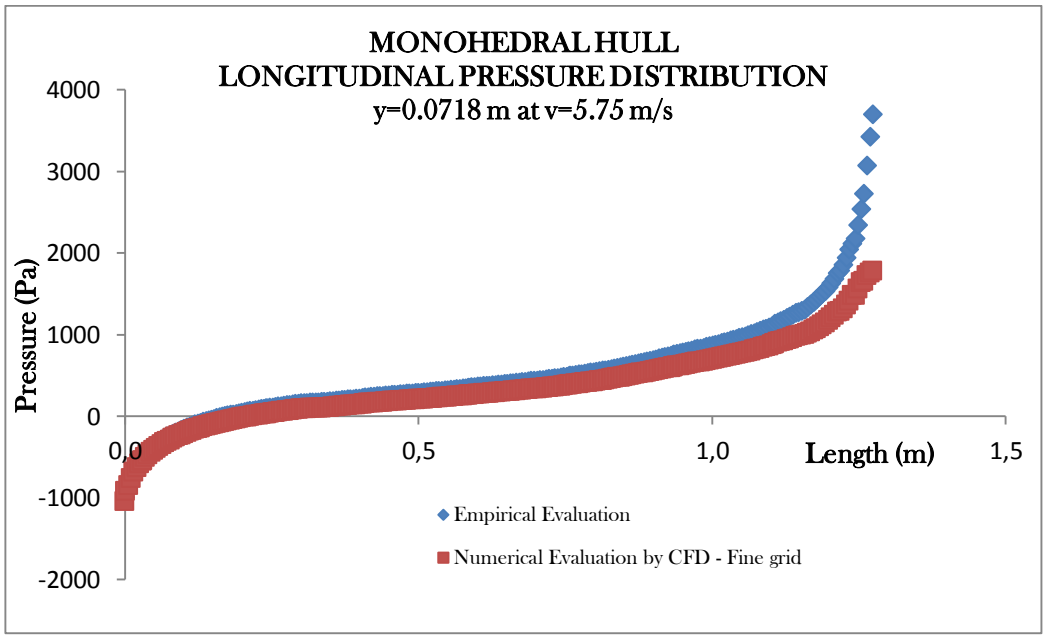

Fig. 5.102 Monohedral hull – Longitudinal pressure distribution at y=0.0718 at v=5.75 m/s

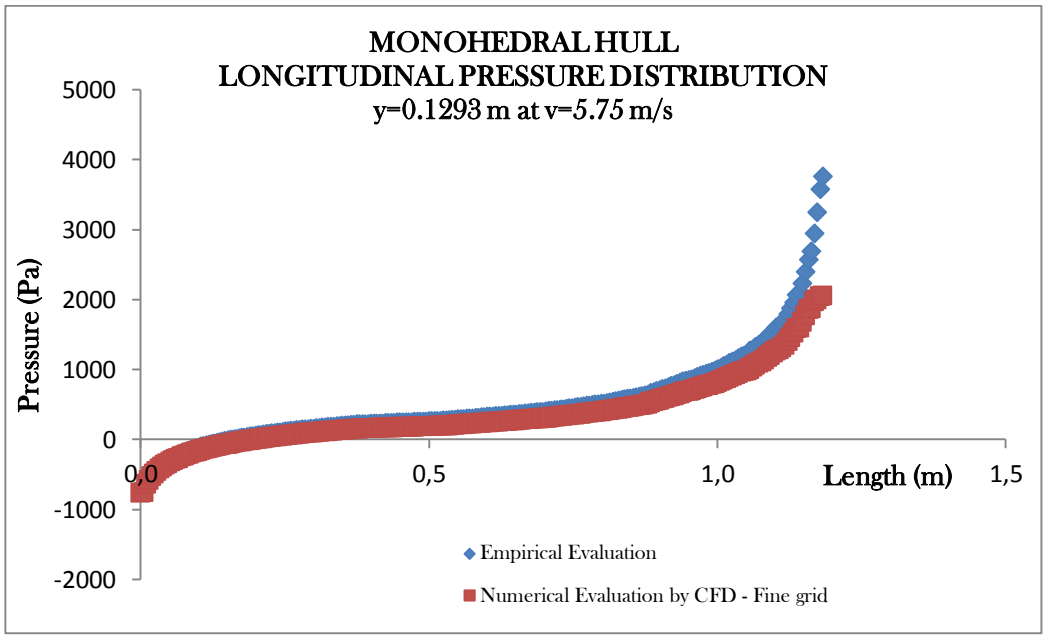

Fig. 5.103 Monohedral hull – Longitudinal pressure distribution at y=0.1293 at v=5.75 m/s

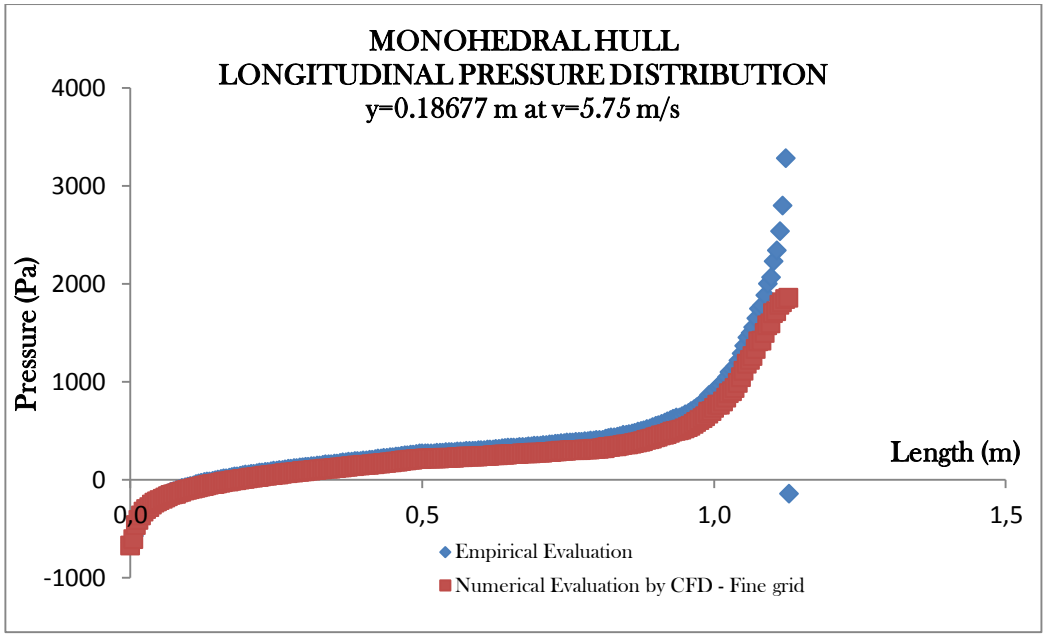

Fig. 5.104 Monohedral hull – Longitudinal pressure distribution at y=0.18677 at v=5.75 m/s

LONGITUDINAL PRESSURE DISTRIBUTION

MONOHEDRAL HULL at v=6.32 m/s

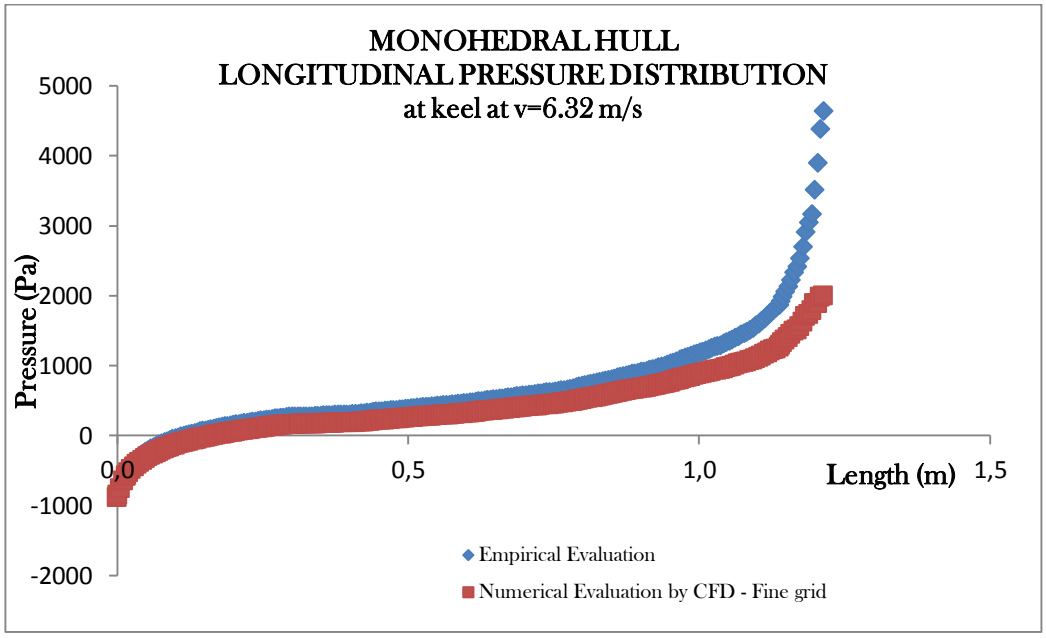

Fig. 5.105 Monohedral hull – Longitudinal pressure distribution at keel at v=6.32 m/s

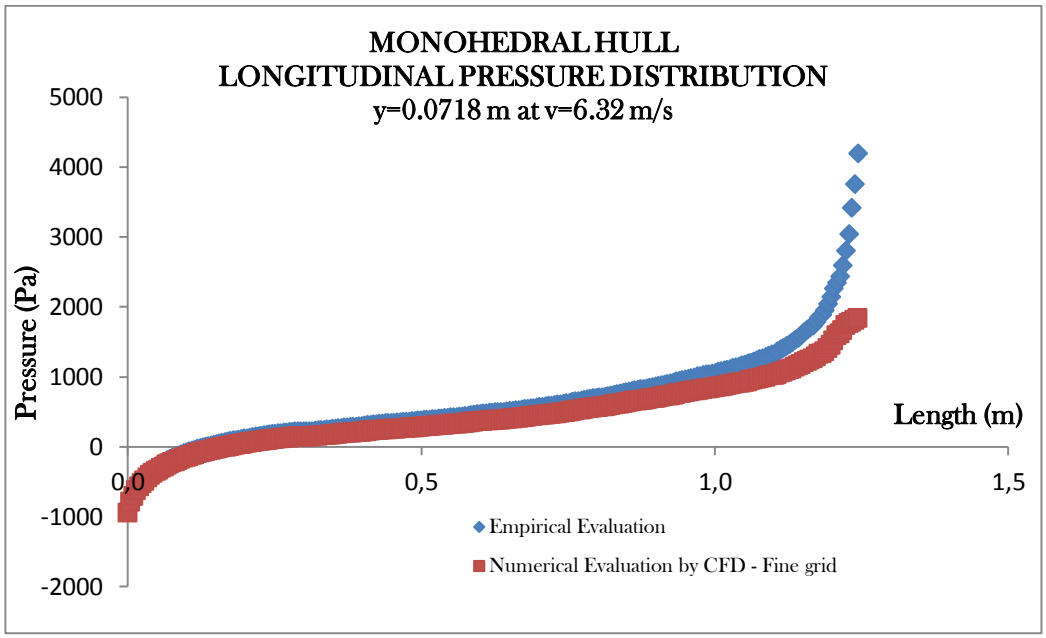

Fig. 5.106 Monohedral hull – Longitudinal pressure distribution at y=0.0718 at v=6.32 m/s

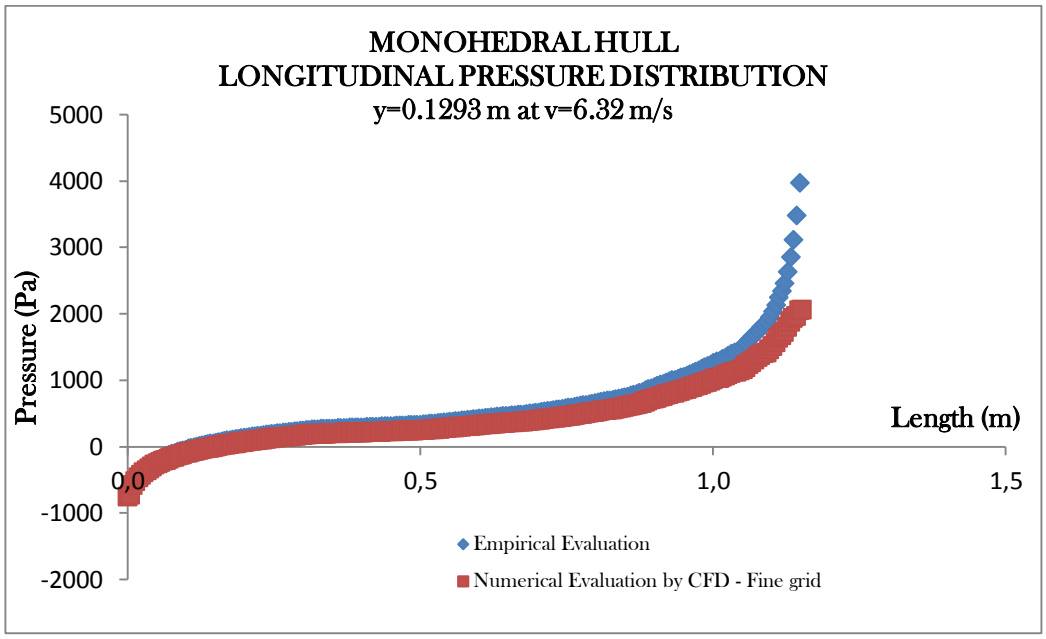

Fig. 5.107 Monohedral hull – Longitudinal pressure distribution at y=0.0129 at v=6.32 m/s

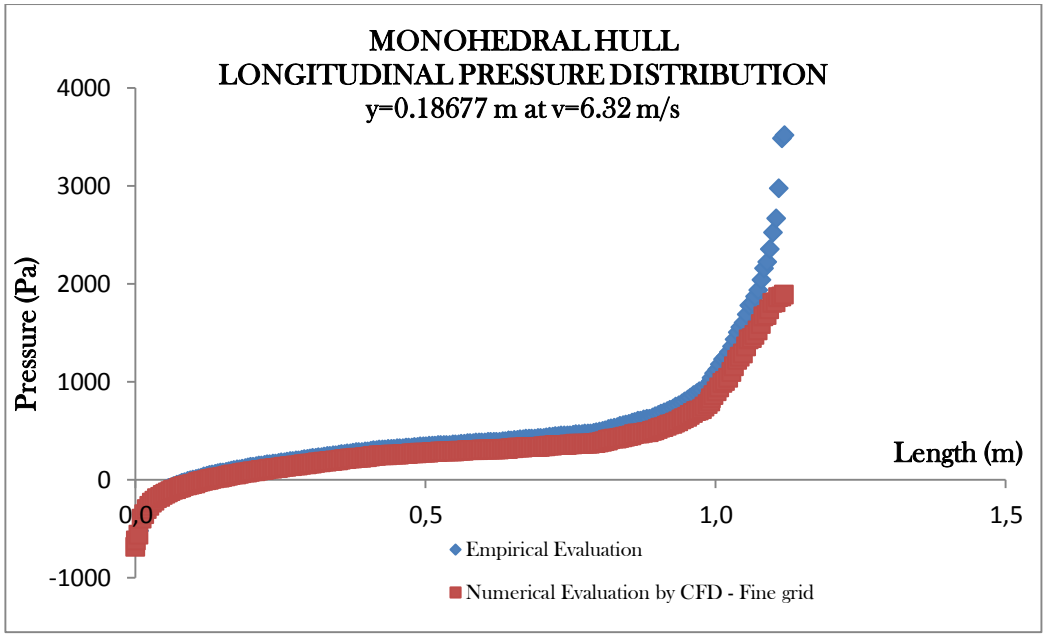

Fig. 5.108 Monohedral hull – Longitudinal pressure distribution at y=0.1867 at v=6.32 m/s

LONGITUDINAL PRESSURE DISTRIBUTION

WARPED 2 HULL at v=3.4 m/s

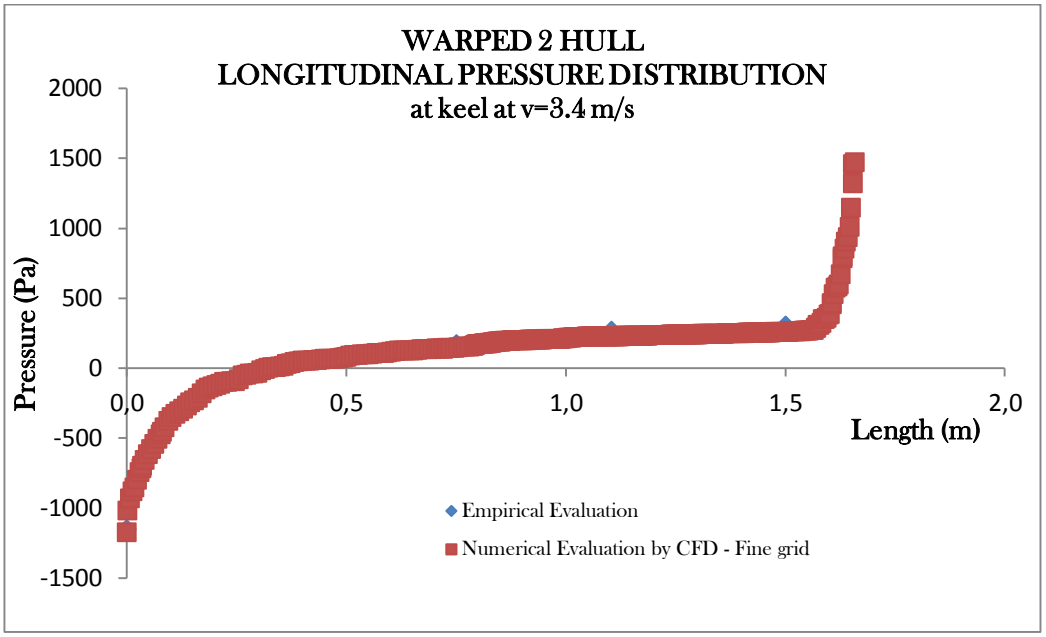

Fig. 5.109 Warped 2 hull – Longitudinal pressure distribution at keel at v=3.4 m/s

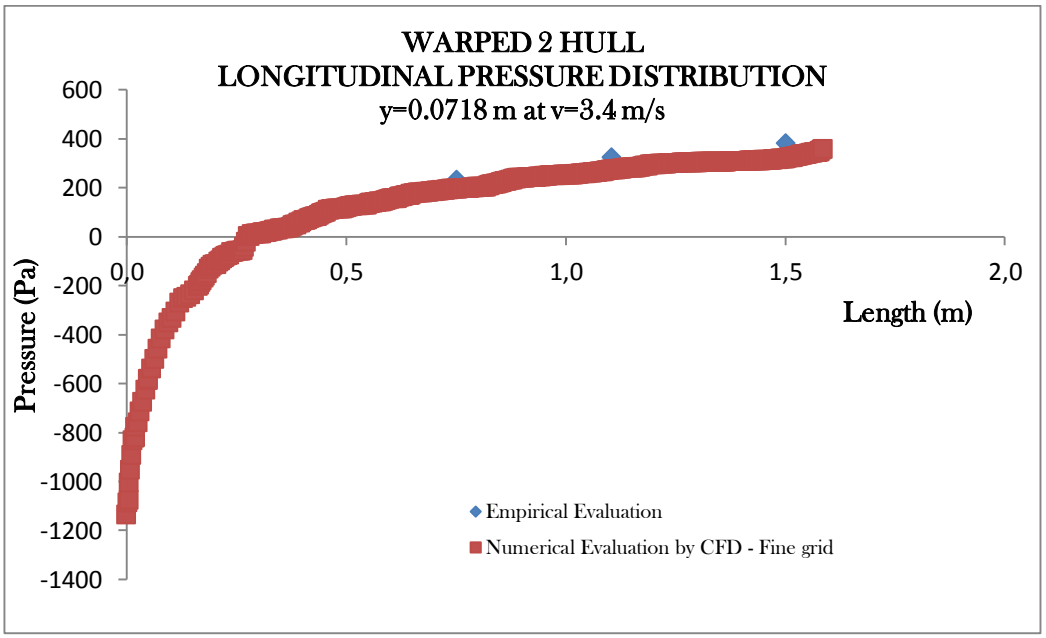

Fig. 5.110 Warped 2 hull – Longitudinal pressure distribution at y=0.0718 at v=3.4 m/s

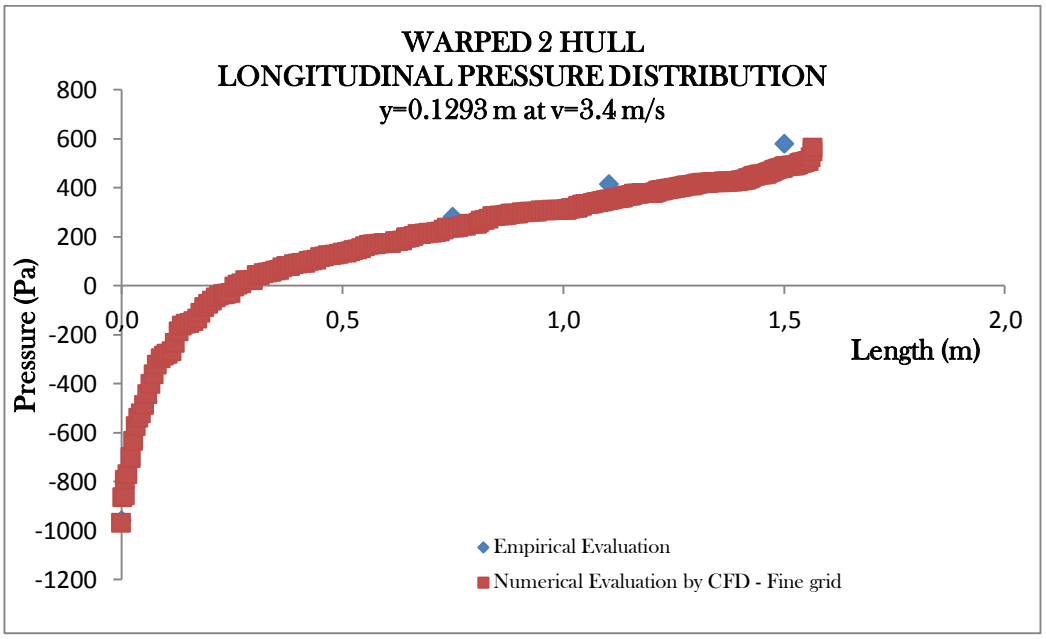

Fig. 5.111 Warped 2 hull – Longitudinal pressure distribution at y=0.1293 at v=3.4 m/s

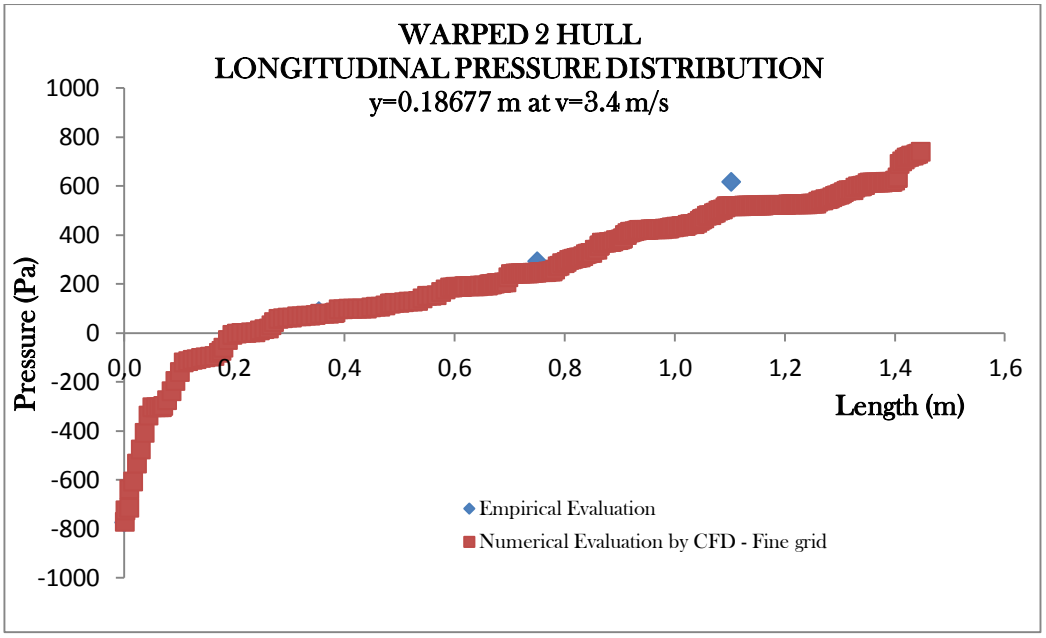

Fig. 5.112 Warped 2 hull – Longitudinal pressure distribution at y=0.18677 at v=3.4 m/s

LONGITUDINAL PRESSURE DISTRIBUTION

WARPED 2 HULL at v=4.6 m/s

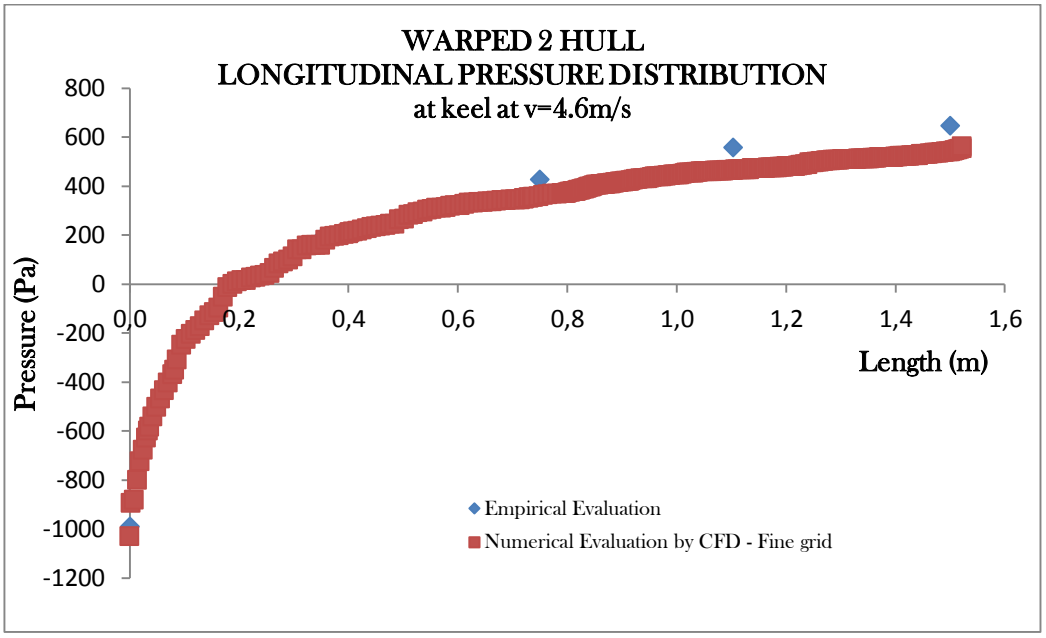

Fig. 5.113 Warped 2 hull – Longitudinal pressure distribution at keel at v=4.6 m/s

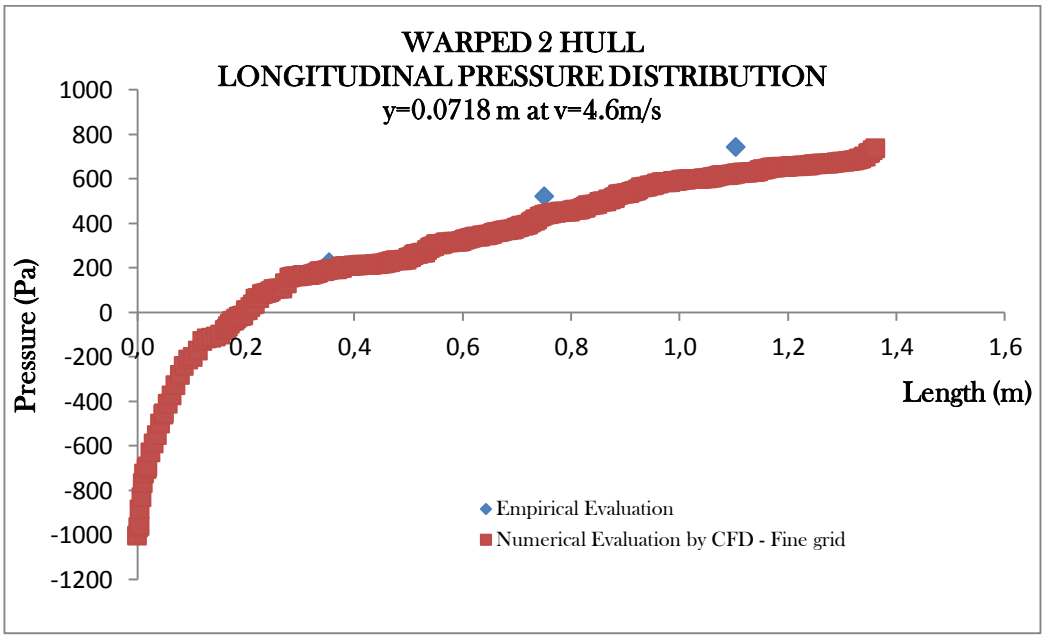

Fig. 5.114 Warped 2 hull – Longitudinal pressure distribution at y=0.0718 at v=4.6 m/s

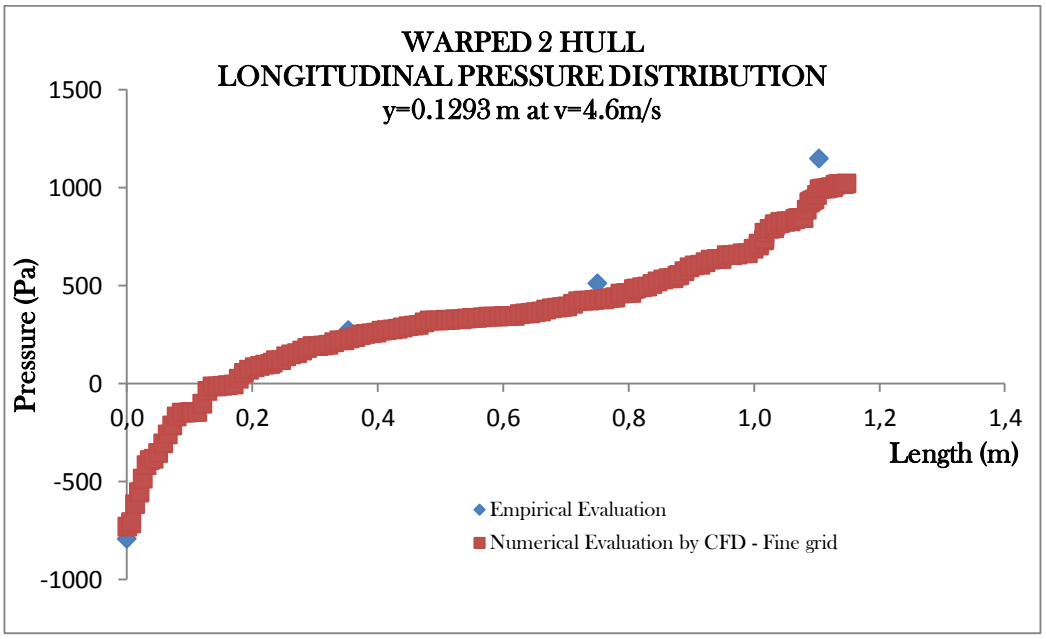

Fig. 5.115 Warped 2 hull – Longitudinal pressure distribution at y=0.1293 at v=4.6 m/s

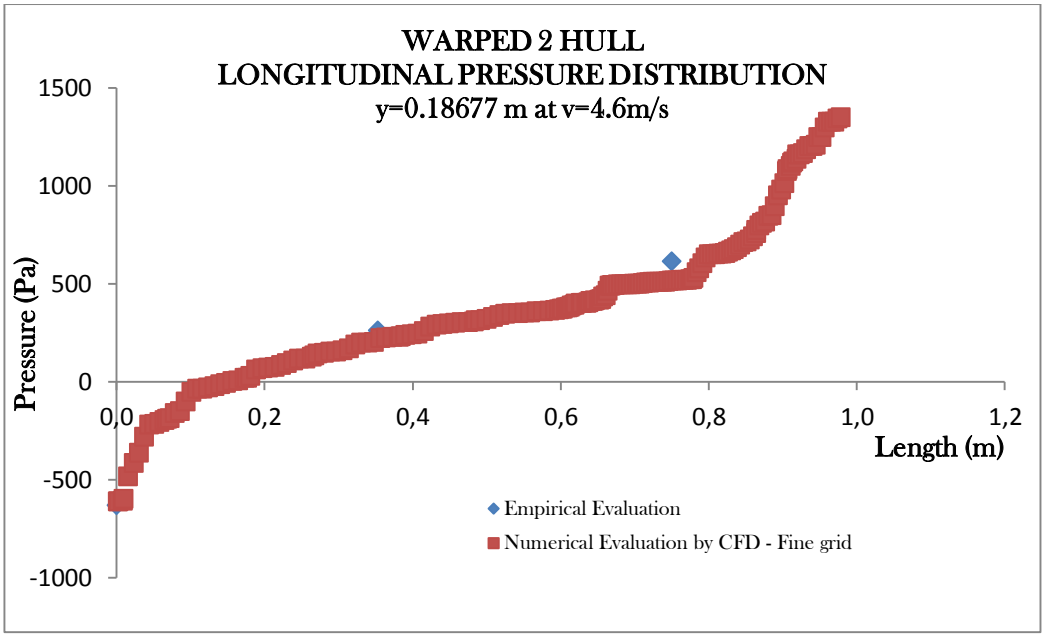

Fig. 5.116 Warped 2 hull – Longitudinal pressure distribution at y=0.18677 at v=4.6 m/s

LONGITUDINAL PRESSURE DISTRIBUTION

WARPED 2 HULL at v=5.75 m/s

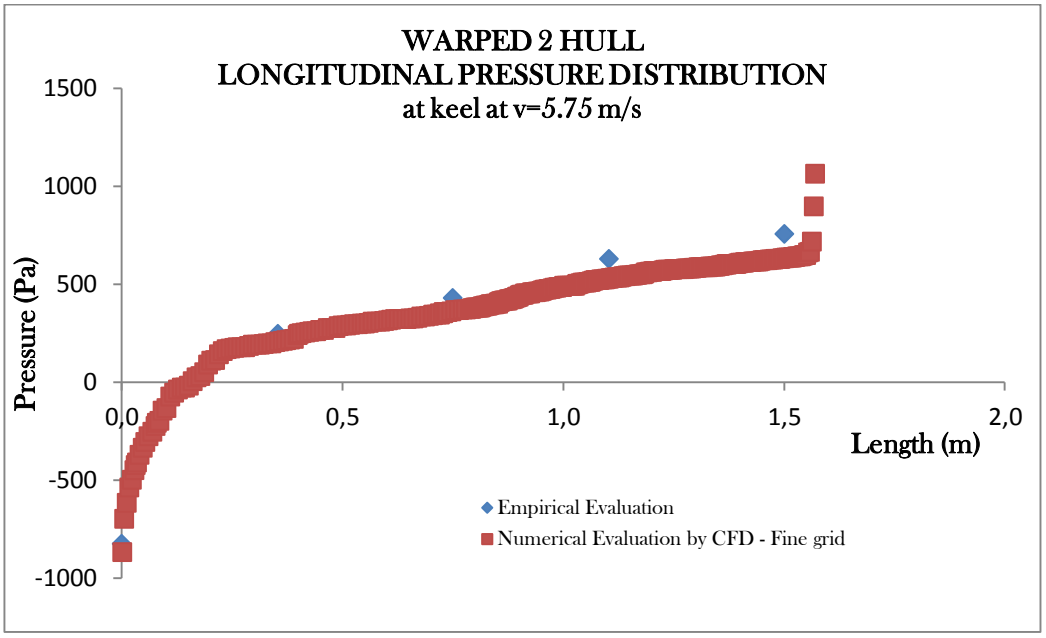

Fig. 5.117 Warped 2 hull – Longitudinal pressure distribution at keel at v=5.75 m/s

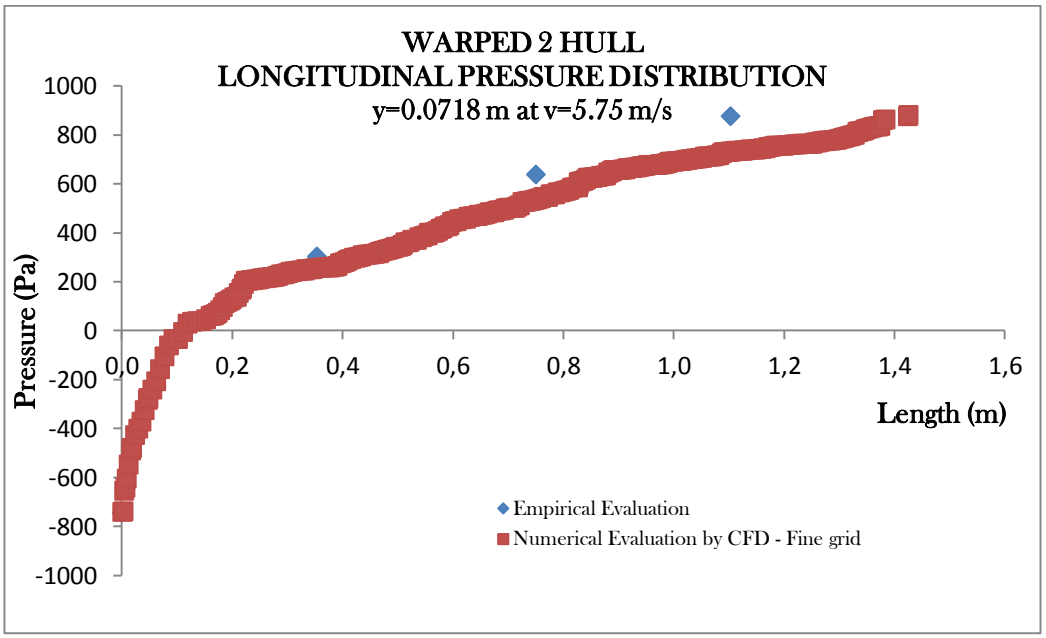

Fig. 5.118 Warped 2 hull – Longitudinal pressure distribution at y=0.0718 at v=5.75 m/s

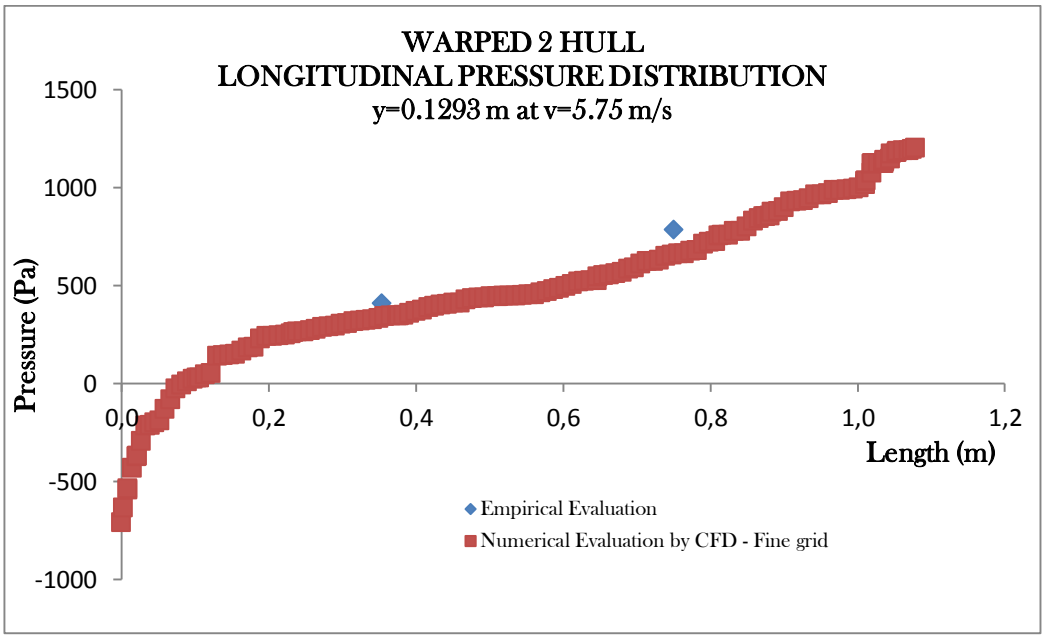

Fig. 5.119 Warped 2 hull – Longitudinal pressure distribution at y=0.1293 at v=5.75 m/s

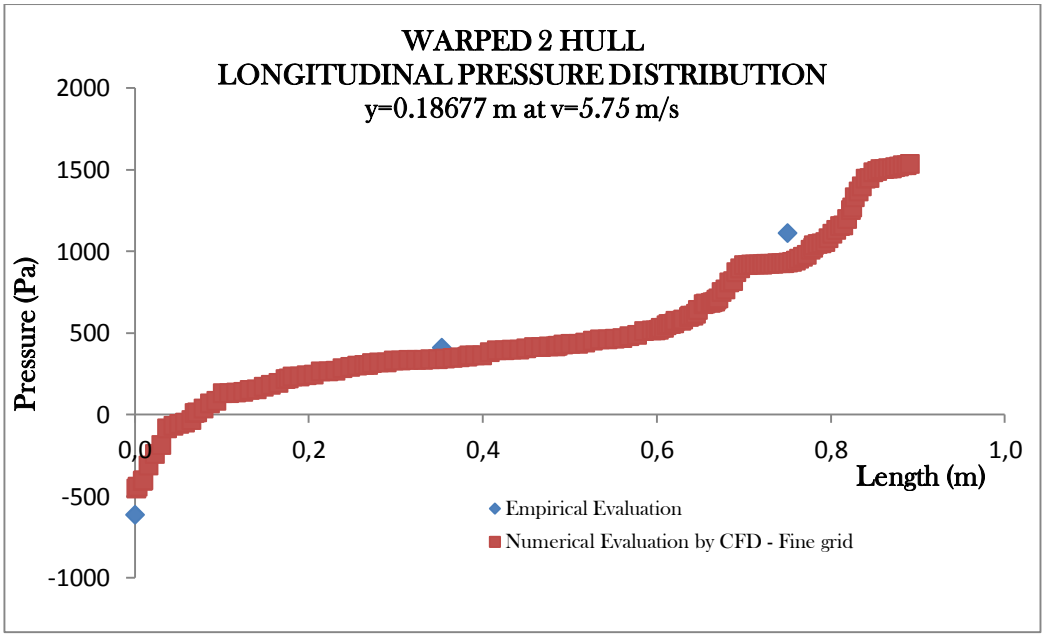

Fig. 5.120 Warped 2 hull – Longitudinal pressure distribution at y=0.18677 at v=5.75 m/s

LONGITUDINAL PRESSURE DISTRIBUTION

WARPED 2 HULL at v=6.32 m/s

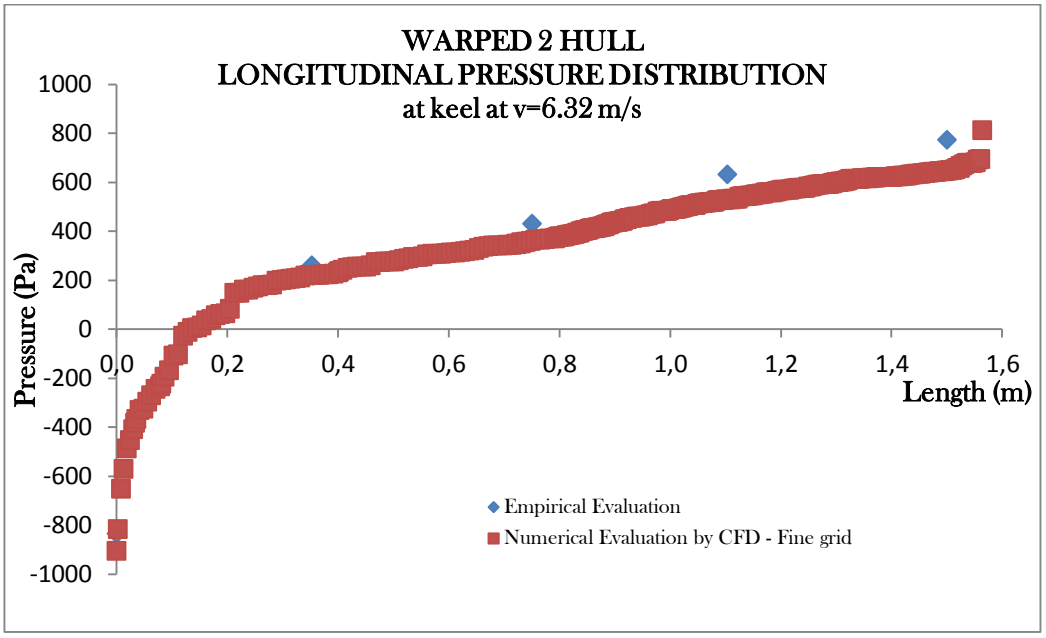

Fig. 5.121 Warped 2 hull – Longitudinal pressure distribution at keel at v=6.32 m/s

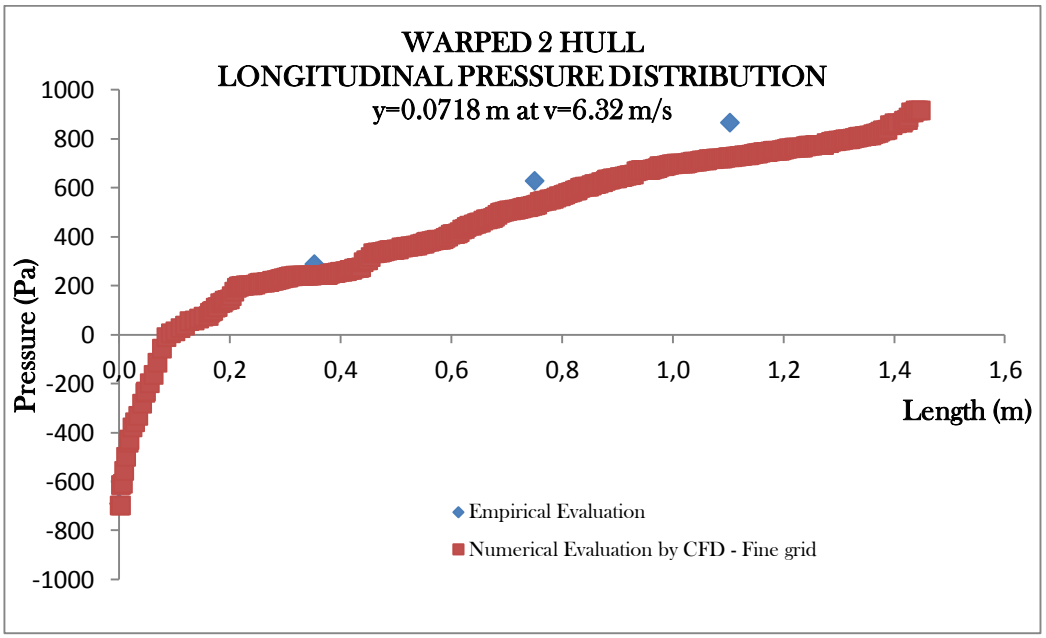

Fig. 5.122 Warped 2 hull – Longitudinal pressure distribution at y=0.0718 at v=6.32 m/s

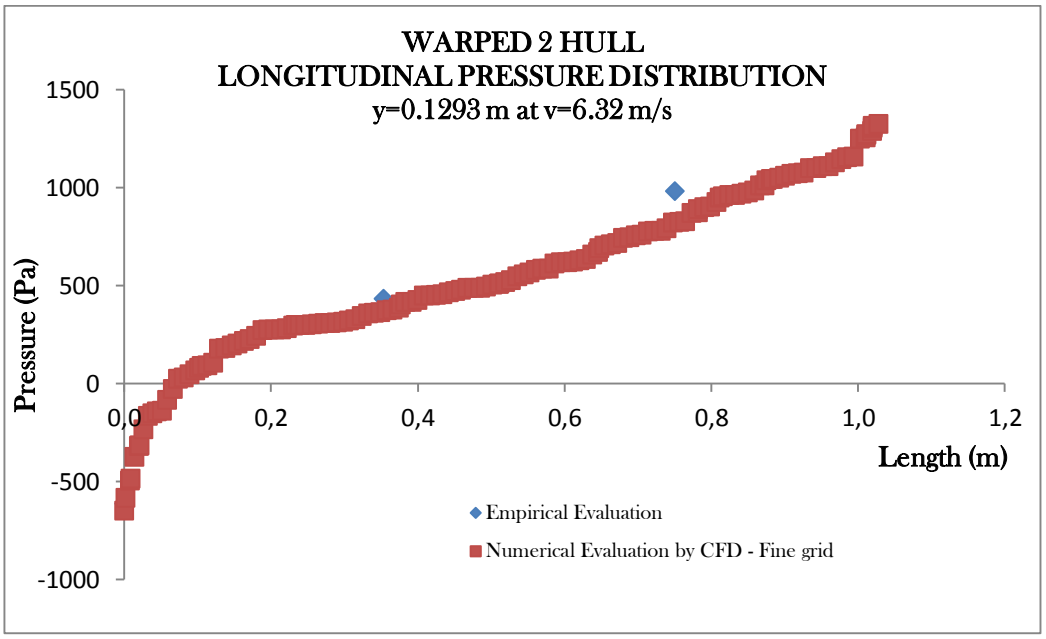

Fig. 5.123 Warped 2 hull – Longitudinal pressure distribution at y=0.1293 at v=6.32 m/s

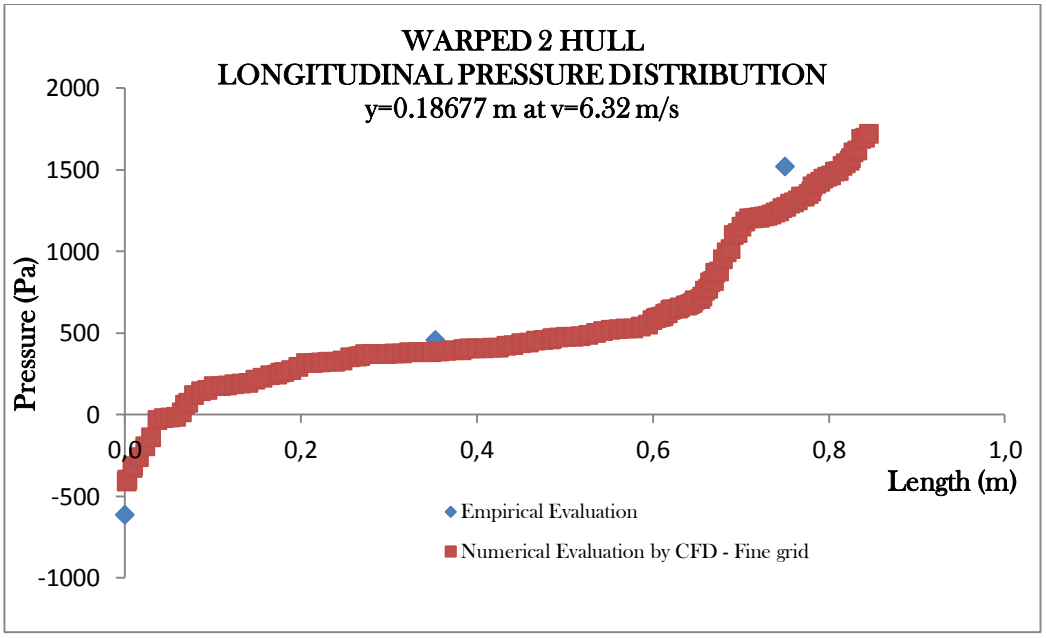

Fig. 5.124 Warped 2 hull – Longitudinal pressure distribution at y=0.18677 at v=6.32 m/s

5.4 Comparison of results

- Monohedral hull

  - The accuracy of numerical results improved significantly with mesh refinement (cells number increased from 1004229 to 1432240 and 2147253).

  - As regard the resistance, Fig. 5.33 and Fig. 5.37, Savitsky short form method and Numerical-fine-grid results are comparable: with respect to experimental results, the percentage error is about 1.9%. Numerical-medium-grid and Numerical-coarse-grid results have been compared against experimental results and the percentage errors is about 2.6% and 5.3% respectively.
  - As regard the trim, Fig. 5.34 and Fig. 5.38, Savitsky short form method gives the worst results: with respect to experimental results, the percentage error is about 14.8%. Numerical-fine-grid gives the best results: with respect to experimental results, the percentage error is about 4.5%. Numerical-medium-grid and Numerical-coarse-grid results have been compared against experimental results and the percentage errors is about 6.4% and 12.4% respectively.
  - As regard the sinkage, Fig. 5.35 and Fig. 5.39, Numerical-fine-grid, Numerical-medium-grid and Numerical-coarse-grid results are comparable. There isn't significant improvement among different grids. There isn't possibility comparing numerical results with Savitsky short form method.
  - As regard the wetted surface, Fig. 5.36 and Fig. 5.40, Savitsky short form method and Numerical-fine-grid results are comparable: with respect to experimental results, the percentage error is about 4.2%. Numerical-medium-grid and Numerical-coarse-grid results have been compared against experimental results and the percentage errors is about 7.0% and 11.7% respectively.

  - The longitudinal pressure distributions evaluated through Morabito method follow the trend of longitudinal pressure distributions numerically evaluated, Fig. 5.94 to Fig. 5.108. The percentage error between these two methods is about 4.3%. It was not possible to compare them against experimental results.

- Warped 2 hull

  - The accuracy of numerical results improved significantly with mesh refinement (cells number increased from 984437 to 1422707 and 2090231).

  - As regard the resistance, Fig. 5.41 and Fig. 5.45, Savitsky short form method gives the best results: with respect to experimental results, the percentage error is about 1.8%. Numerical-fine-grid, Numerical-medium-grid and Numerical-coarse-grid results have been compared against experimental results and the percentage errors are about 4.8%, 5.8% and 8.1% respectively.
  - As regard the trim, Fig. 5.42 and Fig. 5.46, Numerical-coarse-grid gives the worst results: with respect to experimental results, the percentage error is about 18.6%. Numerical-fine-grid gives the best results: with respect to experimental results, the percentage error is about 5.2%. Numerical-medium-grid and Savitsky short form methods have been compared against experimental results and the percentage errors are about 10.3% and 14.9% respectively.
  - As regard the sinkage, Fig. 5.43 and Fig. 5.47, Numerical-fine-grid, Numerical-medium-grid and Numerical-coarse-grid results are comparable. There is no significant improvement among different grids. It was not possible to compare them with Savitsky short form method.
  - As regard the wetted surface, Fig. 5.44 and Fig. 5.48, Savitsky short form method gives the best results: with respect to experimental results, the percentage error is about 1.6%. Numerical-fine-grid, Numerical-medium-grid and Numerical-coarse-grid results have been compared against experimental results and the percentage errors is about 6.1%, 8.1% and 14.3% respectively.

  - The longitudinal pressure values evaluated through Morabito method follow the trend of longitudinal pressure distributions numerically evaluated, Fig. 5.109 to Fig. 5.124. The percentage error between these two methods is about 2.6%. It was not possible to compare them against experimental results.

  At 0.25 L and 0.4 L, for each speed and for all half beam, the peaks and transversal pressure distributions of warped hull are always bigger than that

monohedral one, Fig. 5.81 to Fig. 5.88. At 0.55 L, just for v=3.4 m/s, the peak and transversal pressure distribution of warped hull is bigger than that monohedral, Fig. 5.89. At 0.55 L at v=4.6 m/s, the transversal pressure distribution of Warped hull is bigger than that monohedral one, but not the peak, Fig. 5.90. At 0.55 L, at v=5.75 and v=6.32 m/s, the transversal pressure distributions and peaks of monohedral hull are bigger than that warped one for all half beam, Fig. 5.91 and Fig. 5.92.

6 Conclusions

Estimation of hydrodynamic performances is very important step in the analysis of planing hulls. Several methods are commonly used, such as drawing on experience from similar vessels, using empirical data, or performing tests of a scaled-down prototype. Experimental tests are the best way to predict the hydrodynamic performance of hulls. Model tests, however, are costly, as they require the construction of a model prototypes to tight tolerances, as well as the use of a test facility and appropriate electronic instrumentation. With the advancement in the computer hardware and software, numerical techniques have become effective tools for hydrodynamic analysis. The most important advantage of numerical methods is that they do not suffer limitations that are normally encountered in model testing such as the size of the hull, environmental conditions, analysis and interpretation of results for prototype hulls. They also eliminate the cost for construction of laboratory models. Numerical techniques allow for hydrodynamic modeling of real size hulls, investigation of design components in early phases, and obtaining detailed information, which are otherwise impossible to obtain with experiments.

The software chosen to evaluate hydrodynamics performance is Star CCM+, developed by CD-adapco, which can perform calculations of the discretized Reynolds Averaged Navier-Stokes (RANS) equations including viscous effects, turbulence modelling, and free surface constraints on unstructured adaptive grids.

Two hulls: a monohedral hull and a warped hull, already experimentally studied by E. Begovic and C. Bertorello (2012) at Department of Naval Architecture, University of Naples Federico II, at steady speed in calm water were studied. The convergence of the

numerical results is controlled for three mesh refinements: coarse, medium and fine mesh with cells number variation from 1004229, 1432240 to 2147253.

In addition, hydrodynamics performances were also determined by empirical methods: resistance, trim and wetted surfaces through Savitsky method and longitudinal hydrodynamic pressure distribution by Morabito method. The results by experimental, empirical and numerical methods are compared.

The reported results shown that Savitsky method gives the best results for resistance and wetted surface (difference from experimental in the order of 2%), while CFD calculations are more accurate than Savitsky method for trim angle. Longitudinal pressure distributions evaluated from CFD calculations are very close to results of Morabito method.

As regard transversal pressure distributions at 0.25 L and 0.4 L, for each speed and for all half beam, the peaks and transversal of warped hull are always bigger than that monohedral one. At 0.55 L, just for v=3.4 m/s, the peak and transversal pressure distribution of warped hull is bigger than that monohedral. At 0.55 L at v=4.6 m/s, the transversal pressure distribution of warped hull is bigger than that monohedral one, but not the peak. At 0.55 L, at v=5.75 and v=6.32 m/s, the transversal pressure distributions and peaks of monohedral hull are bigger than that warped one for all half beam.

The results of numerical simulations showed that the numerical model was qualitatively consistent with experimental observations. The stagnation and spray root lines are in good agreement with photographs of the physical models. Pressure profiles follow the expected trends with a peak in correspondence of the stagnation point and a tendency to decrease along the stagnation line, until reaching the trailing edge of chine, and along the longitudinal sections, until reaching the trailing edge of the stern. It can be concluded that as regard resistance, trim, wetted surface and pressure distribution good qualitative and quantitative agreement between the numerical and experimental results is obtained.

It is well known that the quality of the results by CFD is affected by the quality of mesh, and very often this means very huge calculation time, in this thesis the calculation time for the fine mesh was about 24 hours at 32 processors offered by Scope Calculation Centre. It can be also commented that the empirical methods both well known Savitsky and the new one Morabito are very efficient specially at the design stage. They can't predict all physical properties and are limited on the planning regime but are extremely fast and easy to use and surely more "convenient" for the designer practice.

References[3]

Almeter J.M., *Resistance Prediction of Planing Hulls: State of the Art*, Marine Technology, Vol. 30, No. 4, Oct. 1993, pp. 297-307.

Azcueta R., Caponetto M., Soding H., 2003, *Motion simulations for planing boats in waves*. Ship Technology Research, 4, 182-198.

Bastide G., 2014, *Resistance computation of a fast planning vessel by a commercial CFD code*, Master Thesis at University of Genova.

Battistin D., and Iafrrati, *A Numerical Model for Hydrodynamoc of planing Surfaces*, Proc. 7th Int. Conf. Fast Sea Transportation FAST2003, , 2003.

Begovic E., Bertorello C., Pennino S., 2014, *Experimental seakeeping assessment of a warped planing hull model series*, Ocean Eng. 83, 1-15.

Begovic E., Bertorello C., 2012, *Resistance assessment of warped hull forms*. Ocean Eng. 56, 28–42.

Begovic E., Bertorello C., 2009, *Experimental assessment of seakeeping characteristics for non-monohedral planing hull*, Proceeding 13th Conference of Inter- national Maritime Association of the Mediterranean, IMAM'09, Istanbul, Turkey, October 2009.

Bertorello C., Muggiasca S., Fossati F., 2010, *High Speed Small Craft Aerodynamic Lift and Drag*, 7th International Conference HIPER 2010, Melbourne, FL, USA, October 2010.

Bertorello C., Oliviero L., 2009, *Hydrodynamic resistance assessment for non- monohedral planing hull*, Proceeding 13th Conference of International Maritime Association of the Mediterranean, IMAM '09, vol. 2, pp. 703–707, Istanbul, Turkey, October 2009.

Bertorello, C., Oliviero, L., 2007, *Hydrodynamic Resistance Assessment of Non- Monohedral Planing Hull Forms based on Savitsky's Method*. Australian Journal of Mechanical Engineering, vol. 4, No.2, pp 209–224. Engineers Media, CROWS NEST, Australia. (ACN 001311511).

Bertorello, C., Oliviero, L., 2006, *Hydrodynamic Resistance Assessment of Non- Monohedral Planing Hull forms based on Savitsky's Method*. In High performance marine vehicles, Lounceston, Australia, pp. 432–446.

Best practice guidelines for marine applications of computational fluid dynamics.

Blount D., Fox W., 1976, *Small-Craft Power Prediction*. Marine Technology, January, Society of Naval Architects and Marine Engineers, Jersey City, NJ.

[3] In alphabetical order

Brizzolara S., Bovio M., Federici A., Vernengo G., 2011, *Hydrodynamics design of a family of hybrid SWATH unmanned surface vehicles*. Proceedings of the 11th International Conference on Fast Sea Transportation, Honolulu (USA), September 2011.

Brizzolara S., Serra F., 2007, *Accuracy of CFD codes in the prediction of planing surfaces hydrodynamic characteristics*, 2nd International Conference on Marine Research and Transportation, Naples, Italy.

Caponetto M., 2001, *Practical CFD Simulations for planing hulls*, HIPER.

Cao H., 2008, *The computation and research on resistance of planing craft based on the software FLUENT*. PhD thesis, Harbin Engineering University, Harbin, 44-53.

CD-adapco (2014) *STAR-CCM+ User Guide*, version 9.04.

CD-adapco (2011) *STAR-CCM+ User guide*, version 7.02.

Cimolin F, Serra F, Vatteroni G, 2014, *Optimization of the hull resistance for the Azimut 95' yacht with CFD*, HSMW Naples, October 2014.

Clement E.P., Blount D.L., 1963, *Resistance Tests of a Systematic Series of Planing Hull Forms*, Transactions SNAME pp 491–579.

De Luca F, Pensa C., *The Naples warped hard chine hulls systematic series – First part: resistance in still water*, University of Naples Federico II, Naples. X HSMV 2014.

Du Cane P., 1974, *High Speed Small Craft*. David & Charles (Holdings) Limited, Abbot, England.

Faltinsen O. M., *Hydrodynamics of high-speed marine vehicles*, Norwegian University of Science and technology, 2005.

Ferziger J., Peric M., 2003, *Computational methods for fluid dynamics*, 3rd edition, Springer-Verlag.

Fu T.C., Ratcliffe T., O'shea T.T., Brucker K.A., Graham R.S., Wyatt D.C., Dommermuth D.G., 2010, *A comparison of experimental measurements and computational predictions of a deep-V planing hull*, 28th Symposium on Naval Hydrodynamics. Pasadena, California, 12-17 September 2010.

Ghadimi P., Mirhosseini S.H., Dashtimanesh A., Amini M., 2013, *RANS simulation of dynamic trim and sinkage of a planing hull*, Department of Marine Technology, Amirkabir University of Technology, Tehren, Iran. No. 1, 6-10.

Ghadimi P., Tavakoli S., Dashtimanesh A., Djeddi S. R., 2013, *Three-Dimensional mathematical investigation of dynamic and hydrostatic distributions on planing hulls*, Department of Marine Technology, Amirkabir University of Technology, Hafez Avenue, No. 424, P.O. Box 15875-4413, Tehran, Iran.

Ghadimi P., Dashtimanesh A., Farsi M., and Najafi S., *Investigation of free surface flow generated by a planing flat plate using smoothed particle hydrodynamics method and FLOW3D simulations*, Journal of Engineering Maritime Environment, 2012.

Ikeda Y., Yokomizo K., Hamasaki J., Umeda N, Katayama T., 1993, Simulation of running attitude *and resistance of a high speeds craft using a database of hydrodynamic forces obtained by fully captive model experiments*, Proceedings of FAST'93.

ITTC – Recommended Procedures and Guidelines, 24th ITTC 7.5-03-02-03, 2011.

ITTC – Quality Manual, 23rd ITTC 7.5-03-01-01, 2002.

Kapryan W. J. and Boyd G. M., *Hydrodynamic pressure distribution obtained during a planing investigation of five related prismatic surfaces*, NACA Technical Note, 1955.

Keuning J.A., Gerritsma J., van Terwisga P.F., 1993, *Resistance tests of a series planing hull forms with 30 degrees deadrise angle and a calculation method based on this and similar systematic series*. International Shipbuilding Progress. 40(424),333–382.

Keuning J.A., Gerritsma J., 1982, *Resistance tests of a series planing hull forms with 25 degrees deadrise angle*. International Shipbuilding Progress Vol. 29 (337), 333–382.

Kihara H., *A Computing Method for the Flow Analysis around a Prismatic Planing-Hull*, 2nd International Conference on High Performance Marine Vehicles, Australia, 8-10 November 2006.

Kowalyshyn D., Metcalf B., 2006, *AUSCG systematic series of high speed planing hulls*. Trans SNAME, 268–309.

Malin S., 2013, *Application of CFD to seakeeping*, Master Thesis an NTNU, Norwegian University of Science and Technology, Department of Marine Technology.

Maysam Mousaviraad S., Wang Z., Stern F., 2015, *URANS studies of hydrodynamic performance and slamming loads on high-speed planing hulls in calm water and waves for deep and shallow conditions*, IIHR-Hydroscience & Engineering, The University of Iowa, Iowa City, IA 52242-1585, USA. Ocean Research 51 (2015) 222–240.

Metcalf B,J., Faul L., Bumiller E., SlutskyJ., 2005, *Resistance Tests of a Systematic Series of U.S. Coast Guard Planing Hulls*, Carderock Division, Naval Surface Warfare Center, Report no. NSWCCD-50-TR-2005/063 December 2005.

Morabito M. G., *On the spray and bottom pressures of planing surfaces,* Ph.D. thesis, Stevens Institute of Technology, 2010.

Oliviero L., 2010, *Hydrodynamics of Planing Hulls. A Power Prediction Method for Warped V-Bottom Hull Forms*, Ph.D. Thesis, University of Naples Federico II.

Ozdemir Y. H., Barlas B., Yilmaz T., Bayraktar S., *Numerical and experimental study of turbulent free surface flow for a fast ship model*, 65 (1) 2014.

Ozdemir Y. H., Bayraktar S., Yilmaz T., 2007, *Computational investigation of a hull*, 2nd International Conference on Marine Research and Transportation, Naples, Italy.

Ozum S., Sener B., Unlugencoglu K., 2010, *Resistance prediction of a high speed craft by using CFD.* Department of Naval Architecture and Marine Engineering, Yildiz Technical University, Istanbul, 34349, Turkey.

O'Shea T.T., Brucker K.A., Wyatt D., Dommermuth D.G., Fu T.C., 2012, *A detailed validation of numerical flow analysis (NFA) to predict the hydrodynamics of a deep-V planing hull.* 3th Chesapeake Power Boat Symposium. 2012.

O'Shea T.T., Dommermuth D.G., Wyatt D.C., Ratcliffe T., Weymouth G.D., Hendrikson K.L., Yue D.K.P., Sussman M., Adams P., Valenciano M., 2007, *An application of Cartesian-grid and volume-of-fluid methods to numerical ship hydrodynamics*, 9th International Conference on Numerical Ship Hydrodynamics. Ann Arbor, Michigan, August 5-8, 2007.

Payne R.P., *The Dynamic Force on a Two-Dimensional Planing Plate of Arbitrary Camber*, Journal of Ocean Engineering, Volume 9, 1982.

Pranzitelli A, de Nicole C., Miranda S., 2011, *Steady-state calculations of free surface flow around ship hulls and resistance prediction.* Proceedings of the 9th High Speed Marine Vessels Symposium, Naples, May 2011.

Pierson J. D. and Leshnover S., *A study of the flow, pressure and loads pertaining to prismatic vee-planing surfaces*, Report SIT DL 50382, Davison Laboratory, 1950.

Radojcic D., 1985, *An Approximate Method For Calculation of Resistance and Trim of the Planing Hulls*, Ship Science Report No.23, December.

Radojcic D., Zgradic A., Kalajdzic M., Simic A., *Resistance Prediction for Hard Chine Hulls in the Pre-Planing Regime*, Polish Maritime Research 2(82) 2014 Vol 21; pp. 9-26 10.2478/pomr-2014-0014.

Santoro N., Begovic E., Bertorello C., Bove A., De Rosa S., Franco F., 2014, *Experimental study of the hydrodynamic loads on high speed planing craft*, at Department of Industrial Engineering, University of Naples Federico II, Via Claudio 21, Naples 80125, Italy. International Symposium on Dynamic Response and Failure of Composite Materials, DRaF2014. Proceedings Engineering 88 186-193.

Savitsky D., *The effect of bottom warp on the performance of planing hulls*, Davidson Laboratory, Stevens Institute of Technology, 3rd Chesapeake power boat symposium, Annapolis, Maryland, 2012.

Savitsky D., De Lorme M.F., Datla R., 2006, *Inclusion of "Whisker Spray" Drag in Performance Prediction Method For High-Speed Planing Hulls*, Technical Report SIT-DL-06-9-2845, Presented at Meeting of New York Metropolitan Section The SNAME March 14, 2006.

Savitsky D., Koebel J.G., 1993, *Seakeeping Considerations in Design and Operation of Hard Chine Planing Hulls*, Tech. Res. Bull. R-42, 124 Jersey City (USA): SNAME.

Savitsky D., 1964, *Hydrodynamic design of planing hulls.* SNAME Mar. Technol. 1 (1), Oct1964.

Smiley R. F., *A study of water pressure distribution during landing with special reference to a prismatic model having a heavy loading and a 30-degree angle of deadrise*, NACA Translation, 1950.

Smiley R. F., *An experimental study of the water-pressure distributions during landing and planing of a heavily loaded rectangular flat-plate model*, NACA Technical Note 2453, 1951.

Stern F., Wang Z., Yang J., Sadat-Hosseini H., Mousaviraad M., Bhushan S., Diez M., Yoon S., Wu P., Yeon S., Dogan T., Kim D., Volpi S., Conger M., Michael T., Xing T., Thodal R., Grenestedt J., 2014, *Recent progress in CFD for Naval Architecture and Ocean Engineering (Keynote speaker)*. IIHR-Hydroscience and Engineering, University of Iowa City, IA, USA. Proceedings of the 11th International Conference on Hydrodynamics (ICHD 2014), October 19-24, Singapore.

Su Y., Chen Q., Shen H., Lu W., 2012, *Numerical simulation of a planing vessel at high speed*. State key Laboratory of Autonomous Underwater Vehicle, Harbin Engineering University, Harbin 150001, China.

Taunton D.J., Hudson D.A., Shenoi R.A., 2011, *Characteristics of a series of high speed hard Chine planing hulls—Part I: Performance in Calm Water*. Int. J. Small Craft Technol.153.

Taunton D.J., Hudson D.A., Shenoi R.A, 2011, *Characteristics of a series of high speed hard Chine planing hulls—Part II*: Performance in waves. Int. J. Small Craft Tecnol.153.

Thornhill E., 2002, *Application of a general CFD code to planing craft performance*. National Library of Canada, 395 Wellington Street Ottawa ON K1A 0N4 Canada. ISBN: 0-612-84073-5.

Thornhill E., Veitch B., Bose N., 2000, *Dynamic instability of a high speed planing boat model*. Marine Technology.

Thornhill E. Oldford D., Bose N., Veitch B., Liu P., 2001, *Planing hull model test for CFD validation*, 6th Canadian Marine Hydrodynamics and Structures Conference. 23-26 May, 2001, Vancouver BC.

Versteeg H.K., Malalasekera W., 1995, *An introduction to computational fluid dynamics – The finite volume method*. Longman Scientific & Technical. ISBN: 0-582-21884-5.

Wackers J., Deng G., Leroyer a., Queutey P., Visoneaun M., 2012, *Adaptive grid refinement for hydrodynamic flows. Journal of Computers and Fluids*, vol. 36, no. 9, pp. 1481-1510.

Wagner H., *Phenomena associated with impacts and sliding on liquid surfaces*, NACA Translation, 1932.

Wellicome J. F. and Jahangeer Y. M., *The prediction of pressure loads on planing hulls in calm water, Royal Institution of Naval Architects*, no. 2, pp. 53–70, 1978.

Zhaoli W., Jianglong N., Zaibai Q., Yongjie P., 2009, *The computation resistance of planing craft based on the CFD techniques*, 14th conference on China Ocean Engineering, Hohbot, 309-315.